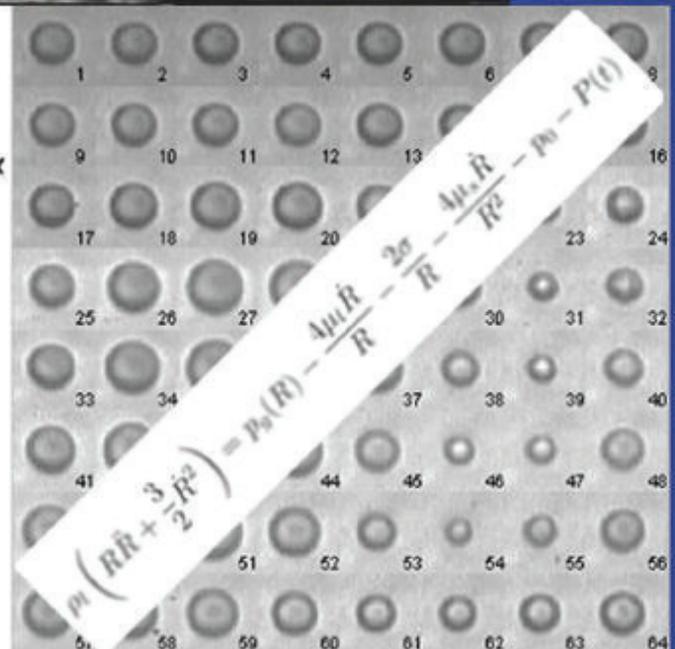
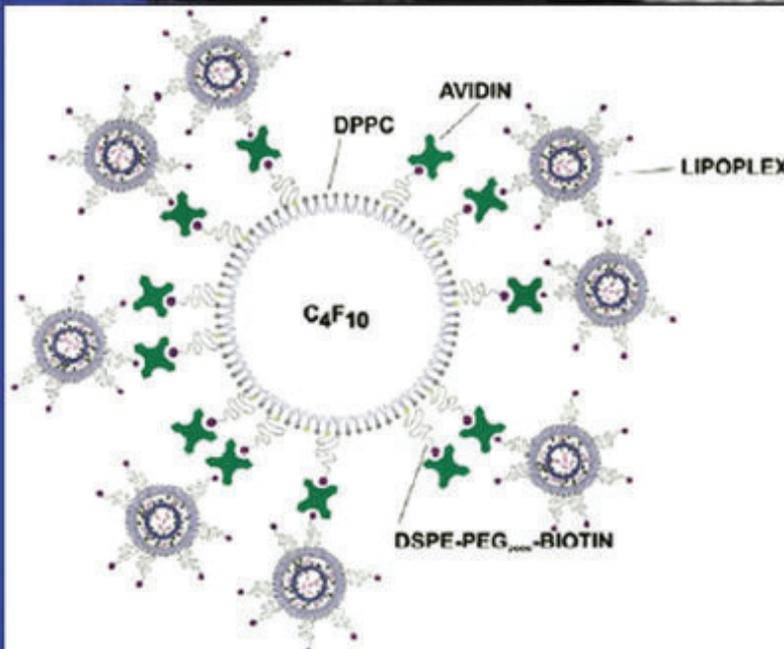
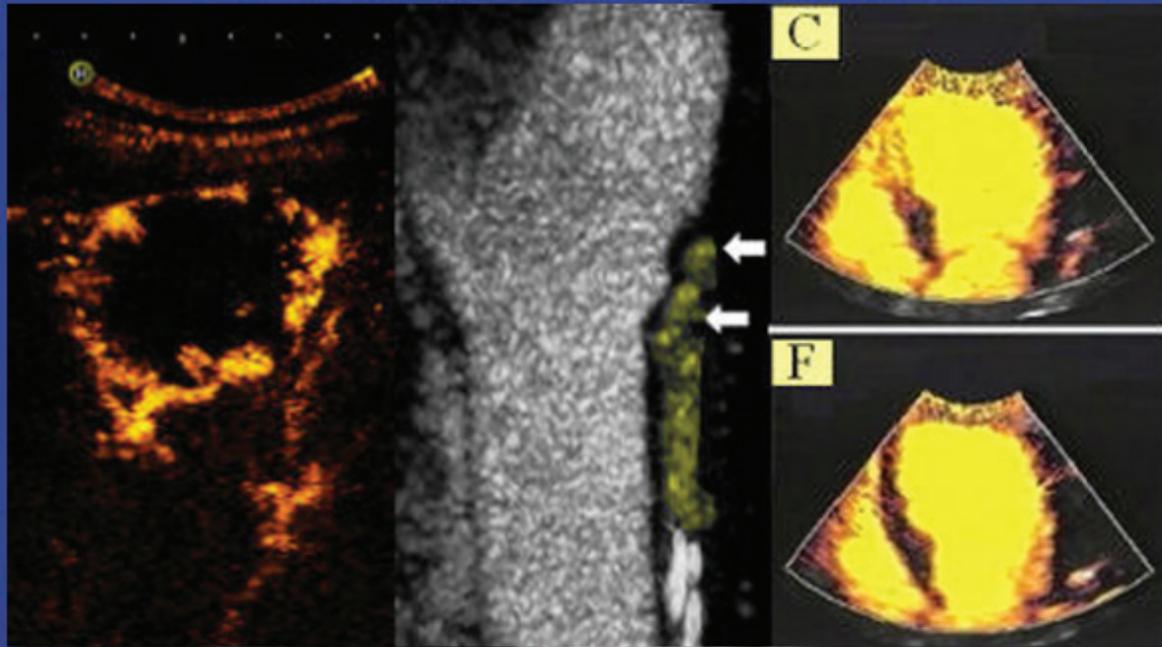


# The 23<sup>rd</sup> European Symposium on Ultrasound Contrast Imaging - An ICUS Conference -



## Abstract book

18-19 January 2018, Rotterdam, The Netherlands

Organised by Nico de Jong, Folkert ten Cate, Rik Vos, Klazina Kooiman, and Arend Schinkel

Erasmus MC Rotterdam



Thursday, 18 January 2018

## Evening Program

Grillcafé Bar Bowling “DOK 99”

Straatweg 99 Rotterdam

Dinner Buffet: around 19:00

Coaches will be leaving from Hilton at 18:30 and will be back in Hilton around 22:30

**23<sup>rd</sup> EUROPEAN SYMPOSIUM ON ULTRASOUND CONTRAST IMAGING**  
**18-19 JANUARY 2018, Rotterdam, The Netherlands**

**WEDNESDAY, 17 January 2018**

11.00 – 15.00	Mini Symposium Unveils Confocal Microscope combined with Brandaris 128 Location: Erasmus MC – 23 <sup>rd</sup> floor, room Ee2389 Registration to attend (in order to arrange access to the building): <a href="mailto:m.pruijsten@erasmusmc.nl">m.pruijsten@erasmusmc.nl</a>
10:30	Welcome
11:00 Ine Lentacker	A confocal's perspective on sonoporation
11:25 Liza Villanueva	An ultra-high-speed camera's perspective on sonoporation
11:50 Michel Versluis	Future of ultra-high-speed camera's for microbubble research
12:15	<b>Lunch</b>
13:00 Ayache Bouakaz	Clinical perspective on sonoporation
13:25 Nikon	A1R confocal microscope
13:40 Klazina Kooiman	Future studies with confocal microscope combined with Brandaris 128 ultra-high-speed camera
14:00	Unveiling of confocal microscope combined with Brandaris 128 by Prof.dr. Hans van Leeuwen, dean of Erasmus MC, followed by live demonstration
15:00	<b>Adjourn</b>
18.00 – 20.00	Registration - Welcome Drinks [1 <sup>st</sup> floor, Hilton hotel Rotterdam]

**THURSDAY, 18 January 2018**

**Oral program**

08.00 – 09.00	Registration	
09.00 – 09.10	Introduction and opening .....	<i>Olivier Couture</i>
09.10 – 10.40	<b>ULTRAFAST / HIGH-RESOLUTION IMAGING</b> .....	<i>Chairpersons: Rik Vos and Olivier Couture</i>
Paul Dayton	Superharmonic Ultrasound Imaging and Acoustic Angiography .....	1
Pengfei Song	Towards super-resolution imaging under clinical settings: initial experience in animals and humans .....	2
Matthew Bruce	High(er) frequency contrast enhanced ultrasound (CEUS) .....	4
Anastasiia Panfilova	On what dynamic contrast-enhanced ultrasound tells us about the underlying vascular architecture .....	7
Baptiste Heiles	Volumetric ultrafast Ultrasound Localization Microscopy using a 32x32 Matrix Array .....	12
10.40 – 11.10	<b>Intermission</b>	
11.10 – 12.25	<b>CEUS - Imaging I</b> .....	<i>Chairpersons: Otto Kamp and Folkert ten Cate</i>
Francois Tranquart	Kupffer cell imaging with Sonazoid during liver contrast-enhanced ultrasound examination .....	14
Stefan Engelhard	Ultrasound Particle Image Velocimetry in the Abdominal Aorta: first results in humans and comparison with Phase Contrast Magnetic Resonance Imaging .....	16
Daisy Liu	Changes in renal perfusion precede increased urinary protein excretion caused by weight gain and normalize after weight-loss in dogs .....	18
Lynda Juffermans	The use of contrast-enhanced ultrasound in the assessment of uterine fibroids – a feasibility study .....	20
12.25 – 12.40	<b>David Cosgrove Memorial Lecture</b> .....	<i>Chairperson: Nico de Jong</i>
Rob Eckersley		
12.40 – 13.45	<b>LUNCH</b>	

**THURSDAY, 18 January 2018**

## Oral program

13.45 – 14.15 Peter Burns	<b>Dutch Heart Foundation lecture</b> ..... <i>Chairperson: Liza Villanueva</i> Contrast Ultrasound in the Coming Decade .....	21
14.15 – 15.45 Beat Kaufmann Steven Freear Samir Cherkaoui	<b>MICROBUBBLES: IMAGING AND THERAPY</b> ..... <i>Chairpersons: Mike Averkiou and Ayache Bouakaz</i> Ultrasound molecular imaging of cardiovascular disease ..... Subharmonic Imaging of Liposome-loaded Microbubbles ..... Anti-Inflammatory Therapeutic Treatment Monitoring in Swine Model of Inflammatory Bowel Disease using Dual-Selectin-Targeted Contrast-Enhanced Ultrasound Imaging .....	24 25 28
Jiaqi Zhu Inés Beekers	High frame rate contrast enhanced ultrasound imaging of lymph node in vivo ..... Microbubble – cell interactions revealed with combined confocal microscopy and Brandaris 128 ultra-high speed imaging .....	31 34
15.45 – 16.15	<b>Intermission</b>	
16.15 – 17.45 Thomas Porter	<b>THERAPY - I</b> <i>Chairpersons: Klazina Kooiman and Margaret Wheatley</i> Delayed Enhancement Ultrasound Imaging with Acoustically Activated Definity Droplets in Detecting and Quantifying Myocardial Infarct Size .....	36
Hong Chen Liza Villanueva Jean-Michel Escoffre Filip Istvanic	Microbubble perivascular pump effect for enhancing the local delivery efficiency of intranasally-administered agents ..... Sonodynamic therapy using protoporphyrin IX encapsulated microbubbles inhibits tumor growth ..... New insights in the role of ROS in mechanisms of sonoporation-mediated gene delivery ..... Sonoreperfusion of Microvascular Obstruction: a Step towards Clinical Translation .....	38 40 41 44
18.30 – 22.30	<b>EVENING PROGRAM (Incl. Dinner buffet)</b>	

**FRIDAY, 19 January 2018**

**07.30 – 08.00 Registration**

## Poster sessions

<b>07.30 – 09.00</b>		<b>MODERATED POSTER SESSION A: BIOLOGY</b> ..... Moderator: Klazina Kooiman	
A1)	Filip Plazonic	Ultrasound-activated microbubbles enhance the activity of low-concentration gentamicin against <i>Pseudomonas aeruginosa</i> biofilms .....	46
A2)	Virginie Papadopoulou	Short and long-term effects of oxygen microbubble administrations in a rat fibrosarcoma model and radiotherapy sensitization .....	50
A3)	Mukesh Punjabi	Contrast enhanced ultrasound molecular imaging (CEUMI) of atherosclerosis: Development of a clinically translatable ..... tracer for targeting of vascular cell adhesion molecule 1 (VCAM-1) .....	52
A4)	Silke Roovers	Interactions of drug-loaded microbubbles and ultrasound with a soft tissue environment .....	56
A5)	Sophie Morse	On the safety of brain drug delivery using Rapid-Short Pulse (RaSP) sequences.....	59
A6)	Sandeep Kasoji	Early assessment of tumor response to radiation therapy using super-harmonic contrast enhanced microvascular ultrasound imaging.....	62
A7)	Samantha Fix	Accelerated clearance of ultrasound contrast agents containing polyethylene glycol (PEG) is associated with a PEG-specific immune response.....	64
A8)	Shashank Sirsi	Monitoring and Control of Liposomal Doxorubicin in Tumors using Ultrasound Contrast Agents .....	66
<b>07.30 – 09.00</b>		<b>MODERATED POSTER SESSION B: TECHNOLOGY</b> ..... Moderator: Rik Vos	
B1)	Massimo Mischi	Exploiting Microbubble Flow Dynamics to Improve Super-resolution Ultrasound imaging.....	68
B2)	Takeshi Okada	Experimental study on acoustic effects of an elastic wall on translational dynamics of an oscillating bubble .....	71
B3)	Mengxing Tang	3D Flow Reconstruction Based on Multiple 2D Contrast Enhanced High-Frame-Rate Ultrasound Measurements .....	73
B4)	Nadir Cohen/Dan Adam	Semi-Automatic Segmentation of the LV Cavity in Contrast Enhanced Echocardiographic Clips .....	76
B5)	Alec Thomas	Shell Mechanics of Lung Surfactant Microbubbles .....	78
B6)	Vincent Hingot	Incompressible perfusion time of microbubbles in capillaries drives the fundamental compromise between spatial resolution and acquisition time in Ultrasound Localization Microscopy.....	80
B7)	Kai Riemer	Mapping blood flow and wall shear stress in the rabbit abdominal aorta in vivo using native blood speckle and microbubble contrast agent.....	82
B8)	Sara Keller	High Resolution Ultrafast Imaging of Microbubble Activity During Sonoporation .....	85
<b>Wednesday–Friday</b>		<b>POSTER SESSION C: NEW DIRECTIONS I</b> ..... Election by the audience	
C1)	Daisy Liu	Long-term variability of renal perfusion parameters measured by contrast-enhanced ultrasound in healthy dogs.....	89
C2)	Dongwon Lee / Kang Changsun	Molecularly Engineered H <sub>2</sub> O <sub>2</sub> -Activatable Nanoparticles for Contrast-enhanced Photoacoustic Imaging of Thrombosed Vessels .....	91
C3)	Ryo Suzuki	Cancer therapy by the combination of ultrasound contrast imaging agent and non-focused ultrasound induce cancer immune response.....	93
C4)	Olga Koshkina	Perfluorocarbon-loaded Polymeric Nanoparticles with Multi-domain Structure for Multiscale In Vivo Imaging with Ultrasound and 19F MRI .....	94
C5)	Guillaume Lajoinie	Laser-activated microparticles: multimodal contrast imaging .....	96
C6)	Shashank Sirsi	Development of “Microbubble Clusters”: Potential New Applications in Ultrasound Imaging and Drug Delivery.....	98
C7)	Damiano Palmieri	Polymer/lipid hybrid shelled microdroplets behave as attractive ultrasound and photo-thermal phase-change integrated systems .....	100
C8)	Hongjian Chen	Polymer Microbubbles as Dual Modal Contrast Agent for Ultrasound and Computed Tomography.....	102
C9)	Elliott Teston	A versatile and robust microfluidic device for simple or multiple emulsion production .....	106
C10)	Estelle Beguin	Interplay between functionalising and stabilising lipid microbubbles for magnetic targetin .....	108
<b>Wednesday–Friday</b>		<b>POSTER SESSION D: NEW DIRECTIONS II</b> ..... Election by the audience	
D1)	Elizabeth Herbst / John Hossack	NSSA-Based Classification of Tissue and Adherent Microbubble Signals in a Mouse Tumor Model .....	111
D2)	Rogier Wildeboer	Prostate cancer localization through convective-dispersion estimation in three-dimensional contrast ultra-sound .....	113
D3)	Thomas Lacour	Dynamics and vaporization threshold of bubble/droplet system within a nonlinear elastic shell during ADV: a model .....	117
D4)	Baudouin Denis de Senneville	Quantitative Contrast-Enhanced Ultrasound Imaging using a fluid dynamic model.....	118
D5)	Pilsu Kim	Evaluation of Accuracy of Passive Acoustic Mapping for Cavitation Monitoring in Therapeutic Ultrasound.....	122
D6)	Rachel Bott	Characterizing Microbubble Count and Size Distribution Using the Innovative Technique of MEMS Resonant Mass Measurement.....	124
D7)	Martynas Maciulevičius	The Analysis of Sonoporation Metrics.....	125
D8)	Elahe Moghimirad	Contrast enhanced ultrasound imaging: effect of flow on contrast measurements using plane wave versus focused transmissions.....	128
D9)	Ting-Yu Lai	Modeling the acoustic field produced by diagnostic ultrasound arrays in plane wave mode .....	132

**23<sup>rd</sup> EUROPEAN SYMPOSIUM ON ULTRASOUND CONTRAST IMAGING**  
**18-19 JANUARY 2018, Rotterdam, The Netherlands**

**FRIDAY, 19 January 2018**

## Oral program

<b>09.00 – 10.30</b>	<b>BUBBLE TECHNOLOGY</b> ..... <i>Chairpersons: Paul Dayton and Mikhail Shapiro</i>	
Margaret Wheatly Sophie Heymans	Evolution of a Polymer-shelled Ultrasound Contrast Agent.....	136
Juan Rojas	Single-Element Transducer for Simultaneous Ultrasound Therapy and Monitoring of Microbubble-Seeded Acoustic Cavitation.....	139
Tim Segers	Explaining The Differences in Vaporization Threshold of Low Boiling-Point Phase Change Contrast Agents Between in Vivo and In Vitro Activation .....	143
Brandon Helfield	Monodisperse Ultrasound Contrast Agents: Synthesis, Stability, Efficiency, and Dilatational Elasticity .....	145
	Investigating the accumulation of submicron phase-shift droplets in tumours.....	147
<b>10.30 – 11.00</b>	<b>Intermission</b>	
<b>11.00 – 12.30</b>	<b>CEUS – Imaging II</b> ..... <i>Chairpersons: Beat Kaufmann and Dan Adam</i>	
James Choi	On contrast agents for elasticity imaging .....	149
Jeannot Victor	In vivo evaluation of monosize microbubbles: acoustic efficiency and safety .....	151
Arend Schinkel	Safety and feasibility of contrast echocardiography for the evaluation of patients with HeartMate 3 left ventricular assist devices .....	153
Virginie Papadopoulou	Nonlinear microbubble ultrasound imaging for improved decompression stress quantification in humans .....	154
Jason Voorneveld	High Frame Rate Echo-Particle Image Velocimetry for Estimating Flow Patterns in a Left Ventricular Phantom.....	157
<b>12.30 – 13.30</b>	<b>LUNCH</b>	
<b>13.30 – 14.00</b>	<b>COEUR LECTURE</b> ..... <i>Chairperson: Peter Burns</i>	
Mikhail Shapiro	Gas Vesicles: Acoustic Biomolecules for Ultrasound Imaging.....	159
<b>14.00 – 16.00</b>	<b>COMPETITION: DROPLETS</b> ..... <i>Chairpersons: Nico de Jong and Mark Borden</i>	
Yosra Toumia	A Versatile Chromo-responsive Photopolymerized Phase-Change Droplets as Contrast Agent for Ultrasound Imaging .....	160
Oliver Vince	Magnetically and biochemically targeted ultrasound-responsive nanodroplets for therapy of brain metastases .....	162
Kevin Haworth	Tunable Oxygen Scavenging Using Acoustic Droplet Vaporization .....	164
Catharina de Lange	Acoustic Cluster Therapy Microdroplets boost microbubbles enhanced drug delivery .....	169
Ge Zhang	Super-Localisation Ultrasound Imaging using Sparse Activation of Low-Boiling-Point Nanodroplets.....	171
Alexander Klibanov	Perfluorocarbon nanodroplets in liposomes: preparation and triggered contents release by ultrasound.....	175
<b>16.00 – 16.10</b>	<b>CLOSING REMARKS</b> ..... <i>Nico de Jong</i>	
<b>16.10</b>	<b>FAREWELL DRINKS</b>	
	<b>ANNOUNCEMENT OF THE WINNERS OF THE COMPETITION AND POSTER PRIZES</b>	

**Organised by:** Nico de Jong, Folkert ten Cate, Rik Vos, Klazina Kooiman, and Arend Schinkel  
**Scientific board:** Mike Averkiou, Mark Borden, Paolo Colonna, Olivier Couture, Beat Kaufmann, and Eleanor Stride.

# Superharmonic Ultrasound Imaging and Acoustic Angiography

*Paul A. Dayton*

*UNC-NC State Department of Biomedical Engineering*

It has been known for nearly two decades that microbubbles produce highly broadband content with excited with acoustic pulses. Acoustic responses of excited microbubbles can extend past the fourth and fifth harmonics of the excitation frequency. Unfortunately, due to the limited bandwidth of commercial ultrasound transducers, imaging systems have been unable to take advantage of this extremely broad bandwidth content of microbubble echoes. Typical piezoelectric transducers with an optimal bandwidth of 100% perform poorly to even detect the third harmonic. Hence, it has been our goal to develop novel transducer technologies optimized for superharmonic detection. Through the use of multi-frequency piezoelectric transducers or ultra-broadband cMUTs, high-frequency contrast superharmonic imaging can be performed. Superharmonic imaging with Tx/Rx signal separation from multi-frequency transducers provides high resolution images of contrast with a very high contrast-to-noise ratio. When performed in 3-D, this approach provides detailed volumetric maps of contrast flow, reconstructing blood vessel patterns, in-vivo (Figure 1). We refer to high-frequency receive, 3-D implementation of superharmonic imaging as ‘acoustic angiography’ for this reason, as images resemble those of x-ray angiography. Although optimal signal amplitude is derived at pressures that are partially destructive to microbubbles, this approach can be performed at a mechanical index on the order of 0.4-0.6, well within the indicated pressure range for safe use of ultrasound contrast agents. The high frequency receive component limits depth of imaging, however, acoustic angiography can be performed at depths of several centimeters with reduced receive center frequency bandwidth. We demonstrate applications of this microvascular imaging approach in small animals, where malignant angiogenesis can be observed and utilized to differentiate diseased from healthy tissue, as well as first-in human studies.

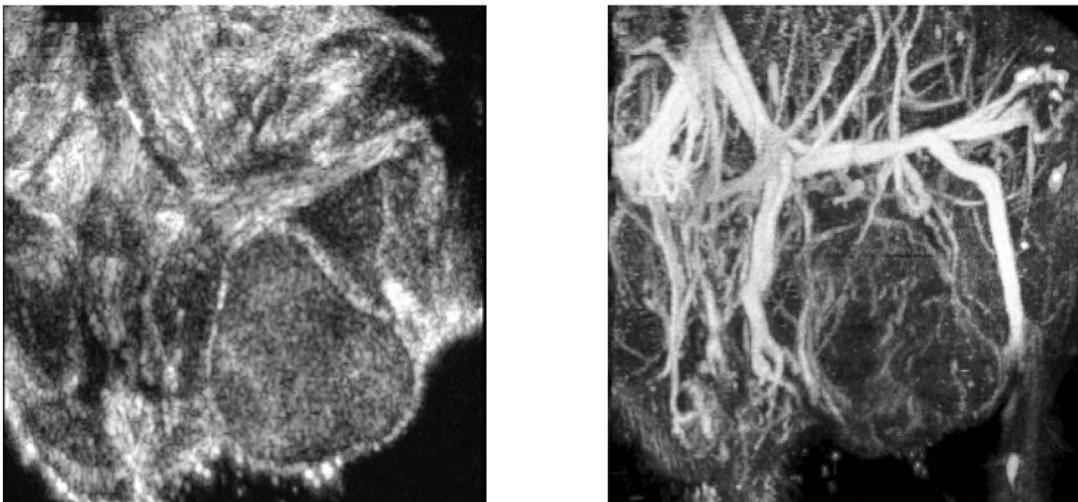


Figure 1. B-mode (left) and a maximum intensity projection of 3-D superharmonic ‘acoustic angiography’ of the same region of interest, showing abdominal vasculature as well as angiogenic vasculature feeding a tumor in a rodent. Image sizes are approximately 2.5 cm x 2.5 cm.

# Towards Super-Resolution Imaging Under Clinical Settings: Initial Experience in Animals and Humans

*Pengfei Song, Ph.D.*

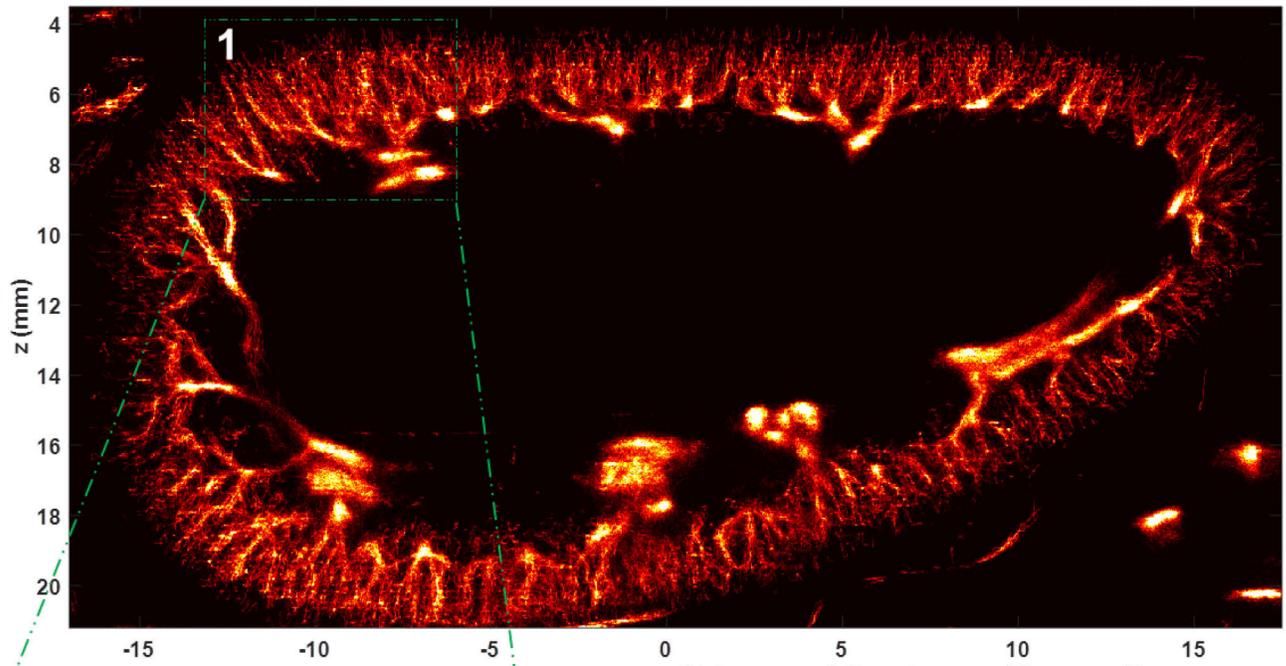
*Department of Radiology, Mayo Clinic College of Medicine, Rochester, Minnesota, USA*

Recently multiple studies have demonstrated microbubble (MB)-based super-resolution imaging (SRI) with  $\sim\lambda/10$  subwavelength resolution on mice and rats. Clinical translation of SRI, however, faces many technical challenges such as low signal-to-noise-ratio (SNR) of the MB signal and physiologic and operator-induced motion in humans. Here we present several methods that take advantage of the rich spatiotemporal information and high frame rate recording of MB signals by ultrafast imaging, and propose a spatiotemporal nonlocal means (NLM) denoising filter and bipartite graph (BG)-based MB pairing and tracking algorithm to achieve robust SRI in vivo under clinical settings.

The SRI signal processing chain consists of signal registration, blinking MB signal extraction, spatiotemporal NLM filtering, MB localization, and BG-based MB pairing and tracking. The NLM filter operates on the spatiotemporal MB data where the moving MB presents unique movement “tracks” while noise manifests in incoherent patterns. This distinct contrast provides strong features for NLM to achieve robust denoising without blurring. The BG-based MB pairing and tracking is based on the principle that with ultrafast imaging, the most likely position that a MB in frame  $n$  will appear in frame  $n+1$  is the location closest to where that MB was in frame  $n$ . An MB pairing algorithm was developed to pair MBs between consecutive frames in a BG fashion with the goal of minimizing total pairing distance. A persistence control was also proposed to facilitate more robust MB tracking in multiple consecutive frames.

For the in vivo animal study, a Verasonics Vantage system and a L11-4v transducer (Verasonics Inc.) were used to image a rabbit kidney with a single bolus injection of microbubbles, with the rabbit free-breathing and freehand scanning. We found substantially decreased noise and significantly improved SRI imaging quality with NLM filtering and BG-based MB pairing. A comparison study showed that the proposed method had lower overall pairing distance than the classic Hungarian assignment algorithm. Fig. 1a shows the final accumulated SRI microvessel image where  $\sim 20\ \mu\text{m}$  microvessels can be visualized in the kidney cortex. Fig. 1b shows the corresponding super-resolution microvessel flow speed image. In vivo human imaging feasibility was demonstrated under a standard clinical imaging setting to image inflamed bowel walls from patients with Crohn’s disease. A single bolus injection of Bracco Lumason was used with the patient free-breathing and the sonographer freehand scanning. The actively inflamed bowel wall showed significantly higher counts of microbubble events and microvessel blood flow speed than the mildly inflamed bowel wall.

(a) VesselQuest<sup>SR</sup> super-resolution microvessel density image of an *in vivo* rabbit kidney



(b) Super-resolution microvessel flow speed image

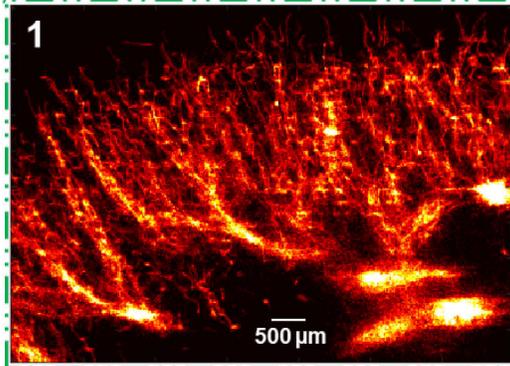
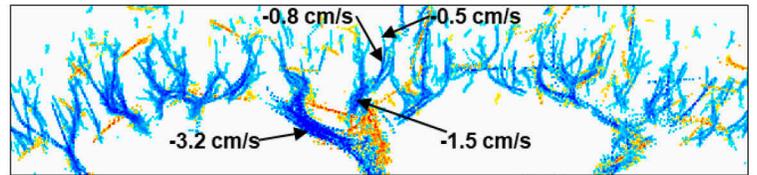


Figure 1. *In vivo* rabbit kidney microvessel super-resolution imaging. A single bolus microbubble injection was used with the rabbit free breathing and the sonographer free-hand scanning. (a) shows the super-resolution microvessel density image (with a sub-region magnified) accumulated from 15 seconds of data acquisition. Microvessels with diameters of  $\sim 20 \mu\text{m}$  can be resolved. (b) shows the super-resolution microvessel blood flow speed map obtained from microbubble tracking. The blood flow speed measurement is Doppler-angle independent.

# High(er) frequency contrast enhanced ultrasound (CEUS)

*Matthew Bruce,<sup>1</sup> Alex Hannah,<sup>1</sup> Charles Tremblay-Darveau,<sup>2</sup> Zin Khaing,<sup>1</sup> Peter Burns,<sup>2</sup> Christophe Hofstetter<sup>1</sup>*

<sup>1</sup> University of Washington, Seattle, USA, <sup>2</sup>University of Toronto, Toronto, Canada

## Introduction

Current methods for in-vivo microvascular imaging are limited by trade-offs between depth of penetration, resolution and acquisition time. For example, microcomputed tomography images vessels down to 10's  $\mu\text{m}$  with deep tissue penetration ( $>3\text{mm}$ ), but requires sacrificing the animal.[1] While noninvasive, MRI requires expensive infrastructure, generates relatively low resolution images and is sensitive to motion. Fluorescence imaging has high spatial resolution ( $\sim 50\mu\text{m}$ ) and fast acquisition times ( $<200\text{ms}$ ), but is limited in penetration of 1-3mm.[2] Optical approaches such as optical computed tomography and photoacoustics, are also limited to imaging depths of a few millimeters.[3]. A robust, economical, easy to use, high resolution technique to assess changes in blood flow at depths of 1-3cm with sub-millimeter resolution would impact a broad range of pre-clinical imaging applications and research, ranging in areas such as oncological, cardiac, vascular and neurological.

Ultrasound has a number of advantages for pre-clinical imaging. It's real-time imaging capabilities provide a non-invasive, economical tool to assess structural tissue and blood flow changes in longitudinal studies. Newer Doppler approaches are enabling the visualization of lower velocity flow in smaller vasculature.[4] However, as Doppler shifts from lower velocity blood flow drop below that of tissue motion, the visualization of blood flow in smaller vasculature including perfusion in the microcirculation is lost. CEUS removes this limitation of detection of lower velocity blood flow by the addition of intra-venously injected microbubbles.

However, traditional approaches of CEUS requiring higher resolution ( $\sim$ sub-millimeter) has been hampered by the diminishing oscillatory response from microbubbles as the frequency increases ( $>7\text{Mhz}$ ).[5] Super resolution approaches borrowed from optical microscopy have been applied to CEUS to produce amazing maps of different vascular trees.[6,7] However, these super-resolution approaches are hampered by long acquisition times and are sensitive to motion artifacts. We demonstrate that plane wave Doppler approaches can both compensate for the weak nonlinear response from microbubbles at elevated frequencies (15MHz) through signal averaging, while at the same time enabling the segmentation and quantification of higher velocity blood flow in typical pre-clinical scenarios (e.g. tissue motion and limited acquisition times). [8,9]

## Methods

The Vantage ultrasound research platform (Verasonics, USA) was used to program plane-wave nonlinear Doppler sequences, using a 15 MHz linear array transducer (Vermon, France). Bolus injections of Definity (Lantheus, USA) were given via tail vein injections in rat and mice models. This approach enabled visualization of both perfusion and macrovascular blood flow. Changes in blood flow in both the micro- and macro- circulations were evaluated in two small animal models. The first model is a spinal cord injury model in evans rats. Acoustic access to the spinal cord is obtained following laminectomy, where the top or lamina are removed by surgery. The second being a transgenic model of an adenocarcinoma lesion in the pancreas of mouse.

## Results

Figure 1 illustrates the improvement in resolution while maintaining sensitivity between the current state of the art (Figure 1a, Epiq ultrasound system, Philips Med. Systems, Netherlands) and our CEUS plane wave Doppler (Figure 1b) approach of a longitudinal plane of a rat spinal cord following injury. The hypoechoic region illustrates loss of blood flow in the microcirculation from a contusion. A slight increase in microbubble signal can also be seen in the center of the spinal cord in Figure 1b, where it is known the grey matter has a higher vascular density.[1] Figure 2 illustrates Doppler processing of the same acquisition and data used for Figure 1b showing perfusion, where the larger vasculature is extracted in Figure 2b and velocity estimates are shown in Figure 2b.

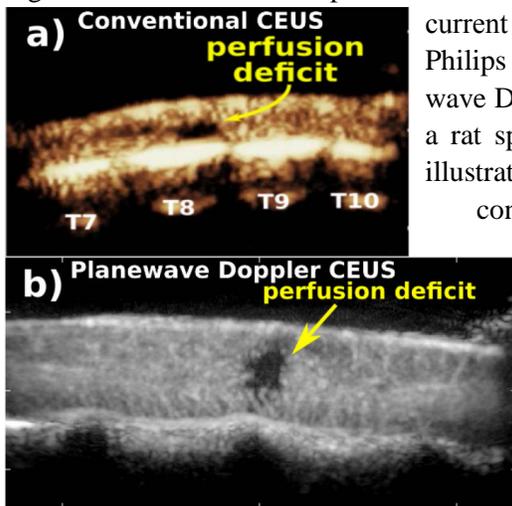


Figure 1. Improvement in resolution and sensitivity between current state of the art (a) and our plane wave 15 MHz CEUS (b) results of rat spinal cord injury.

Except for minor respiratory and spinal cord pulsation motion, the rat spinal cord is relatively stationary enabling long acquisitions, extending into seconds, with minimal blurring. Figure 3 illustrates the resulting perfusion and vascular images of a pancreatic tumor in a mouse following ablative treatment by high intensity focused ultrasound. The mouse respiratory rate of roughly 2 Hz limited the length of the Doppler acquisition and our sensitivity for both perfusion and ability to segment lower velocity blood flow within the tumor. Figures 3a and 3b illustrate an acquisition at a relatively stationary portion of the respiratory cycle. Figures 3c and 3d illustrate an acquisition at in a portion of the respiratory cycle with more motion, illustrating a resulting blurring of both the perfusion and vascular images.

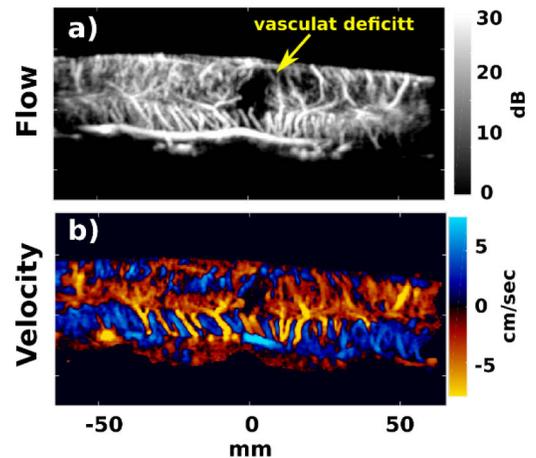


Figure 2. Plane wave 15Mhz CEUS images of rat spinal cords post-injury a) Doppler power showing larger vasculature disruption, b) velocity image.

## Conclusions

The feasibility of imaging of microbubbles using plane-wave nonlinear Doppler sequences at 15 MHz has been demonstrated in both rat and mice models. This approach is able to visualize and quantify blood flow changes in both the micro and macro circulations of rat and mice models under practical imaging conditions with moderate tissue motion. The ability to visualize and quantify blood flow in tissue affected by respiratory and cardiac motion is key in many pre-clinical applications such as the abdomen (e.g. liver, kidney, spleen).

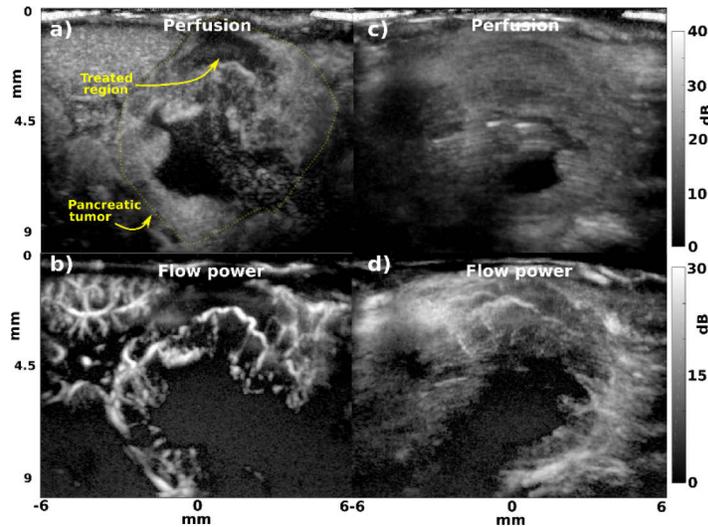


Figure 3. Plane wave 15MHz CEUS images of mouse pancreatic lesion a) perfusion, b) vascular image. c) perfusion image with blurring from respiratory motion. d) vascular image with blurring.

## References

1. Y. Cao, T. Wu, D. Li, S. Ni, J. Hu, H. Lu, et al. Three-dimensional imaging of microvasculature in the rat spinal cord following injury. *Scientific reports, Nature*, 5:12643, 2015.
2. J. Yao, L. Wang, J.-M. Yang, K. I. Maslov, T. T. Wong, L. Li, C.-H. Huang, J. Zou, and L. V. Wang. High-speed label-free functional photoacoustic microscopy of mouse brain in action. *Nature methods*, 12(5):407-410, 2015.
3. F. Yu, H. Kamada, K. Niizuma, H. Endo, P. H. Chan. Induction of mmp-9 expression and endothelial injury by oxidative stress after spinal cord injury. *Journal of neurotrauma*, 25(3):184-195, 2008.
4. J. Bercoff, G. Montaldo, T. Loupas, et al. Ultrafast compound Doppler imaging. *IEEE trans. on ultrasonics, ferroelectrics, and frequency control*, 58(1), 2011.
5. D. Goertz, E. Cherin, A. Needles, R. Karshafian, A. Brown, P.N. Burns, S. Foster. High frequency nonlinear B-scan imaging of microbubble contrast agents. *IEEE trans. on ultrasonics, ferroelectrics, and frequency control*, 52(1), 65-79, 2005.
6. C. Errico, J. Pierre, Y. Desailly, Z. Lenkei, O. Couture, M. Tanter. Ultrafast US localization microscopy for deep super-resolution vascular imaging. *Nature*, 527(7579):499-502, 2015.
7. K. Christensen-Jeffries, R. Browning, M.X. Tang, C. Dunsby, R. Eckersley. In vivo acoustic super-resolution and super-resolved velocity mapping using microbubbles. *IEEE trans. on medical imaging*, 34(2), 433-440, 2015.
8. O. Couture, M. Fink, and M. Tanter, Ultrasound contrast plane wave imaging, *IEEE trans. on ultrasonics, ferroelectrics, and frequency control*, vol. 59, no. 12, pp. 2676-2683, 2012.
9. C. Tremblay-Darveau, R. Williams, L. Milot, M. Bruce, and P. N. Burns. Visualizing the tumor microvasculature with a nonlinear plane-wave Doppler imaging scheme based on amplitude modulation. *IEEE trans. on medical imaging*, 35(2):699-709, 2016.

# On what dynamic contrast-enhanced ultrasound tells us about the underlying vascular architecture

*Anastasiia Panfilova<sup>1</sup>, Sarah E. Shelton<sup>2</sup>, Cristina Caresio<sup>3</sup>, Ruud J.G. van Sloun<sup>1</sup>, Filippo Molinari<sup>3</sup>, Hessel Wijkstra<sup>1,4</sup>, Paul A. Dayton<sup>2</sup>, Massimo Mischì<sup>1</sup>*

<sup>1</sup>*Eindhoven University of Technology, Department of Electrical Engineering, Eindhoven, the Netherlands*

<sup>2</sup>*University of North Carolina at Chapel Hill and North Carolina State University, Joint Department of Biomedical Engineering, United States*

<sup>3</sup>*Politecnico di Torino, Department of Biomedical Engineering, Torino, Italy*

<sup>4</sup>*Academic Medical Center, University of Amsterdam, Department of Urology, Amsterdam, the Netherlands*

## Introduction

Cancer vascular morphology differs from that of healthy tissue [1]. These differences influence the tumor's blood flow dynamics, making dynamic contrast-enhanced ultrasound (DCE-US) a useful technique for cancer diagnostics. By quantitative DCE-US, time intensity curves (TICs) measured at each pixel are typically linearized to represent the time evolution of the ultrasound-contrast-agent (UCA) concentration. The shape of the resulting curves, referred to as indicator dilution curves (IDCs), has been shown useful for cancer diagnostics and is considered to reflect morphological properties of the underlying vascular system [2], [3].

DCE-US can be used for quantification of tissue perfusion, which is expected to increase in cancer lesions due to angiogenic hypervascularization. However, clinical research has demonstrated that perfusion alone is insufficient for an accurate diagnosis: cancer lesions can be iso- or hypo-perfused [4] as well as benign lesions can be hyper-perfused (e.g., fibro adenoma, [5]). A more recent approach quantifies the dispersion of UCAs flowing through the multipath trajectories provided by the numerous branches of the vascular network [6]. To this end, the shape similarity (correlation coefficient) between neighboring IDCs is estimated as an indicator of dispersion. This approach demonstrated its value for prostate cancer diagnostics in several preliminary clinical studies [6], [7]. However, its validation was mainly based on a comparison with histological measures of cell differentiation, disregarding the analysis of vascular features [8].

Characterization of the vasculature can be performed with acoustic angiography (AA), a high-resolution US technique that enables delineation of vessels as small as 100-200 micrometers in diameter [1], [9]. It utilizes a dual frequency transducer, transmitting at 4 MHz, close to the UCA bubble resonance frequency, and receiving the nonlinear UCA signal with a bandwidth centered at 30 MHz. The visualized vasculature can be segmented and characterized for its geometric properties.

The aim of this work is to determine which features of the vascular architecture are reflected in the standard perfusion and dispersion parameters, namely, the wash-in-rate (WIR) and the correlation coefficient between neighboring IDCs. To this end, DCE-US and AA imaging was executed on 9 rats implanted with a fibrosarcoma. Imaging was performed every 3 days, at 4 time

points in total, monitoring the longitudinal evolution of the tumors. We sought for similar longitudinal trends. Moreover, a comparison of the spatial distribution of DCE-US and AA parameters was also performed for several cases.

## Methods

Fibrosarcoma tumor models (Fischer 344 rats) were established from propagated tumor tissue implanted subcutaneously on the left flank of 9 rats. When the tumors were palpable, DCE-US and AA acquisitions of the tumor-bearing flank were performed while the animals were anesthetized with vaporized isoflurane in oxygen.

DCE-US imaging was executed with a Siemens Sequoia US scanner and a 15L8-A probe used in Contrast Pulse Sequencing mode at 7 MHz, following a UCA bolus injection ( $2 \times 10^8$  microbubbles). 3D AA images were acquired with a dual-frequency transducer, insonifying at 4 MHz and receiving at 30 MHz. A continuous infusion of UCA was administered using a syringe pump (PHD 2000, Harvard Apparatus) at a rate of  $1.5 \times 10^8$  microbubbles per minute.

DCE-US dispersion maps were obtained by computing for each pixel the average correlation coefficient between the measured IDC and the IDCs extracted for the surrounding pixels over a ring with inner radius of 0.6 mm and outer radius of 2 mm. Assessment of DCE-US perfusion was performed by estimation of the UCA WIR, computed as the slope of a line fitted to the IDC in a 2-s interval after the appearance time, before the IDC peak.

Visible vessels were manually segmented in the AA volume, and their vessel radius (VR) and the sum of angles tortuosity metric (SOAM) were calculated [10]. The microvascular density (MVD) was calculated as the number of visible vessels per  $\text{cm}^3$ . Values extracted from the tumor regions were assigned to the malignant group, while the surrounding region served as control.

A longitudinal study of the tumor evolution was performed by binning together parameter values for rats from the same time point. The same procedure was performed for the control.

It was noticed in this study that the WIR maps highlight large vessels, clearly visible in the AA volumes (indicated by arrows in Fig.1). When present in the DCE-US plane, these vessels were used as markers to identify the DCE-US plane in the AA volume. The identified corresponding slice ( $\sim 1$  mm thickness) in the AA volume was then processed with an extension of the skeletonization algorithm in [11]. This facilitated a qualitative comparison of the spatial distributions of the VR, SOAM, and MVD with those of perfusion and dispersion in the same plane.

All experiments were approved by the Institutional Animal Care and Use Committee at the University of North Carolina at Chapel Hill.

## Results

The longitudinal analysis shows a relatively stable dispersion for control and tumor, with significantly higher values in tumor (Fig. 1 a.). Perfusion peaks for the young tumors at the second time point, and declines as the tumor develops, remaining higher in tumor compared to control (Fig. 1 b.). The MVD shows a similar trend as perfusion (Fig. 1 b. and c.). Areas with high perfusion, besides large vessels (shown by arrows in the AA in Fig 2. a. and perfusion images in Fig. 2 e.), correspond to areas with high MVD (Fig. 2).

Dispersion and the SOAM have a similar longitudinal trend (Fig. 1 d.). However, different from dispersion, the difference between the SOAM for control and tumor is small. We were not able to find an agreement between the spatial distribution of dispersion and the characteristics extracted from the AA slices (Fig. 2).

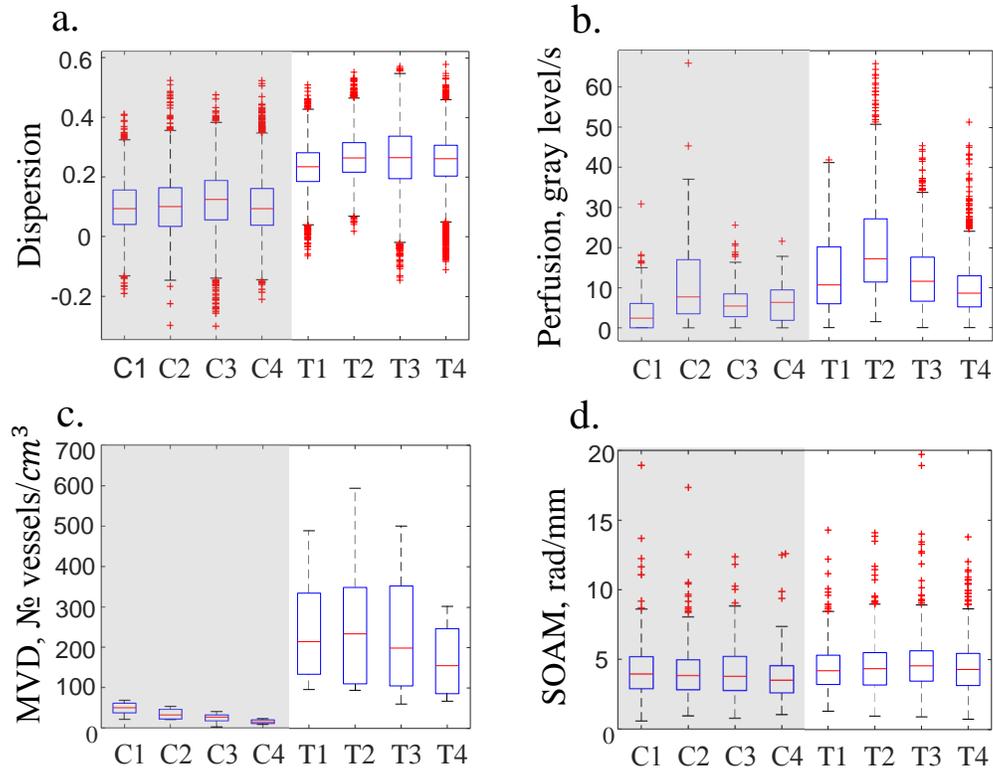


Fig. 1. Longitudinal trends. a-b: DCE-US dispersion and perfusion; c-d: microvascular density and sum of angles metric extracted from AA. Control evolution at time points 1 to 4 (C1, C2, C3, C4) is shown on a gray background. Tumor evolution is on a white background (T1, T2, T3, T4).

## Conclusions and Discussion

The parametric maps of dispersion and perfusion seem complementary (Fig. 2), highlighting different regions of the tumor. No agreement could be found between dispersion and the extracted AA features. Instead, the performed analysis indicates perfusion and MVD to be better correlated. Yet, we should consider that the MVD extracted in this work is limited to vessels larger than 100-200 micrometers in diameter. Interestingly, dispersion provided the best tumor classification, also compared to AA parameters. Altogether, we may conclude that important microvascular features relate to smaller vessels, which could not be investigated by AA. Indeed, additional studies are required to investigate the relationship between smaller vessels with the corresponding perfusion and dispersion maps. Such studies may elucidate the relation between cancer angiogenic processes and the estimated perfusion and dispersion maps.

## Acknowledgement

This work was supported by the European Research Council Starting Grant (\#280209) and the Impulse2 program within TU/e and Philips.

This work was also supported by R01CA170665, R43CA165621, R01CA189479, and F99CA212227 from the National Institutes of Health. Paul Dayton is an inventor on a patent describing acoustic angiography and a co-founder of a company which has licensed this technology.

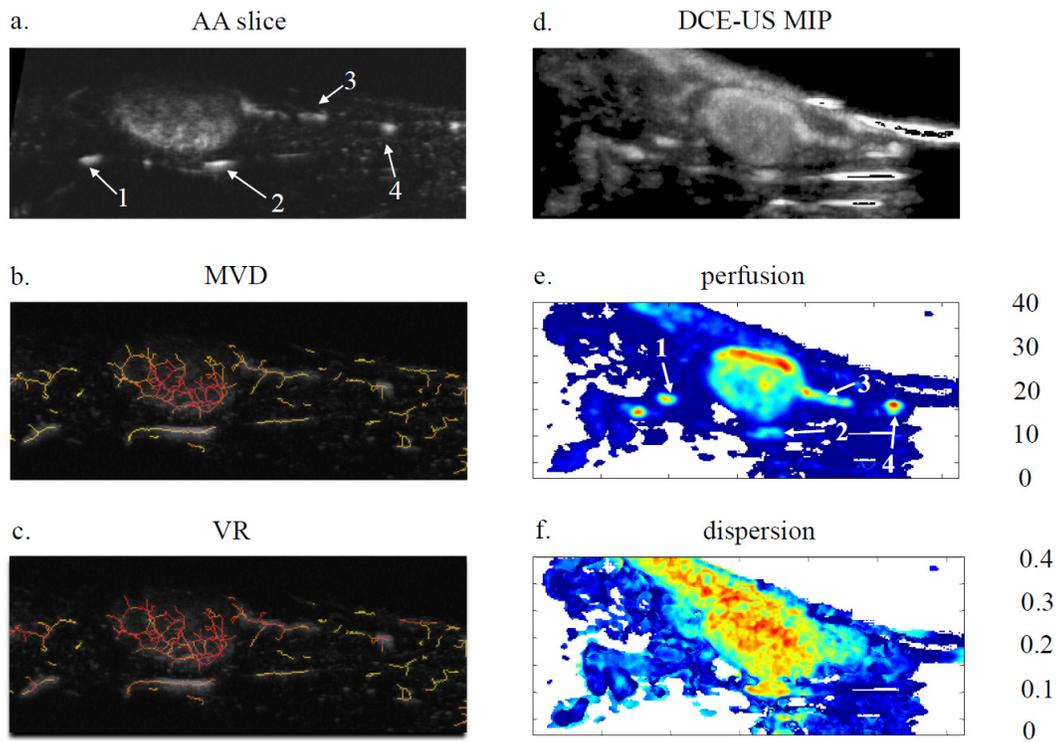


*Fig. 2. Maps illustrating the spatial distribution of the DCE-US and AA parameters. a: AA image reconstructed from 25 slices (~1 mm thickness); b-c: vascular skeleton with the color-coded microvascular density and mean vessel radius, respectively (red indicating high values and yellow - low values). d: DCE-US maximum intensity projection with the black regions corresponding to low intensity regions. e-f: maps of perfusion and dispersion, respectively, with white regions corresponding to low intensity regions, excluded from the analysis. The numbers in the figures point to the large vessel structures that were used to register the DCE-US plane in the AA volume.*

## References

1. S. E. Shelton et al., "Quantification of microvascular tortuosity during tumor evolution using acoustic angiography," *Ultrasound Med. Biol.*, vol. 41, no. 7, pp. 1896–1904, 2015.
2. M. P. J. Kuenen, M. Mischi, and H. Wijkstra, "Contrast-ultrasound diffusion imaging for localization of prostate cancer," *IEEE Trans. Med. Imaging*, vol. 30, no. 8, pp. 1493–1502, 2011.
3. M. P. J. Kuenen, T. A. Saidov, H. Wijkstra, and M. Mischi, "Contrast-Ultrasound Dispersion Imaging for Prostate Cancer Localization by Improved Spatiotemporal Similarity Analysis," *Ultrasound Med. Biol.*, vol. 39, no. 9, pp. 1631–1641, 2013.
4. [M. Brock et al., "Multiparametric ultrasound of the prostate: adding contrast enhanced ultrasound to real-time elastography to detect histopathologically confirmed cancer.," *J. Urol.*, vol. 189, no. 1, pp. 93–8, 2013.
5. E. M. Jung et al., "Contrast enhanced harmonic ultrasound for differentiating breast tumors - first results.," *Clin. Hemorheol. Microcirc.*, vol. 33, no. 2, pp. 109–120, 2005.
6. M. Mischi, M. P. J. Kuenen, and H. Wijkstra, "Angiogenesis imaging by spatiotemporal analysis of ultrasound contrast agent dispersion kinetics," *IEEE Trans. Ultrason. Ferroelectr. Freq. Control*, vol. 59, no. 4, pp. 621–629, 2012.
7. M. P. J. Kuenen, T. A. Saidov, H. Wijkstra, J. J. M. C. H. De La Rosette, and M. Mischi, "Spatiotemporal correlation of ultrasound contrast agent dilution curves for angiogenesis localization by dispersion imaging," *IEEE Trans. Ultrason. Ferroelectr. Freq. Control*, vol. 60, no. 12, pp. 2665–2669, 2013.
8. M. Mischi, C. Heneweer, J. Von Broich-Oppert, T. Saidov, and H. Wijkstra, "Fractal dimension of tumor microvasculature by dynamic contrast-enhanced ultrasound," in *2015 IEEE International Ultrasonics Symposium, IUS 2015*, 2015.
9. R. C. Gessner, C. B. Frederick, F. S. Foster, and P. A. Dayton, "Acoustic angiography: A new imaging modality for assessing microvasculature architecture," *Int. J. Biomed. Imaging*, vol. 2013, 2013.
10. E. Bullitt, G. Gerig, S. M. Pizer, W. Lin, and S. R. Aylward, "Measuring Tortuosity of the Intracerebral Vasculature from MRA Images," *IEEE Trans. Med. Imaging*, vol. 22, no. 9, pp. 1163–1171, 2003.
11. K. M. Meiburger, S. Y. Nam, E. Chung, L. J. Suggs, S. Y. Emelianov, and F. Molinari, "Skeletonization algorithm-based blood vessel quantification using in vivo 3D photoacoustic imaging," *Phys. Med. Biol.*, vol. 61, no. 22, pp. 7994–8009, 2016.

# Volumetric ultrafast Ultrasound Localization Microscopy using a 32x32 Matrix Array

*Baptiste Heiles, Mafalda Correia, Mathieu Pernot, Jean Provost, Mickael Tanter\*, Olivier Couture\**

*Institut Langevin, CNRS, INSERM, ESPCI Paris, PSL Research University, 17 rue Moreau, 75012, Paris*

To overcome the penetration/resolution compromise in ultrasound imaging, localising microbubbles was proposed [Couture et al IEEE IUS 2011]. Inspired by FPALM in optics and thanks to ultrafast ultrasound imaging, ultrafast ultrasound localisation microscopy (uULM) yielded full velocity maps of the rat brain vasculature with a micrometric resolution ( $8\mu\text{m}$ ) [Errico et al. Nature, 2015]. Despite additional successes for tumour imaging [Lin et al, Theranostics, 2017], this plane-by-plane technique suffers from minute-long acquisitions, out-of-plane microbubbles and tissue motion which cannot be corrected for [Hingot et al, Ultrasonics 2017] and the loss of information due to the projection of a 3D vascular structure into a 2D image. It is possible to overcome some of these problems using 2D arrays whether in the same probe [Desailly et al, APL, 2013], or with two confocal probes [Christensen-Jeffries et al, IEEE, UFFC, 2017]. However, the field of view is narrow, tracking microbubbles through frames is difficult because of insufficient pulse repetition frequency, and these techniques are difficult to implement in vivo. We present here a method using an isotropic 2D matrix transducer and a 3D ultrafast ultrasound scanner to perform uULM in a full volume.

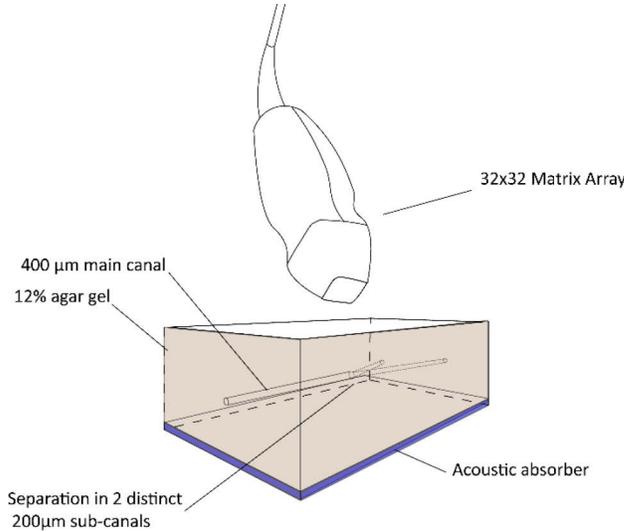


Figure 1 Schematics of the setup

The surface, a Y-shaped microcanal ran with a diameter ranging from  $400\mu\text{m}$  to  $200\mu\text{m}$ . This canal was perfused with a solution of Sonovue microbubbles at controlled flow rates ( $[0.1-2]$  ml/min) for concentration ranging from  $[1/10000:1/100]$  of the Sonovue solution. A 3D uULM process was implemented to determine the position of the microbubbles and render a super-resolved isotropic volume. A 3D tracking algorithm yielded trajectories and velocimetry maps.

The 2D matrix array is made of  $32 \times 32$  transducers arranged in isotropic fashion on a plane. It is controlled by a fully customised programmable 1024-channel system presented in [Provost et al. 2014]. The field of view was insonified with plane waves at 9MHz, 4 different angles for a compounded frame rate of 500Hz for 1 second. The peak-negative pressure (PNP) in this condition is  $-294$  kPa, and the ISPTA is  $385$  mW/cm<sup>2</sup>. Beamforming was done a posteriori on the same computer used for acquisition. The medium to image was a custom built wall-less agar phantom. 12 millimeters away from the

An estimate of  $[10^4-10^5]$  bubbles were recovered depending on the concentration and rendered a super-resolved isotropic volume with a 10x factor (figure 2). Thanks to ultrafast imaging, it was possible to track the microbubbles during the entire duration of each acquisition which is 1 second (figure 3). This yielded velocimetry data allowing us to determine complete speed profiles of the flow inside the phantom. Average velocities measured ranged from 11 to 43 mm/s in magnitude and complete streamlines were reconstructed for each connected bubbles. The streamlines were superresolved with a precision of  $8\mu\text{m/s}$  along the  $[x,y,z]$  axis which allowed to determine average speed profiles depending on the Reynolds number used  $[0.89-5.72]$ . The standard deviations of the speed profiles investigated were calculated for different acquisitions at the same flowrate and ranged from 3 to 9 mm/s depending on the flow conditions. It also proved to be a valuable tool for predicting false positive in the uULM process. Finally, it was possible to determine precisely the position at which the branching begins in the bifurcation by counting the number of particles passing through  $42\mu\text{m}$  slices (figure 4).

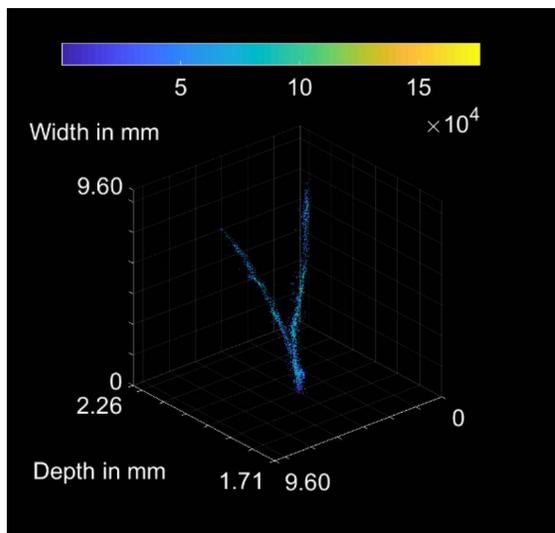


Figure 2 Superresolved volume focused on Y canal (a.u)

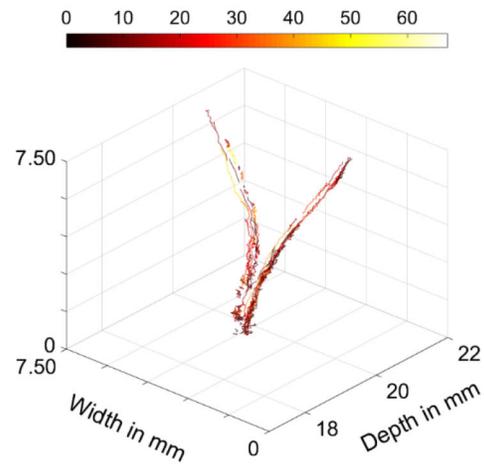


Figure 3 Trajectories of microbubbles tracked during 4 seconds.

The color represents the length of the track in number of consecutive frames

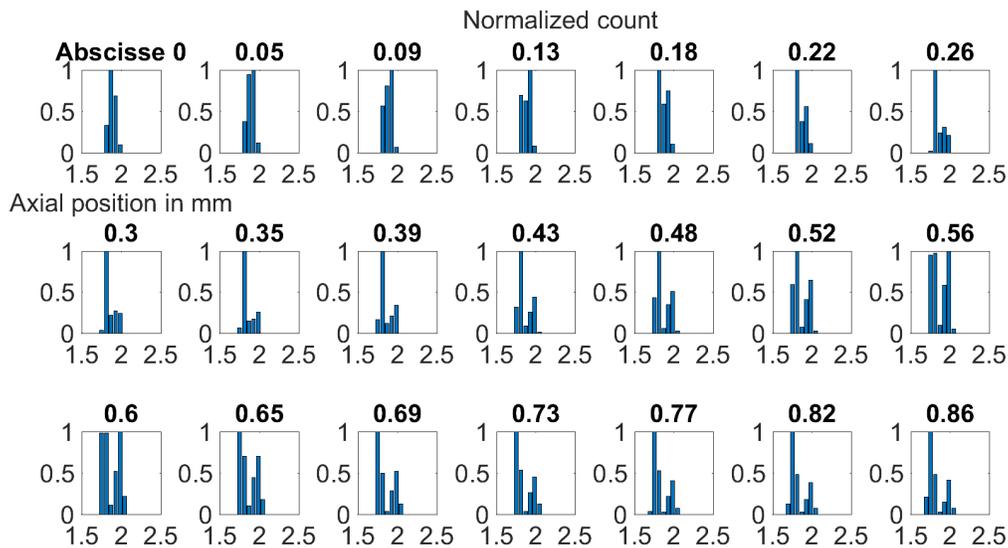


Figure 4 Normalized count of microbubbles for  $42\mu\text{m}$  slices. We can see the bifurcation appearing at abscisse  $0.39\mu\text{m}$

# Kupffer cell imaging with Sonazoid during liver contrast-enhanced ultrasound examination

*F Tranquart, Y Luan*

*R&D Core Imaging, General Electric Healthcare, Amersham UK*

The most recent Guidelines and Good Clinical Practice Recommendations for Contrast-Enhanced Ultrasound (CEUS) in the Liver – Update 2012 [1] emphasizes unique properties of Sonazoid: “Because of their physical size (equal to or smaller than red blood cells), ultrasound contrast agents (UCA) act as blood pool agents and allow depiction of both the macrovasculature and the microvasculature. Despite their varied physicochemical composition, all UCA have similar behaviours for CEUS imaging, rapidly enhancing the vascular pool after intravenous injection, with slow dissipation over about 5 min. An exception to this behaviour occurs with Sonazoid, which has an extended late phase, herein termed the ‘post-vascular phase’ in which it persists for several hours in the liver and spleen, long after it has disappeared from the detectable vascular pool. Sonazoid is phagocytized by Kupffer cells and this undoubtedly contributes to its persistence in the liver. This post-vascular phase is often referred to as ‘the Kupffer phase’.”

Previous studies have shown stable physicochemical characteristics of Sonazoid and have demonstrated its safety and efficacy in clinical application [2]. The potential clinical utility of this long-lasting enhancement in the post-vascular phase in terms of detecting focal liver lesions was first demonstrated in animal studies [3]. Then, it was demonstrated in the pivotal phase 3 registration study performed by Daiichi-Sankyo in Japan [4]. The very stable Kupffer phase imaging is suitable for repeated scanning from 10 to 60 min after contrast injection [5]. The different patterns observed during vascular phase (0-2 min after injection), late phase (2-10 min) and very late phase of Kupffer phase (>10 min) contrast enhancement can be used to distinguish between different types of focal liver lesions effectively.

It has been shown that the long-lasting parenchyma-specific contrast enhancement is due to Sonazoid microbubbles associating with and being taken up exclusively by the macrophages (i.e., Kupffer cells) that line the sinusoids and not by parenchyma, stellate or endothelial cells [6]. Further studies provide good evidence that intact Sonazoid microbubbles are taken up into Kupffer cells [7-8]. While Watanabe et al. concluded that the long-lasting hepatic parenchyma-specific contrast provided by Sonazoid is due to distribution of the microbubbles in Kupffer cells, it is likely that this phase of contrast enhancement is due to a combination of entrapment of microbubbles within the liver sinusoids due to association with the Kupffer cells and uptake of intact microbubbles by the Kupffer cells.

All these elements demonstrate that the Kupffer cell uptake that is related to specific properties of Sonazoid, thanks to its shell constituents is offering significant opportunities for focal liver lesion detection and characterization.

## References

1. Claudon et al., *Guidelines and good clinical practice recommendations for contrast enhanced ultrasound (CEUS) in the liver--update 2012: a WFUMB-EFSUMB initiative in cooperation with representatives of AFSUMB, AIUM, ASUM, FLAUS and ICUS*, *Ultraschall Med.* 34(1), 2013.
2. Sontum, *Physicochemical characteristics of Sonazoid™, a new contrast agent for ultrasound imaging*, *Ultrasound in Med. & Biol.*, 34(5), 2008.
3. Forsberg et al., *Hepatic tumour detection: MR imaging and conventional US versus pulse-inversion harmonic US of NC100100 during its reticuloendothelial system-specific phase*, *Radiology*, 222(3), 2002.
4. Moriyasu and Itoh, *Efficacy of perflubutane microbubble-enhanced ultrasound in the characterization and detection of focal liver lesions: phase 3 multicenter clinical trial*, *AJR Am J Roentgenol.*, 193, 2009.
5. Hatanaka et al., *Contrast enhanced ultrasonography for diagnosis of hepatic malignancies: comparison with contrast-enhanced CT.*, *Oncology*, 75, 2008.
6. Kindberg et al., *Hepatic clearance of Sonazoid perfluorobutane microbubbles by Kupffer cells does not reduce the ability of liver to phagocytose or degrade albumin microspheres.*, *Cell Tissue Res.* 312(1), 2003.
7. Watanabe R. et al., *Characterization of tumor imaging with microbubble-based ultrasound contrast agent, Sonazoid™, in rabbit liver.*, *Biological and Pharmaceutical Bulletin*, 28, 2005.
8. Watanabe et al., *Mechanism of hepatic parenchyma-specific contrast of microbubble-based contrast agent for ultrasonography: microscopic studies in rat liver.*, *Invest Radiol.*, 42(9), 2007.

# Ultrasound Particle Image Velocimetry in the Abdominal Aorta: first results in humans and comparison with Phase Contrast Magnetic Resonance Imaging

*Stefan Engelhard<sup>1</sup>, Jason Voorneveld<sup>2</sup>, Hendrik Vos<sup>2</sup>, Jos Westenberg<sup>3</sup>, Frank Gijsen<sup>2</sup>, Pavel Taimr<sup>4</sup>, Michel Versluis<sup>5</sup>, Nico de Jong<sup>2</sup>, Jean Paul de Vries<sup>6</sup>, Erik Groot Jebbink<sup>1,5</sup>, Johan Bosch<sup>2</sup>, Michel Reijnen<sup>1</sup>*

<sup>1</sup> Department of Vascular Surgery, Rijnstate Hospital, Arnhem, The Netherlands

<sup>2</sup> Department of Biomedical Engineering, Thorax Center, Erasmus MC, Rotterdam, The Netherlands

<sup>3</sup> Department of Radiology, Leiden University Medical center, Leiden, The Netherlands

<sup>4</sup> Gastroenterology & Hepatology, Erasmus MC, Rotterdam, The Netherlands

<sup>5</sup> Physics of Fluids group, MIRA Institute, University of Twente, Enschede, The Netherlands

<sup>6</sup> Department of Vascular Surgery, Sint Antonius Hospital, Nieuwegein, The Netherlands

**Keywords:** *contrast enhanced ultrasound - particle image velocimetry – abdominal aorta – phase contrast magnetic resonance imaging*

## Introduction

Visualisation of local flow patterns in the aorto-iliac artery is challenging, but clinically relevant as specific flow perturbations could affect atherosclerotic disease progression, aneurysm growth and stent patency. Spatial and temporal quantification of blood flow around the aortic bifurcation could provide insights into these mechanisms. In this study, the in vivo feasibility of high frame rate contrast enhanced ultrasound (HFR-CEUS) imaging in combination with particle image velocimetry (PIV), or echoPIV, was studied and compared to 3-dimensional, time resolved phase contrast MRI (PC-MRI).

## Method

14 healthy volunteers (age 18 to 35 and BMI < 25) received multiple HFR-CEUS measurements using a Verasonics ultrasound machine. Different ultrasound contrast agent (UCA) dosages (0.25ml, 0.5ml, 0.75ml, 1.5ml) and transducer transmitter voltages (30V, 20V, 10V and 5V) were assessed, using a C5-2 abdominal transducer and a diverging “plane” wave acquisition scheme. PIV analysis was performed through pairwise cross-correlation of all HFR-CEUS images. PC-MRI volume scans were performed on a Phillips Ingenia 3.0T MRI scanner and velocity data was extracted from oblique planes that were anatomically matched to the HFR-CEUS images. Qualitative and quantitative comparison of the two-dimensional echoPIV and PC-MRI velocity data was performed.

## Results

HFR-CEUS measurements were successful in all volunteers. Optimal PIV results were achieved with a 0.25 or 0.5 mL bolus of UCA in combination with 10V or 5V transmitter voltage. Qualitative analysis showed that similar flow patterns (such as slow recirculation zones during diastole) could be observed in both the echoPIV and PC-MRI data. EchoPIV velocity profiles showed good agreement to the PC-MRI data with a mean similarity index (SI) of 0.98 (range 0.96-0.99) and a mean difference in peak systolic velocity of 8.5% (range 0.12% – 29%).

## **Conclusion**

Quantification of blood flow in the human abdominal aorta with echoPIV was proven to be feasible. The velocity data in this study showed good agreement to corresponding PC-MRI datasets. The echoPIV technique has a high potential clinical value in the diagnosis and follow-up of various arterial diseases, due to its low cost, ease of use and accurate two-dimensional flow visualisation. Patient studies with echoPIV should be performed to further investigate this clinical value.

# Changes in renal perfusion precede increased urinary protein excretion caused by weight gain and normalize after weight-loss in dogs

*Daisy J.X. Liu<sup>1</sup>, Emmelie Stock<sup>1</sup>, Evelien Bogaerts<sup>1</sup>, Bart J.G. Broeckx<sup>2</sup>, Siska Croubels<sup>3</sup>, Mathias Devreese<sup>3</sup>, Sylvie Daminet<sup>4</sup>, Patrick Nguyen<sup>5</sup>, Myriam Hesta<sup>2\*</sup>, Katrien Vanderperren<sup>1\*</sup>*

\* Both authors contributed equally

<sup>1</sup>Department of Veterinary Medical Imaging and Small Animal Orthopedics, Faculty of Veterinary Medicine, Ghent University, Merelbeke, Belgium

<sup>2</sup>Department of Nutrition, Genetics and Ethology, Faculty of Veterinary Medicine, Ghent University, Merelbeke, Belgium

<sup>3</sup>Department of Pharmacology, Toxicology and Biochemistry, Faculty of Veterinary Medicine, Ghent University, Merelbeke, Belgium

<sup>4</sup>Department of Small Animal Medicine and Clinical Biology, Faculty of Veterinary Medicine, Ghent University, Merelbeke, Belgium

<sup>5</sup>Oniris, National College of Veterinary Medicine, Food Science and Engineering, Nantes, France

## Introduction

High-fat feeding in dogs causes hemodynamic alterations, such as increased glomerular filtration rate (GFR) and renal plasma flow, similar to that observed in humans with obesity-related kidney disease<sup>1</sup>. In humans, weight-loss improves these abnormalities<sup>2</sup>. Although measured GFR is the gold standard of determining renal function, contrast-enhanced ultrasound (CEUS), which provides information on density and function of the microvascular network of a tissue, may be a more practical alternative<sup>3</sup>. The aim of this study was to determine the effect of body weight gain and weight loss on renal perfusion by CEUS in dogs.

## Materials and Methods

In this 83-week study, eight healthy lean beagles in a control group (group C) were fed to maintain weight throughout the study. Another eight healthy lean beagles in a treatment group (group T) were fed the same diet to induce obesity (week 0-47), to maintain stable obese weight (week 47-56) and to lose weight (week 56-83). At weeks 0, 12, 24, 36, 47, 56 and 83, body composition<sup>4</sup> and urinary protein-to-creatinine ratio (UPC) were measured. GFR was measured by plasma clearance of exo-iohexol after an intravenous bolus injection of iohexol (64.7 mg/kg, Omnipaque 300<sup>®</sup>, GE healthcare)<sup>5</sup>. While sedated (0.4 mg/kg, Dolorex<sup>®</sup> 10 mg/ml, Intervet), CEUS of both kidneys was performed using an intravenous bolus of Sonovue<sup>®</sup> (0.04 ml/kg, Bracco Diagnostics Inc.) and a linear transducer (12–5 MHz) on a dedicated machine (iU22, Philips) with contrast-specific software. Intensity-related parameters representing blood volume (peak enhancement (PE), wash-in area under the curve (WiAUC), wash-out AUC (WoAUC) and total AUC (AUC)) and time-related parameters representing blood velocity (rise time (RT), mean transit time (mTT), time-to-peak (TTP), wash-in rate (WiR), wash-in perfusion index (WiPI), fall time (FT), wash-out rate (WoR)) were determined from manually drawn region-of-interests in the renal cortex and medulla.

## Results and Discussion

Within group T, significant associations ( $P < 0.05$ ) were found between several CEUS renal perfusion parameters and body fat percentage (BF%), percent overweight (%OW), and lean mass (kg); between UPC and BF% ( $P = 0.003$ ) and %OW ( $P = 0.015$ ); and between GFR and BF% ( $P = 0.002$ ). A comparison between group T and C revealed that during the weight gain phase, TTP was significantly shorter at weeks 12 and 24 and UPC was significantly higher at weeks 47 and 56 in dogs in group T ( $P < 0.05$  (Bonferroni correction for multiple testing, respectively)). At week 56, mild proteinuria was observed in two dogs and borderline proteinuria in four other dogs in group T. Unexpectedly, GFR was not significantly different between both groups. After weight-loss of  $23.4\% \pm 6.8\%$ , TTP and UPC values of group T returned back to their initial values, which was in agreement with other studies in both dogs and humans<sup>6,7</sup>. Shorter TTP without differences in blood volume and GFR may have been due to increased vascular endothelial growth factor (VEGF) in glomeruli as observed in mice<sup>8</sup>.

In conclusion, CEUS detected increased renal blood flow in the absence of glomerular hyperfiltration and precedes increased urinary protein excretion during early development of obesity in dogs. Both changes were reversed after weight-loss. Therefore, CEUS examination of renal perfusion may have potential diagnostic value in obesity-related kidney dysfunction.

## References

1. Henegar, J. R., Bigler, S. A., Henegar, L. K., Tyagi, S. C. & Hall, J. E. Functional and structural changes in the kidney in the early stages of obesity. *J. Am. Soc. Nephrol.* 12, 1211–1217 (2001).
2. Chagnac, A. et al. The effects of weight loss on renal function in patients with severe obesity. *J. Am. Soc. Nephrol.* 14, 1480–1486 (2003).
3. Dizeux, A., Payen, T., Barrois, G., Le Guillou Buffello, D. & Bridal, S. L. Reproducibility of Contrast-Enhanced Ultrasound in Mice with Controlled Injection. *Mol. Imaging Biol.* 18, 651–8 (2016).
4. Ferrier, L., Robert, P., Dumon, H., Martin, L. & Nguyen, P. Evaluation of body composition in dogs by isotopic dilution using a low-cost technique, Fourier-transform infrared spectroscopy. *J. Nutr.* 132, 1725S–7S (2002).
5. De Baere, S. et al. Quantitative determination of exo- and endo-iohexol in canine and feline samples using high performance liquid chromatography with ultraviolet detection. *J. Pharm. Biomed. Anal.* 61, 50–56 (2012).
6. Tvarijonaviute, A. et al. Effect of weight loss in obese dogs on indicators of renal function or disease. *J. Vet. Intern. Med.* 27, 31–8 (2013).
7. D'Agati, V. D. et al. Obesity-related glomerulopathy: clinical and pathologic characteristics and pathogenesis. *Nat. Rev. Nephrol.* 12, 453–71 (2016).
8. Klanke, B. et al. Effects of vascular endothelial growth factor (VEGF)/vascular permeability factor (VPF) on haemodynamics and permselectivity of the isolated perfused rat kidney. *Nephrol. Dial. Transplant* 13, 875–85 (1998).

# The use of contrast-enhanced ultrasound in the assessment of uterine fibroids – a feasibility study

*B. Stoelinga<sup>1,2</sup>, A. Dooper<sup>1,2</sup>, LJM. Juffermans<sup>1,2</sup>, A. Postema<sup>3</sup>, H. Wijkstra<sup>3,4</sup>, H. Brölmann<sup>1,2</sup>, J. Huirne<sup>1,2</sup>*

*<sup>1</sup>Department of Obstetrics and Gynaecology, VU University Medical Center, Amsterdam, the Netherlands. <sup>2</sup>Institute for Cardiovascular Research, VU University Medical Center, Amsterdam, the Netherlands. <sup>3</sup>Department of Urology, Academic Medical Center Amsterdam, the Netherlands. <sup>4</sup>Signal Processing Systems, Electrical Engineering, Eindhoven University of Technology, the Netherlands.*

## Background

Contrast-enhanced ultrasound (CEUS) is an innovative ultrasound technique capable of visualizing both the macro- and microvasculature of tissues, and has the ability to discriminate malignant from benign and normal tissue. In the field of gynaecology, the fact that detailed information can be obtained from microvascular structures and vascular filling patterns has been acknowledged quite recently. Whilst gynaecologists are in fierce need of an imaging technique that discriminates a benign fibroid from an occult and highly aggressive malignant uterine sarcoma in an early stage. However, to date only a limited number of clinical studies have been performed using CEUS in diagnosing uterine disorders. Therefore, CEUS should be set up and developed in gynaecology. The aim of this pilot study was to evaluate the feasibility of CEUS in visualizing the microvasculature of benign uterine fibroids and compare CEUS with conventional ultrasound techniques.

## Methods and Results

Four women with uterine fibroids ( $\varnothing$  3.2-6.0 cm) underwent greyscale ultrasound, sono-elastography and power Doppler scans followed by CEUS examination. Analysis of CEUS images showed initial perfusion of the peripheral rim, i.e. pseudocapsule, followed by enhancement of the entire lesion through vessels traveling from exterior to interior of the fibroid. The pseudocapsules showed slight hyper-enhancement, making a clear delineation of the fibroids possible. The center of three fibroids showed areas lacking vascularization, information that could not be obtained from the other imaging techniques. Time-intensity curves and perfusion parameters of specific regions-of-interest could easily be obtained from CEUS images for further quantification of the vasculature.

## Conclusion

CEUS is a feasible technique for imaging and quantifying the microvasculature of fibroids. CEUS could be of added clinical value in diagnosing uterine disorders, both benign and malignant.

# Contrast Ultrasound in the Coming Decade

*Peter N. Burns*

*Department of Medical Biophysics, University of Toronto, Toronto, Canada  
Sunnybrook Research Institute, Toronto, Canada*

It is famously hazardous to make predictions, especially, as they say, about the future. But occasionally it may be helpful to pause to take stock of some of the trends that are leading us into the next decade of research and clinical translation. For this we might divide our field into three (overlapping) categories: the instruments, the bubbles and the clinical applications.

## **The Instruments**

For diagnostic imaging, the contrast specific modes that we spent so much time developing and discussing in this meeting appear to have stabilised into a set of approaches to nonlinear echo detection that most machines share. But following a long tradition in ultrasound, just when we think that no improvements are left to be made, a method appears that turns everything on its head. This time it is the realisation of synthetic aperture and plane wave imaging methods enabled by a new generation of software beamformers. Almost all of the existing contrast imaging methods rely on multipulse sequences with progressive phase and/or amplitude modulation. A result of implementing this line by line is that many functional modes are compromised by framerate. Thus, for example, Doppler frequency resolution and clutter filtering are so poor that most systems do not allow a colour Doppler mode for contrast at all. The ensemble length for cardiac imaging is rarely more than a few pulses so high pass filtering is very crude. All of this changes with planewave systems, where ensemble lengths of more than 100 are feasible while still providing framerates that are superior to those of conventional imaging. One aspect of these methods that is likely to prove fruitful for contrast is that acquisitions rates comparable to the PRF can provide frame-to-frame coherence of the scattered echo from a cohort of bubbles. Experiments show that at low MI this coherence time can be very long, allowing new forms of 'bubble-tracking' modes. In fact, coherence can itself be used as a criterion to segment the bubble echo with high specificity. Amongst other things, this allows tracing of the path of a group of bubbles and hence a new way to delineate echoes which is independent of - or at least better than - the imaging resolution. In an extreme form, individual bubbles can be tracked for long periods to form 'super-resolution' images of the microcirculation. The challenge here is rejection of clutter from moving tissue, a problem that may not be solved without high speed volumetric acquisition, requiring new matrix transducers and very complex, high channel count, beamformers. At present these imaging modes are being implemented using experimental programmable beamforming systems but these are likely to find their way into commercial systems in the coming years: their integration with other scanning modes such as cardiac 3D imaging will be a stimulating challenge.

As the developing applications of bubbles in medicine slowly moves from diagnosis to therapy, so new demands will be placed on the instruments, whose imaging function will migrate from diagnosis to guidance of therapy, but which will also be called upon to provide insonation to induce a therapeutic effect. It has taken many years to elucidate the interaction between the sound

field and the bubbles used for imaging; the focus will now shift to understanding the acoustic aspects of bubble interactions with tissue, which is sorely needed in order to provide a scientific basis for the design of excitation regimes which are optimised for specific effects such as sonoporation. The new confocal high speed microscope camera at Erasmus is therefore timely, and likely to maintain the group's position at the forefront of this important field.

## **The Bubbles**

We are exceedingly fortunate that bubbles designed two or more decades ago, with practically no knowledge of their acoustic properties, have proven so spectacularly successful as diagnostic contrast agents for clinical ultrasound and more recently, as therapeutic agents to induce such dramatic effects as opening of the blood-brain barrier. It is extraordinary to recall that most of the pivotal clinical trials for dosing and efficacy were performed without harmonic or any other nonlinear imaging modes, yet these methods work so well that today they are available on almost every clinical imaging system. Yet there are so many ways that these bubbles could - and have been - refined. These include optimising their nonlinear resonant response to ultrasound by manipulation of the shell properties or the size distribution of their population; targeting bubbles by means of ligands to cellular or molecular targets; creating bubbles that can be loaded with drugs or genetic material or attached to entities such as stem cells; making bubbles with specific ability to disrupt at a determined threshold, or to exhibit nonlinear behaviour that amplifies diameter changes in response to ambient fluid pressure; the use of polymer shell materials with carefully controlled properties; and so on. On the contrary, the past decades have seen the thinning of the many experimental bubble constructs to a very small handful that are commercially available. The \$100 million elephant in the room is, of course, the process for regulatory approval. Many of the big pharma companies have dropped development not just of ultrasound bubbles, but of the much more widely used contrast agents for CT and MR, simply because they are not as profitable as the therapeutic drug products that drive the industry. This might provide a clue to the future: that if any new bubble is to be developed over the coming decade - and it can certainly be expected to take that long - it is likely to one aimed at a therapeutic application. But which application? And what are the optimal properties of a bubble tailored for it? These must surely be major agenda items for the next decade's research in our field.

## **The Clinical Applications**

While the list of indications approved for microbubble contrast has remained unchanged for many years, this belies trends in the adoption and use of contrast in the clinic, which itself may reflect changes in the use of ultrasound imaging. The US FDA finally approved an extra-cardiac bubble indication more than a year ago, but few expect this to herald significant penetration into an abdominal radiology practice dominated by CT and MR. Indeed, the American Association for the Study of Liver Diseases (AASLD) guidelines continue to exclude contrast US for diagnosis of hepatocellular carcinoma, an area in which extensive global evidence seems to support its use. In the meantime, approximately half of the contrast studies carried out worldwide are now being carried out in China, a country in which ultrasound is heavily integrated into clinical practice. It seems likely, then, that trends in the use of contrast, for example in the imaging guidance of thermo-ablative therapy for cancer, may be developed there. In Japan too, the first approved indication was for guidance of RF ablation for liver lesions, an application that we continue to

hear at this meeting is underutilized in the west. Adoption ultimately may depend on the economic structure of the healthcare system, with ultrasound imaging – and therefore ultrasound contrast - favoured by cost-based systems but unattractive to profit-based ones like that of the US. Unless inflation of costs can be tamed, the coming decade is likely to render all of these systems, but especially the latter group, unsustainable. The cost-efficacy of ultrasound and bubbles has been established by numerous studies, the importance of which work may thus become apparent to us in the coming decade.

It is hard to imagine that the newest of applications of bubbles in therapy, in sonoporation, thrombolysis and BBB opening, for example, will not be the principal focus of future clinical development. Here, the required trick is evident: if one can take an existing, approved contrast agent, together with an existing approved imaging modality such as MR or US, and an existing approved sonication modality such as focused ultrasound, and combine them all with an existing approved chemotherapeutic agent, to provide a new method of treating, say, brain cancer, the regulatory bar is set much lower than it would be for the approval of an entirely new drug, and clinical translation within the decade is a possibility. We are forced, then, to consider how to best make use of an existing set of tools provided by ultrasound, bubbles and approved therapeutic modalities and drugs, in some combination that will create clinical impact. This will surely require meticulous study of fundamental interactions, both biological and acoustical, within a parameter space defined by what is feasible in clinical reality, rather than by fundamental design. While this will be a disappointment to scientific purists, it is within similar constraints that our field has been so successful in the creation of a new diagnostic imaging modality, and it is reasonable to anticipate that it will produce equally exciting new results in the development of the application of bubbles to therapy.

# Ultrasound Molecular Imaging of cardiovascular disease

*Beat A. Kaufmann*

*University Hospital Basel*

## **Molecular imaging**

Molecular imaging has been developed for the non-invasive detection of the expression of relevant, disease specific molecules. For ultrasound molecular imaging, microbubbles are targeted to disease markers by using one of two strategies. The first strategy takes advantage of modifications of the microbubble shell surface for attachment of microbubbles to activated leukocytes that reside in inflamed blood vessels. The second and more versatile strategy uses surface conjugation of specific disease ligands to the microbubble surface for targeting. In recent years, these novel applications have been tested in several animal models of clinically relevant cardiovascular diseases.

## **Molecular imaging in atherosclerosis**

In clinical cardiology, risk assessment for atherosclerosis currently relies on established clinical risk factors. This approach places a large proportion of individuals in an intermediate risk category, where the value of interventions to reduce the risk for events is uncertain. Therefore, tools to better assess the risk in these patients are needed. Atherosclerosis is an inflammatory disease that involves endothelial activation. In this process, the expression of endothelial cell adhesion molecules leads to recruitment of inflammatory cells to the vessel wall and thus to atherosclerotic plaque formation. Work in animal models has shown that ultrasound molecular imaging can be used to non-invasively detect endothelial activation in early and late stages of atherosclerosis, and that the effects of therapies aimed at decreasing inflammation can be assessed.

## **Molecular imaging in myocarditis**

Myocarditis is an inflammatory disease of the myocardium caused by a variety of infectious and noninfectious diseases. Myocarditis can present with highly variable symptoms but can also be asymptomatic, and carries a risk for sudden death or later development of dilated cardiomyopathy. Autopsy studies show histologic evidence of myocarditis in 1% and suggest that the disease is underdiagnosed. In animal models of autoimmune myocarditis, it has been shown that molecular imaging can detect endothelial inflammation and leukocyte infiltration in myocarditis in the absence of a detectable decline in left ventricular performance by functional imaging.

## **Developments for clinical translation**

For clinical translation, developments in conjugation chemistry for ligand attachment, and development of non-immunogenic, safe and affordable ligands will be necessary. An examples of a clinically applicable conjugation chemistry is maleimide covalent conjugation. Novel ligands such as nanobodies or designed ankyrin repeat proteins are currently being studied for their use in molecular imaging. These developments should allow clinical translation.

# Subharmonic Imaging of Liposome-loaded Microbubbles

*Luzhen Nie<sup>1</sup>, James R. McLaughlan<sup>1,2</sup>, Thomas Carpenter<sup>1</sup>, David M.J. Cowell<sup>1</sup> and Steven Freear<sup>1</sup>*

*<sup>1</sup>School of Electronic and Electrical Engineering, University of Leeds, UK. LS2 9JT*

*<sup>2</sup>Leeds Institute of Cancer and Pathology, School of Medicine, University of Leeds, Leeds, LS9 7TF, UK*

## Introduction

Drug delivery using liposome-loaded microbubbles (LLMBs) has the potential to become a new theranostic approach for targeted cancer treatments [1]. As the typically toxic chemotherapy agents can be encapsulated and released locally, it has significant potential for reduction in side effects compared with a systematic delivery [2]. For personalized medicine with LLMBs, the capability of estimation of dose through contrast ultrasound imaging could further reduce the toxicity to healthy tissue. Of multi-pulse contrast imaging schemes tested, the modulation of pulse amplitude (AM) and combining both phase and amplitude modulation (PIAM) show enhanced contrast levels by preserving both even and odd harmonics [3]. Essentially two-pulse AM is dependent on nonlinearities within the fundamental band of the transmitted pulse [4]. The resultant signal with AM processing will be the combination of MB nonlinear responses and decorrelation within the AM packet which is irrelevant to real concentration [5]. This might suggest that one-pulse based nonlinear imaging schemes are suitable for quantification of LLMBs since the influence of MB motion will not be incorporated into the nonlinear imaging sequence. With the addition of drug-filled liposomes to the bubble shell, ‘expansion-only’ behaviour when bubbles are enforced to a buckled state by the packed liposome layer, can result in the decreased threshold for the detection of subharmonic emissions [6]. This could allow for the subharmonic plane wave imaging (PWI) of LLMBs, where good quality images can be obtained through a number of plane-wave transmissions with non-destructive pressure levels. The objective of this study was to investigate the subharmonic imaging of LLMBs with either established linear scanning or PWI.

## Methods

LLMBs were produced referring to [6], except that the microfluidic manufacturing system was replaced with a mechanical shaker to assemble the bubble–liposome complex. Sequences of plane-wave and focused-beam subharmonic imaging were designed and implemented on the Ultrasound Array Research Platform II (UARP II) [7-9] with a fixed PRF at 6 kHz. With a Verasonics L11-4 probe, six-cycle sinusoids centred at 9 MHz were used for both schemes and the receiving bandwidth was 3-4.5 MHz to separate the subharmonics. Pressure measurements were performed with a calibrated needle hydrophone and used to ensure the maximum MI was 0.1, for all exposures. Conventional 83-line linear imaging was performed with a single-focus at 37 mm with a-f number of 4. A 15-angle PWI sequence was used to perform compounded PWI and the angle was steered from -5 to 5 degree with an equal step of 5/7 degree. LLMB solutions

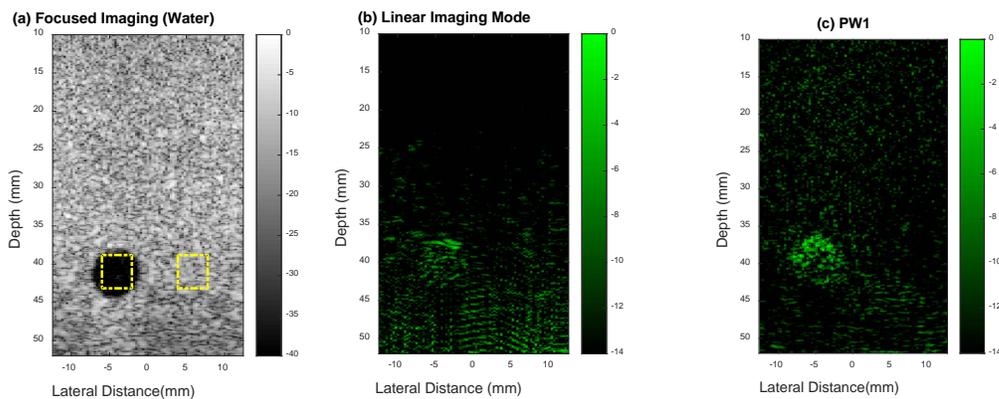
with a concentration of  $2.5 \times 10^6$  mb/ml were flowed through a wall-less tissue mimicking flow phantom, at a rate of 7.8 ml/min ( $V_{\text{mean}} = 20$  mm/s). In each experiment five frames were captured with a time gap of  $\sim 2$  s, and the contrast-to-tissue ratios (CTRs) were then calculated from three repeated experiments. Fig.a shows the regions of interest to calculate CTRs.

## Results and Discussions

Typical subharmonic contrast frames with LLMBs introduced are given in (b), (c), (d) and (e). The pressure drops gradually with increased depths when emitting the plane-wave field as highlighted

in [10]. While the energy is focused with conventional scanning. The difference of field patterns could account for the phenomenon that noise is dominant at deep locations with focused beams, as seen in (a) and (b). The transducer used in this study has an elevation focal depth of 20 mm, and the beam steering out of the elevation focal depth may also result in the compromised focal performance. The use of plane waves led to worse resolution as shown in (c), (d) and (e), but image SNR was improved with multi-angle frames compounded. Worse resolution might not be a problem in quantification of microbubbles where the overall microbubble brightness would be of interest. Fig. f shows results of CTR with two imaging schemes. The difference between the focused imaging mode and one-angle (zero degree) plane wave pulse is not significant. With the increased number of compounding angles, the background noise has been gradually reduced and this has improved CTRs. With the same flow speed of 20 mm/s as used in [4], Viti et al. demonstrated an increase of 9 dB in CTR with 15-angle AM, while the increase is smaller than 2 dB in this study. The difference between these results might be caused by motion, which will lead to residual signals within multi-pulse nonlinear imaging schemes, but treated as MB nonlinear responses in [4].

In conclusion, this study demonstrated the use of ultrafast ultrasound to perform the subharmonic LLMB detection with the potential for microbubble quantification and could be further for the estimation of loaded drug volume on LLMBs.



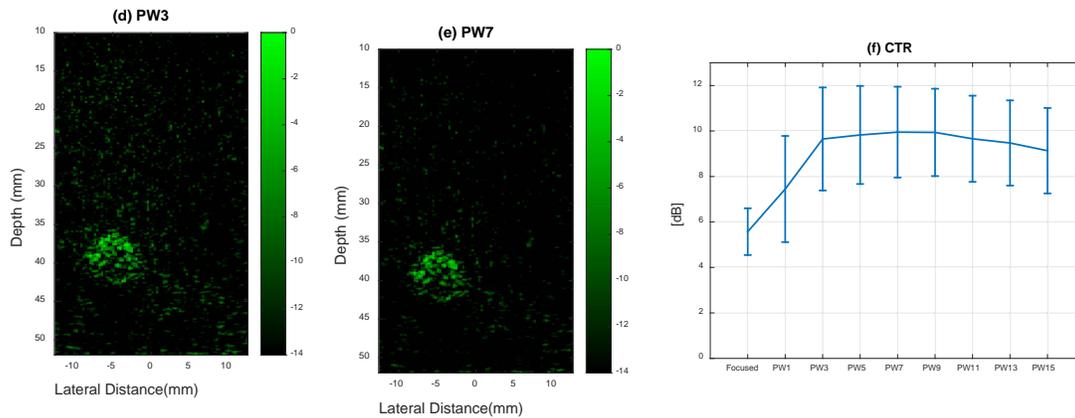


Figure: Typical imaging results. (a) fundamental B-mode, (b) subharmonic imaging with focused beams, (c) subharmonic imaging with one-angle (zero degree) plane wave, (d) subharmonic imaging with three angled (-5/7, 0, 5/7) plane waves, (e) subharmonic imaging with seven angled (-15/7, -10/7, -5/7, 0, 5/7, 10/7, 15/7) plane waves and (f) CTRs for different non-linear detection methods.

## References

1. Peyman SA, Abou-Saleh RH, McLaughlan JR, Ingram N, Johnson BRG, Critchley K, Freear S, Evans JA, Markham AF, Coletta PL, Evans SD. Expanding 3D geometry for enhanced onchip microbubble production and single step formation of liposome modified microbubbles. *Lab Chip* 2012;12:4544–4552.
2. J. M. Escoffre, C. Mannaris, B. Geers, A. Novell, I. Lentacker, M. Averkiou, and A. Bouakaz, "Doxorubicin liposome-loaded microbubbles for contrast imaging and ultrasound-triggered drug delivery," *IEEE Transactions on Ultrasonics, Ferroelectrics, and Frequency Control*, vol. 60, no. 1, pp. 78–87, January 2013.
3. Eckersley, Robert J., Chien Ting Chin, and Peter N. Burns. "Optimising phase and amplitude modulation schemes for imaging microbubble contrast agents at low acoustic power." *Ultrasound in Medicine & Biology* 31.2 (2005): 213-219.
4. J. Viti, H. J. Vos, N. d. Jong, F. Guidi and P. Tortoli, "Detection of Contrast Agents: Plane Wave Versus Focused Transmission," in *IEEE Transactions on Ultrasonics, Ferroelectrics, and Frequency Control*, vol. 63, no. 2, pp. 203-211, Feb. 2016.
5. F. Lin, C. Cachard, R. Mori, F. Varray, F. Guidi and O. Basset, "Ultrasound contrast imaging: influence of scatterer motion in multi-pulse techniques," in *IEEE Transactions on Ultrasonics, Ferroelectrics, and Frequency Control*, vol. 60, no. 10, pp. 2065-2078, Oct. 2013.
6. J. R. McLaughlan, S. Harput, R. H. Abou-Saleh, S. A. Peyman, S. Evans, and S. Freear, "Characterisation of liposome-loaded microbubble populations for subharmonic imaging," *Ultrasound in Medicine & Biology*, vol. 43, no. 1, pp. 346–356, 2017.
7. D. Cowell and S. Freear, "Quinary excitation method for pulse compression ultrasound measurements," *Ultrasonics*, vol. 48, no. 2, pp. 98–108, 2008.
8. P. R. Smith, D. M. J. Cowell, B. Raiton, C. V. Ky, and S. Freear. "Ultrasound array transmitter architecture with high timing resolution using embedded phase-locked loops," *IEEE Transactions on Ultrasonics, Ferroelectrics, and Frequency Control*, vol. 59, no. 1, pp. 40–49, January 2012.
9. D. M. J. Cowell, P. R. Smith, and S. Freear, "Phase-inversion-based selective harmonic elimination ( $\pi$ -she) in multi-level switched-mode tone- and frequency- modulated excitation," *IEEE Transactions on Ultrasonics, Ferroelectrics, and Frequency Control*, vol. 60, no. 6, pp. 1084–1097, June 2013.
10. Wang, Diya, et al. "Ultrasound contrast plane wave imaging based on bubble wavelet transform: in vitro and in vivo validations." *Ultrasound in Medicine & Biology* 42.7 (2016): 1584-1597.

# Anti-Inflammatory Therapeutic Treatment Monitoring in Swine Model of Inflammatory Bowel Disease using Dual-Selectin-Targeted Contrast-Enhanced Ultrasound Imaging

Samir Cherkaoui<sup>1</sup>, Huaijun Wang<sup>2</sup>, Jean-Marc Hyvelin<sup>1,\*</sup>, Thierry Bettinger<sup>1</sup> and Jürgen K. Willmann<sup>2</sup>

<sup>1</sup> Bracco Suisse SA, Geneva, Switzerland

<sup>2</sup> Department of Radiology, Molecular Imaging Program at Stanford, Stanford University, School of Medicine, Stanford, California, USA

\*, formerly Bracco

## Background

Inflammatory bowel disease (IBD) is an idiopathic disease caused by an abnormal immune response to intestinal microbes. IBD refers to related but distinct diseases, namely Crohn's disease (CD) and Ulcerative Colitis (UC). While the former can affect any segment of the gastrointestinal (GI) tract from the mouth to the anus, the latter is limited to the colon and the rectum. IBD is estimated to affect more than 1.4 million people in the United States, most of whom are diagnosed before age 35. IBD is raising worldwide, particularly in those regions that have become more industrialized and is associated with a high economic burden to the society

According to the 2013 European ECCO/ESGAR guidelines, the management of patients with IBD requires evaluation both at the time of original diagnosis and throughout the course of the disease, to determine the location, extension, activity and severity of inflammatory lesions, as well as the potential existence of complications. This information is crucial to select appropriate therapeutic strategies in a particular patient, and has prognostic implications. Therefore, it is of utmost importance to develop sensitive, specific and non-invasive imaging tools for the IBD patient management.

Due to their unique features such as inertness (safety profile), enhanced stability and acoustic properties, gas-filled microbubbles have gained increased popularity in the field of contrast-enhanced ultrasound (US) imaging. These agents are nowadays widely used clinically in echocardiography and radiology applications to mention few of them. Cost-effectiveness, noninvasiveness, portability, wide array of applications are the main reasons for this success. More recently, these microbubbles are also applied as Ultrasound Molecular Imaging (USMI) agents by targeting specific cellular biomarkers of disease (1). In practice, feasibility of clinical USMI has been demonstrated in patients with prostate, breast and ovarian cancer lesions using BR55, a vascular endothelial growth factor receptor 2 (VEGFR2)-specific molecularly targeted contrast agent (2,3). Using the same strategy, molecular imaging of inflammation through specific binding to P- and E-selectin receptors over-expressed in the vasculature is also under evaluation thanks to the use of selectin microbubbles (MBselectin) (4). Targeting ability of this USMI platform is achieved by functionalizing the microbubbles with a recombinant P-selectin glycoprotein ligand (the so-called PSGL-Variant; Figure 1).

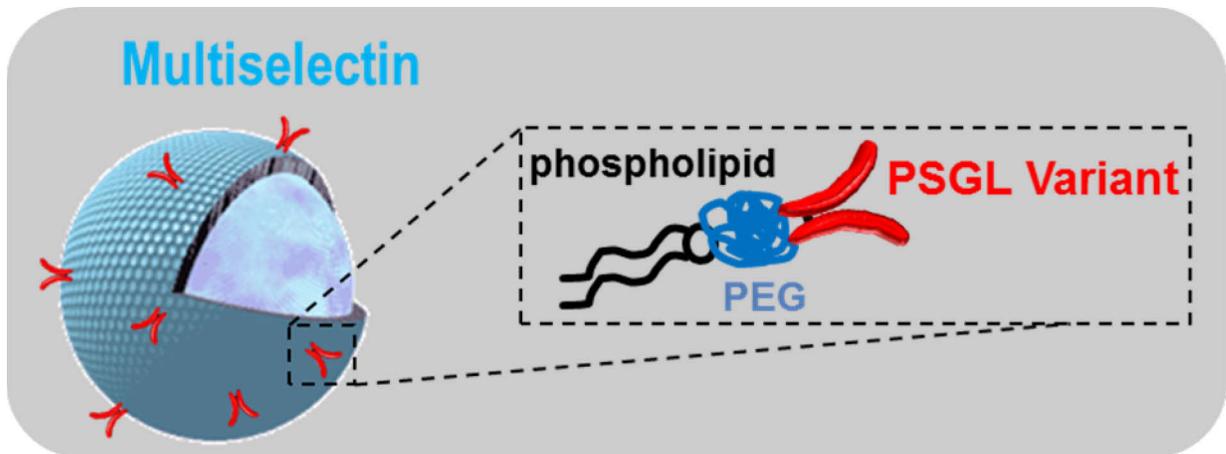


**Figure 1:** Schematic representation of dual-selectin-targeted microbubbles (MBselectin) MBselectin, as a molecular contrast agent has been evaluated *in vitro* and *in vivo* for several applications. In particular, by targeting P- and E-selectin receptors, MBselectin have been proven powerful for the accurate detection, monitoring and quantification of inflammation (sensitivity, specificity and predictive value) in rodent and swine models of IBD using current clinical US equipment (5,6). The aim of the present study was to assess whether clinically translatable dual-selectin targeted USMI allows longitudinal monitoring of anti-inflammatory treatment effects in a swine model of acute ileitis.

## Materials and Methods

Fourteen swine with chemically-induced acute terminal ileitis through direct contact of ileum mucosa with TNBS/ethanol solution at day 0 were randomized into 1) an anti-inflammatory treatment group (n=8; with meloxicam at 0.25 mg/kg and prednisone at 0.5 mg/kg) and 2) a control group (n=6; saline only). USMI was performed on a clinical ultrasound machine (Acuson Sequoia 512; 7MHz) after intravenous injection of clinically translatable dual P- and E-selectin targeted microbubbles ( $5 \times 10^8$ /kg). Three inflamed bowel segments per swine were imaged at baseline, as well as day 1, 3 and 6 after treatment initiation. Images were processed using the VueBox<sup>®</sup> molecular imaging software package. This analysis method improves the conspicuity of fixed microbubbles by suppressing the echoes originating of the remaining circulating bubbles.

At day 6, scanned bowel segments were analyzed *ex vivo* for both inflammation grading on H&E staining as well as for selectin expression levels using quantitative immunofluorescence.

## Results

Data gathered in the context of the present investigation showed:

Normalized Peak Enhancement (PE) and WiAUC values: no differences were observed between control and treated animals (for both SonoVue<sup>®</sup> and MB<sub>selectin</sub>).

Normalized Fixed microbubble values: significant differences (Anova, Bonferonni multiple comparison test,  $P < 0.05$ ) were observed between control and treated pigs on day 3 and day 6. It is noteworthy that all treated animals showed a decrease of FBI values through the treatment f-up.

Ex Vivo Analysis: Compared to non-treated control small bowel, the histological inflammation scores on H&E stained tissues sections did not reveal significant differences between treated and non-treated animals art day 6. In contrast, vascular

expression of both P- and E-selectin were significantly lower in treated bowel segments compared to non-treated control tissues.

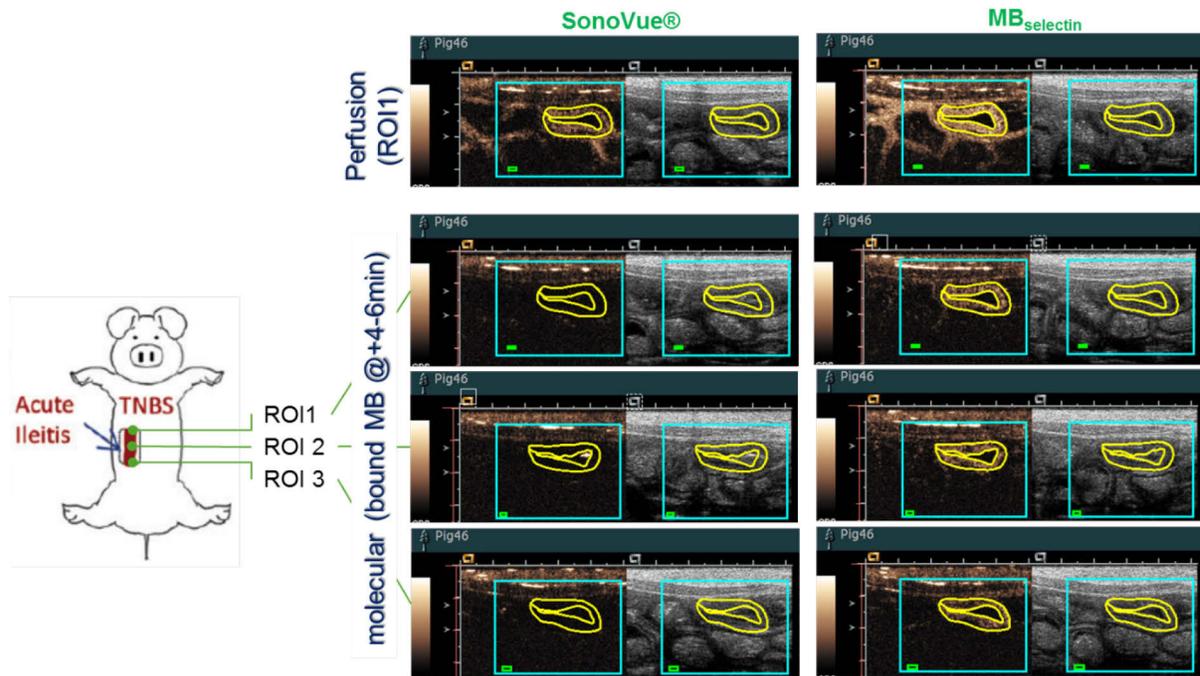


**Figure 2:** USMI with dual-selectin-targeted microbubbles at three locations of terminal ileum

## Conclusion

These results suggest that USMI, using MBselectin, can be efficiently used for the non-invasive monitoring of expression levels of molecular markers of inflammation in the ileitis pig model during the course of an anti-inflammatory treatment. MBselectin might be applied in patients with inflammatory bowel disease (IBD), to evaluate lesions for active inflammation, and in concert with a dedicated software to quantify the degree of inflammation and provide information on the response to ongoing therapies, and thus contribute to guide for optimal patient management.

## References

1. Pochon S., Tardy I, Bussat P. Et al. BR55: a lipopeptide-based VEGFR-2 targeted ultrasound contrast agent for molecular imaging of angiogenesis. *Invest Radiol* 2010;45:89-95
2. Willmann JK, Bonomo L, Carla Testa A, et al. Ultrasound Molecular Imaging With BR55 in Patients With Breast and Ovarian Lesions: First-in-Human Results. *J Clin Oncol* 2017 Epub.
3. Smeenge M, Tranquart F, Mannaerts CK, et al. First-in-Human Ultrasound Molecular Imaging With a VEGFR2-Specific Ultrasound Molecular Contrast Agent (BR55) in Prostate Cancer: A Safety and Feasibility Pilot Study. *Invest Radiol* 2017;52(7):419-427.
4. Bettinger T, Bussat P, Tardy I, et al. Ultrasound molecular imaging contrast agent binding to both E- and P-selectin in different species. *Invest. Radiol.* 2012;47(9):516-523.
5. Deshpande N, Lutz AM, Ren Y, et al. Quantification and monitoring of inflammation in murine inflammatory bowel disease with targeted contrast-enhanced US. *Radiology* 2012;262(1):172-180.
6. Wang H, Felt SA, Machtaler S, et al. Quantitative Assessment of Inflammation in a Porcine Acute Terminal Ileitis Model: US with a Molecularly Targeted Contrast Agent. *Radiology* 2015;276(3):809-817.

# High frame rate contrast enhanced ultrasound imaging of lymph node in vivo

*Jiaqi Zhu<sup>1</sup>, Ethan Rowland<sup>1</sup>, Chee Hau Leow<sup>1</sup>, Kai Riemer<sup>1</sup>, Antonio Stanziola<sup>1</sup>, Sevan Harput<sup>1</sup>, Karina Cox<sup>2</sup>, Peter D. Weinberg<sup>1</sup>, Meng-Xing Tang<sup>1</sup>*

<sup>1</sup>*Department of Bioengineering, Imperial College London, London, SW7 2BP, UK*  
<sup>2</sup>*Department of Surgery, Maidstone and Tunbridge Wells NHS Trust, Hermitage Lane, Maidstone, Kent ME16 9QQ, UK*  
*mengxing.tang@imperial.ac.uk*

## Introduction

In cancer patients, the presence and size of metastases in tumour-draining lymph nodes (LN) provide important prognostic information to help guide treatment decisions. Primary tumours can induce angiogenesis and lymphangiogenesis within regional LN. Prior to the establishment of metastasis, LN undergo changes in the morphology of vasculature and lymphatic channels, as well as functional changes in blood flow(1,2). The detection of these changes using diagnostic imaging alone has the potential to revolutionise modern cancer management.

Contrast enhanced ultrasound (CEUS) has shown great potential for the pre-operative identification of sentinel lymph nodes (SLN) in patients with early breast cancer(3–5). CEUS has also been used for the evaluation of nodal vasculature and vessel architecture(6–8). However, accurate node characterisation and metastasis detection using CEUS are challenging due to the limited image quality, such as the presence of significant tissue artefacts. Current advances in high frame rate (HFR) CEUS have demonstrated improved signal-to-noise ratio (SNR) in small vascular imaging(9,10), arterial flow imaging(11) and cardiac imaging(12). These benefits of HFR CEUS enable the tracking of both fast moving targets in major arteries/vein and slow moving targets in small vessels such as microvasculature and lymphatic channels in lymph node.

The aim of this study is to investigate the feasibility of HFR CEUS in LN imaging and its potential for the pre-operative characterisation of metastatic and normal LN through identifying changes in intra-nodal microvasculature and lymphatic channels.

## Methods

The popliteal LN of a terminally-anaesthetised male New Zealand white rabbit was imaged. Experiments complied with the Animal (Scientific Procedures) Act 1986 and were approved by the Animal Welfare and Ethical Review Board of Imperial College London. After a bolus of 0.1 ml in-house microbubbles ( $5 \times 10^9$  MB/ml) was injected through the marginal ear vein, B-mode images were acquired using a research platform (Verasonics Vantage), a linear probe L22-14v and a 15-angle compounding plane-wave imaging sequence. Transmitted pluses were centred at 18 MHz and the frame rate was 500 Hz.

Acquired radio-frequency (RF) data were beamformed to give 800 frames of compounded B-mode images for post-processing. A spatio-temporal coherence processing method, ASAP (13), was performed to generate high contrast images. The method capitalises on the dramatically

increased temporal frequency of HFR CEUS images and signal coherence similar to traditional Doppler techniques. Furthermore, singular value decomposition (SVD)-based clutter filtering was performed (14) to separate microbubble echoes from tissue signals.

## Results and Discussion

Qualitative evaluation was performed by applying temporal average of consecutive original B-mode images and processed images. In the original B-mode image (Fig. 1a), the red contour indicated the popliteal lymph node. From the same RF data, the high contrast image (Fig. 1b) generated by SVD and spatio-temporal coherence processing ASAP enabled clearer visualisation of the rich intra-nodal microvasculature. At the same time, the major vessels (white arrow) can also be resolved which is not visible in the B-mode image.

Visualising LN microvasculature by using HFR CEUS offers new opportunities in distinguishing between metastatic and normal LN. Discrimination can be achieved by identifying reorganisation of vasculature and functional changes in blood flow. This is only a preliminary study and further work is required to optimise the imaging technique before applying it to studying in vivo cancer models.

## Conclusion

In this study, we present the first in vivo demonstration of HFR CEUS imaging of LN and demonstrate its feasibility in a rabbit model.

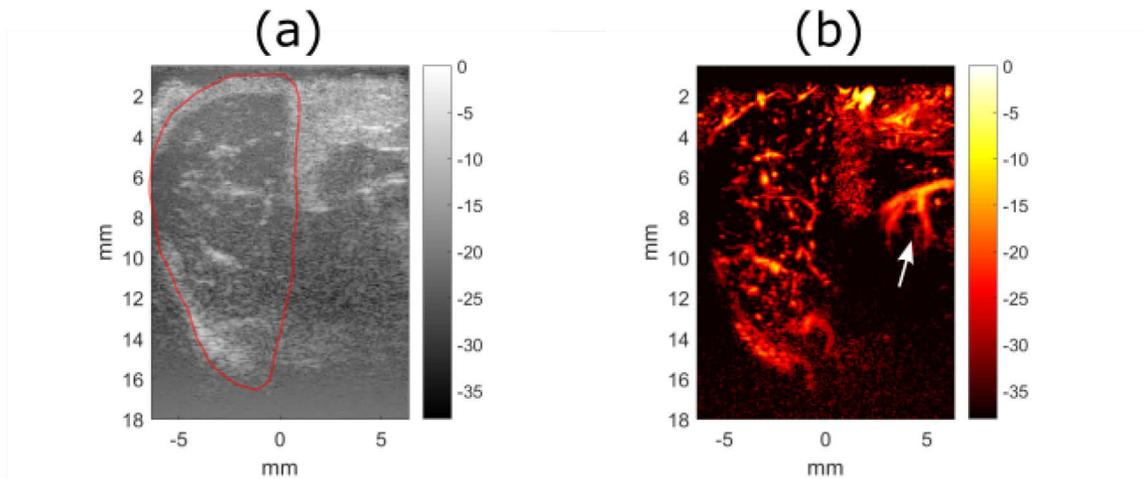


*Figure 1 HFR CEUS image of rabbit popliteal lymph node (a) B-mode image (b) vascular image generated by spatio-temporal processing method, ASAP. Red contour indicated the region of lymph node which was confirmed via blue dye injection and white arrow indicated the major blood vessels.*

## References

1. Qian C-N, Berghuis B, Tsarfaty G, Bruch M, Kort EJ, Ditlev J, et al. Preparing the “Soil”: The Primary Tumor Induces Vasculature Reorganization in the Sentinel Lymph Node before the Arrival of Metastatic Cancer Cells. *Cancer Res.* 2006 Nov 1;66(21):10365–76.
2. Lee SY, Qian C-N, Ooi AS, Chen P, Wong HMB, Myint SS, et al. Changes in specialized blood vessels in lymph nodes and their role in cancer metastasis. *J Transl Med.* 2012 Oct 4;10:206.
3. Cox K, Taylor-Phillips S, Sharma N, Weeks J, Mills P, Sever A, et al. Enhanced pre-operative axillary staging using intradermal microbubbles and contrast-enhanced ultrasound to detect and biopsy sentinel lymph nodes in breast cancer: A potential replacement for axillary surgery. *Br J Radiol.* 2017 Nov 10;20170626.
4. Goldberg BB, Merton DA, Liu J-B, Thakur M, Murphy GF, Needleman L, et al. Sentinel Lymph Nodes in a Swine Model with Melanoma: Contrast-enhanced Lymphatic US. *Radiology.* 2004 Mar 1;230(3):727–34.
5. Cox K, Sever A, Jones S, Weeks J, Mills P, Devalia H, et al. Validation of a technique using microbubbles and contrast enhanced ultrasound (CEUS) to biopsy sentinel lymph nodes (SLN) in pre-operative breast cancer patients with a normal grey-scale axillary ultrasound. *Eur J Surg Oncol EJSO.* 2013 Jul 1;39(7):760–5.
6. Ahuja AT, Ying M. Sonographic Evaluation of Cervical Lymph Nodes. *Am J Roentgenol.* 2005 May 1;184(5):1691–9.
7. Cui X-W, Jenssen C, Saftoiu A, Ignee A, Dietrich CF. New ultrasound techniques for lymph node evaluation. *World J Gastroenterol WJG.* 2013 Aug 14;19(30):4850–60.
8. Hong Y-R, Luo Z-Y, Mo G-Q, Wang P, Ye Q, Huang P-T. Role of Contrast-Enhanced Ultrasound in the Pre-operative Diagnosis of Cervical Lymph Node Metastasis in Patients with Papillary Thyroid Carcinoma. *Ultrasound Med Biol.* 2017 Nov 1;43(11):2567–75.
9. Tremblay-Darveau C, Williams R, Milot L, Bruce M, Burns PN. Combined perfusion and doppler imaging using plane-wave nonlinear detection and microbubble contrast agents. *IEEE Trans Ultrason Ferroelectr Freq Control.* 2014 Dec;61(12):1988–2000.
10. Zhu J, Lin S, Harput S, Toulemonde M, Leow CH, Tang MX. High frame rate contrast enhanced ultrasound imaging of lymphatic vessel phantom. In: *2017 IEEE International Ultrasonics Symposium (IUS).* 2017. p. 1–4.
11. Leow CH, Bazigou E, Eckersley RJ, Yu ACH, Weinberg PD, Tang M-X. Flow Velocity Mapping Using Contrast Enhanced High-Frame-Rate Plane Wave Ultrasound and Image Tracking: Methods and Initial in Vitro and in Vivo Evaluation. *Ultrasound Med Biol.* 2015 Nov 1;41(11):2913–25.
12. Toulemonde M, Li Y, Lin S, Tang MX, Butler M, Sboros V, et al. Cardiac imaging with high frame rate contrast enhanced ultrasound: In-vivo demonstration. In: *2016 IEEE International Ultrasonics Symposium (IUS).* 2016. p. 1–4.
13. Stanzola A, Tang M-X. Super contrast imaging using high frame-rate CEUS and spatial and temporal signal processing. *Proc 21st Eur Symp Ultrasound Contrast Imaging.* 2017;1–14.
14. Song P, Manduca A, Trzasko JD, Chen S. Ultrasound Small Vessel Imaging With Block-Wise Adaptive Local Clutter Filtering. *IEEE Trans Med Imaging.* 2017 Jan;36(1):251–62.

# Microbubble – cell interactions revealed with combined confocal microscopy and Brandaris 128 ultra-high speed imaging

*Inés Beekers<sup>1</sup>, Merel Vegter<sup>1</sup>, Kirby R. Lattwein<sup>1</sup>, Frits Mastik<sup>1</sup>, Robert Beurskens<sup>1</sup>, Rogier Verduyn Lunel<sup>3</sup>, Antonius F. W. van der Steen<sup>1,2</sup>, Nico de Jong<sup>1,2</sup>, Klazina Kooiman<sup>1</sup>*

<sup>1</sup>*Department of Biomedical Engineering, Erasmus MC, Rotterdam, the Netherlands*

<sup>2</sup>*Acoustical Wavefield Imaging, Delft University of Technology, Delft, the Netherlands*

<sup>3</sup>*Nikon Instruments Europe, Amsterdam, the Netherlands*

Ultrasound in the presence of gas-filled microbubbles can be used to enhance local uptake of drugs [1]. However, the mechanism is still unknown. To better predict and control the different drug delivery pathways, underlying physical and biological mechanisms of the microbubble-cell interaction need to be studied. A state-of-the-art optical imaging system was developed by connecting an upright custom built Nikon A1R confocal microscope to the Brandaris 128 ultra-high speed camera [2], thereby achieving the nanometer and nanosecond resolution necessary to visualize cellular effects and resolve microbubble oscillation upon ultrasound insonification.

To study ultrasound-mediated vascular drug delivery, Human Umbilical Vein Endothelial Cells (HUVECs) were cultured in a CliniCell (50  $\mu\text{m}$  membrane, Mabio, France) to a confluent monolayer. Homemade biotinylated DSPC-based microbubbles (mean diameter of 2.9  $\mu\text{m}$ ) were fluorescently labeled (DiD) and targeted to an angiogenic endothelial receptor ( $\alpha_v\beta_3$ ) with a biotinylated  $\alpha_v\beta_3$ -antibody using biotin-avidin bridging [3]. The HUVECs were incubated with Cell Mask Green to stain the cell membrane, Hoechst to stain the nucleus, and propidium iodide (PI) to evaluate sonoporation. After the addition of  $2.4 \times 10^6$  microbubbles, the CliniCell was incubated for 5 min at 37°C to allow the  $\alpha_v\beta_3$ -targeted microbubbles to bind to the HUVECs. All experiments were performed within 2 h and in a 37°C waterbath. The cellular response upon ultrasound insonification of a single microbubble was monitored with the confocal microscope (0.65 fps, 100x water dipping objective) with four lasers: 405 nm for Hoechst, 488 nm for Cell Mask Green, 561 nm for PI, 640 nm for DiD microbubbles. The confocal recording started before insonification (2 MHz, 250 kPa (n=39) and 300 kPa (n=55) peak negative pressure (PNP), single 10-cycle burst) and continued for at least 3 min afterwards. Microbubble oscillation was recorded with the Brandaris 128 ultra-high speed camera (~16 Mfps). Analyses were performed using MATLAB and NIS-Elements AR software.

The cellular response was classified based upon the PI uptake. Confocal microscopy revealed either uptake of PI within both the cytoplasm and the nucleus (Fig. 1A), only within the cytoplasm (Fig. 1B), or no detectable uptake (Fig. 1C). The amount of PI uptake is closely related to the size of the pore induced in the cellular membrane by sonoporation [4]. We hypothesize that when PI uptake is observed only within the cytoplasm a quick reseal of the pore takes place, limiting the amount of PI entering the cell and reaching the nucleus.

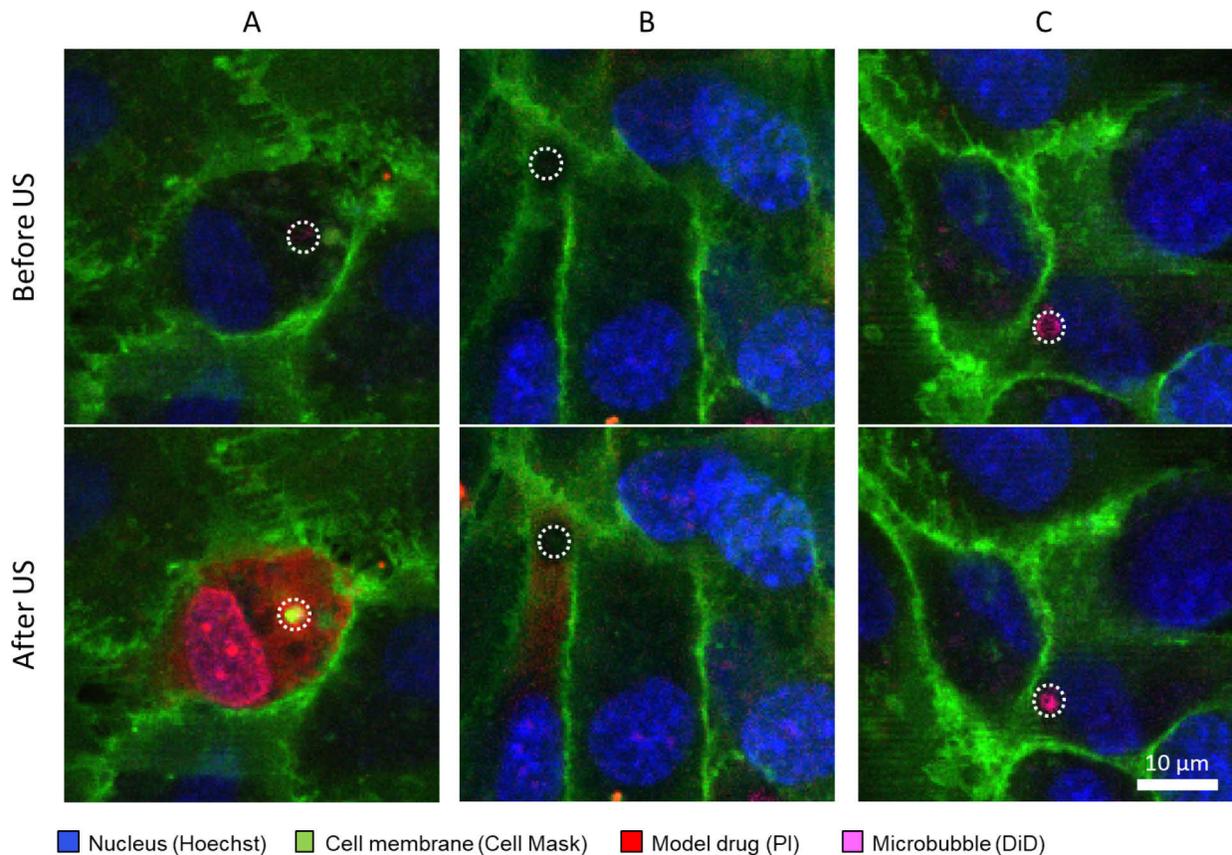


**Fig. 1.** Confocal microscopy images of the cellular response before (top row) and after (bottom row) ultrasound (US). The microbubble is delineated by the white dashed circle. **A)** PI uptake was detected in both the cytoplasm and the nucleus. **B)** PI uptake was detected only within the cytoplasm. **C)** No PI uptake was detected.

Uptake within the cytoplasm and nucleus was observed in 41% of the cases at 250 kPa PNP, while this was 45% at 300 kPa PNP. On the other hand, PI uptake was detected only within the cytoplasm for 13% of the cases at both pressures. The change of diameter as a function of time for an oscillating microbubble was obtained from the ultra-high speed recordings. Initial results show that PI uptake in both the cytoplasm and nucleus ( $n=5$ ) was observed for microbubble oscillation with a mean absolute excursion amplitude of  $x=2.0\ \mu\text{m}$ . When PI uptake only takes place within the cytoplasm ( $n=5$ ) the microbubble oscillated with  $x=1.4\ \mu\text{m}$ . Finally, when no PI uptake was detected ( $n=7$ ), the oscillation amplitude was only  $x=1.0\ \mu\text{m}$ .

In conclusion, using this state-of-the-art optical system, drug delivery uptake profiles can be obtained with high sensitivity at short timescales while also achieving the nanosecond resolution needed to resolve microbubble oscillation. The knowledge gained is expected to greatly advance microbubble-mediated drug delivery.

**Acknowledgements:** the authors thank Gert van Cappellen and Adriaan Houtsmuller from the Optical Imaging Center, Erasmus MC, and Nikon Instruments Europe for fruitful discussions.

## References

1. Kooiman et al., *Adv Drug Del Rev* 2014, 72C: p.28
2. Chin et al., *Rev Sci Instru* 2003, 74: p. 5026
3. Skachkov et al., *IEEE Trans Ultrason Ferroelectr Freq Control* 2014, 61: p. 1661
4. Fan et al., *Proc Natl Acad Sci USA*, 109: p. 16486

# Delayed Enhancement Ultrasound Imaging with Acoustically Activated Definity Droplets in Detecting and Quantifying Myocardial Infarct Size

*Songita A Choudhury, Feng Xie, John Lof, Thomas R Porter*

*University of Nebraska Medical Center; Omaha, NE*

## Introduction

Commercially available Definity (Lantheus Medical) microbubbles (MB) can be converted to nanometer-sized droplets (DD) using cooled compression at the bedside. These droplets have prolonged survival in vivo and are activated back to MB by diagnostic ultrasound (DU) only at higher mechanical indices (MI). Due to their nanometer size and prolonged persistence, DD may be an effective method of delineating myocardial ischemia and viability. HYPOTHESIS. We hypothesized that DD could be utilized to highlight and quantify infarct size (IS) through delayed high MI imaging following intravenous injection (IVI).

## Methods

Rats (n=14) and pigs (n=4) underwent prolonged left anterior descending ischemia (45-90 minutes) via either left coronary artery ligation in rats or balloon occlusion in pigs followed by transthoracic imaging at 48-72 hours. In rats, end-systolic triggered DU imaging with contrast specific sequences (Contrast Pulse Sequencing or CPS; Siemens 15L8) was performed at 2-4 minutes post injection starting with a low 0.5 MI at 2-4 minutes post IVI followed by a brief train of 1.5 MI impulses to examine for myocardial enhancement within the infarct zone and remote normal myocardium. In pigs a different imaging approach was used following IVI of DD, using a triggered end systolic (1:1) mode and ultraharmonic imaging (1.3 MHz transmit/3.4 MHz receive) as well as a real time (10 Hz) harmonic only mode (1.7/3.4 MHz) during the train of 0.5-1.3 MI impulses at 2-4 minutes post IVI. Fluorescently labelled DD were also injected and rats were sacrificed at 10 minutes IVI. Any contrast defect was correlated with IS on post-mortem (TTC) stains and droplet location on fluorescent microscopy (FM).

## Results

Following DD injection, no contrast was observed at any time with 0.5 MI, but a transient myocardial enhancement zone (TEZ) was observed at 2-4 minutes post IVI when the 1.5 MI impulses were applied (Arrows; Figure 1). This TEZ correlated with DD presence within the infarct by fluorescent microscopy and IS by TTC staining ( $r=0.84$ ,  $p<0.001$ ). In pigs, a TEZ was observed with the triggered 1.3/3.4 MHz imaging during the high MI train at 2-4 minutes post IVI that correlated with infarct size by both TTC and delayed enhancement magnetic resonance imaging (Figure 2). The real time 1.7/3.4 MHz imaging produced myocardial opacification within the normal zones and no enhancement within the infarct zone or left ventricular cavity.

## Conclusions

Nanodroplets created from commercially available MB may accumulate within infarct zones following IVI. Their detection with delayed high MI echo activation can be utilized for infarct detection and quantification. Lower frequency ultraharmonic only activation produces selective myocardial enhancement within the infarct zone while harmonic only real time imaging resulted in myocardial and not left ventricular cavity activation resulting in exquisite delineation of the infarct size in real time. This imaging modality significantly alters the potential for delayed contrast echocardiographic imaging to detect and quantify infarct size.

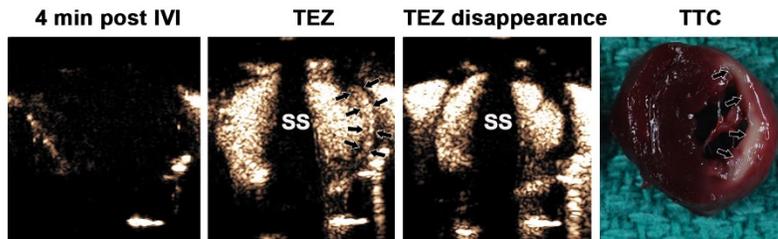


Figure 1. Delayed enhancement with 7 MHz CPS at 4 minutes post IVI of DD, creating a transiently enhanced infarct zone which then became a defect with continued high MI imaging

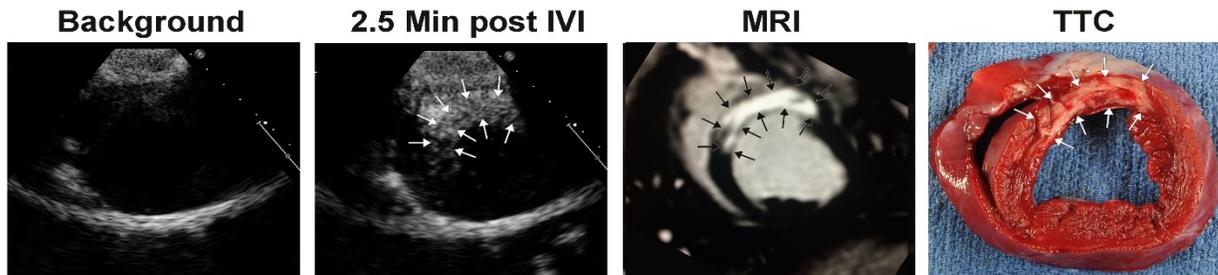


Figure 2. Transient activation within the infarct zone (arrows) utilizing 1.3/3.4 MHz imaging (ultraharmonic) at 2.5 minutes post IVI. The spatial extent of delayed enhancement correlated with delayed enhancement magnetic resonance imaging (MRI: arrows; third panel) and with post mortem TTC staining (arrows; fourth panel). No cavity activation was noted with ultraharmonic triggered imaging or real time harmonic imaging.

# Microbubble perivascular pump effect for enhancing the local delivery efficiency of intranasally-administered agents

*Dezhuang Ye<sup>a</sup>, Xiaohui Zhang<sup>b</sup>, Yimei Yue<sup>c</sup>, Sara Taylor<sup>d</sup>, Yuan-chuan Tai<sup>b</sup>, Joshua B. Rubin<sup>d</sup>, Yongjian Liu<sup>b</sup>, Hong Chen<sup>c,e</sup>*

<sup>a</sup> *Department of Mechanical Engineering and Material Science, Washington University in St. Louis, Saint Louis, Missouri, 63130, USA.*

<sup>b</sup> *Mallinckrodt Institute of Radiology, Washington University School of Medicine, St. Louis, Missouri 63110, USA*

<sup>c</sup> *Department of Biomedical Engineering, Washington University in St. Louis, Saint Louis, Missouri, 63130, USA.*

<sup>d</sup> *Department of Pediatrics, Department of Neuroscience, Washington University School of Medicine, St. Louis, Missouri 63110, USA*

<sup>e</sup> *Department of Radiation Oncology, Washington University School of Medicine, Saint Louis, Missouri, 63108, USA.*

There is an unmet clinical need in brain disease treatment that is to efficiently and locally deliver therapeutics to targeted brain site without jeopardizing healthy regions of the brain and other normal organs. A major challenge is the restricted access of therapeutics to the brain owing to the blood-brain barrier (BBB). Available techniques for circumventing the BBB are either invasive, non-localized, or associated with systemic exposure. Here, we introduce focused ultrasound-mediated intranasal delivery (FUSIN) as a brain drug delivery technique for noninvasive and localized brain drug delivery with minimized systemic exposure.

Delivery of molecules occurs through the olfactory and trigeminal nerve, which innervate the nasal epithelium, to the olfactory bulb and brains stem and further to different parts of the brain. They distribute to the whole brain along the cerebral perivascular spaces – thin annular regions surrounding cortical blood vessels – and may be propelled through perivascular spaces by heartbeat-driven expansion and contraction of blood vessel walls, called “perivascular pump effect”. Our previous ultra-high speed photomicrography studies of microbubble dynamics in microvessels found that microbubble oscillation leads to the expansion and contraction of the blood vessel (Fig. 1), which may generate “microbubble perivascular pump effect” that enhances the penetration and accumulation of IN-administered rugs. Based this observation, we hypothesized that FUS-activated microbubbles could enhance the local delivery efficiency of intranasal (IN)-administered agents.

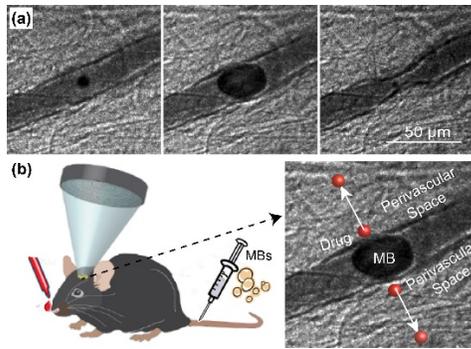


**Figure 1** (a) Ultra-high speed photomicrography of microbubble dynamics in microvessels. These photographs show vessel expansion and contraction induced by the oscillation of microbubbles. (2) Illustration of the focused ultrasound-enhanced intranasal delivery experimental setup and the “microbubble perivascular pump effect.”

Our previous studies have shown the feasibility of FUSIN in the delivery of dextrans and brain-derived neurotrophic factor to caudate putamen. Our recent studies demonstrated its application for the delivery of nanoparticles to the pons. Compared with the results of IV injection, microPET/CT images and gamma counting revealed significantly lower radio-labeled nanoparticle accumulation in the blood and lungs, liver, spleen, kidney, and heart by IN administration. Only the stomach had significantly higher radioactivity than IV injection. These findings suggest that FUSIN may be a platform technology for the noninvasive and localized delivery of various therapeutic agents to different brain locations with minimized systemic exposure.

# Sonodynamic therapy using protoporphyrin IX encapsulated microbubbles inhibits tumor growth

*Xucaï Chen, Bin Qin, Daniel Whitehurst, Brandon Helfield, Linda Lavery, Flordeliza S. Villanueva*

*Center for Ultrasound Molecular Imaging and Therapeutics, University of Pittsburgh, PA, USA*

## **Background, Motivation and Objective**

Sonodynamic therapy is a cancer treatment using drugs called “sonosensitizers” which, upon exposure to ultrasound (US), generate reactive oxygen species (ROS), thereby causing cell death. Despite the potential of sonodynamic therapy, many ideal sonosensitizers, such as protoporphyrin IX (PpIX), are hydrophobic compounds; poor water solubility limits systemic delivery and constrains clinical translation. We hypothesized that a PpIX-loaded lipid microbubble (MB) would have advantages over PpIX alone by ultimately allowing systemic delivery and also by locally concentrating US energy for greater PpIX activation. Accordingly, we developed an efficiently PpIX-loaded MB formulation and characterized its US-induced cytotoxicity in vitro and in an in vivo tumor model.

## **Statement of Contribution/Methods**

PpIX was loaded in the hydrocarbon tail region of the lipid monolayer that forms the encapsulation shell of perfluorocarbon gas-filled MBs (“MB-PpIX”). Suspensions of MB-PpIX or PpIX alone were exposed to various US conditions (1 MHz, 1-8 W/cm<sup>2</sup> spatial average pulse average intensity ( $I_{SAPA}$ ), 1-10% duty cycle), and ROS generation was measured with Amplex Red. MB-PpIX or equivalent amount of PpIX alone (PpIX concentration: 2.9  $\mu$ M) was added to cultured squamous cell carcinoma (SCC-7) cells, followed by US treatment for 2 min and alamarBlue Assay for viability 24 hrs post US. To evaluate anti-tumor effect in vivo, SCC-7 tumor-bearing mice received intratumoral injection of  $1 \times 10^8$  MB-PpIX (n=4), equivalent dose (18.4  $\mu$ g) of PpIX only (n=5), or blank MB (no PpIX, n= 3), followed by 4 min of US treatment (1 MHz,  $I_{SAPA}=3$  W/cm<sup>2</sup>, 10% duty cycle). Tumor volume was serially imaged and quantified by high-resolution 3D US.

## **Results, Discussion and Conclusion**

A stable MB-PpIX-formulation was achieved with high drug loading (mean MB diameter 1-2  $\mu$ m;  $184 \pm 49$   $\mu$ g PpIX per 109 MB). ROS was generated with MB-PpIX and PpIX solution alone, in an US- and time-dependent manner, with more ROS generated by MB-PpIX compared to PpIX alone for a given US condition. For both MB-PpIX and PpIX alone, similar US-dependent cytotoxicity was observed; e.g. for MB-PpIX, more than 90% of SCC-7 cells were killed with US at  $I_{SAPA}=2$  or 4 W/cm<sup>2</sup> and 10% duty cycle. In vivo, MB-PpIX + US caused the greatest tumor growth inhibition, with doubling time ( $2.8 \pm 0.5$  days) more prolonged compared to that for US-treated tumors injected with only PpIX ( $2.1 \pm 0.3$  days;  $p=0.026$ ) or blank MB ( $1.7 \pm 0.6$  days;  $p=0.050$ ). These data indicate that in conjunction with pulsed US, MB-PpIX is an effective sonodynamic therapy platform that may be superior to US + PpIX alone. Our findings set the stage for non-invasive sonodynamic therapy using systemic delivery of PpIX, whereby PpIX-carrying lipid MBs allow circulation of this otherwise insoluble compound, while also focusing and augmenting US energy for enhanced sonodynamic effect.

**Keywords:** ultrasound, microbubble contrast agents, sonodynamic therapy, cancer

# New insights in the role of ROS in mechanisms of sonoporation-mediated gene delivery

*Jean-Michel Escoffre<sup>1</sup>, Pablo Campomanes<sup>2</sup>,  
Mounir Tarek<sup>2</sup>, Ayache Bouakaz<sup>1</sup>*

*<sup>1</sup>Imagerie et Cerveau, Université François-Rabelais, Inserm, Tours, France*

*<sup>2</sup>CNRS, UMR 7565, Université de Lorraine, Nancy, France*

## **Rationale and Aim**

Reactive oxygen species (ROS) are hypothesized to play a role in the sonoporation mechanisms. So far, the production of ROS has been mainly reported inside the cytoplasm of permeabilized cells after sonoporation. However, the acoustical phenomenon triggering the production of ROS is unknown. In this context, we investigated whether the interaction between microbubbles (MBs) and ultrasound (US) induce the production of ROS using biochemical and molecular simulation techniques.

## **Material & Methods**

**Molecular simulations** – We used a multi-scale approach in which the reactive fragments are described with a high-level quantum mechanics (QM) method, while the rest of the system (the lipid component of the MBs + surrounding solvent) was treated by molecular mechanics (MM). This hybrid QM/MM strategy offers the best compromise to study the formation and reactivity of ROS while enabling the extensive configuration sampling that was required to compute their behavior and outcome.

**ROS detection assay** – A MBs suspension (6.25 or 62.5  $\mu$ L of BR14 in 1.5 mL) was placed in a plastic cuvette and mixed using magnetic stirrer. In a deionized water tank at 37°C, the MBs suspension was exposed to 1 MHz US waves with a duty cycle of 40%, and for 30 s, with PNP of 100 kPa and 400 kPa. ROS production was measured, immediately after US application, using fluorescent ROS and OH• detection assays. Using the same set-up and procedure previously described for the in-vitro detection of ROS, gene delivery was assessed by adding plasmid DNA encoding the enhanced green fluorescence protein. The transfection level and the cell viability were evaluated using flow cytometry and MTT assay, respectively

## **Results & Discussion**

The molecular simulations showed that under ultrasound conditions, ROS can form inside the bubbles. These radicals could easily then diffuse through the MB shell toward the surrounding aqueous phase and participate to the nearby permeabilization of plasma membrane (Figure 1).

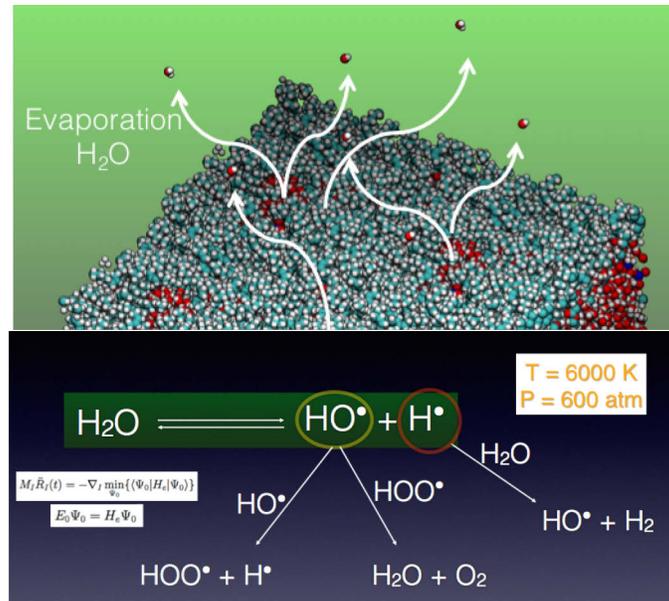


**Figure 1. Molecular simulations**

Our experimental data showed that no ROS was detected at 100 kPa independently of the MB concentrations (Figure 2;  $p > 0.05$ ). At 400 kPa, a low concentration of MBs (6.25  $\mu\text{L}$ ) did not generate ROS ( $p > 0.05$ ). However, the increase in MB concentration to 62.5  $\mu\text{L}$  induced a significant production of ROS ( $p < 0.05$ ).

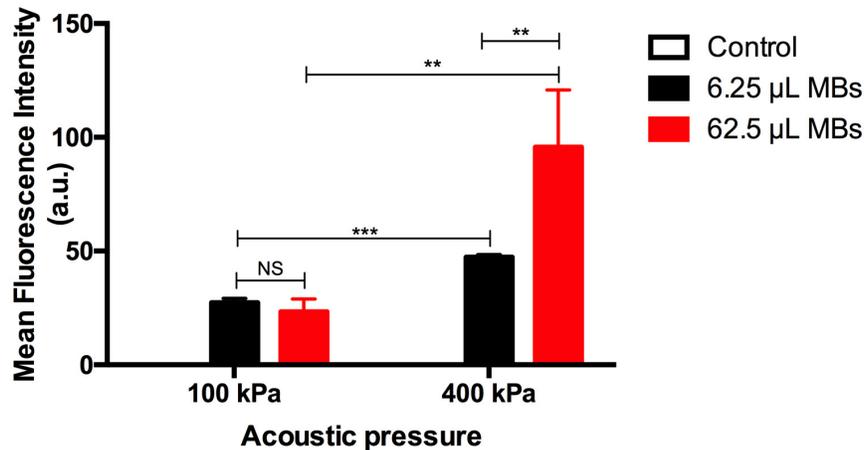


**Figure 2. In-vitro detection of ROS immediately after sonoporation.**

Using specific  $\text{OH}\cdot$  detection assay, we confirmed that lipid coated MBs undergo, favored spontaneous formation of a host of free radicals where  $\text{OH}\cdot$  was the main ROS species after sonoporation (400 kPa, 62.5  $\mu\text{L}$  MBs). The presence of ROS scavengers/inhibitors (Ascorbic acid or Tempol at 2 mM) during the sonoporation (400 kPa, 62.5  $\mu\text{L}$  MBs) process inhibited the production of ROS (Figure 3).

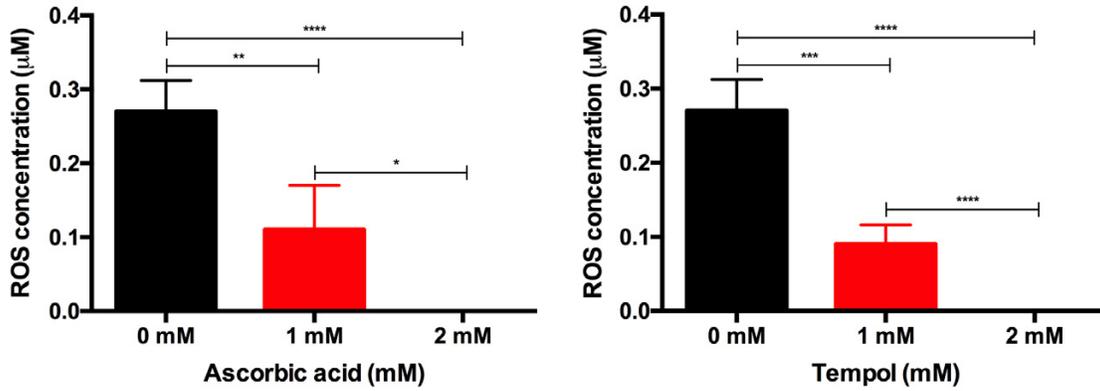


**Figure 3. In-vitro detection of ROS during sonoporation.**

Using flow cytometry, we demonstrated that the presence of ROS scavengers/inhibitors (Ascorbic acid or Tempol at 2 mM) during the sonoporation (400 kPa, 62.5 µL MBs) process decreased the transfection level without significant loss of cell viability (data not shown). In conclusion, the exposure of MBs to US might be the origin of chemical effects, which play a role in the in-vitro permeabilization of the cell membrane and in the in-vitro gene delivery when generated in its proximity.

# Sonoreperfusion of Microvascular Obstruction: a Step towards Clinical Translation

*Filip Istvanic*<sup>1,2,3</sup>, *Francois T.H. Yu*<sup>1</sup>, *Xucaai Chen*<sup>1</sup>, *Flordeliza S. Villanueva*<sup>1</sup>, *John J. Pacella*<sup>1</sup>

<sup>1</sup> *Center for Ultrasound Molecular Imaging and Therapeutics, University of Pittsburgh School of Medicine, Pittsburgh, PA, USA*

<sup>2</sup> *Physician Scientist Training Program, University of Pittsburgh School of Medicine, Pittsburgh, PA, USA*

<sup>3</sup> *Medical Research Fellows Program, Howard Hughes Medical Institute, Chevy Chase, MD, USA*

## Background

Microembolization during percutaneous coronary intervention for acute myocardial infarction causes microvascular obstruction (MVO). We have shown that sonoreperfusion therapy using ultrasound (US) and microbubbles restores microvascular perfusion in an in vitro model of MVO, and that reperfusion efficacy increases with US pulse length.<sup>1</sup> To enable clinical translation of this technique, we compared the reperfusion efficacy of an experimental long-pulse US system (Philips EPIQ) to that of a clinical short-pulse US system (Philips Sonos 7500), which has been shown to enhance perfusion in a rodent hindlimb arterial ligation model of ischemia.<sup>2</sup> We hypothesized that the experimental long-pulse US delivery system would relieve MVO to a greater extent in a rat hindlimb model of MVO than would the clinical short-pulse US delivery system.

## Methods

Our rat hindlimb model of MVO was created by injecting microthrombi into the hindlimb muscle microvasculature via the contralateral femoral artery.<sup>3</sup> Lipid encapsulated microbubbles were infused through the femoral artery while therapeutic US was delivered to the obstructed microvasculature for two 10-minute treatment sessions using either a long-pulse (400 cycles repeated 4 times, 1.6 MHz, 1.1 MPa, 0.33 Hz framerate) or a “short” pulse (5 cycles repeated 7 times, 1.3 MHz, 1.3 MPa, 0.33 Hz framerate). Control rats were injected with microthrombi but did not receive US therapy. Contrast enhanced US perfusion imaging (Sequoia, CPS, 7 MHz) of the microvasculature was conducted at baseline (BL), MVO, post-treatment 1 (Tx1), and post-treatment 2 (Tx2). DEFINITY® microbubble contrast agent was infused through the jugular vein during perfusion imaging. Microvascular blood volumes (MBV) were calculated from videointensity-time data measured in hindlimb muscle regions of interest. Data are expressed as mean ± standard deviation in Figure 1.

## Results

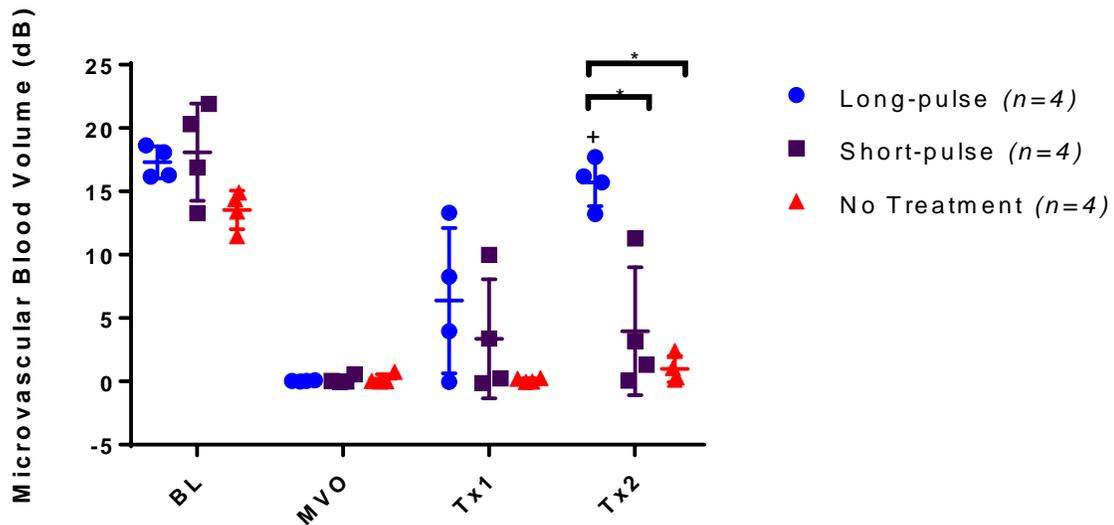
MBV were similar at baseline and markedly reduced after MVO for all groups. In the long-pulse rats (n=4), MBV increased to 91% of BL after Tx2 ( $15.7 \pm 1.9$  dB, n.s vs BL, adj p value <0.0001 vs MVO, adj p value <0.0001 vs Short-pulse Tx2, adj p value <0.0001 vs No Treatment Tx2). In

the short-pulse group (n=4), MBV remained reduced at 22% of BL after Tx2 ( $4.0 \pm 5.0$  dB, n.s. vs MVO). In the “No Treatment” group (n=4), MBV remained reduced at 7.2% of BL after Tx2 ( $0.98 \pm 1.0$  dB, n.s. vs MVO).

## Conclusion

These data demonstrate the superior reperfusion efficacy of a long-pulse (1600 cycles) vs. short-pulse (35 cycles) US delivery system in the setting of MVO. This in vivo observation aligns with our previous in vitro findings, showing that longer pulse length is associated with greater reperfusion efficacy.<sup>1</sup> Results obtained from this study should inform clinical translation and optimization of sonoreperfusion of MVO.

**Figure 1:** Microvascular blood volume (dB) assessed by contrast enhanced ultrasound perfusion imaging. Imaging was conducted at baseline (BL), after microvascular obstruction (MVO), and after two successive 10-minute sessions of sonoreperfusion therapy (Tx1 and Tx2). The three experimental groups were Long-pulse, Short-pulse, and No Treatment. + adjusted  $p < 0.0001$  vs. MVO. \* adjusted  $p < 0.0001$ .



## References

1. Leeman JE et al. Effect of acoustic conditions on microbubble-mediated microvascular sonothrombolysis. *Ultrasound Med Biol* 2012;38(9):1589-98.
2. Belcik JT et al. Augmentation of limb perfusion and reversal of tissue ischemia produced by ultrasound-mediated microbubble cavitation. *Circ: Cardiovasc Imaging*. 2015;8:e002979.
3. Pacella JJ et al. Treatment of microvascular microembolization using microbubbles and long-tone-burst ultrasound: an in vivo study. *Ultrasound Med Biol* 2015;41(2):456-64.

# Ultrasound-activated microbubbles enhance the activity of low-concentration gentamicin against *Pseudomonas aeruginosa* biofilms

*Filip Plazonic*<sup>1</sup>, *Charlotte Hind*<sup>2</sup>, *Michael Gray*<sup>3</sup>, *Martyn Hill*<sup>1</sup>, *Eleanor Stride*<sup>3</sup>, *Peter Glynne-Jones*<sup>1</sup>, *Mark Sutton*<sup>2</sup>, *Dario Carugo*<sup>1\*</sup>

<sup>1</sup> *Faculty of Engineering and the Environment, University of Southampton, Southampton, United Kingdom*

<sup>2</sup> *Public Health England, Porton Down, Salisbury, Wiltshire, United Kingdom*

<sup>3</sup> *Institute of Biomedical Engineering (IBME), University of Oxford, Oxford*  
*E-mail: fp3g10@soton.ac.uk \*D.Carugo@soton.ac.uk*

## Introduction

Antimicrobial resistance (AMR) is an ever-increasing threat, and is often associated with excessive antibiotic (AB) usage. For instance, *Escherichia Coli* is reported to have 18% resistance rate to the most common antibiotics, and multidrug resistant bacteria are becoming more frequent in post-operative infections [1]. Diabetic foot ulcers (DFUs) are a type of chronic wound with high risk of bacterial infections that are poorly susceptible to antimicrobial agents, and cause 50% of all lower-leg amputations in the UK [2]. Thus, there is a growing need for the development of more effective therapeutic approaches.

The specific biofilm investigated in this project is *Pseudomonas aeruginosa*. This biofilm forming bacteria is a major cause of bronchopneumonia in patients with cystic fibrosis, a disease which currently requires lifelong treatment [3]. It is highly susceptible to developing AMR, as it has protective layers and defences which reduce the effectiveness of antibiotics [4]. Some specific strains of *Pseudomonas* require only 40 µg/ml of antibiotic (i.e., gentamicin) to prevent regrowth, while a wild-type could require up to 500 µg/ml and has a higher risk of developing AMR [5].

Gas microbubbles (MB) stabilised by a coating layer have demonstrated potential for enhancing delivery of bioactive compounds in cells and tissues. When exposed to an ultrasound field they can undergo volumetric oscillations and, due to radiation forces, they can move along with the traveling field, or towards nodes or anti-nodes in a standing wave field [6]. This makes them a useful tool for penetrating loose solids [7] and biofilms [8]. MB oscillations may also cause disruption of the biofilm or promote advection of chemical species, potentially resulting in more effective antibiotic penetration.

There have been some studies investigating the effect of microbubbles and ultrasound on biofilms, both in the presence and absence of antibiotics [9]. Overall, the addition of MBs and ultrasound provides an improvement to conventional treatments in vitro. Moreover, earlier studies have shown that ultrasound-activated microbubbles can enhance the activity of 50 µg/ml gentamicin on *P. aeruginosa*, thus significantly increasing the antibiotic effectiveness [10]. In this study, we systematically investigate different MB-mediated therapeutic protocols with the aim of lowering further the amount of antibiotic required to induce an antimicrobial effect.

## Methods

A device for in-vitro exposure of bacterial biofilms was designed to be robust as well as easy to assemble, operate, and sterilise. It comprised a 1 MHz transducer positioned above a plastic dish, where the microbubble-antibiotic solution was injected. The dish was sealed using an acoustically transparent PDMS lid [11], and a PDMS holder was designed for securing a biofilm-coated coupon at the bottom of the dish. Layers of a polyurethane ultrasound absorber were placed below the dish and laterally, in order to mimic free-field conditions and avoid reflections. All these elements were aligned using three equidistant threaded rods on which the components were fixed. Figure 1a shows an image of the device, while Figure 1b shows its schematic. The device can be assembled and operated in less than three minutes, and given its limited size (15×15×45 cm) it only requires a small amount of fluid for immersion and transducer coupling, which makes it compatible with usage under microbiological safety cabinets.

Numerical simulations (using COMSOL Multiphysics) were performed in order to characterise the acoustic field within the device. A travelling wave field occurred when an acoustically transparent material (i.e., polypropylene) was used as a biofilm substrate (Figure 2a), whilst a standing wave formed when a reflecting material (i.e., stainless steel) was employed (Figure 2b). The device was then assembled and calibrated experimentally to achieve a maximum peak-to-peak acoustic pressure of 0.6 MPa at the biofilm surface (US frequency = 1 MHz).

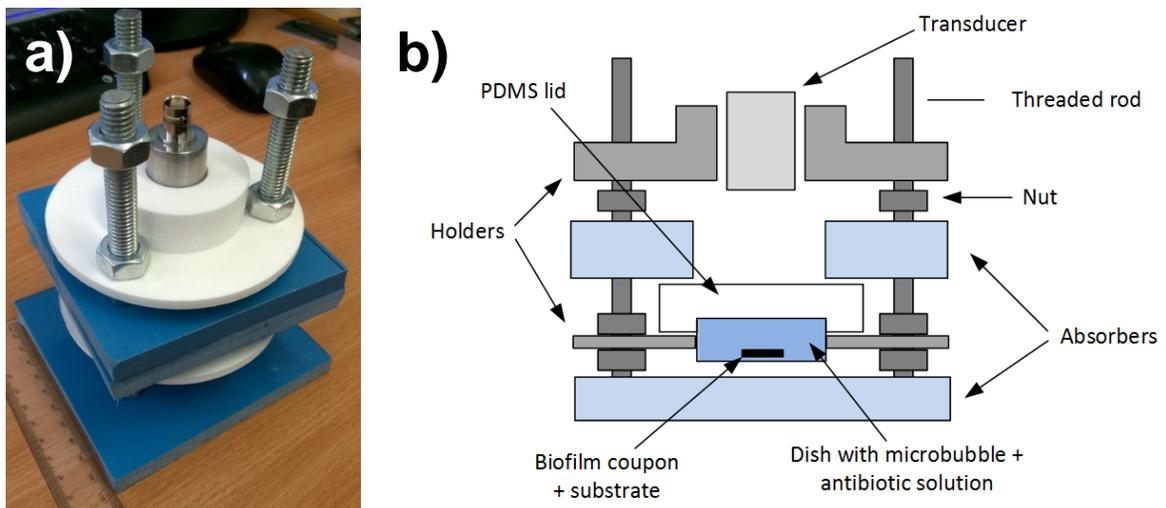


**Figure 1:** In-house developed device for ultrasound stimulation of biofilms. A photograph of the assembled device is reported in (a), whilst a schematic illustration is reported in (b).

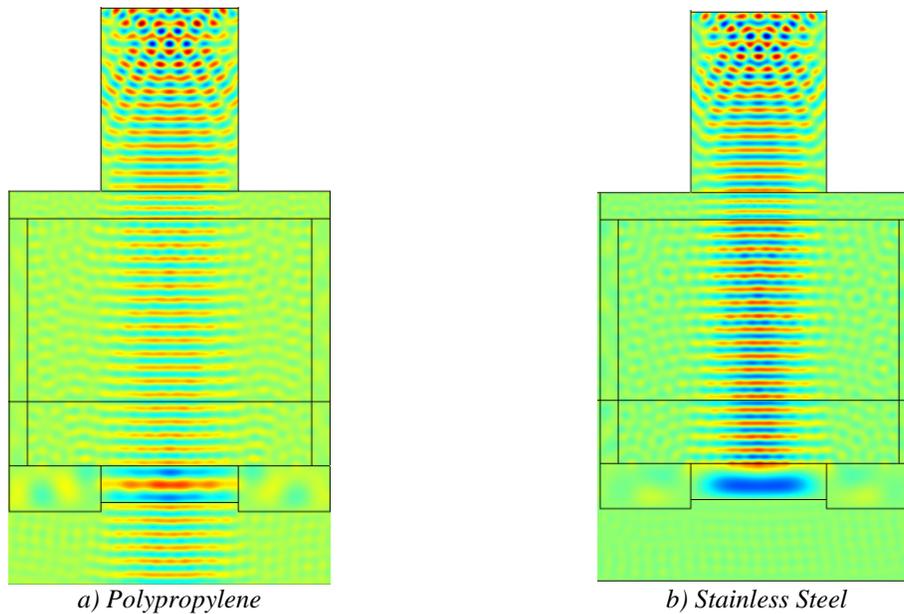


**Figure 2:** Numerical simulation of the acoustic field inside the active area of the device. Simulations were performed to investigate biofilm substrates with different acoustic behaviour, including polypropylene (a) and stainless steel (b).

Microbubbles were produced by sonication of a DSPC:PEG40s (9:1 molar ratio) suspension, and had a mean diameter of 1.8  $\mu\text{m}$ . For experiments utilising positively charged microbubbles, DSEPC was added to the lipid mixture. *Pseudomonas aeruginosa* was grown over small coupons (flat disks) inside a bioreactor. The antibiotic used, gentamicin, was dosed at sub-inhibitory concentrations (<10  $\mu\text{g/ml}$ ).

A variety of conditions were tested to identify an effective biofilm treatment protocol. These included (i) microbubble net charge, (ii) microbubble concentration, (iii) continuous vs. pulsed ultrasound exposure (100 kHz PRF, at 25% duty cycle), (iv) effect of priming the biofilm with the bubble suspension before and in-between multiple ultrasound exposures, (v) varying the recovery period between exposures, and (vi) the physical properties of the substrate (acoustically transparent vs. acoustically reflective), to mimic infections grown in proximity to soft or hard (bone) tissue.

For all experiments, the bubble-antibiotic mixture was injected inside the dish, removing any exogenous air pocket. The dish was placed on a holder inside the device, which was then fully submerged in a small tank. The transducer was activated for 5 minutes, during which either a pulsed or continuous 1 MHz ultrasound wave was generated. After treatment, the biofilm coupon was incubated in tryptic soy broth (with or without antibiotic) for 24 hours, after which the Miles-Misra technique was used to count the number of colony forming units on each coupon.

## Results

A single exposure to neutral microbubbles and ultrasound enhanced the antibiotic activity, and gave a 73% improvement in % killing over antibiotic alone. Charged microbubbles had a lower killing rate, potentially due to complex interactions with the antibiotic and the biofilm (both having a net charge). Therefore, a neutral microbubble formulation was selected for the

remaining experiments. Microbubble concentration had a significant effect on the treatment performance. At the highest concentration investigated ( $6 \times 10^7$  MB/ml) the % killing was significantly lower when compared to more diluted microbubble suspensions ( $1.2 \times 10^7$  and  $0.6 \times 10^7$  MB/ml), likely due to a shielding effect at the higher MB concentrations that limited ultrasound propagation towards the biofilm surface. The most effective MB concentration was equal to  $1.2 \times 10^7$  MB/ml, and gave a % killing increase of 99% compared to antibiotic alone. Using pulsed instead of continuous ultrasound exposure gave a further small increase in antimicrobial efficacy.

By allowing 15 min priming periods before ultrasound exposure and resting periods between multiple exposures, a 93% killing increase over antibiotic alone was achieved, and an overall % killing of 99.9% as the antibiotic is allowed to more effectively penetrate the biofilm. Chemicals present in the MB suspension (and particularly PEG40s) may also have an antimicrobial effect during priming.

### Conclusions

High concentration antibiotics ( $>50$   $\mu\text{g/ml}$ ) can achieve a desired 99.9% bacterial killing in biofilms [5], but through repeated use bacteria are likely to develop AMR. We have shown that ultrasound-activated microbubbles have potential for enhancing the antimicrobial activity of low-concentration ( $<10$   $\mu\text{g/ml}$ ) antibiotics on *Pseudomonas Aeruginosa* biofilms. Among the different treatment protocols investigated, repeated pulsed ultrasound exposures (2 exposures) with recovery intervals between exposures (15 min) in the presence of neutral microbubbles, led to the most effective antimicrobial performance (99.9% bacterial killing). Lowering the antibiotic concentration would not only reduce the chances of AMR developing, but would also reduce toxic side effects.

### References

1. "UK 5 Year Antimicrobial Resistance (AMR) Strategy 2013-2018, Annual progress report", 2016, <https://www.gov.uk/government/collections/antimicrobial-resistance-amr-information-and-resources>
2. "Diabetic foot problems: prevention and management", NICE guideline, August 2015, <https://www.nice.org.uk/guidance/ng19/chapter/introduction>
3. Høiby, N., Bjarnsholt, T., Givskov, M., Molin, S., Ciofu, O., "Antibiotic resistance of bacterial biofilms" (2010), *Int J Antimicrob Agents*, 34, pp. 322-332
4. Breidenstein, E.B.M., Fuente-Núñez, C., Hancock, R.E.W., "Pseudomonas aeruginosa: all roads lead to resistance" (2011), *Trends Microbiol*, 19, pp. 419-426
5. Mah, T., Pitts, B., Pellock, B., Walker, G.C., Stewart, P.S., O'Toole, G.A., "A genetic basis for Pseudomonas aeruginosa biofilm antibiotic resistance" (2003), *Nature*, 426, pp. 306-310
6. Leighton, T.G., *The Acoustic Bubble* (1994), Academic Press, London, UK
7. Birkin, P.R., Offin, D.G., Leighton, T.G., "An activated fluid stream – new techniques for cold water cleaning" (2016), *Ultrason Sonochem*, 29, pp. 612-618
8. Mott, I.E.C., Stickler, D.J., Coakley, W.T. and Bott, T.R., "The removal of bacterial biofilm from water-filled tubes using axially propagated ultrasound" (1998), *Journal of Applied Microbiology*, 84, pp. 509–514.
9. Erriu, M., Blus, C., Szmukler-Moncler, S., Buogo, S., Levi, R., Barbato, G., Madonnaripa, D., Denotti, G., Piras, V., Orrù, G., "Microbial biofilm modulation by ultrasound: Current concepts and controversies" (2014), *Ultrason Sonochem*, 21, pp. 15-22
10. Ronan, E., Edjiu, N., Kroukamp, O., Wolfaardt, G., Karshafian, R., "USMB-induced synergistic enhancement of aminoglycoside antibiotics in biofilms" (2016), *Ultrasonics*, 69, pp. 182-190
11. Carugo, D., Owen, J., Crake, C., Lee, J.Y., Stride, E., "Biologically and acoustically compatible chamber for studying ultrasound-mediated delivery of therapeutic components" (2015), *Ultrason in Med & Biol*, 41, pp. 1927-1937

# Short and long-term effects of oxygen microbubble administrations in a rat fibrosarcoma model and radiotherapy sensitization

*Virginie Papadopoulou<sup>1</sup>, Samantha M. Fix<sup>2</sup>, Hunter Velds<sup>3</sup>, Connor Slagle<sup>3</sup>, Sandeep K. Kasoji<sup>1</sup>, Judith N. Rivera<sup>4</sup>, Mark A. Borden<sup>3</sup>, Sha Chang<sup>4</sup>, Paul A. Dayton<sup>1,2</sup>*

<sup>1</sup>*Joint Department of Biomedical Engineering, The University of North Carolina and North Carolina State University, Chapel Hill, NC;*

<sup>2</sup>*Eshelman School of Pharmacy, UNC Chapel Hill, Chapel Hill, NC;*

<sup>3</sup>*Department of Mechanical Engineering, University of Colorado, Boulder, CO;*

<sup>4</sup>*Department of Radiation Oncology, UNC Chapel Hill, Chapel Hill, NC.*

*\*corresponding author: padayton@email.unc.edu*

Solid cancer tumors are characterized by the presence of disorganized, leaky vessels that promote regions of low oxygenation (hypoxia), which is a key factor in treatment failure or recurrence after treatments with radiotherapy (RT), chemotherapy and surgery. Recently, oxygen microbubbles (OMB), which are similarly formulated to micrometer-sized ultrasound vascular contrast agents but comprise an oxygen gas core, have been shown to sustain asphyxiated animals for over two hours as well as improve sonodynamic therapy *in vivo*. However, to date a) no dose-response or time-dynamic tumoral reoxygenation data exists, and b) their therapeutic potential for improving RT has not been evaluated. We report on (1) real-time measurements via non-invasive spectroscopic absorbance of OMB-induced tumor hypoxia modulation, (2) long-term effects of repeated IT delivery of OMB, and (3) improved radiotherapy tumor control improvement with a single administration of OMB immediately prior to RT, all using a validated tumor hypoxia model (Fisher 344 rats with fibrosarcoma xenografts).

For spectroscopic measurements, 3 administration routes (direct tumoral injection (IT), intravenous (IV), and intra-peritoneal (IP)) were compared to 3 min pure oxygen breathing (oxygen challenge, serving as a positive control), and to the respective nitrogen microbubble negative controls for each route of administration. Both IT and IV OMB administrations are shown to significantly relieve tumor hypoxia, and percent increase in oxygenation was proportional to baseline hypoxia (Fig. 1).

In addition to the potential of OMB to transiently relieve tumor hypoxia, the long-term effect of repeated reoxygenation via OMB IT injections was investigated. In the absence of any other therapy, daily OMB IT injections for 7 days (but not a single injection) are shown to significantly slow down tumor growth compared to both no intervention or saline injection controls.

For our initial radiotherapy study, animals were stratified based on tumor size and divided into size-matched groups. Animals received radiotherapy (single 15 Gy dose of 6 MV photons with clinical linear accelerator), and initial results (n=6 per group, monitored 31 days post RT) demonstrate a significant increase in tumor control time (defined as the time to maximum tumor burden = 2.5 cm in any direction) with a single IT administration of OMB immediately prior to RT compared to RT alone or RT with nitrogen microbubble administration (Fig. 2). As expected, for a fixed RT and fixed OMB dose, a significant dependence on initial tumor volume is demonstrated and normalized tumor control time improvement was about 35% for tumors above

a threshold volume (below this, no improvement is detected since tumor are likely less hypoxic and RT is efficient at providing tumor control for the full observation period of 31 days). These results offer an exciting development towards an agent for image-guided and ultrasound-triggered oxygen release for RT.

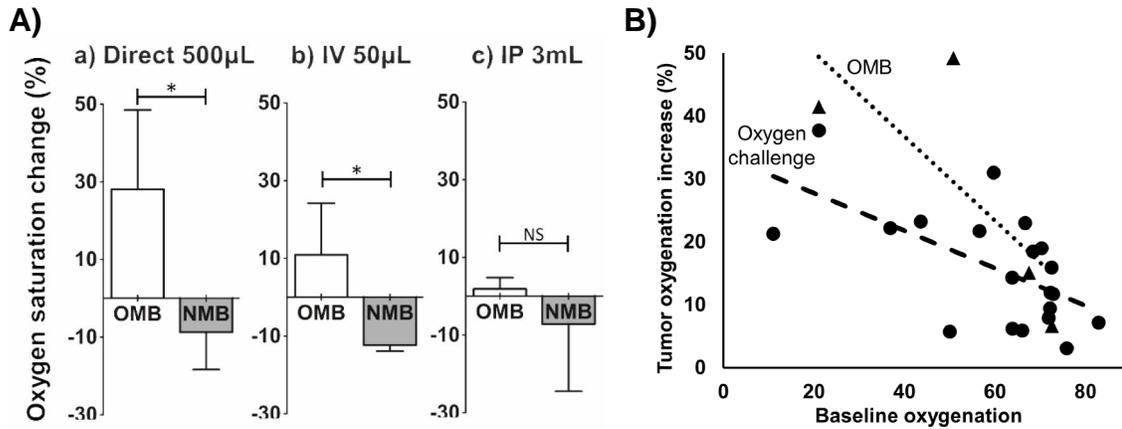


**Fig.1:** A) Change in tumoral oxygenation after a) direct IT ( $p < 0.05$ ), b) IV ( $p < 0.05$ ) or c) IP injections of MB. On average peak OMB increase was reached after a) 97s & sustained for 18min ( $n=4$ ), b) 8.9min & returned to baseline after 12.8min ( $n=3$ ), c) not significant ( $n=4$ ). B) The oxygen challenge (triangles) and OMB-induced (circles) tumor oxygenation increase is shown inversely proportional to baseline tumor oxygenation.

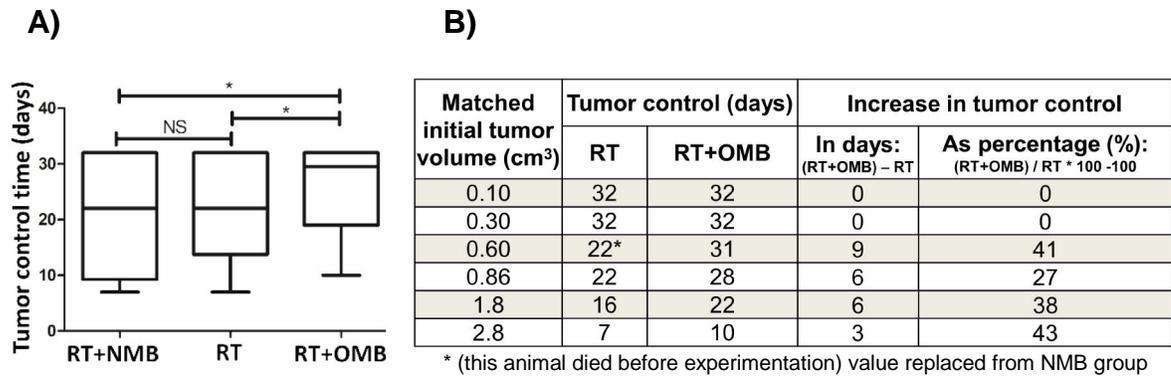


**Fig.2:** A) Tumor control time comparison between RT groups. RT+OMB significantly increased tumor control time ( $p < 0.05$ ), whereas no difference was found between no treatment and OMB alone without RT. B) Table detailing tumor volume stratification. The effect size dependency on initial tumor volume was found as expected for a fixed OMB dose and a fixed RT dose. For very small tumors: RT dose is already very efficient + monitoring capped at 31 days & tumors likely less hypoxic. For very large tumors: tumors likely very hypoxic and same OMB dose used.

# Contrast enhanced ultrasound molecular imaging (CEUMI) of atherosclerosis: Development of a clinically translatable tracer for targeting of vascular cell adhesion molecule 1 (VCAM-1)

*Mukesh Punjabi<sup>1</sup>, Amanda Ochoa-Espinosa<sup>1</sup>, Lifen Xu<sup>1</sup>, Alexis Broisat<sup>3</sup>, Nick Devoogdt<sup>4</sup>, Beat A. Kaufmann<sup>1,2</sup>*

<sup>1</sup>Cardiovascular Molecular Imaging, Department of Biomedicine, <sup>2</sup>Department of Cardiology, University Hospital Basel, University of Basel, Basel, Switzerland; <sup>3</sup>Bioclinical Radiopharmaceuticals Laboratory, Grenoble-Alpes University, France; <sup>4</sup>In vivo Cellular and Molecular Imaging Laboratory, Vrije Universiteit Brussel, Brussels, Belgium.

## Background

Risk assessment for atherosclerotic complications relies on established clinical risk factors and places 40% of the adult population in an intermediate risk category, for which management is uncertain [1, 2]. Ultrasound molecular imaging of endothelial expression of VCAM-1 involved in inflammatory processes that initiate and propagate atherosclerosis [3] could improve risk stratification for atherosclerotic complications. This will improve primary prevention and better allocate existing and emerging preventive therapies. However, the microbubble (MB) contrast agents that have been studied so far [4-8] use biotin-streptavidin conjugation chemistry and full-size antibodies, and thus are not suitable for clinical translation. Nanobodies [9] are small antibody fragments derived from heavy-chain-only antibodies present in camelids and provide several advantages (stable, highly target specific, weakly immunogenic) over conventional antibodies for clinical applications. Nanobodies targeted to VCAM-1 have already been used for imaging of atherosclerotic lesions using nuclear tracers and SPECT/CT imaging [10].

Aim: Development, characterization, in-vitro and in-vivo validation of a MB contrast agent with a clinically translatable nanobody ligand targeted to VCAM-1 using maleimide conjugation chemistry for detection of VCAM-1 in large arteries.

## Methods

Nanobody with cross-reactivity for mouse and human VCAM-1 (cAbVcam1-5) [10] were modified to carry a C-terminal cysteine thiol for covalent conjugation to a maleimide-3400K polyethylene glycol (PEG3400)-DSPE lipid anchor on the surface of lipid-shelled decafluorobutane targeted MBs (MBcAbVcam1-5). Isotype control nanobody (VHH2E7) was similarly used to prepare control MBs (MBVHH2E7). Before conjugation to MBs, the nanobodies underwent a reduction step with 2-mercaptoethylamine to preserve the domain's stability.

Characterization: Initially the specific attachment of cAbVcam1-5 to murine VCAM-1 was evaluated by using a fluorescence linked ligand binding assay. Next, MBcAbVcam1-5 were incubated with an Alexa-488 labeled secondary nanobody that recognized a C-terminal EPEA tag on the cAbVcam1-5 nanobody. The conjugation of cAbVcam1-5 to the MB surface was subsequently verified with fluorescence microscopy. Nanobody concentration resulting in optimal

saturation of maleimide binding sites on the MB surface was determined by measuring the fluorescence intensity with a flow cytometer after incubating the MBs with increasing concentrations of NHS Fluorescein labeled cAbVCAM1-5. Coulter counter measurements of MB concentration and surface area were combined with fluorescent spectroscopy standard curves of NHS-Fluorescein labeled cAbVCAM1-5 to measure the ligand site density.

In-vitro validation: Parallel plate flow chamber adhesion assays using tumor necrosis factor (TNF)-alpha activated bEnd.3 endothelial cells expressing VCAM-1 were performed. Initially the attachment efficiency under flow conditions was tested with continuous shear stress of 1, 2, 4 and 8 dynes/cm<sup>2</sup>. Since aortic flow is pulsatile, adhesion at the higher shear rate of 8 dynes/cm<sup>2</sup> was also assessed after transient (5-second) reductions of shear to <0.5 dyne/cm<sup>2</sup>. After maximal attachment of MBcAbVcam1-5 at lowest shear stress of 0 to 0.5 dynes/cm<sup>2</sup>, the detachment characteristics of the tracer were determined by sequentially increasing the shear stress by 5 dynes/cm<sup>2</sup> up to a maximum of 43 dynes/cm<sup>2</sup>. Further a comparison of the attachment efficiency was made with MBs bearing conventional antibodies against VCAM-1 (MBmABVcam1).

In-vivo validation: A male mouse model (referred to as double knockout (DKO)) deficient in low density lipoprotein receptor and a mutation in the ApoB48 gene (only apolipoprotein B-100 is expressed) was used. These mice are maintained on chow diet and closely mimic human atherosclerosis. In a terminal experiment after jugular vein catheterization, CEUMI of the aortic arch using contrast pulse sequencing at 7 Mhz frequency and a mechanical index of 0.87 was performed with MBcAbVcam1-5 and MBVHH2E7 in DKO and wildtype (WT) mice at an early stage (10 weeks age) and late stage (40 weeks age) of plaque development. High frequency ultrasound imaging was performed to measure aorta internal diameter, peak systolic flow velocity and left ventricular ejection fraction. The mice were subsequently euthanized, and the aortic tissue stored for immunohistology.

## Results

The ligand binding assay showed specific attachment of cAbVcam1-5 ligand to mouse VCAM-1. Fluorescent microscope images confirmed conjugation of cAbVcam1-5 to the MB surface. Fluorescent spectroscopy calculations revealed  $\sim 3.5 \times 10^5$  cAbVcam1-5 molecules coupled to the MB surface which corresponded to one cAbVcam1-5 molecule per  $\sim 74$  nm<sup>2</sup> or  $\sim 1.3 \times 10^4$  cAbVcam1-5 molecules per  $\mu\text{m}^2$  of the MB surface.

In-vitro validation: Compared to MBVHH2E7, MBcAbVcam1-5 showed increased retention on endothelial cells under continuous flow at different shear rates (MBcAbVcam1-5 vs. MBVHH2E7: 18.6 $\pm$ 2.8 vs. 4.9 $\pm$ 1.4,  $p < 0.005$  at 1 dynes/cm<sup>2</sup>; 9.1 $\pm$ 1.3 vs. 4.6 $\pm$ 0.7,  $p < 0.005$  at 2 dynes/cm<sup>2</sup>; 4.5 $\pm$ 1.2 vs. 1.9 $\pm$ 0.5,  $p < 0.05$  at 4 dynes/cm<sup>2</sup>; 1.1 $\pm$ 0.1 vs. 0.5 $\pm$ 0.1,  $p < 0.005$  at 8 dynes/cm<sup>2</sup>). MBcAbVcam1-5 showed decreased retention with increasing shear stress (detachment at 35 ( $p < 0.05$ ), 40 ( $p < 0.01$ ) and 43 ( $p < 0.001$ ) dynes/cm<sup>2</sup>) as compared to maximal retention at baseline. Additionally, sequential brief reductions in shear resulted in a stepwise increase ( $p < 0.0001$ ) of the attachment of MBcAbVcam1-5 to permanently bind at the high shear rate of 8 dynes/cm<sup>2</sup>. Finally, in comparison to MBmABVcam1, MBcAbVcam1-5 at 2 dynes/cm<sup>2</sup> showed no difference in retention on activated endothelial cells.

In-vivo validation: Analysis of the CEUMI data using showed significant difference of medians at 10 weeks ( $p = 0.0003$ ) and at 40 weeks age ( $p = 0.0069$ ). Multiple comparisons at age 10 weeks

showed signal enhancement for VCAM-1 between: DKO MB<sub>cAbVcam1-5</sub> and DKO MB<sub>VHH2E7</sub> group ( $p < 0.001$ ); DKO MB<sub>cAbVcam1-5</sub> and WT MB<sub>cAbVcam1-5</sub> group ( $p < 0.005$ ). Multiple comparisons at age 40 weeks showed signal enhancement for VCAM-1 between: DKO MB<sub>cAbVcam1-5</sub> and DKO MB<sub>VHH2E7</sub> group ( $p < 0.005$ ); DKO MB<sub>cAbVcam1-5</sub> and WT MB<sub>cAbVcam1-5</sub> group ( $p < 0.05$ ). High frequency ultrasound data analysis showed the aorta internal diameter and peak systolic flow velocity to be similar for DKO and WT mice at age 10 weeks. Aorta internal diameter and peak systolic flow velocity were higher for DKO ( $p < 0.0001$  and  $p < 0.005$  respectively) as compared to WT mice at age 40 weeks. The left ventricular ejection fraction was reduced for DKO as compared to WT mice at age 10 weeks ( $p < 0.05$ ) and 40 weeks ( $p < 0.001$ ).

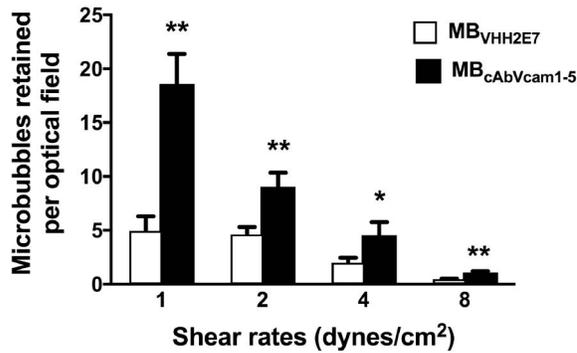


**Fig 1:** Compared to control MBs (MB<sub>VHH2E7</sub>), targeted MBs (MB<sub>cAbVcam1-5</sub>) showed increased retention under continuous flow on activated endothelial cells at different shear rates (\* $p < 0.05$ , \*\* $p < 0.005$ ;  $n = 7$  each).

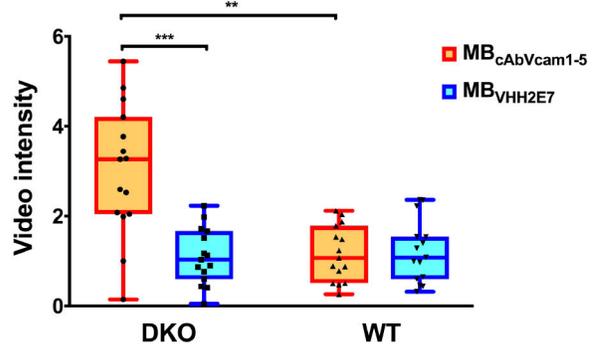


**Fig 2:** Background subtracted CEUMI signal intensity from the aortic arch 8 minutes after intravenous injection of targeted (MB<sub>cAbVcam1-5</sub>) and control (MB<sub>VHH2E7</sub>) MBs in DKO and WT mice at age 10 weeks (\*\*\* $p < 0.001$ , \*\* $p < 0.005$ ;  $n = 15$  each).

## Conclusion

We have characterized a targeted contrast agent using a nanobody with maleimide covalent bonding to the MB surface for detection of VCAM-1 in large arteries. The nanobody attaches specifically to VCAM-1 and we have determined the surface density of the nanobody ligand on the MB surface. The VCAM-1 targeted contrast agent shows attachment to endothelial cells under continuous flow with increasing shear stress. At high shear stress, the tracer indicates its ability to firmly attach when flow occurs in pulsatile rather than continuous conditions. In mouse models of atherosclerosis, the VCAM-1 targeted contrast agent can successfully detect vascular inflammation at an early stage before development of advanced lesions. These findings will facilitate the use of this tracer in further ex-vivo human artery experiments and pave the way for clinical translation to detect early pathophysiological changes and improve risk stratification for atherosclerotic complications.

## References

1. Assmann, G., P. Cullen, and H. Schulte, *Simple scoring scheme for calculating the risk of acute coronary events based on the 10-year follow-up of the prospective cardiovascular Munster (PROCAM) study. Circulation, 2002. 105(3): p. 310-5.*
2. Ginhina, C., I. Bejan, and C.D. Ceck, *Modern risk stratification in coronary heart disease. Journal of Medicine and Life, 2011. 4(4): p. 377-386.*
3. Huo, Y., A. Hafezi-Moghadam, and K. Ley, *Role of vascular cell adhesion molecule-1 and fibronectin connecting segment-1 in monocyte rolling and adhesion on early atherosclerotic lesions. Circ Res, 2000. 87(2): p. 153-9.*
4. Kaufmann, B.A., et al., *Molecular imaging of inflammation in atherosclerosis with targeted ultrasound detection of vascular cell adhesion molecule-1. Circulation, 2007. 116(3): p. 276-84.*
5. Kaufmann, B.A., et al., *Molecular imaging of the initial inflammatory response in atherosclerosis: implications for early detection of disease. Arterioscler Thromb Vasc Biol, 2010. 30(1): p. 54-9.*
6. Khanicheh, E., et al., *Noninvasive ultrasound molecular imaging of the effect of statins on endothelial inflammatory phenotype in early atherosclerosis. PLoS One, 2013. 8(3): p. e58761.*
7. Khanicheh, E., et al., *Molecular imaging reveals rapid reduction of endothelial activation in early atherosclerosis with apocynin independent of antioxidative properties. Arterioscler Thromb Vasc Biol, 2013. 33(9): p. 2187-92.*
8. Steinl, D.C. and B.A. Kaufmann, *Ultrasound imaging for risk assessment in atherosclerosis. Int J Mol Sci, 2015. 16(5): p. 9749-69.*
9. Vincke, C., et al., *General strategy to humanize a camelid single-domain antibody and identification of a universal humanized nanobody scaffold. J Biol Chem, 2009. 284(5): p. 3273-84.*
10. Broisat, A., et al., *Nanobodies targeting mouse/human VCAM1 for the nuclear imaging of atherosclerotic lesions. Circ Res, 2012. 110(7): p. 927-37.*

# Interactions of drug-loaded microbubbles and ultrasound with a soft tissue environment

Roovers Silke<sup>1</sup>, De Cock I.<sup>1</sup>, Lajoinie G.<sup>2</sup>, Prakash. J.<sup>2</sup>, Versluis M.<sup>2</sup>, De Smedt S.C.<sup>1</sup>,  
Lentacker I.<sup>1</sup>

<sup>1</sup>*Ghent Research Group on Nanomedicines, Ghent University, Ghent, Belgium;*

<sup>2</sup>*MIRA institute, University of Twente, Enschede, The Netherlands*

*E-mail: Silke.Roovers@UGent.be*

## Introduction

Drug-loaded microbubbles have proven very promising for drug delivery purposes since they not only allow localized drug release but can also enhance the delivery of the drugs into the tissue [1]. Recently, we have proposed “sonoprinting” as a third possible mechanism, next to sonoporation and enhanced endocytosis, that may be responsible for the improved drug delivery when using drug-loaded microbubbles and ultrasound [2-4]. Sonoprinting is defined as the direct deposition of elongated patches of nanoparticles along with parts of the bubble shell upon applying ultrasound to nanoparticle-loaded microbubbles [2]. However, earlier studies have shown that the presence of a stiff membrane on which the cells are cultured in vitro, can cause asymmetrical oscillations of microbubbles [5,6] and as such influence microbubble-cell interactions. To be certain that this effect is not due to the presence of a stiff membrane in our in vitro set-up, this study aims to evaluate the interactions of drug-loaded microbubbles with cells in a in vivo-like 3D soft tissue environment.

## Materials and methods

4T1 murine breast cancer cells and 3T3 fibroblasts were used to form co-spheroids by self-aggregation in ultra-low adhesion agar microwells [7]. The 3D micro-environment of these multicellular spheroids resembles the in vivo situation, as an extracellular matrix is formed that acts as a major physical barrier for drug penetration [8,9]. Liposome-loaded microbubbles were prepared by attaching biotinylated liposomes containing doxorubicin (DOX) and/or DiD as a fluorescent marker, to the shell of biotinylated lipid microbubbles with the aid of an avidin linker. The spheroids were incubated with liposome-loaded microbubbles in an ultrasound transparent chamber, after which ultrasound of 1 MHz center frequency, 10% duty cycle, 2 W/cm<sup>2</sup> was applied for 10 seconds. The spheroids were subsequently studied using confocal microscopy, flow cytometry and toxicity assays. Cryosections of 10 µm were made to investigate the DOX and liposome penetration into the spheroids in further detail.

## Results

When treating the multicellular spheroids with liposome-loaded microbubbles and ultrasound, the mean liposomal fluorescence that was found on the spheroid cells using flow cytometry was 90x higher compared to incubation with liposomes alone and 74x higher than when the liposomes and microbubbles were co-administered before ultrasound radiation.

When studying intact spheroids under confocal microscopy, it became clear that this increase in liposome delivery was caused by a large deposition of liposomes on the outer cell layers of the tumor spheroid, as seen in figure 1. Cryosections confirmed that these patches were limited to the first few cell layers of the spheroids and show that doxorubicin was able to leak out and penetrate deeper in the tissue.

Toxicological assays further show that the tumor cell killing is improved when the tumor spheroids were treated with the DOX liposome-loaded microbubbles and ultrasound compared to the DOX liposomes alone and to the DOX liposomes co-administered with microbubbles and ultrasound.

## Discussion

The results show that sonoprinting can also occur in soft tissue environments and that it is therefore not an artefact caused by the formation of asymmetrical bubble jets directed towards a stiff membrane. The liposomes seem to be stuck in the outer layers of the tumor tissue which can provide a depot system in close proximity of the tumor tissue from which the drug can leak out. This could be a promising delivery strategy for chemotherapeutics such as doxorubicin, that have the correct biophysical characteristics to reach the target site when leaking out of the liposomes [10]. However for gene therapy purposes, this could be a pitfall, since the gene products will get degraded before being able to enter target cells. Moreover, it will be interesting to see if this system also applies to models where there is an intact endothelial cell layer.

## Conclusion

Microbubble and ultrasound guided-delivery of doxorubicin-containing liposomes can provide a local delivery of the liposome material on a 3D tumor culture surface, followed by a drug release into the deeper layers of the tissue. This study shows that sonoprinting can also occur in a soft tissue environment and that it can be an interesting method to form a local drug reservoir in close proximity to target sites.

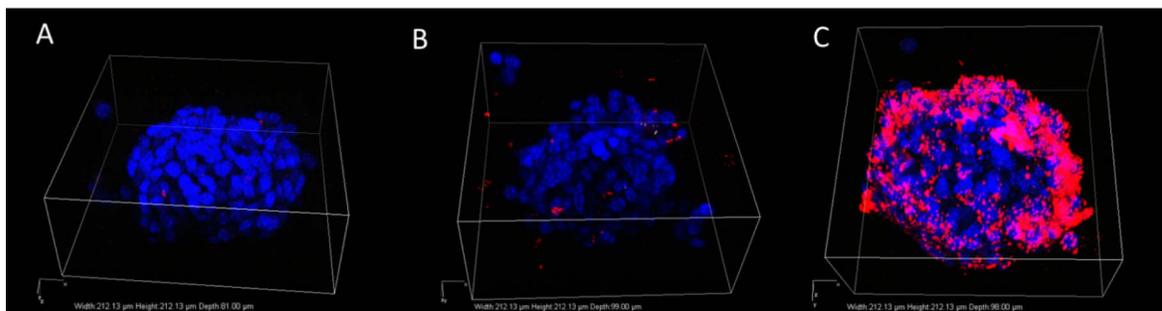


Figure 1: 3D Z-stacks taken on confocal microscopy show the difference between liposomal delivery using (A) DiD-labeled liposomes alone, (B) DiD-labeled liposomes co-administered with microbubbles and treated with ultrasound and (C) DiD-labeled liposomes coupled to the microbubble surface and treated with ultrasound.

## References

1. Hernot S. and Klivanov A.L., *Microbubbles in ultrasound-triggered drug and gene delivery*. *ADDR*, 2008.
2. De Cock I. et al, *Sonoprinting and the importance of microbubble loading for the ultrasound mediated cellular delivery of nanoparticles*, *Biomaterials*, 2016.
3. Meijering B.D. et al, *Ultrasound and microbubble-targeted delivery of macromolecules is regulated by induction of endocytosis and pore formation*. *Circ. Res.* 104 (5), 2009.
4. De Cock I. et al, *Ultrasound and microbubble mediated drug delivery: Acoustic pressure as a determinant for uptake via membrane pores or endocytosis*, *JCR* 197, 2015.
5. Doinikov A.A. et al, *Acoustic scattering from a contrast agent microbubble near an elastic wall of finite thickness*, *Phys Med Biol*, 2011.
6. Zhang A.M. et al, *The dynamic behavior of a gas bubble near a wall*, *Ocean Eng.* 36, 2009.
7. Vrij E. et al, *Directed assembly and development of material-free tissues with complex Architectures*, *Advanced Materials*, 2016.
8. Leong D.T. et al, *Probing the relevance of 3D cancer models in nanomedicine research*, *ADDR*, 2014.
9. Alemany-Ribes M. et al, *Bioengineering 3D environments for cancer models*, *ADDR*, 2014.
10. Barenholz Y. et al, *Doxil®--the first FDA-approved nano-drug: lessons learned*. *JCR*, 2012

# On the safety of brain drug delivery using Rapid-Short Pulse (RaSP) sequences

*Sophie V Morse, Tiffany G Chan, Matthew J Copping, Antonios N Pouliopoulos, Nicholas J Long, James J Choi*

*Noninvasive Surgery and Biopsy Laboratory, Department of Bioengineering, Imperial College London, London, SW7 2AZ, United Kingdom*

## Introduction

One third of the worldwide disease burden is caused by brain diseases, such as Alzheimer's, Parkinson's and glioblastoma (DiLuca & Olesen 2014). Patients suffering from these diseases have no effective treatment available to them because drugs are unable to cross the blood-brain barrier (BBB) (Pardridge 2005). Focused ultrasound and microbubbles have been shown to non-invasively and locally enhance the permeability of the BBB, allowing drugs into the brain (Hynynen et al. 2001). This technique has been used to deliver an array of drugs, ranging from small peptides to nanoparticles, and has progressed to multiple human clinical trials. However, despite over a decade of optimisation, concerns with the efficacy and safety of this technique remain; current techniques still produce an unpredictable and patchy distribution of drugs and lead to the release of red blood cells and substances such as albumin, which have been associated with an inflammatory response (Baseri et al. 2010; Choi et al. 2007; Kovacs et al. 2016; Shlosberg et al. 2010). We hypothesised that these adverse effects may be due to the excessive mechanical stress exerted on the vascular walls when using conventional long-pulse ultrasound sequences (pulse length: 1-20 ms, pulse repetition frequency: 0.5-10 Hz). Such sequences produce a chaotic mixture of cavitation activity (Choi & Coussios 2012) which may be responsible for both the desired and undesired bioeffects produced within the focal region. Our group has shown that Rapid Short-Pulse (RaSP) sequences can reduce the cavitation diversity and improve the cavitation distribution (Pouliopoulos et al. 2016). Here, we evaluated whether such improvements with RaSP sequences translate to improvements in the safety and efficacy of drug delivery to the brain, potentially overcoming the current limitations of conventional long-pulse sequences.

## Methods

A RaSP sequence is composed of short, microsecond pulses emitted at rapid, kilohertz rates. Using a 1 MHz focused transducer, we applied ultrasound to the left hippocampus of mice using either a RaSP sequence (n = 5; derated peak-negative pressure: 350 kPa; pulse length (PL): 5 cycles; pulse repetition frequency (PRF): 1.25 kHz; burst length: 10 ms; burst repetition frequency: 0.5 Hz) or a long-pulse sequence (n = 5; derated peak-negative pressure: 350 kPa; PL: 10,000 cycles or 10 ms; PRF: 0.5 Hz). SonoVue® microbubbles and fluorescently-tagged Texas Red 3 kDa dextran were then administered systemically. Acoustic emissions from the microbubbles were captured with a 7.5 MHz passive cavitation detector. The safety and efficacy of ultrasound exposure was evaluated from cryostat sectioned and immunohistochemically stained brain slices. Albumin (66.5 kDa) extravasation was assessed using a primary rabbit anti-mouse serum albumin antibody and a secondary donkey anti-rabbit antibody tagged with Alexa Fluor 488. The extent of albumin extravasation was quantified by calculating the fold increase in the intensity of the targeted region compared to the control. Confocal microscopy was used to observe the difference in drug accumulation within the targeted regions.

## Results

Despite a RaSP sequence emitting 150 times less acoustic energy, a similar drug dose and a better drug distribution was delivered with RaSP compared to long-pulse sequences (Figure 1). This resulted in an efficient loading of the brain parenchyma with the drug and a high level of neuronal uptake. This pattern contrasted with observations from long-pulse sequence exposures where high concentrations of dextran were observed near blood vessels and in some glial cells and neurons.

RaSP sequences also reduced the amount of endogenous albumin that was released into the brain (Figure 2). Both albumin and dextran were found to extravasate in similar regions, but there were also regions where albumin and dextran were not co-localised, indicating that the mechanism of albumin and dextran extravasation may be different.

## Conclusions

These results suggest that RaSP sequences improve the efficacy and safety of ultrasound-mediated drug delivery to the brain. RaSP sequences lead to a more homogeneous drug distribution in the parenchyma, higher drug delivery into neurons and reduce the amount of albumin – a potentially neurotoxic species at high concentrations – entering the brain. RaSP sequences provide a new scheme for ultrasound emission and control of microbubbles that can improve performance in blood-brain barrier opening and other therapeutic applications.

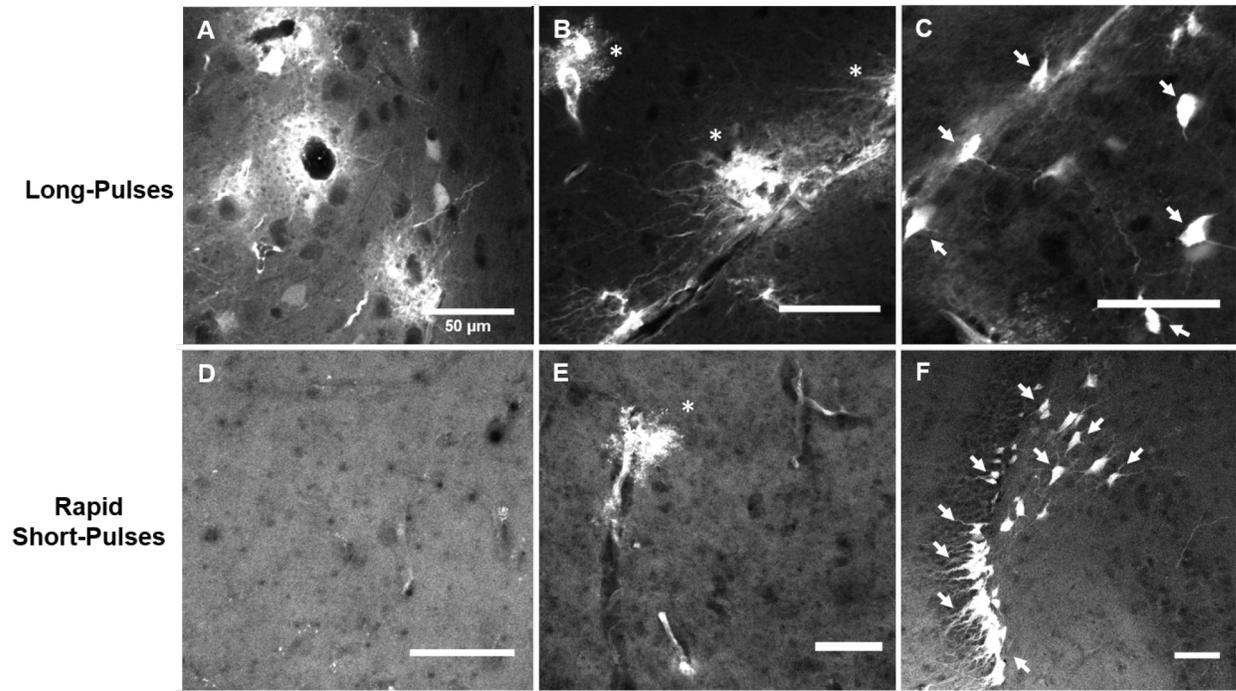


**Figure 1. Dextran distribution differences between long-pulse and RaSP sequences.** Long-pulses display high dextran accumulation around the blood vessels which contributes to a heterogeneous drug delivery (A), glial cell uptake (asterisks, B) and neuronal uptake (white arrows, C). RaSP sequences show a more homogeneous distribution (D), less glial cell uptake (E) and more neuronal uptake (F). The white bar indicates 50 μm.

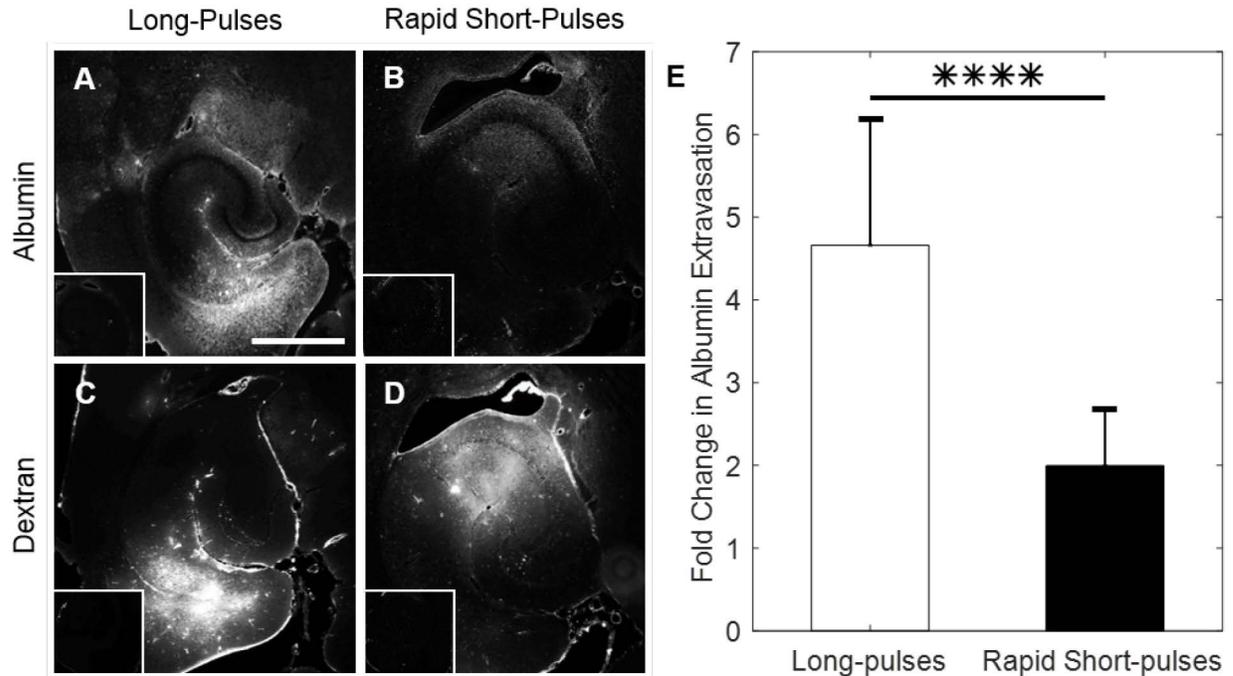


**Figure 2. Albumin and dextran extravasation with long-pulse and RaSP sequences.** Fluorescence images showing the extravasation of albumin (A-B) and dextran (C-D) using long-pulses (A-C) and RaSP sequences (B-D) with the respective controls (small boxes). The fold increase in albumin extravasation (E) compared to the control describes the quantitative difference between the two sequence types at 350 kPa ( $n = 5$ ). A significant increase in albumin extravasation was observed with long-pulses ( $P < 0.0001$ ). The white scale bar in (A) indicates 500  $\mu\text{m}$ .

## References

1. Baseri, B. et al., 2010. Multi-modality safety assessment of blood-brain barrier opening using focused ultrasound and definity microbubbles: A short-term study. *Ultrasound in Medicine and Biology*, 36(9), pp.1445–1459.
2. Choi, J.J. et al., 2007. Noninvasive, transcranial and localized opening of the blood-brain barrier using focused ultrasound in mice. *Ultrasound in Medicine and Biology*, 33(1), pp.95–104.
3. Choi, J.J. & Coussios, C.-C., 2012. Spatiotemporal evolution of cavitation dynamics exhibited by flowing microbubbles during ultrasound exposure. *The Journal of the Acoustical Society of America*, 132(5), pp.3538–49.
4. DiLuca, M. & Olesen, J., 2014. The cost of brain diseases: A burden or a challenge? *Neuron*, 82(6), pp.1205–1208.
5. Hynynen, K. et al., 2001. Noninvasive MR imaging-guided focal opening of the blood-brain barrier in rabbits. *Radiology*, 220(3), pp.640–646.
6. Kovacs, Z.I. et al., 2016. Disrupting the blood–brain barrier by focused ultrasound induces sterile inflammation. *Proceedings of the National Academy of Sciences*, p.201614777.
7. Morse, S. V. et al., 2017. Rapid short-pulse (RaSP) sequences improve the distribution of drug delivery to the brain in vivo. In *Ultrasonics Symposium (IUS), 2017 IEEE International*.
8. Pardridge, W.M., 2005. The blood-brain barrier: bottleneck in brain drug development. *NeuroRx : the journal of the American Society for Experimental NeuroTherapeutics*, 2(1), pp.3–14.
9. Pouliopoulos, A.N. et al., 2016. Rapid short-pulse sequences enhance the spatiotemporal uniformity of acoustically-driven microbubble activity during flow conditions. *The Journal of the Acoustical Society of America*, 140(4), pp.2469–2480.
10. Shlosberg, D. et al., 2010. Blood–brain barrier breakdown as a therapeutic target in traumatic brain injury. *Nature Reviews Neurology*, 6(7), pp.393–403.

# Early assessment of tumor response to radiation therapy using super-harmonic contrast enhanced microvascular ultrasound imaging

*Sandeep K. Kasoji<sup>1</sup>, Judith N. Rivera<sup>1</sup>, Ryan C. Gessner<sup>2</sup>, X. Sha Chang<sup>1,3</sup>, Paul A. Dayton<sup>1</sup>*

<sup>1</sup>*University of North Carolina Chapel Hill / North Carolina State University, Joint Department of Biomedical Engineering*

<sup>2</sup>*Sonovol*

<sup>3</sup>*UNC Chapel Hill School of Medicine, Department of Radiation Oncology*

Radiation therapy (RT) is one of the most common forms of cancer treatment and is currently used to treat approximately 50% of all cancer patients during their first course of treatment. The current clinical standard for assessing tumor response to RT is longitudinal tumor diameter changes, more formally known as the Response Evaluation Criteria in Solid Tumors (RECIST). However, such changes are often inconclusive until weeks to months after the treatment course is complete. The ability to assess response to therapy sooner will enhance the decision making process for continuing or modifying a treatment approach, and afford the patient more time if the original treatment proves to be ineffective. Recent findings have demonstrated that microvascular changes occur as soon as 2-3 days after RT. We hypothesize that microvascular changes are a potential biomarker and quantification of these changes may predict treatment response to RT. Acoustic angiography (AA) is a super-harmonic, contrast enhanced ultrasound imaging technique that can be used for high-resolution 3D visualization of tissue microvasculature. This study demonstrates the use of AA to quantify vascular changes caused by RT that correlate with treatment response and its potential as a method for early assessment.

Rat fibrosarcoma tissue was implanted in Fisher 344 rats (N=30). Control tumors (n=9) were allowed to grow without treatment until they reached the maximum allowable size of 2 cm. Treated tumors were irradiated with a single dose (15, 20, or 25 Gy) of broad beam radiation using a Primus II clinical linear accelerator. All tumors were imaged with standard 3D b-mode imaging and AA at baseline (before treatment), and every three days post-treatment until the tumors either disappeared or grew to >2 cm. Tumor volume (TV) was measured using b-mode images and volumetric vascular density (VVD) was measured by processing AA images at each time point.

Tumors were categorized as either local failure (tumors that initially responded and later regrew) or local control (tumors that responded and disappeared) based on the final tumor volumes. Uninterrupted growth in both TV and VVD was observed in untreated tumors. Both TV and VVD decreased in local control tumors until the tumor mass completely disappeared. Both TV and VVD also decreased in local failure tumors during the initial response phase, and then increased until the tumors reached the maximum allowable size. In local failures, the regrowth of vessels was observed  $10.25 \pm 1.5$  days,  $6 \pm 0$  days, and  $4 \pm 1.4$  days earlier than any measurable regrowth in tumor volume in the 15, 20, and 25 Gy dose groups, respectively. Overall, local failures exhibited increases in vascular density that significantly preceded increases in tumor volume.

These results support our hypothesis that AA may be a potential technique to quantify early vascular changes initiated by RT and assess response to treatment.

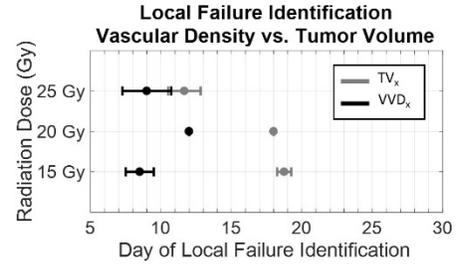
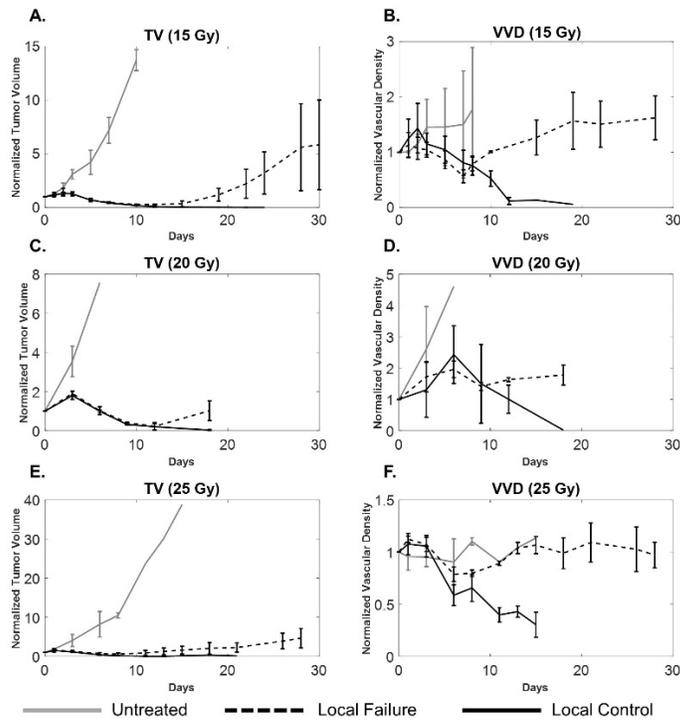


Figure 1 (Left). A comparison of TV and VVD for each dose group. In each group, VVD increases significantly earlier than TV in local failure tumors. Figure 2 (Top). Using VVD, local failures can be identified significantly earlier than using TV.



# Accelerated clearance of ultrasound contrast agents containing polyethylene glycol (PEG) is associated with a PEG-specific immune response

*Samantha M. Fix<sup>a</sup>, A. Gloria Nyankima<sup>b</sup>, Morgan D. McSweeney<sup>a</sup>, James K. Tsuruta<sup>b</sup>, Samuel K. Lai<sup>a,b,c</sup>, Paul A. Dayton<sup>a,b,\*</sup>*

*<sup>a</sup>Eshelman School of Pharmacy, Division of Pharmacoengineering and Molecular Pharmaceutics, University of North Carolina at Chapel Hill, Chapel Hill, North Carolina, USA*

*<sup>b</sup>Joint Department of Biomedical Engineering, University of North Carolina at Chapel Hill and North Carolina State University, Chapel Hill, North Carolina, USA*

*<sup>c</sup>Department of Microbiology and Immunology, University of North Carolina at Chapel Hill, Chapel Hill, NC, USA*

*\*Corresponding author: padayton@email.unc.edu*

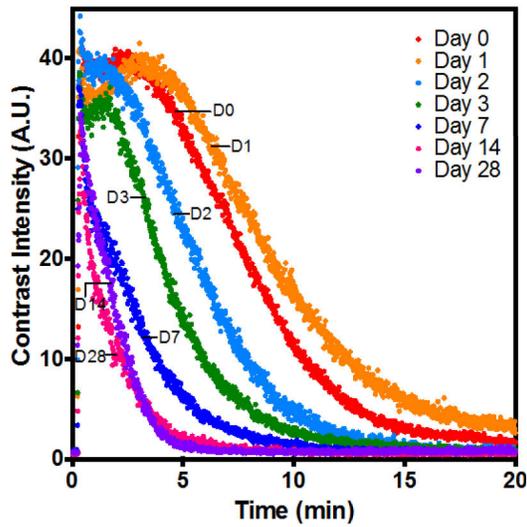
Microbubbles (MBs) are routinely used as contrast agents for ultrasound imaging and are often formulated with polyethylene glycol (PEG) to provide immunological shielding, enhanced stability, and ultimately prolonged intravenous circulation. Paradoxically, the immune system is able to generate specific antibodies that bind to PEG, leading to dramatically accelerated blood clearance (ABC) of PEGylated particles. Here we describe production of anti-PEG antibodies and associated changes in microbubble pharmacokinetics in rats subjected to multiple contrast-enhanced ultrasound imaging sessions over several weeks. Experiments were conducted with PEGylated microbubbles formulated in-house (house-MBs) and commercially available Definity (PEGylated) and Optison (non-PEGylated) contrast agents.

For animals that received multiple doses of house-MBs, we observed ABC starting 2-days after the initial MB dose, which persisted throughout the remainder of the 28-day study (Fig 1A). House-MB clearance was found to be most rapid on Day 14 with a 4.2× reduction in MB half-life. ELISA analysis of the animals' serum indicated a robust anti-PEG IgM and anti-PEG IgG response that peaked 7 and 14 days after the initial MB dose, respectively. Dosing animals with free PEG as a competition agent prior to MB administration resulted in significant prolongation of microbubble intravascular dwell time (Fig 1B), suggesting that the ABC effect for house-MBs is largely driven by anti-PEG antibodies.

Similarly, we observed ABC of Definity when administered multiple times over a 30-day period (Fig 2A), which was associated with anti-PEG antibody production. As expected, repeated administration of non-PEGylated Optison resulted in no anti-PEG antibody production, however, we observed a slight change in Optison pharmacokinetics, which may have been due to the immunogenicity of the human albumin shell in rats (Fig 2B).

We conclude that repeat dosing of PEGylated MBs resulted in dramatically accelerated microbubble clearance, which was related to a PEG-specific immune response. We believe that these data have important implications for contrast-enhanced ultrasound-imaging techniques that (1) involve repeated administration of PEGylated MBs over multiple days or weeks and (2) assume that the circulating concentration and clearance profile of MBs remains consistent throughout the study.

**A. House-MB time intensity curves**



**B. Free PEG competition mitigates ABC effect**

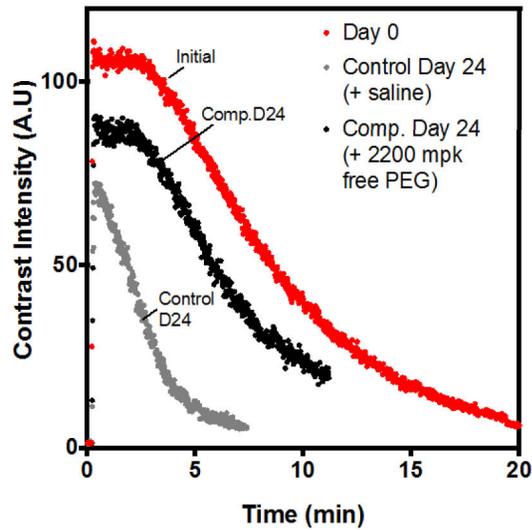
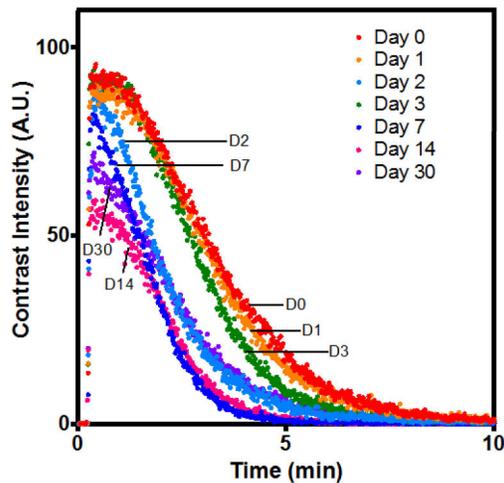


**Figure 1.** (A) Time intensity curves showing accelerated clearance of bolus dose house-MBs when administered multiple times over a 28-day period. A leftward shift in the time-intensity curves (indicating accelerated clearance) is observed starting two days after the initial dose, which becomes more dramatic as the study progressed. (B) In a separate study, we demonstrate that competition with free PEG (after the ABC effect had been mounted) prolongs the circulation of house-MBs to nearly match that of the initial dose.

**A. Definity time intensity curves**



**B. Optison time intensity curves**

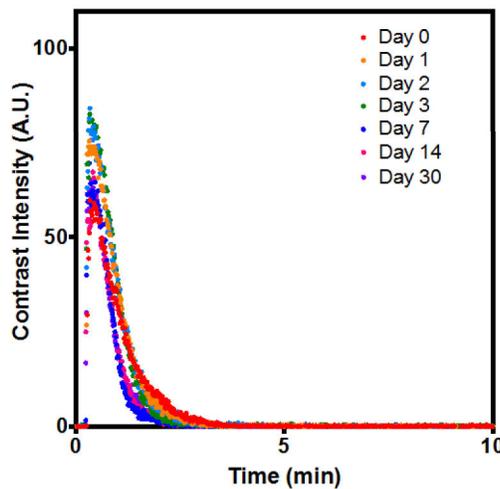


**Figure 2.** (A) Time intensity curves showing accelerated clearance of PEGylated Definity microbubbles when dosed repeatedly over a 30-day period. (B) Optison, which is non-PEGylated, shows rapid clearance at baseline. Optison clearance becomes slightly more accelerated towards the end of the 30-day study; however, this effect was modest in comparison to that seen for either of the PEGylated agents (house-MBs or Definity).

# Monitoring and Control of Liposomal Doxorubicin in Tumors using Ultrasound Contrast Agents

*Rojin Eslami<sup>1</sup>, Aditi Bellary<sup>1</sup>, Arelly Villarreal Jasso<sup>1</sup>, Reyhan Avir Sinha<sup>1</sup>, Sonia L. Hernandez<sup>2</sup>, Bianca Lec<sup>2</sup>, Jessica J Kandel<sup>2</sup>, Rajiv Chopra<sup>3</sup>, Sumbul Shaikh<sup>3</sup>, Mark A Borden<sup>3</sup>, Shashank R. Sirsi<sup>1,3</sup>*

<sup>1</sup>University of Texas at Dallas, Richardson, TX, USA, 75080

<sup>2</sup>University of Chicago Medical Center, Chicago, IL, USA, 60637

<sup>3</sup>University of Texas Southwestern, Dallas, TX, USA, 75390

<sup>4</sup>University of Colorado at Boulder, Boulder, CO, USA, 80309

## Introduction

Doxorubicin is one of the most commonly used chemotherapeutics in pediatric cancers, however off-target effects of doxorubicin can have deleterious consequences, such as cardiomyopathy. The therapeutic index of doxorubicin can be increased by encapsulation in stealth liposome vesicles, sold commercially as Doxil™. While this strategy reduces overall systemic toxicity, accumulation of doxorubicin is heavily reliant on the enhanced permeability and retention (EPR) effect of tumors to take up large molecules. Methods of actively targeting liposome-encapsulated doxorubicin (L-DOX) to tumor tissue would significantly enhance versatility of this drug delivery platform.

Over the last decade, microbubble contrast agents have frequently been cited as promising vehicles for targeted drug delivery applications. Microbubbles are gas filled spheres between 1-10 μm in diameter that circulate in the blood stream when injected systemically. When insonified under specific ultrasound conditions, microbubbles can alter vascular permeability by a technique called “sonoporation”. This is an effective method of promoting delivery of circulating agents beyond the vasculature. By spatially controlling the application of ultrasound energy, drug uptake can be targeted to specific regions, making this technique well suited for tumor-targeted drug delivery. In this study, we develop a novel technique to simultaneously monitor tumor perfusion and apply sonoporation to enhance intratumoral L-DOX uptake. We expect that this technique will be useful for predicting drug delivery efficacy in tumors using quantitative perfusion imaging techniques.

## Materials and Methods

Matrigel plugs (BD Biosciences, Franklin Lakes, NJ) were used as mock tumors that promote neovascular growth when injected subcutaneously in mice. The matrigel was mixed with 1 μg basic fibroblast growth factor (Sigma Aldrich, St. Lois, MO) and heparin (Sigma Aldrich) then injected subcutaneously into 6-8 week old CD-1 mice (Charles River, Wilmington, MA). The vasculature was allowed to grow for 0-28 days in the matrigel plug then imaged using lipid microbubble contrast agents to monitor vascular perfusion. Lipid microbubbles were formed using commercially available lipids 1,2-distearoyl-*sn*-glycero-3-phosphocholine (DSPC) and 1,2-distearoyl-*sn*-glycero-3-phosphoethanolamine-N-[methoxy(polyethylene glycol)-2000] (DSPE-PEG2K) (Avanti Polar Lipids, Alabaster, AL) mixed at a 9:1 DSPC:DSPE-PEG2K ratio in a lipid

suspension at 2 mg/mL in PBS and emulsified with hydrophobic Perfluorobutane (PFB; Round Rock; TX) gas. Microbubbles were injected systemically via tail vein injections ( $5 \times 10^7$  MB in 100  $\mu$ l, 50  $\mu$ l/min) and perfusion was monitored using an Acuson Sequoia 512 ultrasound imaging scanner (Siemens Healthcare, Malvern, PA) with a 15L8 probe and custom Labview Software to analyze US video data (National Instruments, Austin, TX). A custom built motorized stage was built to acquire 3D ultrasound images. After perfusion imaging, matrigel plugs were sonoporated using a therapeutic ultrasound machine (SoundCare Plus, Austin, TX) at 3 W/cm<sup>2</sup> (1 Mhz, 10% duty cycle) for 10 minutes with a high dose of microbubbles ( $1 \times 10^9$  MB's) mixed with 25 mg/kg L-DOX (Doxoves©, FormuMax, Sunnvale, CA). Matrigel plugs (along with liver, contralateral kidney, and heart) were excised to evaluate drug uptake using an acidified isopropanol extraction to recover doxorubicin. The doxorubicin was quantified using a fluorescence plate reader (Synergy H1, BioTek, Winooski, VT).

## **Results and Discussion**

Matrigel sonoporation demonstrated significantly higher levels of doxorubicin uptake compared to non-sonoporated controls (~5 fold increase, \* P<0.05). 3D contrast-enhanced ultrasound (CEUS) imaging of the tumors was performed using custom software to evaluate tumor volume and vascular perfusion prior to Doxil delivery. A strong correlation between tumor perfusion levels and doxorubicin uptake was observed (both with and without sonoporation), indicating that tumor perfusion volumes can be a strong indicator of drug uptake of L-DOX.

## **Conclusions**

Currently we are able to demonstrate significantly improved L-DOX uptake in mock tumors using ultrasound-mediated sonoporation. Additionally, our preliminary data in NGP neuroblastoma models shows higher uptake and intratumoral drug penetration of doxorubicin in sonoporated tumors. In this study we show that quantitative 3D perfusion imaging is an excellent predictor of drug uptake levels in tumors, which would have significant clinical impact for designing tailored drug treatment regimens for patients.

# Exploiting Microbubble Flow Dynamics to Improve Super-resolution Ultrasound imaging

*Oren Solomon<sup>1</sup>, Ruud J.G. van Sloun<sup>2</sup>, Hessel Wijkstra<sup>2,3</sup>, Massimo Mischi<sup>2</sup> and Yonina C. Eldar<sup>1</sup>*

<sup>1</sup>*Department of Electrical Engineering, Technion - Israel Institute of Technology, Haifa, Israel.*

<sup>2</sup>*Department of Electrical Engineering, Eindhoven University of Technology, Eindhoven, The Netherlands.*

<sup>3</sup>*Department of Urology, Academic Medical Center - University of Amsterdam, Amsterdam, The Netherlands.*

## Background

In recent years, super-localization contrast enhanced ultrasound (CEUS) microscopy revealed sub-diffraction capillary vessels in-vivo, by localizing well-separated intravascular ultrasonic contrast agents (UCAs)[1], [2], [3]. Additionally, microbubble tracking techniques [4] have enabled quantification of UCA flow velocities. Although excelling at spatial resolution, standard super-localization methods require tens of thousands of frames to produce a single image. Recently, methods exploiting the inherent sparsity of microbubbles [5], [6] have managed to achieve similar spatial resolution, while reducing the required number of frames dramatically, often achieving sub-second temporal resolution [5], [7]. Here, we propose to improve the reconstruction process of sparsity-based super resolution ultrasound by exploiting the motion kinetics of the UCAs as a prior in the reconstruction process. Concurrently to sparse recovery, we track the detected microbubbles to ascertain quantifiable parameters, such as flow velocity magnitude and direction. We show that the proposed method is directly applicable to a clinically acquired CEUS scan of the prostate, thereby displaying promising results for the reconstruction of vascular architectures and estimation of flow kinetics.

## Methods

CEUS data of a human prostate was acquired at the AMC university hospital (Amsterdam, the Netherlands), using a transrectal ultrasound probe and an iU22 scanner (Philips Healthcare, Bothell, WA) operating in a contrast-specific mode at a frame rate of 10 Hz. A 2.4-ml microbubble bolus of Sonovue® (Bracco, Milan, Italy) was administered intravenously, and 150 frames (15s) were collected for further analysis. Sparse recovery was performed on the first frame, as described in [6], to localize the overlapping microbubbles. Then, a Kalman filter was used to predict the bubbles' state to the next frame, including position and velocity. Optical flow estimation on the low-resolution frames was used to regularize the velocity estimation. Using the estimated state error covariance matrix, a probability map for the possible positions of the bubbles was then calculated and subsequently used as weights for the sparse recovery process of the next frame, via weighted  $l_1$  minimization. Finally, automatic association of new measurements to existing UCA tracks is performed using the multiple hypothesis tracking algorithm [8].

## Results and discussion

Figure 1 shows an exemplary image reconstruction using the proposed method. Panel (a) shows the maximum intensity projection (MIP) image. Panel (b) displays a single frame with estimated UCA velocity maps (optical flow) and localizations marked as green crosses. Panel (c) displays an image which is a smoothed summation of frame-by-frame localizations using the method proposed in [6], where no flow prior was used. Lastly, panel (d) corresponds to the output of the proposed method of simultaneous localization and tracking of individual bubbles, displayed as a smoothed summation of all UCA trajectories. Our proposed method depicts the continuous flow of the UCAs (panel (d) – red box), not only the localizations themselves (panel (c)), resulting in a clearer image of the blood vessels. Moreover, by tracking the flow kinematics of the UCAs using the Kalman filter, we were able to assess the velocities of individual bubbles, as described in Fig. 2. The velocity estimation of the UCAs is on the order of 1 mm/s, in line with previous observations on blood flow in microvessels [9].

## Conclusion

We presented an improvement to frame-by-frame sparsity-based super-resolution CEUS imaging by using the flow kinetics of the UCAs as a prior for the sparse recovery process. By combining sparse recovery with individual tracking of bubbles using a Kalman filter and optical flow estimation, we were able to achieve a clear depiction of sub-diffraction blood vessels in a clinical scenario with many overlapping UCAs. Exploiting the flow kinetics of the bubbles improves upon traditional frame-by-frame sparse recovery in terms of visual quality, displaying smoother blood vessels, as well as ascertaining quantifiable parameters, such as flow velocity magnitude and direction. The preliminary results presented here suggest that this technique can be applied in a clinical setting and by using online tracking algorithms, such as the Kalman filter, might be applicable for real-time.

## References

1. C. Errico, J. Pierre, S. Pezet, Y. Desailly, Z. Lenkei, O. Couture, and M. Tanter, "deep super-resolution vascular imaging," *Nature*, vol. 527, no. 7579, pp. 499–502, 2015.
2. M. A. O. Reilly and K. Hynynen, "A super-resolution ultrasound method for brain vascular mapping A super-resolution ultrasound method for brain vascular mapping," vol. 110701, no. 2013, 2016.
3. A. Bar-Zion, C. Tremblay-Darveau, O. Solomon, D. Adam, and Y. C. Eldar. "Fast vascular ultrasound imaging with enhanced spatial resolution and background rejection". *IEEE transactions on medical imaging*, vol. 36, no. 1, 2017.
4. D. Ackermann and G. Schmitz, "Detection and Tracking of Multiple Microbubbles in Ultrasound B-Mode Images", *IEEE Transactions on Ultrasonics, Ferroelectrics and Frequency Control*, vol. 63. no. 1, 2016.
5. A. Bar-Zion, O. Solomon, C. Tremblay-Darveau, D. Adam, and Y. C. Eldar. "Sparsity-based ultrasound super-resolution imaging". In *Proceedings of the 23rd European symposium on Ultrasound Contrast Imaging*, pages 156–157. ICUS, 2017.
6. R. J. G. van Sloun, O. Solomon, Y. C. Eldar, H. Wijkstra and M. Mischi. "Sparsity-driven super-resolution in clinical contrast-enhanced ultrasound." *Ultrasonics Symposium (IUS), 2017 IEEE International. IEEE*, 2017.
7. A. Bar-Zion, O. Solomon, C. Tremblay-Darveau, D. Adam, and Y. C. Eldar. "Sparsity-based ultrasound super-resolution hemodynamic imaging ". under review.
8. D. Reid, "An algorithm for tracking multiple targets", *IEEE transactions on Automatic Control*, vol. 24, no. 6, 1979.
9. R. J. van Sloun, L. Demi, A. W. Postema, J. J. de la Rosette, H. Wijkstra and M. Mischi. "Ultrasound-contrast-agent dispersion and velocity imaging for prostate cancer localization". *Medical image analysis*, vol. 35, 2017.

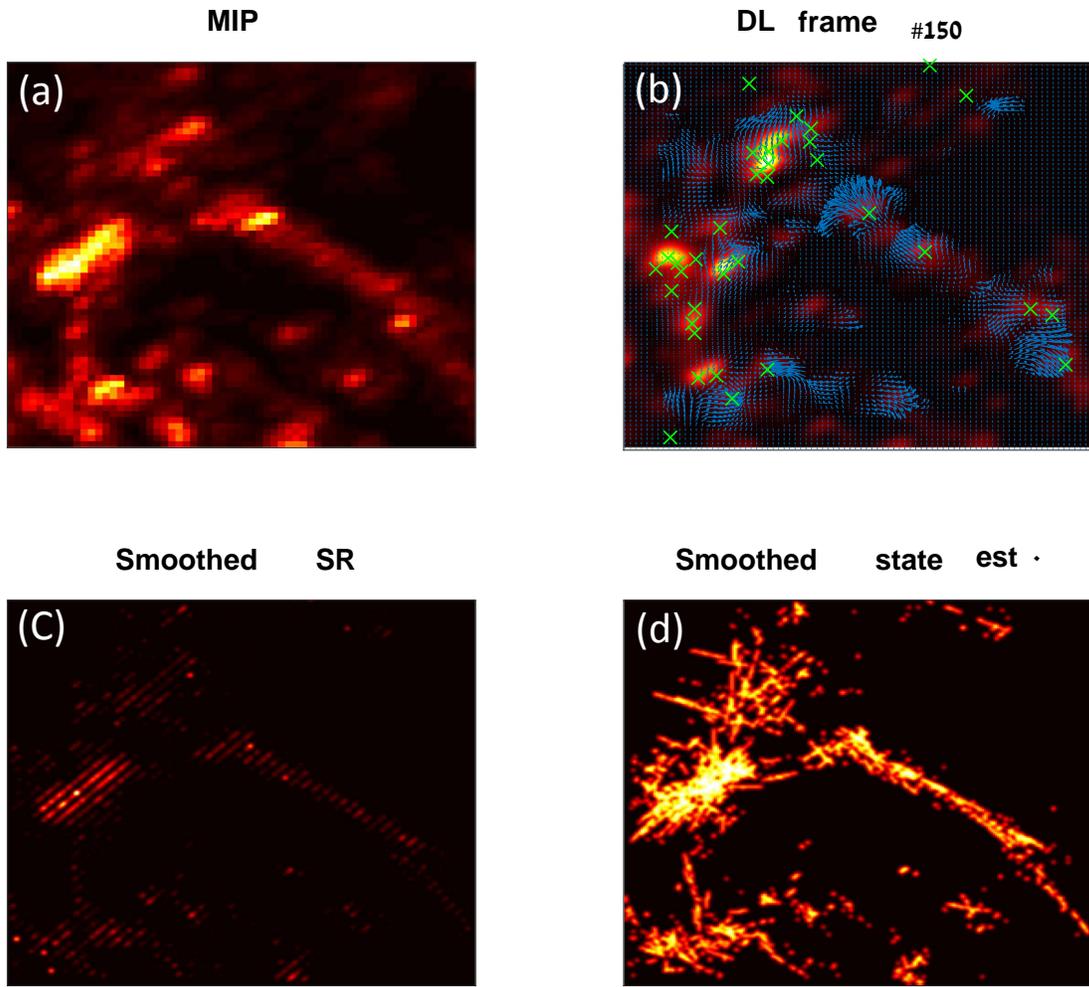


Fig. 1: Human prostate scan. (a) Maximum intensity persistence. (b) A single frame, super imposed with velocity estimation and raw localizations, performed using the method described in [6]. (c) Smoothed accumulation of localized bubbles using the method described in [6]. (d) Proposed method: smoothed super-resolved image with UCA tracks.

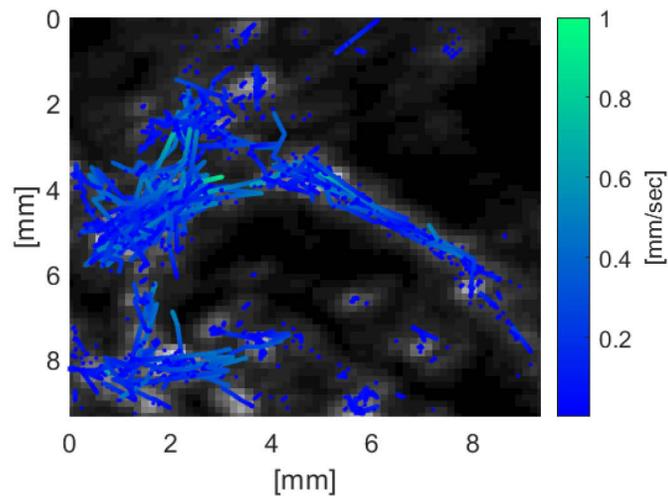


Fig. 2: Velocity map estimation from the super-resolved trajectories, which corresponds to Fig. 1 panel d, overlaid on the diffraction limited MIP image.

# Experimental study on acoustic effects of an elastic wall on translational dynamics of an oscillating bubble

*T. Okada, N. Sugita and T. Sugiura*

*Department of Mechanical Engineering, Keio University, Japan*

## Background

Bubbles are located in the vicinity of an elastic wall like a living body in medical application such as sonoporation. If the wall is a rigid body, the radiation pressure generated by oscillation of a bubble is reflected without attenuation on the wall surface. Effects of this reflection on the translation of the bubble can be evaluated as an action of the mirror image bubble symmetrical on the wall surface. While, for a rigid wall, the reflection coefficient obtained from the characteristic acoustic impedance of the wall is 1, for an elastic wall, it is less than 1. As the reflection coefficient decreases, the translational speed of a bubble decreases. In this research, we experimentally examine the validity of applying the theory of Bjerknes force extended by using the concept of a reflection coefficient to analysis of the translational motion of a bubble near its surrounding walls.

## Material and Methods

Fig.1(a) and (b) show an experimental setup viewed from side and top, respectively. A rectangular acrylic vessel (inside dimension: 50×50×100 mm, thickness: 5 mm) filled with liquid is fixed on a vibration generator (EMIC, 513-BS/Z08). A vacuum pump (DAP-6D, ULVAC KIKO) is connected to the vessel through a valve in order to reduce the hydrostatic pressure in the vessel to 12 kPa. This allows large pressure amplitude to be developed in the liquid at low driving amplitude and frequency of hundreds of Hz. The recording system consists of a high-speed video camera (Photron, FASTCAM SA-X2), a distortion-less macro lens and a LED backlight. A millimeter sized gas bubble as a cavitation nucleus is injected by a needle through a silicone plug. As the driving acceleration is exerted on the liquid vessel, pressure gradient is generated in the vertical direction inside the vessel. Three kinds of walls made of acrylic, aluminum and gelatin gel, respectively, were used in this study. For each wall, we compared experimental values of the translational position of the bubble with numerical ones. The numerical values were calculated by estimating the Bjerknes force  $F_B$  as the following equation,

$$F_B(X) = \langle V(t) \left( \frac{\rho R^2 \ddot{R}}{4(L-X)^2} - \frac{\rho R^2 \ddot{R}}{4(L+X)^2} \right) \rangle R_{wall} ,$$

where  $V(t)$  is the bubble volume,  $\rho$  is the density of liquid,  $R$  is the bubble radius,  $L$  is half the distance between side walls,  $X$  is the horizontal position of the bubble from the center between both the walls, and  $R_{wall}$  is the reflection coefficient. In this study,  $L$  was 20 mm.

## Results

Fig.2(a), (b) and (c) show the translational positions of the bubble for aluminum, acrylic and gelatin gel wall, respectively, as functions of time. For each wall, the bubble moved toward the wall. As  $R_{wall}$  increased, the translational speed of the bubble increased. For rigid wall (the dashed line), the translational speed is faster than that for any other wall. Further, good agreement between the numerical and the experimental values was confirmed.

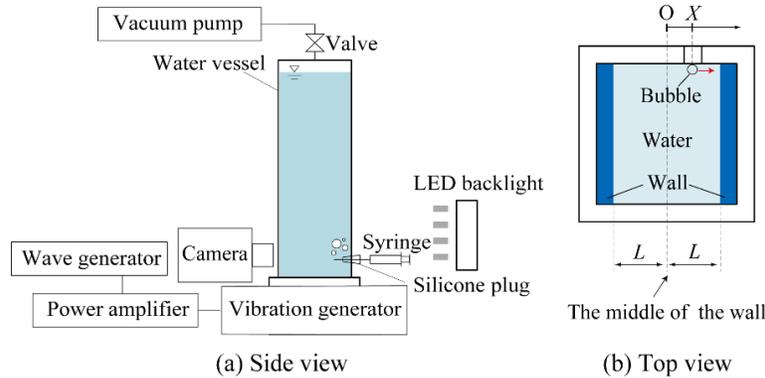


Figure 1. Experimental setup.  $O$  shown in (b) is the center between both side walls.  $X$  shown in (b) is the translational position of the bubble.

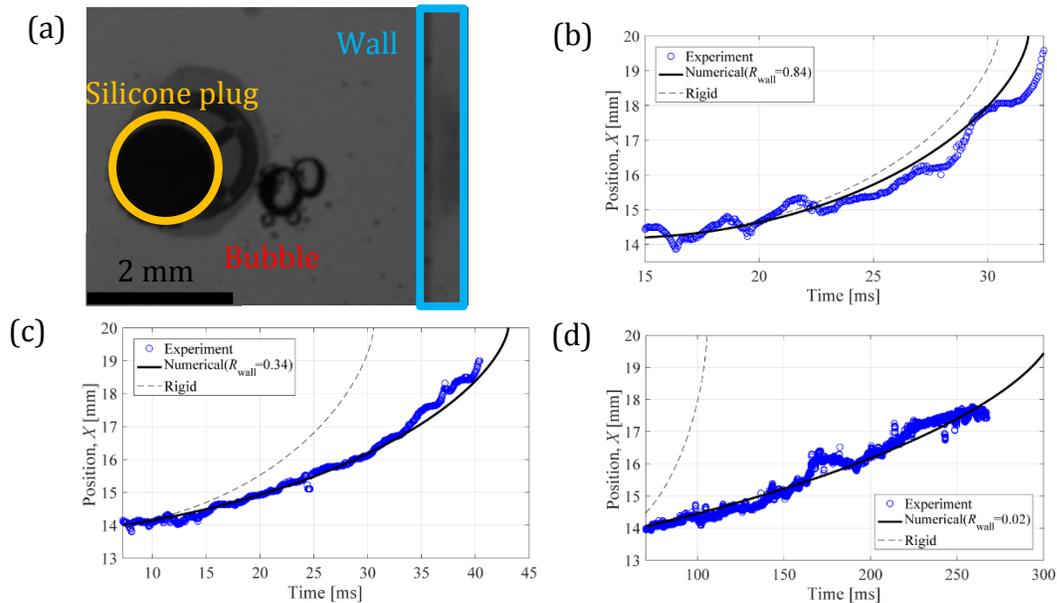


Figure 2. (a) Recorded image of bubble and (b)~(d) translational position of the bubble for (b) aluminum wall ( $R_{wall}=0.84$ ); (c) acrylic wall ( $R_{wall}=0.34$ ); (d) gelatin gel wall ( $R_{wall}=0.02$ ).

# 3D Flow Reconstruction Based on Multiple 2D Contrast Enhanced High-Frame-Rate Ultrasound Measurements

*Xinhuan Zhou<sup>1</sup>, Virginie Papadopoulou<sup>2</sup>, Chee Hau Leow<sup>1</sup>, Peter Vincent<sup>3</sup>, Mengxing Tang<sup>1\*</sup>*

*<sup>1</sup>Department of Bioengineering, Imperial College London, United Kingdom*

*<sup>2</sup>UNC-NCSU Joint Department of Biomedical Engineering, The University of North Carolina at Chapel Hill, USA*

*<sup>3</sup>Department of Aeronautics, Imperial College London, United Kingdom*

*\*Corresponding author: mengxing.tang@imperial.ac.uk*

## Background & Objective

Quantification of 3D full field flow in vessels is valuable as it provides insights into the development of atherosclerosis [1]. Traditional high-fidelity Computational Fluid Dynamics (CFD) is computationally expensive and relies heavily on accurate initial and boundary conditions of the flow. In this study a reconstruction algorithm based on 2D ultrasound imaging velocimetry (UIV) acquisitions is developed for 3D flow visualisation and quantification, taking advantage of the prior knowledge that such physiological flow is divergence free (i.e. non-compressible).

## Experimental Setup

To evaluate the 3D flow, in vitro experiments were performed on a carotid bifurcation phantom shown in Fig. 2a. Decafluorobutane microbubbles with lipid shell were diluted in water to a concentration of  $2 \times 10^5$  microbubbles/mL [2, 3] and used as ultrasound contrast agents. A gravity flow setup was used to create steady laminar flow through the phantom inlet at constant flow rate of 300 ml/min.

Then a high-frame-rate UIV system and microbubble speckle pattern tracking algorithm [2, 3] were used to track ultrasound microbubble contrast agents to generate 2D projected velocity at several imaging planes. A L12-3-v linear probe was connected to a Vantage 128 research platform (Verasonics, Redmond, WA, USA) to acquire high-frame-rate (1000 Hz) ultrasound images. Plane wave pulse inversion imaging with six angles between  $-18^\circ$  and  $18^\circ$  were used and images are coherently compounded. After acquiring many frames (1000 frames) at each position the ultrasound probe was moved by a stepping stage controller at a constant spacing (2 mm in this study, shown in Fig. 1). After scanning the vessel phantom the ultrasound probe was translated back to its original position, rotated  $90^\circ$  and acquisitions repeated, as shown in Fig. 1 [2-4]. Speckle tracking based on cross-correlation [2, 3] was used to track the microbubble contrast agents in consecutive frames to generate 2D velocity maps. This corresponds to the 2D projected velocity at each imaging plane.

After flow tracking of 2D velocity at all scanning planes and spatially registering them, 3D Divergence Free Interpolation (DFI) was used to reconstruct the full field flow, as introduced in the Numerical Methods.

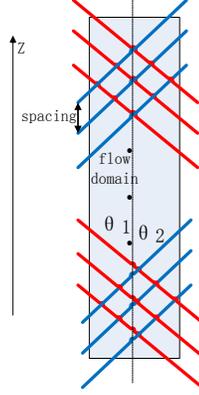


Fig. 1 Acquisition of 2D flow by ultrasound from two angles at multiple locations (top view) where the red and blue lines show the imaging plane intersections for the two transducer orientations respectively, with  $z$  being the direction of flow (and of motor stepping)

## Numerical Methods

We conduct Divergence Free Interpolation (DFI) by Gaussian Radial Basis Function (RBF) and projection inverse algorithm on the 2D projected velocity input, to solve the inverse problem shown in Eq. 1 by Generalized Minimal Residual method (GMRES). The influence of experimental error is maximally suppressed by employing regularisation of discrepancy principle with prior knowledge of relative measurement noise level.

The divergence free interpolation using radial basis function (RBF) is given by:

$$G^* \lambda = v \quad (1)$$

where matrix-valued RBF  $G$  is introduced in Appendix A of [5] and  $\lambda$  is the coefficient vector,  $v$  is 3D velocity. Multiplying the projection matrix  $R$  we can obtain

$$A^* \lambda = b \quad (2)$$

where  $A = RG$  is singular and  $b = Rv$  is the 2D projected velocity from the UIV experiment.  $R$  is the projection matrix. The singular system shown in Eq. 2 is solved by Generalized Minimal Residual method (GMRES) and to maximally suppress the influence of measurement noise, discrepancy principle is used to achieve the regularisation effect. After solving for  $\lambda$  in Eq. 2, the flow velocity at any point within the flow domain can be calculated by constructing another matrix-valued RBF function  $G'$  [5] and 3D velocity  $v$  can be calculated by Eq. 1.

## Results & Discussion

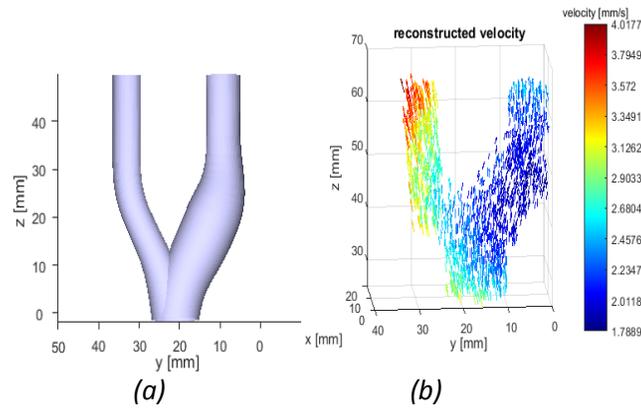


Fig. 2 (a) geometry of the carotid bifurcation flow phantom; (b) full reconstructed 3D flow field

Fig. 2 b shows the reconstructed 3D flow in the bifurcation phantom. The reconstruction can take as short as several seconds with input velocity at thousands of points. The velocity distribution shown in Fig. 2 is smooth because of regularisation, which indicates that Divergence Free Interpolation can filter out large ultrasound measurement errors. By choosing the optimal regularization parameter the noise can be maximally suppressed while small flow features are minimally smoothed.

## Conclusion

We have developed an algorithm and an experimental setup for 3D full field flow reconstruction using divergence free interpolation of multiple 2D ultrasound velocimetry data, and demonstrated its feasibility on a carotid flow phantom. Comparing to CFD it is less dependent on flow domain geometry, and is a promising method for in vivo flow reconstruction [4].

## Acknowledgement

This work is jointly supported by the China Scholarship Council (CSC) and Imperial College under Grant CSC No. 201604100100. The authors acknowledge Professor Alfred Yu from University of Waterloo for providing the bifurcation phantom.

## Reference

1. Glagov, S., et al., *Hemodynamics and atherosclerosis. Insights and perspectives gained from studies of human arteries. Archives of pathology & laboratory medicine*, 1988. 112(10): p. 1018-1031.
2. Leow, C.H., et al., *Flow velocity mapping using contrast enhanced high-frame-rate plane wave ultrasound and image tracking: Methods and initial in vitro and in vivo evaluation. Ultrasound in medicine & biology*, 2015. 41(11): p. 2913-2925.
3. Leow, C.H. and M.-X. Tang, *Spatio-Temporal Flow and Wall Shear Stress Mapping Based on Incoherent Ensemble-Correlation of Ultrafast Contrast Enhanced Ultrasound Images. Ultrasound in Medicine & Biology*, 2017.
4. Papadopoulou, V., et al. *3D flow velocity reconstruction in a human radial artery from measured 2D high-frame-rate plane wave contrast enhanced ultrasound in two scanning directions—A feasibility study. in Ultrasonics Symposium (IUS), 2017 IEEE International. 2017. IEEE.*
5. Zhou, X., et al., *3D Flow Reconstruction Using Divergence Free Interpolation of Multiple 2D Contrast Enhanced Ultrasound Imaging Velocimetry Measurements, in MPEC2017: London.*

# Semi-Automatic Segmentation of the LV Cavity in Contrast Enhanced Echocardiographic Clips

*Nadir Cohen<sup>1</sup>, Michael Becker<sup>2</sup>, Steven Feinstein<sup>3</sup> and Dan Adam<sup>1</sup>*

<sup>1</sup> *Department of Biomedical Engineering, Technion - Israel Institute of Technology, Haifa, Israel.*

<sup>2</sup> *Department of Cardiology, RWTH University, Aachen, Germany.*

<sup>3</sup> *Department of Cardiology Rush University Medical Center, Chicago, USA.*

Myocardial contrast enhanced ultrasound (CEUS) is gaining popularity as an imaging method for assessment of left ventricle (LV) volume and function and for myocardial perfusion estimation. Those parameters may help detect and diagnose cardiac diseases, specifically in ‘difficult patients’. The contrast agent is injected intravenously, flows through the cardiovascular system, and slowly fills up the LV cavity, improving the visualization of the endocardium. This enables better assessment of LV volume, ejection fraction and other myocardial parameters. Segmentation of the LV myocardium using CEUS is a primary yet important stage in variety of these LV analyses.

Though the contrast agent is used in order to enhance visualization of the endocardial boundary, it should be noted that the flow of the microbubbles within the cavity is a non-stationary process, with the gray-scale pattern within the cavity continuously changing. Thus, there exists a paramount need for accurate automatic (or semi-automatic) segmentation, under these ever-changing conditions, as it may help physicians estimate more objectively the function of the heart while performing an ultrasound exam.

Thus, a segmentation algorithm of the LV endocardial boundary is here presented, while using long-axis 2-chamber view CEUS clips. The algorithm is initialized by concentrating on the diastolic frames of the clip. Then the user defines a ROI by marking three points on the first frame of the clip - the center of the LV cavity and the two basal points. Location of the basal points in the following frames is found automatically by cross-correlation. Then, attenuation correction is performed on the images, to enhance the contrast and correct intensity attenuation along the LV cavity. An initial estimation of the endocardial boundary is found using an algorithm based on Canny edge detection and minimization of an energy function. The final and major part of the algorithm is the correction of the initial boundary, a process that consists of three stages: (1) Apical boundary estimation: The estimation is based on several constrains, such as local intensity maximum, intensity level and proximity to previous points of the boundary. (2) Basal area correction: Estimation of the basal points’ movement relative to previous frame, and correction of the boundary at the basal area. (3) Papillary muscle correction: the area of the papillary muscles often has a poor image quality, which requires an additional correction done by a curve fitting of the boundary.

In order to validate our results, we have compared the endocardial boundaries detected automatically to manually segmented boundaries, in 276 frames of 9 clips taken from 9 different patients. The measured mean absolute distance (MAD) between the two boundaries was 6.27 (SD=1.51) pixels, out of a total boundary length of 838 (SD=116) pixels, which represents an error of 0.75% (SD=0.15%). In addition, we have compared the areas defined between the two

boundaries. The mean area of difference (between the two boundaries), divided by the entire cavity area of the boundary drawn manually was 10.48% (SD=2.26%), and the mean Jaccard index was 0.9 (SD=0.02). These results prove high similarity between manual and automatic curves and areas.

Our algorithm provides a semi-automatic and accurate segmentation, which enables an objective and efficient segmentation of the LV cavity. This segmentation algorithm could enable myocardial perfusion measurements, which could lead to improved coronary artery disease diagnosis.

# Shell Mechanics of Lung Surfactant Microbubbles

*Alec Thomas, Jordan Lum, Todd Murray and Mark Borden*

*University of Colorado at Boulder, Mechanical Engineering Department*

Lung surfactant (LS) is a lipid and protein mixture that coats and stabilizes the air/liquid interface of the alveolar surface. The LS monolayer has coexisting solid and fluid domains and surfactant proteins that anchor stacks of bilayer folds extending into the aqueous phase. Sirsi et al. showed that this bulky structure of LS shells increases the loading of lipophilic compounds onto the microbubble surface.<sup>1</sup> Additionally, Garg et al. showed that LS-coated microbubbles are relatively rigid and experience prolonged circulation in vivo.<sup>2</sup> The goal of this work was to characterize the mechanical properties of the LS shell on microbubbles, in order to inform the rational design of LS microbubbles for applications in ultrasound imaging and drug delivery.

In the first experiment, individual microbubbles were observed under the microscope as they were pressurized in a chamber, and their deformation was compared to a physical model accounting for both shell mechanics and gas diffusion. Results showed that LS microbubbles had a strain-rate dependent elasticity. At slower pressurization rates, the elasticity of microbubble shells comprising LS or pure dipalmitoyl-phosphatidylcholine (DPPC), the main component of LS, were equivalent (Fig. 1). At faster pressurization rates, however, LS shells were stiffer.

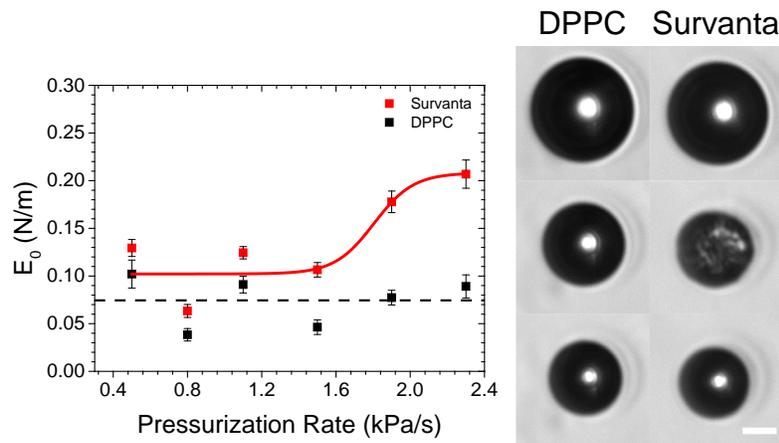


*Figure 1. Pressurization of microbubbles coated with LS (Survanta) vs pure DPPC. LS microbubbles were found to be stiffer, as observed in the elasticity plots to the left and the microscopy images to the right.<sup>3</sup>*

In the second experiment, individual microbubbles coated with LS vs pure DPPC were probed with a laser-ultrasonics technique.<sup>4</sup> Individual microbubbles were followed by light scattering as they were driven by pressure waves at frequencies ranging 1 to 4 MHz emanating from a nearby photoacoustic source. As expected, LS shells were observed to soften with increasing temperature (Fig. 2). Additionally, LS shells were significantly more rigid than pure DPPC shells over this temperature range.

In conclusion, the LS composition appears to increase the rigidity of the microbubble shell over a large range of strains and strain rates. This explains prior observations of prolonged in vivo circulation<sup>2</sup>, and offers tantalizing clues into the role of microstructure in stabilizing microbubbles used for ultrasound imaging and drug delivery.

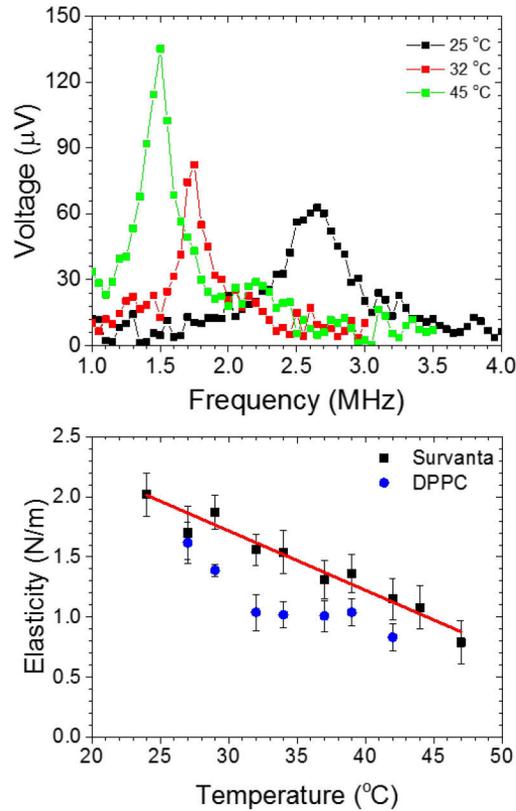


Figure 2. Photoacoustic measurements of microbubble shell mechanics. (Top) Example resonance curves for LS microbubbles at three different temperatures. (Bottom) Shell elasticity as a function of temperature for LS and DPPC microbubbles.

## References

1. Sirsi, S. R.; Fung, C.; Garg, S.; Tianning, M. Y.; Mouniford, P. A.; Borden, M. A. Lung Surfactant Microbubbles Increase Lipophilic Drug Payload for Ultrasound-Targeted Delivery. *Theranostics* 2013, 3 (6), 409–419.
2. Garg, S.; Thomas, A. A.; Borden, M. A. The Effect of Lipid Monolayer in-Plane Rigidity on in Vivo Microbubble Circulation Persistence. *Biomaterials* 2013, 34 (28), 6862–6870.
3. Thomas, A. N.; Borden, M. A. Hydrostatic Pressurization of Lung Surfactant Microbubbles: Observation of a Strain-Rate Dependent Elasticity. *Langmuir* 2017.
4. Lum, J. S.; Borden, M. A.; Murray, T. W. Photoacoustic Evaluation of Temperature Effects on Microbubble Properties. *In Review*.

# Incompressible perfusion time of microbubbles in capillaries drives the fundamental compromise between spatial resolution and acquisition time in Ultrasound Localization Microscopy

*Claudia Errico\**, *Vincent Hingot\**, *Baptiste Heiles*, *Line Rahal*, *Mickael Tanter\*\**,  
*Olivier Couture\*\**

*\*, \*\* These authors have contributed equally*

*Institut Langevin, CNRS, INSERM, ESPCI Paris, PSL Research University, 17 rue Moreau,  
75012, Paris.*

## Background

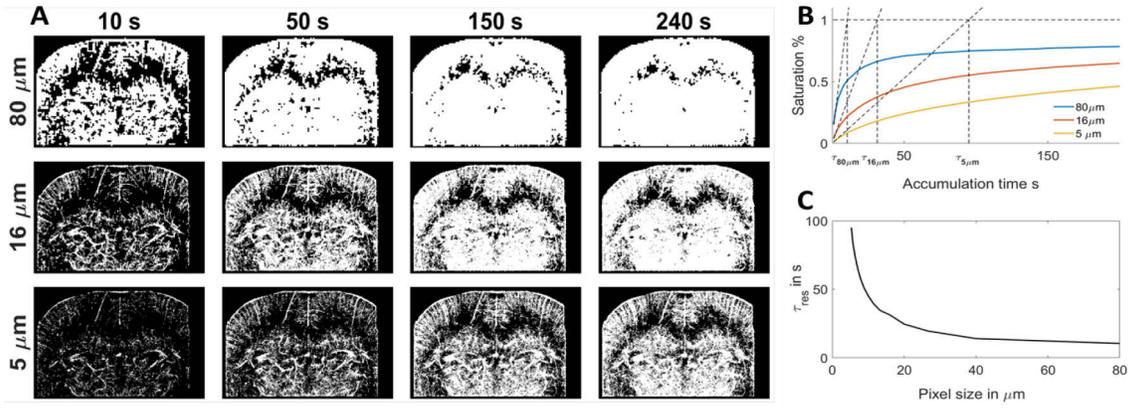
Introduced recently, ultrasound super-resolution techniques such as ultrafast Ultrasound Localization Microscopy (uULM) [Errico et al, Nature 2015] surpass the diffraction-limit over orders of magnitude. We previously exploited uULM to achieve resolution of 8  $\mu\text{m}$  over a depth of 12 mm in the rat brain vasculature. However, to reach such a resolution, about one million micro-bubbles had to be individually localized and tracked for few minutes, highlighting the fundamental tradeoff between temporal and spatial resolutions. In this study, we describe the compromise between the acquisition time and the size of the pixels.

## Methods

Adult Sprague Dawley rats were anesthetized, a catheter was placed in the jugular vein and the head of the animal was fixed in a stereotaxic frame. The skull bone was removed. 320  $\mu\text{l}$  of Sonovue microbubbles were injected through the catheter in the jugular vein at a rate of 80  $\mu\text{l}\cdot\text{min}^{-1}$  for four minutes to keep a stable concentration in the blood stream. 240 blocks of 800 compounded frames at 1000Hz were acquired every second. Singular Value Decomposition clutter filters were used to extract bubbles' signals from surrounding tissues.

## Results

Six million microbubbles were localized with lateral resolution between 5  $\mu\text{m}$  and 80  $\mu\text{m}$ . Saturated images were reconstructed on different fractions of the dataset to form images with various spatial and temporal resolution (Figure A). Hence, we derived the saturation curves to explore the kinetic of micro-bubble accumulation (Figure B). The tradeoff between temporal and spatial resolution in the case of the rat's brain is shown in Figure C with the determination of experimental time constants  $\tau_{\text{res}}$  for every spatial resolution. We consider that a steady state is reached after 5  $\tau_{\text{res}}$ , which is after 50 s for 80  $\mu\text{m}$  pixels, 150 s for 16  $\mu\text{m}$  pixels, and 500 s for 5  $\mu\text{m}$  pixels. This study shows that uULM is inherently limited by the incompressible perfusion time of microbubbles in capillaries, which drives the fundamental compromise between the observation scale and the acquisition time.



**A: Saturation images. B Saturation curves. C: Experimental time constants**

# Mapping blood flow and wall shear stress in the rabbit abdominal aorta in vivo using native blood speckle and microbubble contrast agent

*K Riemer<sup>1\*</sup>, E Rowland<sup>1\*</sup>, K Lichtenstein<sup>1,2</sup>, C H Leow<sup>1</sup>, M X Tang<sup>1</sup>, P D Weinberg<sup>1</sup>*

<sup>1</sup>*Department of Bioengineering, Imperial College London, London, U.K.*

<sup>2</sup>*Division of Cardiovascular Surgery, University of British Columbia, Vancouver, Canada.*

*\*p.weinberg@ic.ac.uk \*mengxing.tang@ic.ac.uk*

## Background

A wide range of cardiovascular diseases such as coronary heart disease (CHD) manifest themselves with, or develop as a result of, abnormalities in blood flow and wall shear stress (WSS) [1]. It is therefore desirable to accurately image and quantify blood flow and its derivatives non-invasively. To assess the spatiotemporally varying magnitude of flow and WSS, good separation of the arterial wall and the blood is essential. Our lab has recently demonstrated a technique for high-frame-rate (HFR) contrast enhanced (CEUS) ultrasound imaging velocimetry (UIV) capable of providing quantitative maps of flow velocity and WSS in vitro, using pulse inversion (PI) to increase image sensitivity and specificity [2]. However, the need for contrast agent might restrict the use of UIV for general health screening. Conventional non-contrast ultrafast ultrasound imaging can distinguish blood flow and the vessel wall. Furthermore, Voornefeld et al. have demonstrated the efficacy of non-contrast UIV in vitro using the speckle pattern of blood mimicking Orgasol particles and a spatiotemporal clutter filtering technique - Singular Value Decomposition (SVD) [3].

## Objective

In this study we first aim to evaluate the UIV derived flow velocity in vivo against an invasive Doppler catheter measurement. Second, we compare the speckle pattern tracking of microbubble contrast agents and native blood speckles (NBS) in vivo to determine whether WSS can be mapped with a non-contrast-agent specific CEUS acquisition scheme and with NBS and spatiotemporal clutter filtering.

## Methods

The abdominal aorta of five terminally-anaesthetised male New Zealand White (NZW) rabbits was imaged using a Verasonics Vantage 64 LE research ultrasound system with a L11-4v broadband probe. B-Mode images were acquired for a period of 1s at a frame rate of 2000fps with a centre frequency of 9MHz and MI < 0.09. A Philips Volcano catheter was inserted through the femoral artery and placed ~12cm proximal from the insertion point/ ~20cm distal to the aortic valve (AV). The positioning of the catheter was examined using the US probe. An ECG signal was recorded simultaneously with the Volcano velocity and pressure measurement. For CEUS, a bolus of 0.05ml of microbubbles were injected via the marginal ear vein. NBS measurements were performed before CEUS. All experiments complied with Animals (Scientific Procedures)

Act 1986 and were approved by the Animal Welfare and Ethical Review Body of Imperial College London.

## Results

Peak and mean velocity of CEUS and NBS UIV showed the same basic features as the Volcano Doppler data for all animals. Peak velocity with CEUS imaging tended to be slightly larger (<5%) than NBS imaging and became still larger (<30%) when the overall B-Mode SNR decreased. An improvement in the wall tracking of NBS over CEUS images was not observed. Low blood flow velocities in diastole and low magnitude flow disturbances appeared to be more recognizable with CEUS imaging. Small vessels originating from the abdominal aorta were also more apparent in CEUS than in NBS images. Maximum and mean WSS for NBS and CEUS were about 5/4Pa and 1.5/1Pa respectively (ranging from -3Pa – +8Pa depending on location; averaged over 20mm along the vessel wall). Contrast to tissue (CTR, [4]) and contrast to noise ratio (CNR, [4]) was larger in SVD filtered NBS images than in CEUS images, but SNR was higher in CEUS images at all times.

## Discussion

Measurements were peak aligned but had to be taken at different times since the Doppler and plane wave imaging system interfered and NBS imaging had to be performed before contrast agents were administered. This gave rise to at least some of the discrepancies between waveforms measured with the different techniques. WSS measurements were in reasonable agreement with in vivo [5] and in silico [6] values; differences between CEUS and NBS can be attributed in uncertainties in wall location and to out-of-plane motion. CNR and CTR appear not to adequately describe the observed level of contrast to noise ratio. This reflects problems caused by using SVD clutter filtering for pulsatile flow: the tissue signal intensity of the SVD filtered CEUS images changes during the cardiac cycle, decreasing overall CNR and CTR.

## Conclusion

In this study we demonstrated the efficacy of the UIV system to quantify blood flow and wall shear stress with high accuracy in vivo using both CEUS and NBS. Speckle tracking of NBS compared to CEUS without a contrast-specific acquisition scheme delivered similar accuracy in velocity and WSS. NBS UIV sensitivity is SNR specific and appears to depend on the individual subject. Both CEUS and NBS UIV might be improved by using Pulse Inversion and imaging with high MI, respectively.

**Acknowledgments:** Kai Riemer is supported by the BHF Centre of Research Excellence of ICL.

## References

1. D. De Wilde, B. Trachet, G. R. Y. De Meyer, and P. Segers, "Shear Stress Metrics and Their Relation to Atherosclerosis: An In Vivo Follow-up Study in Atherosclerotic Mice," *Ann. Biomed. Eng.*, vol. 44, no. 8, pp. 2327–2338, 2016.
2. C. H. Leow and M. X. Tang, "Spatio-Temporal Flow and Wall Shear Stress Mapping Based on Incoherent Ensemble-Correlation of Ultrafast Contrast Enhanced Ultrasound Images," *Ultrasound Med. Biol.*, no. i, 2017.

3. J. Voornveld et al., "Native blood speckle vs ultrasound contrast agent for particle image velocimetry with ultrafast ultrasound - in vitro experiments," *IEEE Int. Ultrason. Symp. IUS*, vol. 2016–Novem, no. Imdi, pp. 3–6, 2016.
4. M. C. Van Wijk and J. M. Thijssen, "Performance testing of medical ultrasound equipment: Fundamental vs. harmonic mode," *Ultrasonics*, vol. 40, no. 1–8, pp. 585–591, 2002.
5. L. Ai, H. Yu, W. Dai, S. L. Hale, R. A. Kloner, and T. K. Hsiai, "Real-time intravascular shear stress in the rabbit abdominal aorta," *IEEE Trans. Biomed. Eng.*, vol. 56, no. 6, pp. 1755–1764, 2009.
6. V. Peiffer, S. J. Sherwin, and P. D. Weinberg, "Computation in the rabbit aorta of a new metric - the transverse wall shear stress - to quantify the multidirectional character of disturbed blood flow," *J. Biomech.*, vol. 46, no. 15, pp. 2651–2658, 2013.

# High Resolution Ultrafast Imaging of Microbubble Activity During Sonoporation

*Sara Keller, Matt Bruce, Michalakis Averkiou*

*Department of Bioengineering, University of Washington, Seattle, WA*

## Introduction

Ultrasound-mediated drug delivery using microbubbles is a growing field with applications ranging from targeted chemotherapy delivery to permeating the blood brain barrier. However, the precise parameters that induce sonoporation, or increased cellular permeability, are not fully understood. There are three time scales important in sonoporation: 1) the time of bubble oscillation, equal to the period of the sound pulse (microseconds), 2) the time it takes for bubble destruction and radiation force to reach cells (milliseconds), and 3) the time scale of cell membrane permeation (seconds to minutes). For the first timeframe, super high frame rate microscopy with a Brannan camera has been used (1), and for the third, in vitro studies of propidium iodide uptake into cells have been performed (2-4). That said, because of the wide range of parameters and lack of standardization in experimental setup and macroscale acoustic field effects, the existing literature does not fully describe or explain how to achieve reproducible sonoporation. We believe that examining the temporal window after application of an ultrasound pulse until the acoustic effect reaches cells may elucidate these processes. High-resolution ultrafast imaging can achieve frame rates up to the tens of kilohertz and therefore is a useful tool for resolving these millisecond timeframe radiation force effects. Our hypothesis is that ultrasound imaging at kHz frame rates will demonstrate the interaction of ultrasound with microbubbles during the sonoporation process to carefully control ultrasound dose. This work has two aims: first, to determine the dependence of microbubble concentration and acoustic environment on cavitation activity, and second, to accurately image the ultrasound delivery to cells with high-resolution ultrafast imaging. This will lead to mechanistic optimization of sonoporation.

## Methods

The main sonoporation parameters evaluated are: pressure (0.1 – 1 MPa), number of cycles (10 – 1000), firing interval (20 ms – 1 s), and microbubble concentration (100k – 5M bubbles/ml).

### Determining acoustic attenuation

Ultrasound transmission from a 1 MHz single element focused transducer through a cell enclosure (Opticell-like) with increasing microbubble concentration was characterized at the acoustic parameters mentioned above with a PVDF membrane hydrophone.

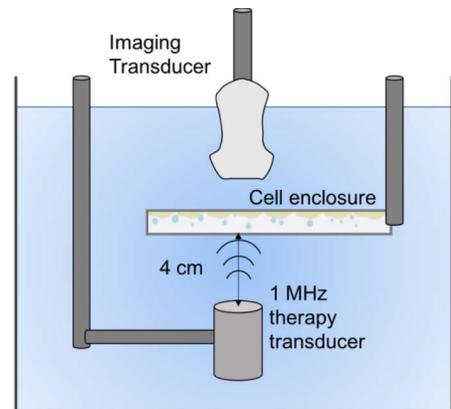


**Figure 1:** Experimental setup for imaging bubble destruction

## High FR Imaging

A Verasonics 128 system was used for high-resolution ultrafast imaging in the orientation as shown in Fig. 1. The same 1 MHz single element transducer was used as in the acoustic attenuation measurements. Frame rates tested ranged from 3 kHz to 10 kHz, with the intention of seeing the degree of immediate bubble destruction as well as subsequent acoustic streaming and bubble motion.

## Results

### Microbubble-dependent acoustic attenuation

As seen in Fig. 2, with increasing concentration of microbubbles, the excess attenuation (acoustic shadowing) increases and the resultant signal decreases. The higher pressure pulses also experienced more attenuation; at a concentration of about 100k bubbles/ml, the RMS pressure received had already decreased by over 50% in the 500 kPa case, while it had only decreased about 20% in the 100 kPa case.

### High FR Imaging

Shown in Fig. 3 are selected frames from video sequences demonstrating initial bubble destruction and subsequent acoustic streaming. All exposures were taken at 1 MPa. The destruction area is dependent on concentration and number of cycles (and therefore total intensity). Fig. 4 shows the resulting complex patterns from various acoustic conditions (pressure: 0.1, 0.5 and 1 MPa; concentration: 400 k bubbles/ml vs 1 M bubbles/ml; cycles: 200 vs. 1000).

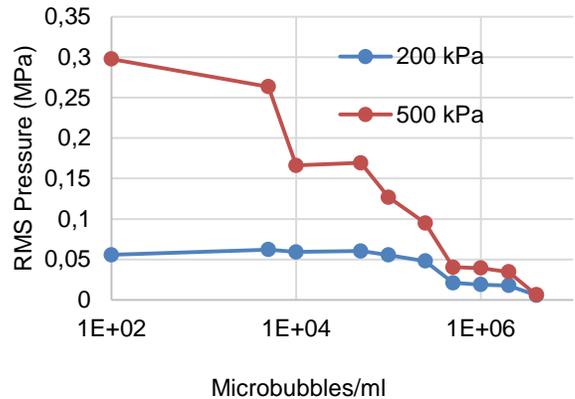


**Figure 2:** RMS pressure measured after propagation in the bubble enclosure. Note that the higher pressure pulse attenuates at a higher rate than the lower pressure pulse

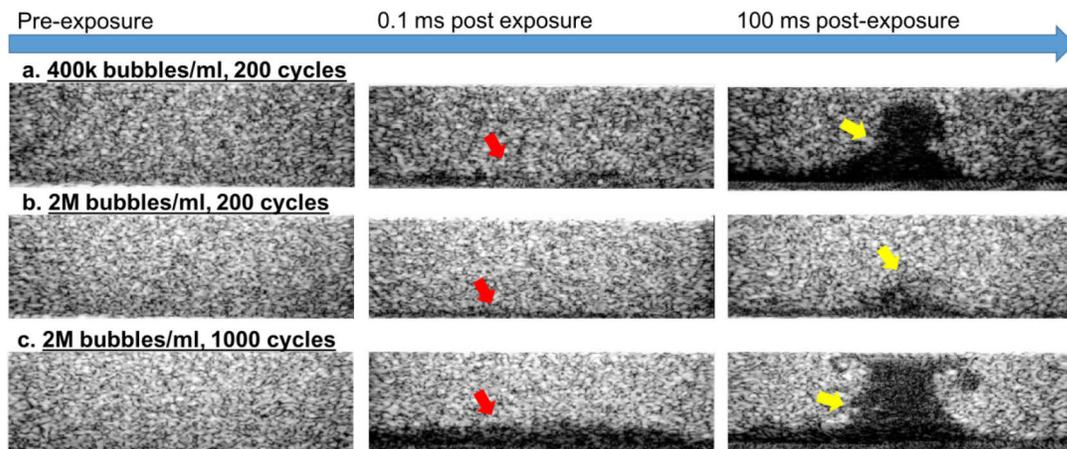


**Figure 3:** Bubble destruction images taken with a Verasonics 128 at a 10 kHz frame rate. Images are organized left to right in time post-exposure. Red arrows represent initial bubble destruction from the ultrasound pulse and yellow arrows represent resultant bubble motion.

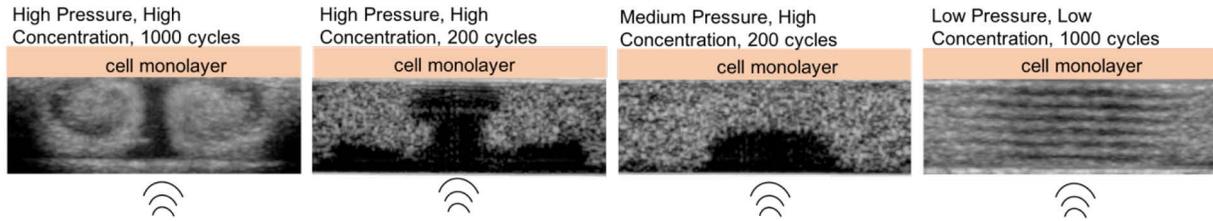


**Figure 4:** Images of cavitation activity near cells during sonication. Note swirling and standing waves.

## Discussion and Conclusions

The most striking result of the first set of experiments is the extreme loss of pressure that occurs with increasing microbubble concentration despite the very short propagation distance (the cell enclosure is only 5 mm thick). This result implies that for single pulsed sonoporation experiments, the calibrated pressures meant to be delivered to microbubbles next to cells are actually very inaccurate. Even at low microbubble concentrations, between 100k and 400k bubbles/ml, there is still an almost 50% loss in signal for both low and high pressures. Interestingly, the effect of concentration-dependent attenuation is more dramatic at higher pressures, possibly due to higher pressures yielding higher inertial force losses upon contact with microbubbles.

A corollary to this argument is that the microbubble concentration that is added to the enclosure is different than the microbubble concentration next to cells (given the 3D geometry of cell enclosures). While efficient sonoporation necessitates high bubble concentrations, these concentrations also greatly reduce the pressure that the cells receive. As shown in Fig. 5, while 100k bubbles/mL already causes a dramatically reduced pressure, there are actually very few bubbles in the vicinity of cells

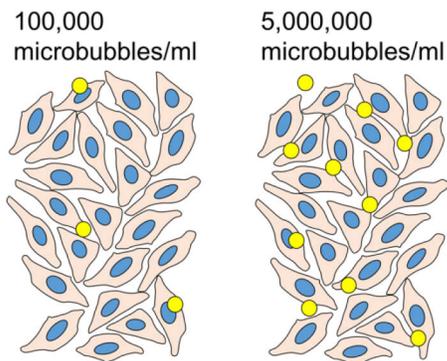


**Figure 5:** Representation of bubble concentrations in relation to 15  $\mu\text{m}$  cells taking into account the 3D geometry of enclosure.

The unique microbubble destruction patterns seen through ultrafast imaging with the Verasonics system show that the acoustic environment near cells can be much more complex than often assumed. Even at destructive pressures greater than 0.5 MI, initial bubble destruction from a single pulse did not make it to the cells. A low number of cycles results in an initial amount of bubble destruction and minimal displacement but no subsequent movement while a high number of cycles results in a large degree of momentum that causes a swirling motion which likely exerts a lateral shear stress on cells. This force is different than the force created by bubble oscillation, which is often hypothesized to be a main mechanism of sonoporation. Ultimately, all experiments

performed in this work showed that the pressures that we believe to be delivered to cells are not the pressures actually felt by cells, because of both bubble attenuation and bubble movement. This work has informed ongoing research into in vitro sonoporation, but instead of the typical “pushing up” conformation used in prior studies that have led to variable results (2-4), we are studying transmitting from the same side as the cells to avoid bubble attenuation. These preliminary results form a baseline for understanding the complex acoustic conditions needed for reproducible sonoporation applications.

## References

1. de Jong N, Emmer M, van Wamel A, Versluis M. Ultrasonic characterization of ultrasound contrast agents. *Medical & Biological Engineering & Computing*. 2009;47(8):861-73. doi: 10.1007/s11517-009-0497-1.
2. Helfield B, Chen X, Watkins SC, Villanueva FS. Biophysical insight into mechanisms of sonoporation. *Proceedings of the National Academy of Sciences*. 2016;113(36):9983-8. doi: 10.1073/pnas.1606915113.
3. De Cock I, Zagato E, Braeckmans K, Luan Y, de Jong N, De Smedt SC, Lentacker I. Ultrasound and microbubble mediated drug delivery: Acoustic pressure as determinant for uptake via membrane pores or endocytosis. *Journal of Controlled Release*. 2015;197:20-8. doi: <http://dx.doi.org/10.1016/j.jconrel.2014.10.031>.
4. van Rooij T, Skachkov I, Beekers I, Lattwein KR, Voorneveld JD, Kokhuis TJ, Bera D, Luan Y, van der Steen AF, de Jong N. Viability of endothelial cells after ultrasound-mediated sonoporation: Influence of targeting, oscillation, and displacement of microbubbles. *Journal of Controlled Release*. 2016;238:197-211.

# Long-term variability of renal perfusion parameters measured by contrast-enhanced ultrasound in healthy dogs

*Daisy J.X. Liu<sup>1</sup>, Emmelie Stock<sup>1</sup>, Evelien Bogaerts<sup>a</sup>, Bart J.G. Broeckx<sup>2</sup>, Myriam Hesta<sup>2\*</sup>, Katrien Vanderperren<sup>1\*</sup>*  
*\* Both authors contributed equally*

<sup>1</sup>*Department of Veterinary Medical Imaging and Small Animal Orthopedics, Faculty of Veterinary Medicine, Ghent University, Salisburylaan 133, 9820 Merelbeke, Belgium*

<sup>2</sup>*Department of Nutrition, Genetics and Ethology, Faculty of Veterinary Medicine, Ghent University, Heidestraat 19, 9820 Merelbeke, Belgium*

## Introduction

Chronic kidney disease (CKD) is clinically challenging to diagnose in early stages in dogs. Contrast-enhanced ultrasound (CEUS) is a technique that has shown potential in diagnosing renal disorders (1,2). Because microbubbles remain completely intravascular and have a rheology similar to that of red blood cells, they can be used to provide information on the density and function of the microvascular network within a tissue (2,3). However, knowledge about long-term variation in a healthy canine population, which is important for developing early CKD detection tools, is scarce. Therefore, the aim of this study was to determine the variation of CEUS renal perfusion parameters in healthy dogs during 1.5 years.

## Materials and Methods

This study was approved by the Institutional Animal Ethics Committee (Faculties of Veterinary Medicine and Bioscience Engineering, Belgium) (EC2015/92). Eight healthy research beagles, fed the same adult maintenance diet, were assessed under sedation (0.4 mg/kg, Dolorex® 10 mg/ml, Intervet, Belgium) at seven time points (week 0, 12, 24, 36, 47, 56, and 83). A linear transducer (12–5 MHz) on a dedicated machine (iU22, Philips, Bothell, WA) with contrast-specific software was used for all CEUS evaluations. A bolus of SonoVue® (0.04 ml/kg, Bracco Diagnostics Inc., Italy) was injected intravenously, followed immediately by 2 mL of sterile saline. A 90-second digital recording was made simultaneously at the start of the injection. Only the recording from the second injection of the left kidney and recording for the right kidney were used for evaluation (4). Microbubbles were destroyed in between each bolus by scanning the caudal abdominal aorta for several minutes. The clips were analyzed using specialized computer software (VueBox®, Bracco Research, Switzerland) for objective quantitative analysis. Two region-of-interests (ROI) were manually drawn in the renal cortex (0.51 cm<sup>2</sup>) and in the medulla (0.37 cm<sup>2</sup>). For every ROI, the software determined mean pixel intensities and created time-intensity curves. Intensity-related parameters representing blood volume (peak enhancement (PE), wash-in area under the curve (WiAUC), wash-out AUC (WoAUC) and total AUC (AUC)) and time-related parameters representing blood velocity (rise time (RT), mean transit time (mTT), time-to-peak (TTP), wash-in rate (WiR), wash-in perfusion index (WiPI), fall time (FT), wash-out rate (WoR)) were determined. A random effects model using restricted maximum likelihood

was used to estimate variance components. Within-dog coefficient of variation (CV) was defined as the ratio of the standard deviation over the mean.

## Results and Discussion

Except for cortical mTT and TTP, the magnitude of variation arising from repeated measurements from the same dog over 1.5 years for all CEUS parameters was high compared to extra variation from measurements between different dogs. RT, TTP and FT in the cortex had the smallest CV (21.9%, 14.7% and 26.1%, respectively) in contrast to the medulla (30.4%, 16.5 % and 45.6%, respectively) and to PE, WiAUC, AUC and WoAUC (range 44.9 – 191.7%). These results were comparable to work in cats from our research group (5). Signal intensity parameters are influenced by imaging depth, ROI placement, and patient factors (e.g., blood pressure, microbubble filtration in the lungs, and phagocytosis of microbubbles by the reticular endothelial system)(6). Especially patient factors can vary in such a long study. Since time-related parameters are indicative of function within the kidney's microvascular network (3) and have lower variability across time, they may be more reliable for use in successive measurements. Moreover, extra variation from measuring left and right kidneys within the same individual was zero for both the cortex and the medulla. Therefore, CEUS can also be used to identify changes in individual kidney function compared to techniques that evaluate only global kidney function.

In conclusion, this longitudinal study showed a wide range of variability in CEUS renal perfusion parameters within and between healthy dogs. Time-related parameters may have potential use in follow-up of renal function. CEUS may also be suitable for evaluating unilateral kidney function.

## References

1. Wang L, Wu J, Cheng JF, Liu XY, Ma F, Guo LH, et al. Diagnostic value of quantitative contrast-enhanced ultrasound (CEUS) for early detection of renal hyperperfusion in diabetic kidney disease. *J Nephrol.* 2015 Dec 25;28(6):669–78.
2. Dong Y, Wang W-P, Cao J, Fan P, Lin X. Early assessment of chronic kidney dysfunction using contrast-enhanced ultrasound: a pilot study. *Br J Radiol.* 2014 Oct;87(1042):20140350.
3. Dizeux A, Payen T, Barrois G, Le Guillou Buffello D, Bridal SL. Reproducibility of Contrast-Enhanced Ultrasound in Mice with Controlled Injection. *Mol Imaging Biol.* 2016 Oct 13;18(5):651–8.
4. Stock E, Vanderperren K, Haers H, Duchateau L, Hesta M, Saunders JH. Quantitative Differences Between the First and Second Injection of Contrast Agent in Contrast-Enhanced Ultrasonography of Feline Kidneys and Spleen. *Ultrasound Med Biol.* 2017 Feb;43(2):500–4.
5. Stock E, Duchateau L, Volckaert V, Polis I, Saunders JH, Vanderperren K. Repeatability of contrast-enhanced ultrasonography of the kidneys in healthy cats. *Ultrasound Med Biol.* 2017;in press.
6. Tang M-X, Mulvana H, Gauthier T, Lim AKP, Cosgrove DO, Eckersley RJ, et al. Quantitative contrast-enhanced ultrasound imaging: a review of sources of variability. *Interface Focus.* 2011 Aug 6;1(4):520–39.

# Molecularly Engineered H<sub>2</sub>O<sub>2</sub>-Activatable Nanoparticles for Contrast-enhanced Photoacoustic Imaging of Thrombosed Vessels

*Eunkyeong Jung, Changsun Kang, Jeonghun Lee, Donghyuck Yoo, Dongwon Lee\**

*Department of BIN Convergence Technology, Chonbuk National University, Baekjedaero 567, Jeonju, Chonbuk 54896, Republic of Korea*

Perfluorocarbon-filled microbubbles have long been widely used as an ultrasound contrast agent due to their high acoustic scattering properties. Interestingly, microbubbles could also produce enhanced photoacoustic responses beyond the traditionally used mechanism, thermoelastic expansion. Several lines of evidence have demonstrated that the contrast-enhanced photoacoustic imaging can be realized through vaporization of nanodroplets consisting of perfluorocarbon and gold nanorods. Under laser irradiation, perfluorocarbon could become easily superheated and undergo liquid-gas transition to form microbubbles which induce one-time, high amplitude of photoacoustic signal. Therefore, upon laser irradiation, photoabsorbers-containing nanodroplets could provide combined photoacoustic signals via two mechanisms: vaporization of perfluorocarbon by liquid-gas phase transition and traditional thermoelastic expansion caused by photoabsorbers. Photoacoustic imaging through vaporization of nanodroplets, therefore, could display significantly higher signal amplitude than those through thermoelastic expansion. Furthermore, once vaporization is initiated, the resulting microbubbles of nanodroplets also provide significant acoustic impedance mismatch between gas bubbles and the surrounding mediums, thereby enhancing ultrasound contrast. Therefore, photoabsorbers-containing nanodroplets would generate contrast-enhanced dual ultrasound/photoacoustic imaging. However, vaporization-based photoacoustic imaging with photoabsorbers-containing nanodroplets has limitations such as poor stability of bubbles, short life-time of signals and precise timing control with laser irradiation.

In this study, we developed H<sub>2</sub>O<sub>2</sub>-triggered bubble-generating fluorescent nanoparticles as self-contrast enhanced ultrasound/photoacoustic imaging agents, which do not require gas precursors (perfluorocarbon) and external pulsed laser. Near infrared fluorescent dye-conjugated boronated maltodextrin (FBM) was employed as a platform of H<sub>2</sub>O<sub>2</sub>-triggered bubble-generating nanoparticles. FBM was prepared by conjugating borylbenzyl carbonate and fluorescent IR780 to maltodextrin. Borylbenzyl carbonate and IR780 were exploited as a H<sub>2</sub>O<sub>2</sub>-triggered bubble-generating moiety and a photoabsorber, respectively. We therefore hypothesized that borylbenzyl carbonate of FBM nanoparticles reacts with H<sub>2</sub>O<sub>2</sub> to form CO<sub>2</sub> bubbles which could amplify both ultrasound and photoacoustic signals, with a mechanism similar to laser-activatable microbubble-generating nanodroplets.

A thrombus (blood clot), composed mainly of activated platelets and fibrin, obstructs arteries or veins, leading to various life-threatening diseases. A lipopeptide, DSPE-PEG-PPRPG is well known to specifically bind fibrin with high affinity. Inspired by the unique physicochemical characteristics of thrombi such as abundant fibrin and the elevated level of hydrogen peroxide (H<sub>2</sub>O<sub>2</sub>), we developed thrombus-specific theranostic (T-FBM) nanoparticles using FBM and

DSPE-PEG-PPRPG that could provide H<sub>2</sub>O<sub>2</sub>-triggered photoacoustic signal amplification and serve as an antithrombotic nanomedicine (Figure 1). T-FBM nanoparticles were designed to target fibrin-rich thrombi and be activated by H<sub>2</sub>O<sub>2</sub> to generate CO<sub>2</sub> bubbles to amplify the photoacoustic signal. In the phantom studies, T-FBM nanoparticles showed significant amplification of ultrasound/photoacoustic signals in a H<sub>2</sub>O<sub>2</sub>-triggered manner. In mouse models of carotid arterial injury, T-FBM nanoparticles significantly enhanced the photoacoustic contrast specifically in thrombosed vessels. We anticipate that T-FBM nanoparticles hold great translational potential as nanotheranostics for H<sub>2</sub>O<sub>2</sub>-associated cardiovascular diseases.

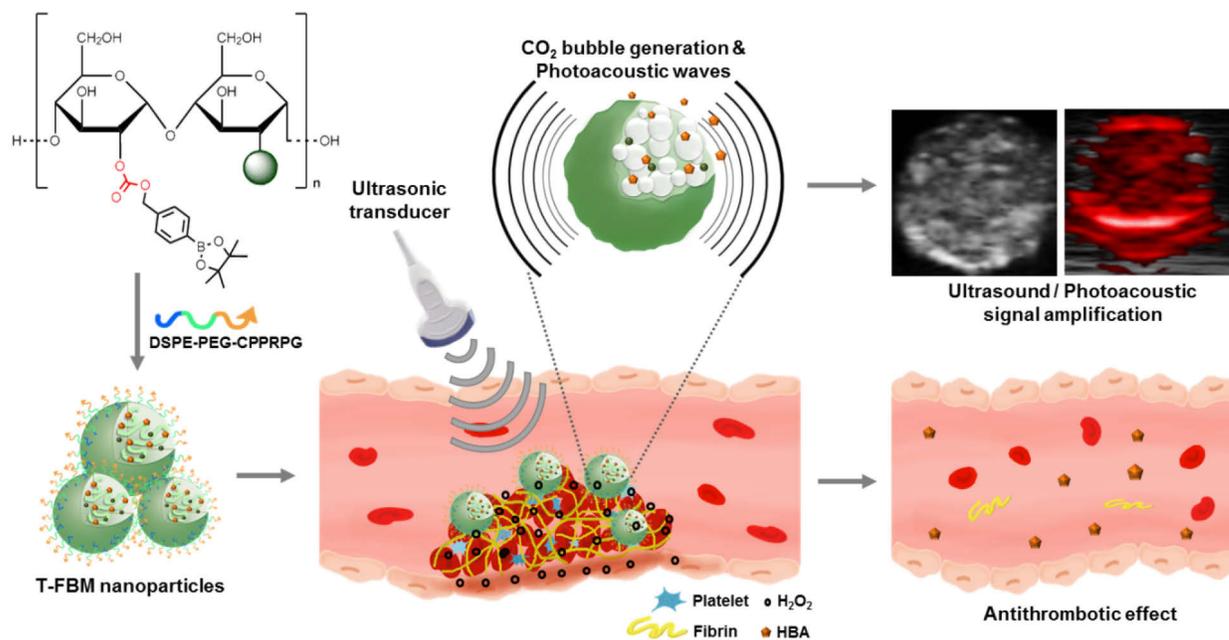


**Figure 1.** Schematic illustration of T-FBM nanoparticles as a thrombus-specific nanotheranostic agent. T-FBM nanoparticles target a fibrin-rich thrombus and serve as a H<sub>2</sub>O<sub>2</sub>-triggered photoacoustic signal amplifier but also an antithrombotic nanomedicine.

# **Cancer therapy by the combination of ultrasound contrast imaging agent and non-focused ultrasound induce cancer immune response**

*Ryo Suzuki, Daiki Omata, Johan Unga, Lisa Munakata, Kazuo Maruyama*

*Faculty of Pharma-science, Teikyo University, Tokyo, Japan*

## **Objectives**

Cancer immunotherapy is an attractive therapy in terms of cancer cell specificity. In the most of cancer patients, cancer immune responses are suppressed in tumor tissue by regulatory T lymphocytes and suppressing signals such as PD-1/PD-L1. Unfortunately, cancer immunotherapies are not so effective. To improve this problem, immuno-checkpoint inhibitors were developed and could prolong the survival time. However, this effect is not enough. It is necessary to develop new approach to enhance cancer immune response and combine with immuno-checkpoint inhibitors. Recently, it is reported that radiotherapy, photodynamic therapy and high intensity focused ultrasound therapy have potency to induce cancer immune response. Recently, it was reported that ultrasound contrast agents such as microbubbles combined with therapeutic ultrasound would be useful for drug and gene delivery. On the other hand, there is no report about the immune response by the combination of ultrasound contrast imaging agent and non-focused ultrasound. In this study, we assessed the tumor growth suppression and the induction of cellular immune response by the combination of our lipid based nanobubble and non-focused ultrasound.

## **Methods**

Colon-26 cells (mouse colon carcinoma) were inoculated into the back of mice. After 8 days, our nanobubbles were intratumorally injected and ultrasound (Frequency: 1 MHz, Intensity: 0-4 W/cm<sup>2</sup>, Duty: 50%, Burst rate: 2Hz, Time: 2 min) was transdermally exposed toward tumor tissue. The anti-tumor effect was evaluated by measuring tumor volume. To assess the effect of cellular immunity on tumor growth suppression, we also examined in CD8 positive T cells depleted mice by injection of anti-CD8 antibody.

## **Results and Discussion**

In the combination of nanobubble and lower intensity (1-3 W/cm<sup>2</sup>) of non-focused ultrasound, tumor growth suppression was not observed. On the other hand, in the treatment of nanobubble and non-focused ultrasound (4 W/cm<sup>2</sup>), tumor growth was effectively suppressed. In addition, this tumor growth suppression was cancelled in the CD8 positive T cell depleted mice. From these results, the combination therapy of nanobubble and non-focused ultrasound would be an effective cancer therapy based on priming the cellular immune response. Therefore, this combination therapy might be a novel cancer immunotherapy based on changing the immunological microenvironment in tumor tissue.

**Acknowledgment:** this study was partially supported by the MEXT-Supported Program for the Strategic Research Foundation at Private Universities.

# Perfluorocarbon-loaded Polymeric Nanoparticles with Multi-domain Structure for Multiscale In Vivo Imaging with Ultrasound and <sup>19</sup>F MRI

*Olga Koshkina*\*<sup>1</sup>, *Edyta Swider*<sup>1</sup>, *Paul White*<sup>2</sup>, *Ernst van Eck*<sup>3</sup>, *Ralf Schweins*<sup>4</sup>, *Sarah Rogers*<sup>5</sup>, *Remco Fokkink*<sup>6</sup>, *Eric van Dinther*<sup>1</sup>, *Neus Villanova Garcia*<sup>7</sup>, *Ilya Voets*<sup>7</sup>, *Guillaume Lajoinie*<sup>8</sup>, *Michel Versluis*<sup>8</sup>, *Chris de Korte*<sup>9</sup>, *Carl Figdor*<sup>1</sup>, *I. Jolanda M. de Vries*<sup>1</sup>, *Francesca Baldelli Bombelli*<sup>10</sup>, *Mangala Srinivas*<sup>1</sup>

<sup>1</sup>*Department of Tumor Immunology, RIMLS, Radboud University Medical Center, Nijmegen, The Netherlands*

<sup>2</sup>*Bio-Organic Chemistry, Radboud University, Nijmegen, The Netherlands*

<sup>3</sup>*Solid State NMR, Radboud University, Nijmegen, The Netherlands*

<sup>4</sup>*The Large Scale Structures group, Institute Laue-Langevin, Grenoble, France*

<sup>5</sup>*Large Scale Structures, ISIS, Rutherford Appleton Laboratory, UK*

<sup>6</sup>*Physical Chemistry and Soft Matter, Wageningen University, Wageningen, The Netherlands*

<sup>7</sup>*Physical Chemistry, Eindhoven University of Technology, Eindhoven, The Netherlands*

<sup>8</sup>*Physics of Fluids group, MESA+ Institute for Nanotechnology and MIRA Institute for Biomedical Technology and Technical Medicine, University of Twente, Enschede, The Netherlands*

<sup>9</sup>*Department of Radiology, Radboud University Medical Center, Nijmegen, The Netherlands*

<sup>10</sup>*Laboratory of Nanostructured Fluorinated Materials (NFMLab), Politecnico di Milano, Milan, Italy*

\* *olga.koshkina@radboudumc.nl*

Cellular therapies are promising for the treatment of currently non-curable conditions such as HIV or cancer. To improve these therapies monitoring of therapeutic cells is essential. Ultrasound (US) is a very attractive and patient-friendly imaging technique. Nevertheless, the low stability of imaging agents, with imaging periods in a time frame minutes, limits the application of US for cell tracking.

We present perfluoro-15-crown-5-ether (PFCE) loaded polymeric nanoparticles (100 nm radius), which are suitable for long-term imaging with ultrasound in a range of days and for quantitative <sup>19</sup>F MRI.[1-3] Using a miniemulsion formulation process enables tailoring the colloidal properties to a desired application.

To relate the unusual acoustic contrast to properties of nanoparticles, we extensively studied our nanoparticles with different physicochemical techniques. The methods include multi-angle light scattering, cryogenic electron microscopy (Fig. 1a), solution 2D NMR (Heteronuclear Overhauser Enhancement Spectroscopy (HOESY, Fig. 1b)) and solid state NMR. Moreover, to unravel the interior structure of nanoparticles, we measured Small Angle Neutron Scattering (SANS, Fig. 1c) at different solvent contrasts to highlight specific compartments of the particles using various controls. These results indicate that both the structure of our nanoparticles and the acoustic contrast generation mechanism are different from other colloidal US contrast agents. To assess the US performance of our particles, we measured US in vitro (Fig. 1d) and in vivo, and

confirmed the results with  $^{19}\text{F}$  MRI and fluorescence microscopy. Finally, we expect a clinical application of the nanoparticles in melanoma patients receiving dendritic cell therapy shortly. [4]

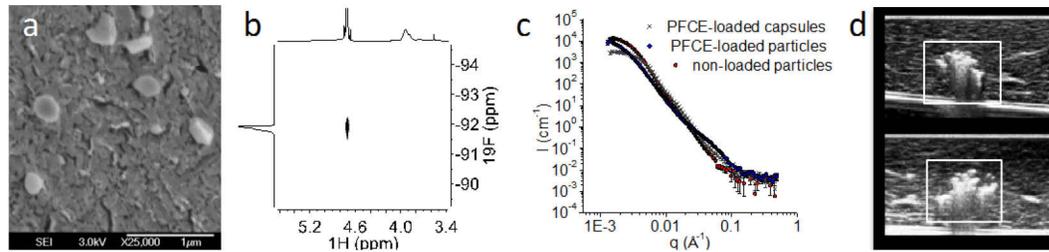


**Figure 1.** a) cryoSEM image of nanoparticles (scale bar 1000 nm). b) HOESY-NMR reveals that superhydrophobic PFCE is close to water. c) SANS patterns of PFCE-loaded particles compared to nanocapsules and non-loaded particles demonstrate structural differences. d) US images in tissue phantom 0 h (top) and 48 h (bottom) after injection.

## References

1. M. Srinivas, L. J. Cruz, F. Bonetto, A. Heerschap, C. G. Figdor, I. J. de Vries, *Biomaterials*, 2010, 31, 7070.
2. L. J. Cruz, P. J. Tacke, R. Fokkink, B. Joosten, M. Cohen Stuart, F. Albericio, R. Torensma, C. G. Figdor, *J. Control. Release*, 2010, 144, 118.
3. O. Koshkina, M. Srinivas, I. J. M. de Vries, C. G. Figdor. Process for preparation of beads for imaging. pending patent application, filed March 11, 2016.
4. [clinicaltrials.gov ID NCT02574377](https://clinicaltrials.gov/ct2/show/study/NCT02574377)

# Laser-activated microparticles: multimodal contrast imaging

*Guillaume Lajoinie<sup>1</sup>, Mirjam Visscher<sup>1</sup>, Emilie Blazjewski<sup>2</sup>, Gert Veldhuis<sup>2</sup>, and Michel Versluis<sup>1</sup>*

<sup>1</sup>*Physics of Fluids Group, MIRA Institute for Biomedical Technology and Technical Medicine and MESA+ Institute for Nanotechnology, University of Twente, P.O. Box 217, 7500 AE Enschede, The Netherlands*

<sup>2</sup>*Nanomi microsphere technology, Zutphenstraat 51, 7575 EJ Oldenzaal, The Netherlands*

The current practice of medical care is facing challenges in the diagnosis and subsequent treatment of a number of diseases such as cancer and genetic deficiency, which have meanwhile reached the limits of traditional pharmacy. These diseases call for novel strategies towards advanced medical imaging and monitoring capability as well as the highest level of precision on the delivery of the drugs. Here, ultrasound imaging is of particular interest as an affordable bedside technique offering an unrivaled combination of resolution, safety and penetration depth however at the expense of a weak contrast and low specificity. Photoacoustic imaging (PI), on the other hand, offers great specificity as compared to US, due to the large variations in optical properties amongst different tissues, while maintaining a good spatial resolution. Such improvement, however, is made at the cost of a much reduced penetration depth, typically limited to only a couple of centimeters. Thus, taking the best of both worlds, a multimodal contrast imaging approach, can provide optimum resolution, penetration and specificity.

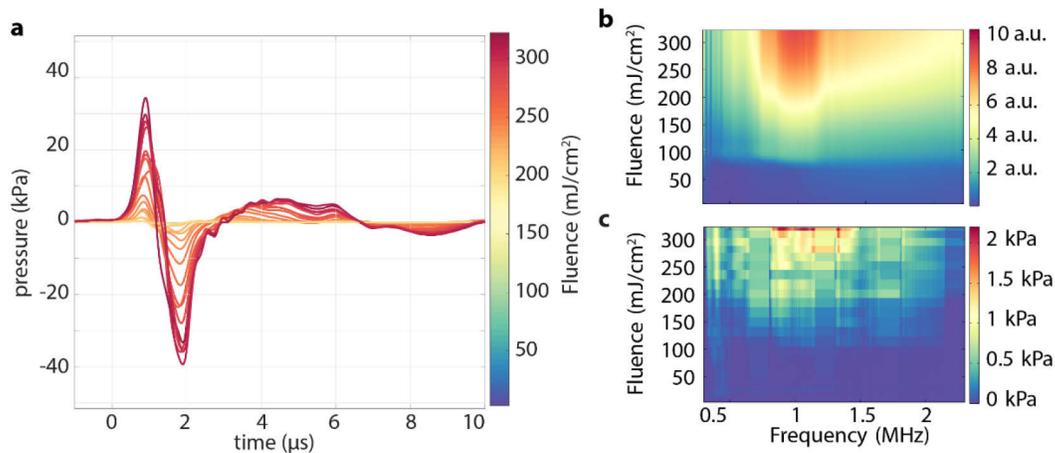


Figure 1: a. Photoacoustic response of Resomer-PFP capsules for increasing laser power. b. calculated response of the bubbles produced by photoacoustic activation to an ultrasound chirp and c. measured response of these bubbles to an acoustic chirp.

Here we develop micron-sized polymeric capsules doped with an absorbing dye located in the capsule shell that can be used as US-PI multimodal contrast agents. Such capsules, triggered by a laser, induce vaporization and bubble generation. Two formulations are investigated, one containing a high boiling point oil (hexadecane) and one containing a low boiling point oil (perfluoropentane). The activation threshold for the latter formulation was found to be much reduced and upon vaporization the bubbles are larger (providing more backscatter) and more stable. The particles are first irradiated with a nanosecond laser pulse and their photoacoustic response is recorded. Within a few milliseconds, the resulting bubbles are probed with an ultrasound chirp with a frequency ranging from 0.3 MHz to 2.3 MHz. The low boiling-point capsules displayed strong acoustic contrast enhancement subsequent to laser activation, with a maximum response near a frequency of 1 MHz. By comparison, high boiling point capsules present a maximum acoustic contrast near 2 MHz, a signature of smaller bubbles, and a reduced acoustic scatter by one order of magnitude. Changing the ambient temperature from 20°C to 37°C induces a measurable decrease in the activation thresholds and does not significantly affect the capability of the particles to generate echogenic bubbles for the monitoring of therapeutic efficacy.

# Development of “Microbubble Clusters”: Potential New Applications in Ultrasound Imaging and Drug Delivery

Ronald L. Hall<sup>1</sup>, Arvin Honari<sup>1</sup>, and Shashank R. Sirsi<sup>1,2</sup>

<sup>1</sup>University of Texas at Dallas, Richardson, TX, USA, 75080

<sup>2</sup>University of Texas Southwestern, Dallas, TX, USA, 75390

## Introduction

Currently, most ultrasound contrast agents (UCAs) are thought of as singular entities with a specific size (1-10  $\mu\text{m}$ ), gas (perfluorocarbons, sulfur hexafluoride or air), and shell compositions (lipids, polymers, or proteins). This study introduces a novel concept and design of “Microbubble Clusters” composed of multiple UCA’s crosslinked together (Figure 1). Microbubble clustering offers several unique advantages compared to individual UCAs. 1) The individual shell and gas components of the microbubbles within the cluster can be manipulated to provide more control and fine-tune acoustic response, 2) Larger size clusters can potentially provide prolonged circulation life and greater acoustic responses, and 3) Cross-linking chemistry can be varied to control stability, increase drug payload, and enable unique methods of releasing encapsulated drugs tethered to the microbubble shells. One of the biggest challenges in developing stable clusters is controlling their aggregation process to achieve cluster sizes viable for in vivo circulation. In this study, we demonstrate that with careful control over the aggregation process, we can generate stable crosslinked microbubble clusters with size distributions adequate for systemic delivery (<10  $\mu\text{m}$  diameter). We propose that this cluster design will allow the development of UCAs that are superior individual point scatterers for contrast-enhanced ultrasound imaging techniques (such as super-resolution imaging) as well as UCA-mediated drug/gene delivery.

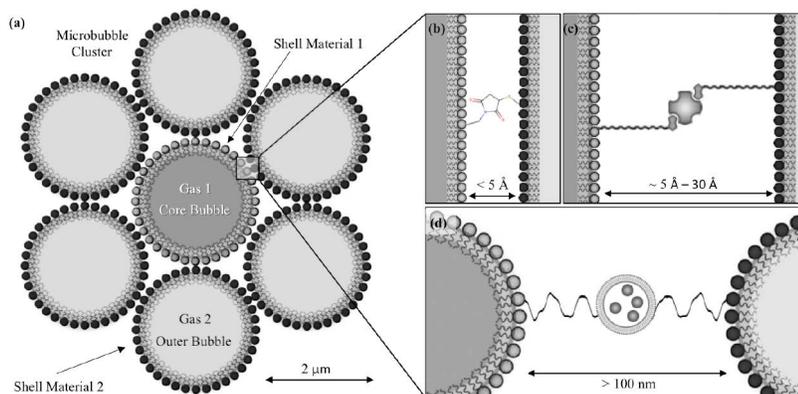


**Fig. 1.** Schematic representation of a microbubble cluster with (a) depicting a microbubble cluster with differing shell material and gas core compositions between the core and outer bubbles. The spacing between the microbubbles within the clusters can be modified by using (b) zero-length cross-linkers (c) protein or polymer interactions and (d) larger molecules such as nanoparticles, microparticles, and vesicles to facilitate the crosslinking.

## **Methods**

In this study, we optimized the development of lipid-based microbubble clusters by mixing avidin-coated UCAs with a molar excess of biotinylated UCAs while varying injection speeds and molar ratios. Flow cytometry and microscopy were used to demonstrate highly efficient cluster formation using fluorescently labeled microbubbles. A custom testing chamber was used to characterize the acoustic response of microbubble clusters using a 2.5 MHz focused transducer (Olympus V303-FU, Waltham, MA) and broadband hydrophone (Sonic Concepts Y109, Seattle, WA).

## **Results and Discussion**

In this study, we demonstrate highly efficient microbubble cluster formations with mean diameters  $\sim 4.5 \mu\text{m}$  and stability for at least 24 hours (and up to 72 hours) at concentrations of  $5 \times 10^8$  MB/ml. By judiciously controlling the mixing process and molar ratios of outer: core microbubbles, we are able to generate controlled microbubble cluster populations without significant aggregation (multiple clusters binding together). We show that microbubble clusters are subject to coalescence by Ostwald ripening over the course of 72 hours and can fuse into larger bubbles with excess lipid retained on the surface. Preliminary in vitro acoustic testing demonstrates that these clusters are able to fuse on demand, potentially generating novel acoustic response and unique methods of rapid drug release. Circulation-life of the clusters is comparable to individual contrast agents indicating the larger size of the microbubble clusters did not impede circulation.

## **Conclusion**

Overall, the development of novel microbubble clusters presents a rapid and facile means of generating novel UCAs with a design that allows more versatility for UCA imaging, molecular imaging, and drug delivery applications.

# Polymer/lipid hybrid shelled microdroplets behave as attractive ultrasound and photo-thermal phase-change integrated systems

*F. Domenici, D. Palmieri, F. Brasili, L. Oddo, A. Bedini<sup>‡</sup>, G. Paradossi*

*Dipartimento di Scienze e Tecnologie Chimiche, Università degli studi di Roma "Tor Vergata",  
IT*

*<sup>‡</sup>Dipartimento Innovazioni Tecnologiche, INAIL, Monteporzio Catone, Rome, IT  
damiano.palmieri@uniroma2.it*

Microdroplets (MDs) with a liquid perfluorocarbon (PFC) core exposed to a proper ultrasound field transform into microbubbles (MBs) by a process known as Acoustic Droplet Vaporization (ADV). The properties of the so-called “phase-change” ultrasound contrast agents rely on this process [1]. The main asset of such systems is the possibility to conjugate their drugs and nanoparticles cargo capability with the dramatically increased ultrasound echogenicity after ADV. The introduction of MDs in the vast theranostics scenario mainly passes through the improvement of their shells to confer greater stability, versatility and higher ADV efficiency, whilst keeping them to the smallest possible size. Recently, our group defined a novel class of MDs (named DexMA MD) based on a biocompatible hybrid shell made up of a surfactant monolayer coated by biodegradable cross-linked dextran-methacrylate (DexMA), and filled with a high boiling decafluoropentane (DFP) core [2,3]. The elastic properties of these systems are comparable to those of the lipid-shelled ones, with a gain in stability and reversibility with respect to the ADV event [3]. However, more efforts are needed to increase the size control and the ADV efficiency of DexMA MDs, and to demonstrate their actual potential as theranostic candidate. In the context, we focused our efforts to integrate DexMA MD shells with gold nanoparticles (AuNPs). The well-known ability of AuNPs to release near-field photothermal energy could in fact be exploited to facilitate the phase transitions of MDs core (yielding a high ADV efficiency), to induce the photoacoustic effect (enhancing the imaging contrast), and to support photothermal therapies [4].

Bearing these aspects in mind, herein we aim to improve our DexMA MDs fabrication: first achieving the control on their size distribution, thus making them more suitable for imaging applications and avoiding the risk of emboli caused by the size increasing occurring upon ADV; then we functionalized the MDs shell with AuNPs to study how NPs affect the liquid-vapour transition of the DFP core. Accurate combined investigation (confocal laser scanning microscopy, absorbance spectroscopy, dynamic light scattering, and acoustic attenuation) will be reported to demonstrate that: i) DexMA MDs size can be tuned to obtain reproducible sharp distributions centred down to 4-fold lower than the size of MBs previously achieved (Figure 1A), by keeping the system stability for several days; ii) AuNPs can be stably bound (covalently or not) to the DexMA shell (Figure 1B); iii) the integrated MD-AuNPs system can be excited by both low intensity 1 MHz ultrasound and laser light at the resonant frequencies of AuNPs (from 525 to 575 nm; ~100 mW) to implement dramatically the ADV efficiency.

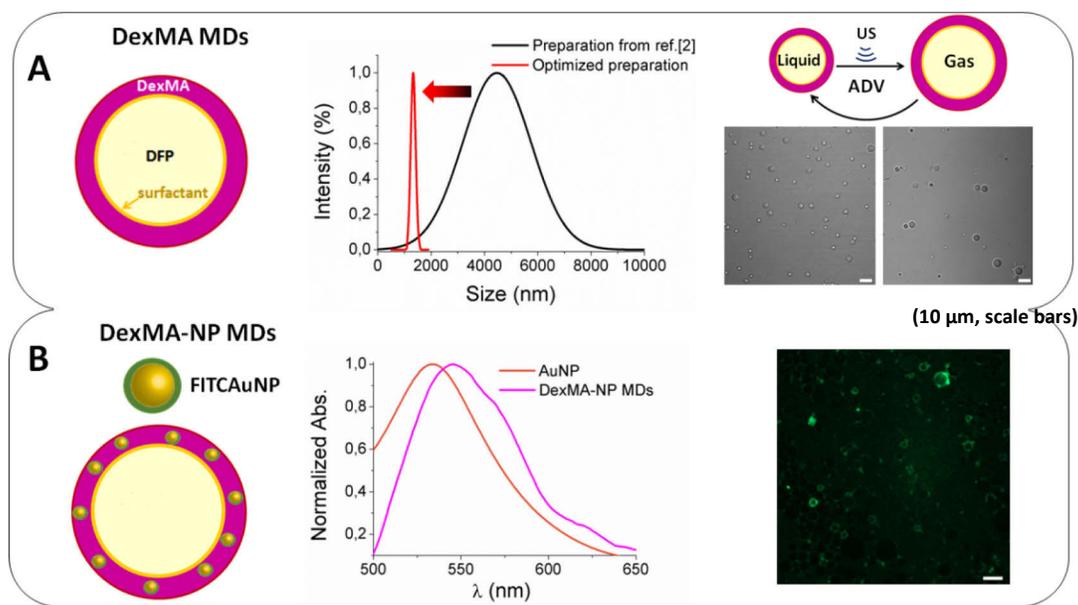


**Figure 1.** From left to right, (A) sketch of the hybrid MD, the compared size distributions, optical images before and after ADV; (B) sketch of the MD conjugated with AuNPs, the corresponding absorbance spectra, representative confocal image.

## References

1. Kripfgans, O.D.; Fabiilli, M.L.; Carson, P.L.; Fowlkes, J.B. *J. Acoust. Soc. Am.* 116, 272–281 (2004).
2. Capece, S.; Chiessi, E.; Cavalli, R.; Giustetto, P.; Grishenkov, D.; Paradossi, G. *Chem. Commun.* 2013, 49, 5763.
3. Capece, S.; Domenici, F.; Brasili, F.; Oddo, L.; Cerroni, B.; Bedini, A.; Bordi, F.; Chiessi, E.; Paradossi, G. *Phys. Chem. Chem. Phys.*, 18, 8378-8388 (2016).
4. Arnal, B.; Perez, C.; Wei, C.-W.; Xia, J.; Lombardo, M.; Pelivanov, I.; Matula, T. J.; Pozzo, L. D.; O'Donnell, M. *Photoacoustics* 3, 3–10 (2015).

# Polymer Microbubbles as Dual Modal Contrast Agent for Ultrasound and Computed Tomography

*Hongjian Chen<sup>1</sup>, David Larsson<sup>1,2</sup>, Birgitta Janerot-Sjöberg<sup>1,2</sup>, Massimiliano Colarietti-Tosti<sup>1</sup>, Dmitry Grishenkov<sup>1</sup>*

<sup>1</sup>*Department of Medical Engineering, School of Technology and Health, KTH Royal Institute of Technology, Stockholm, Sweden*

<sup>2</sup>*Department of Clinical Sciences, Intervention and Technology, Karolinska Institutet, Stockholm, Sweden*

## Background

The hybrid imaging combines the anatomical information with the functional or metabolic information using different conventional single imaging modalities improving the overall diagnosis outcome of the clinical examination. Since the introduction of the first hybrid imaging device PET-CT in 1998 different combinations of hybrid imaging were developed such as PET-MRI, SPECT-CT.

However, lack of multimodal contrast agent specifically aimed for hybrid imaging limits the diagnostic outcome of these novel techniques. Initial attempts in fabrication of hybrid contrast agents were made by combining previously existing single modal contrast agents into one. In this study, polyvinyl alcohol (PVA) microbubbles (MB) and gold nanoparticles - which by themselves are already established contrast agents used in preclinical studies for ultrasound and CT, respectively - were chosen as parent contrast agents to fabricate the dual modal Contrast Agent for UltraSound and CT (CACTUS).

## Method

The fabrication of MBs was adapted from Cavalieri et al.<sup>1</sup>. PVA powder (Sigma Aldrich, MO USA) was dissolved in the water at 80°C. The aqueous PVA-chains were cleaved by sodium metaperiodate (NaIO<sub>4</sub>, purity>99.0%, Sigma Aldrich, MO USA). Vigorous stirring force was applied to the resulting telechelic aldehydic PVA-chains for 2 hours to crosslink the telechelic aldehydic PVA-chains and form the PVA-coated MBs at the water-air interface.

CACTUS MBs were synthesized in a similar fashion to the above, but adding gold nanoparticles (diameter 1.9nm, Nanoprobes, NY, USA) during formation of the MBs.

The size distributions of MBs and CACTUS MBs were determined using an optical microscope (ECLIPSE Ci-S, Nikon, Tokyo, Japan) and a Neubauer counting chamber (Brand GmbH, Wertheim, Germany).

The acoustic attenuation coefficients of the MBs suspension were acquired at peak negative pressure (PNP) from 10 - 300 kPa. Three MBs suspension samples with concentrations of 10<sup>7</sup> (sample A), 5 \* 10<sup>6</sup> (sample B) and 10<sup>6</sup> ml<sup>-1</sup> (sample C) were prepared and loaded in a 1 cm thick two-cavity chamber. A flat single crystal ultrasound transducer with central frequency

---

<sup>1</sup> Cavalieri, F., El Hamassi, A., Chiessi, E., Paradossi, G., Villa, R., & Zaffaroni, N. (2006). Tethering functional ligands onto shell of ultrasound active polymeric microbubbles. *Biomacromolecules*, 7(2), 604-611.

3.5MHz was used to generate the ultrasound beam. The amplitude of received echoes through samples and water were compared at the fundamental frequency, as well as the 2<sup>nd</sup> and 3<sup>rd</sup> harmonic for each value of the concentration used.

The mass attenuation of water, suspension of gold nanoparticles with concentration 160mg/L, plain MBs, and CACTUS MBs, was measured by quantum FX-CT micro-CT (PerkinElmer Inc, MA, USA). The micro-CT was operated at a current of 200mA with exposure time of 120s and varied voltage 50kV, 70kV and 90kV. Each 3D image has a size of 512\*512\*512 pixels or 75.8\*75.8\*75.8 mm. Contrast to noise ratios (CNR) between water and all samples were calculated following Eq. 1.

$$\begin{aligned}
 CNR &= \frac{\text{Signal difference}}{\text{Noise}} = \frac{\iiint \langle S(x,y,z) + n_s(x,y,z) - W(x,y,z) - n_w(x,y,z) \rangle dx dy dz}{\sqrt{\iiint \frac{1}{2} \langle n_s^2(x,y,z) + n_w^2(x,y,z) \rangle dx dy dz}} \\
 &= \sqrt{N} * \frac{M_s - M_w}{\sqrt{\frac{1}{2}(\sigma_s^2 + \sigma_w^2)}} = \sqrt{N} * CNR \text{ per voxel} \quad (Eq. 1)
 \end{aligned}$$

Where S(x,y,z) and W(x,y,z) are the mass attenuation of the sample and water per voxel, respectively. ns(x,y,z) and nw(x,y,z) are the noise function with zero mean of sample and water respectively. Ms and Mw are the mean mass attenuation acquired for the sample and water in the volume of interest. The  $\sigma_s^2$  and  $\sigma_w^2$  are the variance of the mass attenuation read out of the sample and water in the volume of interested.

In addition to the gas-core MBs for the CT tests, liquid-core gold loaded capsules were synthesized in two steps. In the first step, PVA shelled liquid-core capsules were obtained by exposing MBs to 66% v/v ethanol solution. In the second step, the resulting liquid-core capsules were mixed with high concentration gold nanoparticles suspension and homogenized by a shaker (MS 3 basic, IKA, Königswinter Germany) at 500rpm for 1 hour for gold loading. The resulting gold loaded capsules were washed with Milli-Q water using centrifuge (Galaxy 5D digital microcentrifuge, VWR, USA) at a speed of 1000 g for 5 min.

## Results and discussion

The mean diameter of MBs is 3.6±1.1 μm. The mean diameter of CACTUS MBs is 3.2±0.7 μm. The size distribution of the gold loaded capsules was not investigated separately, but rather assumed identical to the plain MBs. The number and the volume distribution of MBs and CACTUS MBs are shown in figure 1. The results demonstrate that most of the CACTUS MBs and MBs have a diameter from 1 to 6 μm. Therefore, they are able pass through the capillaries and will resonate within typical clinical diagnostic ultrasound frequency below 15 MHz.

Pressure dependent acoustic attenuation coefficients of the sample A, B, and C are shown in figure 2. The results show that attenuation coefficients of sample A and B at the fundamental frequency stay constant and slightly increase at the second harmonic at the PNP below 100kPa, indicating a linear oscillation of MBs. As the PNP reaches 200kPa, the attenuation coefficient of sample A at fundamental frequency decreases while at 2nd and 3rd harmonics increases, indicating that the energy of the echo shifts from the fundamental frequency to the 2nd and 3rd harmonics. As the PNP goes higher to 300kPa, the attenuation coefficient of sample A at the fundamental frequency, 2nd, and 3rd harmonics decreases, suggesting that the energy shifts to an

even higher harmonic. At the same time, the attenuation coefficient of sample B stays constant at fundamental frequency, decreases at 2nd harmonics, and increases at the 3rd harmonic, suggesting the energy starts to shift to the 3rd harmonic. The attenuation coefficient of sample C at fundamental frequency, 2nd and 3rd harmonics keep constant and low due to low sample concentration. The test reveals the energy shifting of the echo to the higher harmonics at PNP higher than 100 kPa, indicating the nonlinear oscillation of MBs at PNP higher than 100 kPa. Moreover, the concentration of the MBs seems to influence the energy shifting: the higher the concentration the earlier the shift to the higher harmonics occurs, in the range of the concentration consider in this study.

The pilot results of the micro-CT tests are presented in Table 1. The reference, gold nanoparticles solution, has the highest CNR per voxel at all CT operating voltages. The CNR per voxel of CACTUS MBs suspensions is below 0.1, virtually equaling the MBs at all operating voltages, suggesting that no gold or very little gold were loaded into the shell of the CACTUS MBs. The gold loaded capsules suspension has higher CNR per voxel than the capsule supernatant (the surrounding environment of capsules) and the MBs suspension, implying that the gold nanoparticles were loaded into the capsules. However, it is not clear whether the gold nanoparticles were loaded in the core of the MBs or in the MBs shell. The expected sharp increase of CNR per voxel at the k-edge of gold did not appear. We believe that is because even at our highest operating voltage of 90kV, the percentage of the photons with energy higher than 80.7 keV is still low. Introduction of a high-pass metal filter could increase the percentage of high energy photon. On the other hand, the metal filter will reduce the total number of the photons which would increase the noise of the images. Since same current was applied on every CT test, less X-ray photons reached the sensors when the CT was operated at low voltage. Therefore, it might be worth performing additional calibration tests to adjust the operating currents to make sure that the numbers of the photons that reach the sensor at every operating voltage are the same.

## **Conclusion**

In this study, the CACTUS MBs and gold loaded capsules were fabricated as potential candidates for dual modal contrast agent. The characterization revealed that gold loaded capsule is a promising initial step. Nevertheless, the method to convert back liquid-core capsules to gas-core MBs needs to be established.

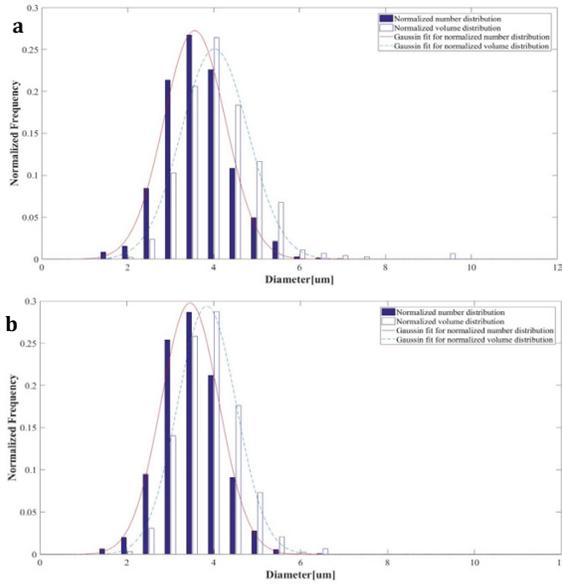


**Figure.1** The number and volume distribution of MBs (a) and CACTUS (b) with their Gaussian fit

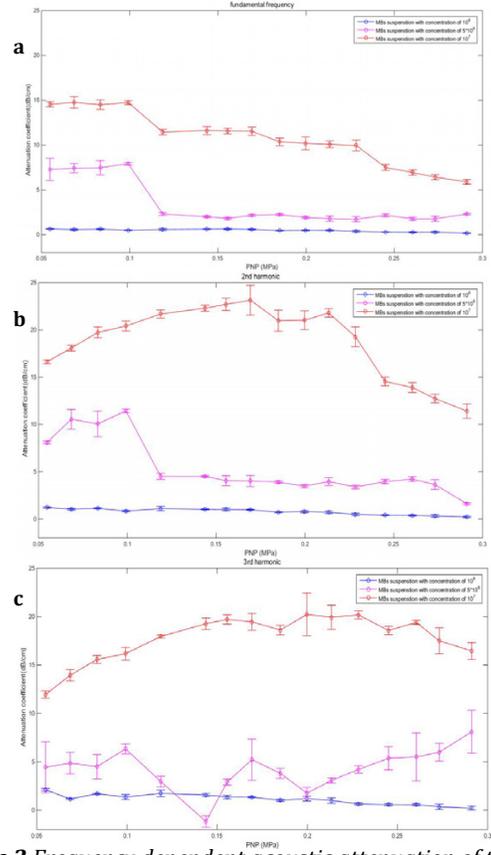


**Figure.2** Frequency dependent acoustic attenuation of the MBs at the fundamental (a), 2<sup>nd</sup> (b) and 3<sup>rd</sup> (c) harmonic

**Table 1** Mass attenuation and CNR of samples

Operating Voltage(kV)	Sample name	Mean mass attenuation of sample (HU)	Sample SD(HU)	Mean mass attenuation of water (HU)	Water SD (HU)	CNR per voxel
50	MBs	1655,7	116,2	1647.9	116,3	0,068
	CACTUS MBs	1656.0	116,2	1647.9	116,3	0,069
	Gold loaded Capsule	1705,7	125,7	1631.5	113.8	0,618
	Capsule Supernatant	1665,3	119,6	1631.5	113.8	0,289
	Gold nanoparticles solution	1807,9	149,3	1647.9	116,3	1,195
70	MBs	1088.0	72,7	1079.3	73.9	0,071
	CACTUS MBs	1086,8	72,7	1079.3	73.9	0,055
	Gold loaded Capsule	1120,1	79,7	1068.7	72.3	0,676
	Capsule Supernatant	1089,5	74,7	1068.7	72.3	0,283
	Gold nanoparticles solution	1207,9	102,3	1079.3	73.9	1,398
90	MBs	782,4	56,6	774.5	57.9	0,112
	CACTUS MBs	781,5	56,7	774.5	57.9	0,098
	Gold loaded Capsule	808,8	61,8	769.2	58.1	0,66
	Capsule Supernatant	778,9	59,7	769.2	58,1	0,165
	Gold nanoparticles solution	877,6	80,5	774.5	57.9	1,443

# A versatile and robust microfluidic device for simple or multiple emulsion production

*E. Teston, V. Hingot, V. Faugeras, C. Errico, M. Tanter, O. Couture*

The recent development of microfluidic devices lead to the optimization of many techniques for microdroplet production. Advances on both theoretical and practical aspects of emulsion preparation yielded in the possibility to realize kilo-scale production of microdroplets with a low dispersity (Shang, Chem. Rev. 2017). However, there is still a lack of versatility of production systems and so far, none was shown to be used for both simple droplets or multiple emulsions production, with biocompatible size ( $< 5\text{-}7\ \mu\text{m}$ ), a low polydispersity as well as reasonable production rates. Furthermore, the majority of microfluidic multiple emulsion production systems are based on the fine tuning of flowing fluid parameters, and hence hydrodynamic forces, to break drops (Christopher, J. Phys. D: Appl. Phys. 2007). Some innovations using rupture of confinement introduced microfluidic devices that allow the control of droplet formation through geometrical optimisation and less on fluid properties or flow rates, leading to the possibility of large-scale production (Vladislavjevic, Microfluid. Nanofluid. 2012). Here, we present a long lifetime versatile microchip for both simple and multiple emulsion production. This system based on microchannel emulsification was designed to produce perfluorocarbon in water (P/W) or water in perfluorocarbon in water (W/P/W) microdroplets with biocompatible sizes and  $\text{PDI} < 0,06$  for in vivo applications such as spatiotemporally-triggered drug delivery using ultrasounds (Couture, Med. Phys. 2012). This new microchip is composed of 225 microchannels separated by  $100\ \mu\text{m}$  from each other and linking two millimeter-wide channels (Figure 1).

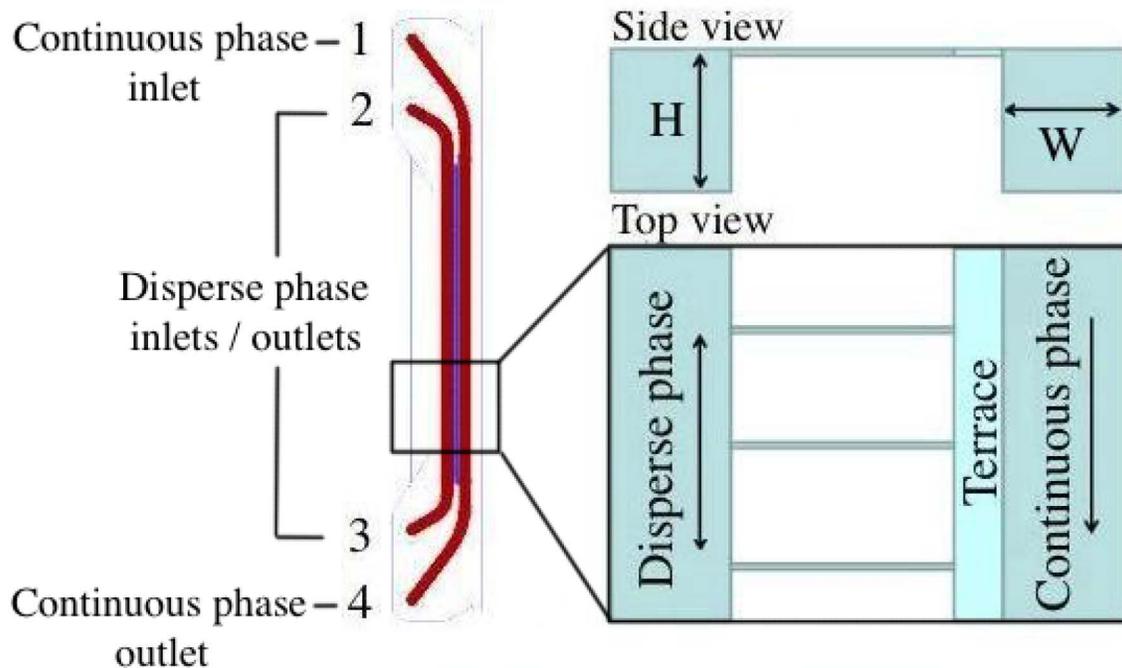


Figure 1. Schematic representation of our microfluidic device. Left: representation of millimeter-wide channels (red) and microchannels in between (blue). Continuous phase is flowing from hole number 1 to hole number 4 and disperse phase alternatively from 2 to 3 or 3 to 2. Pressures are controlled so disperse phase also goes through microchannels. Right: Side and top views of the production system. Schemes are not at scale :  $H = 0.1\ \text{mm}$  and  $W = 1\ \text{mm}$ , while microchannels and terrace height are  $0.6$  and  $0.8\ \mu\text{m}$ , respectively.

This configuration allows an increase in the production rate of microdroplets (up to 40.106 min<sup>-1</sup> for simple emulsions) and avoids obstructions to stop the production. We show that droplet production at this scale is mainly controlled by interfacial tension forces but that depending on flow rate ratio, we observe different production regimes. Thus we obtain P/W emulsions of 4.5  $\mu\text{m}$  diameter and PDI = 5.8 % (Figure 2) or W/P/W double emulsions of 3.3  $\mu\text{m}$  and PDI = 5.4 %. These characteristics are stable for different pressures applied in both disperse and continuous phases. A better understanding of droplet formation and influent factors such as velocity ratios, surfactant concentration or viscosity is supported by observations with a high-speed camera (up to 100 kHz).

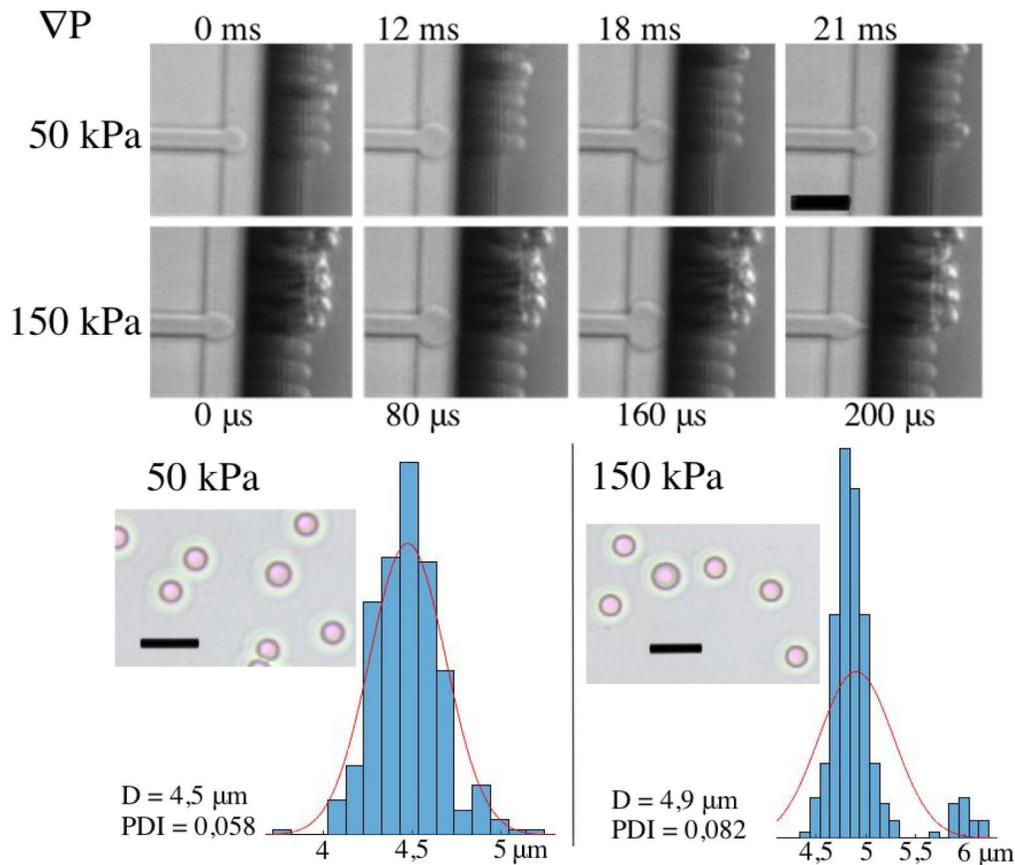


Figure 2. (Top) Perfluorohexane microdroplet formation using microchannel emulsification with different pressure drops. (Bottom) Corresponding photographs of produced microdroplets and size characterizations. Scale bars represent 10 $\mu\text{m}$

If many microfluidic devices are developed in order to enhance production rate or to lower polydispersity, none had yet offered the opportunity to produce compatible double emulsions with enough efficiency to easily consider further in vivo applications. This microchip design meets our needs to be able to use these microdroplets in theragnostics studies in small animals.

# Interplay between functionalising and stabilising lipid microbubbles for magnetic targeting

*Estelle Beguin<sup>1</sup>, Luca Bau<sup>1</sup>, Shamit Shrivastava<sup>1</sup>, Heather Nesbitt<sup>2</sup>, Anthony McHale<sup>2</sup>, John Callan<sup>2</sup>, and Eleanor Stride<sup>1</sup>*

<sup>1</sup>*Department of Engineering Science, Institute of Biomedical Engineering, University of Oxford, Oxford OX3 7DQ, United Kingdom.*

<sup>2</sup>*Biomedical Sciences Research Institute, University of Ulster, Coleraine, Northern Ireland, U.K. BT52 1SA, United Kingdom.*

Microbubbles were initially developed as contrast agents for medical ultrasound imaging. Yet, if sufficient acoustic energy is provided, microbubble oscillations can produce substantial biological effects in the surrounding tissue. Thus, there has been considerable research aimed at understanding these biological effects in order to harness them for therapeutic applications. With the development of microbubble agents for therapeutic applications, the demand for effective targeting strategies has also increased. Magnetic targeting is one approach that has been investigated for this purpose and was shown to be effective for enhancing the delivery of a variety of therapeutic molecules both in vitro and in vivo in small animal models. [1]–[4]

To facilitate magnetic targeting, previous studies have commonly incorporated superparamagnetic iron oxide nanoparticles into the microbubble coating. [5]–[7] As an advantage, this enables the imaging of microbubbles under magnetic resonance. However, modifying the microbubble coating in this way can negatively impact stability-related properties like echogenicity and clearance time in vivo. This study focuses on how functionalising phospholipid-coated microbubbles with iron oxide nanoparticles affects microbubble stability, acoustic response and magnetic trapping efficiency. The effect of nanoparticle characteristics and the means of incorporation into the bubble shell are investigated.

The results indicate that microbubble stability is significantly affected by the surface characteristics of iron oxide nanoparticles. Amongst other formulations, the loading of lipid-coated iron oxide nanoparticles into the microbubble shell during production (hydrophobic loading) was found to significantly decrease the stability of the system if the lipid used for nanoparticle coating is composed of a mixture of phospholipids such as L- $\alpha$ PC. However, when the lipid used was identical to the one composing the bubbles, DBPC in this study, the stability of the system was enhanced over a period of three-hours under flow at 37°C (Figure ). The iron loading of microbubbles and thus their magnetic response is characterised using inductively coupled plasma optical emission spectroscopy and nanoparticles are visualised through transmission electron microscopy images (Figure 2). With this method, a comparison between hydrophobic loading and external loading on existing microbubbles through avidin-biotin interactions is also provided. Finally, the effect of added nanoparticles on microbubble acoustic emissions (broadband, harmonics and ultra-harmonics) is provided through an analysis of passive cavitation detection data. Each microbubble formulation was exposed to ultrasound at 1 MHz, 0.85 MPa<sub>pk-pk</sub>, 30% DC, 100 Hz PRF and exposure duration of 30 seconds.

Investigating the addition of iron oxide nanoparticles into the shell of phospholipid microbubbles provides a deeper understanding of the interplay between functionalising microbubbles for magnetic targeting and the impact on system stability, which is ultimately relevant for enhanced efficacy in in vivo studies and beneficial for the clinical translation of this platform.

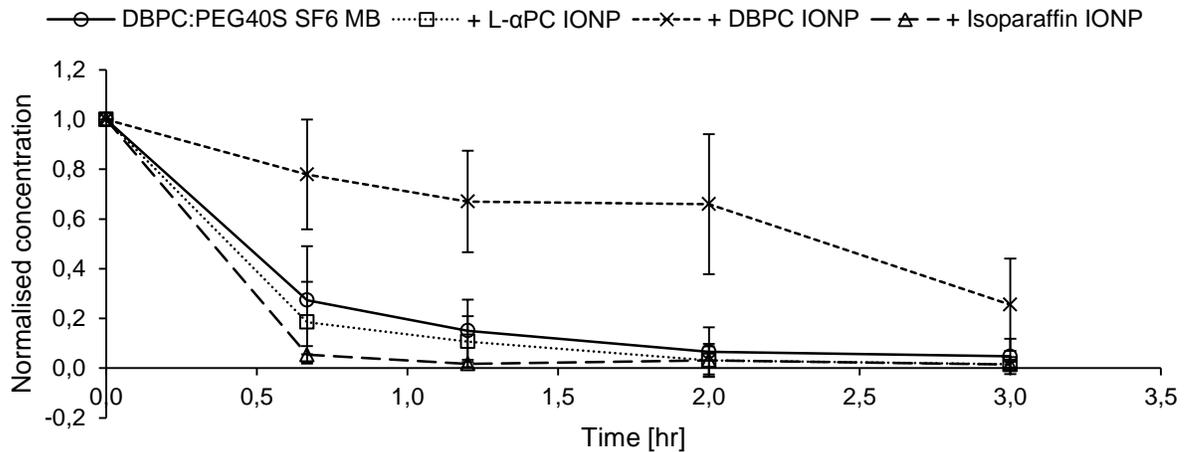


Figure 1 Normalised microbubble concentration over time determined by image analysis of optical microscope images. Microbubbles flown at 10 mL/min at 37°C for 3 hrs. Time points recorded: T = 0, 45mins, 1hr10mins, 2hrs, 3hrs, all lines between markers are used as guide to the eyes.

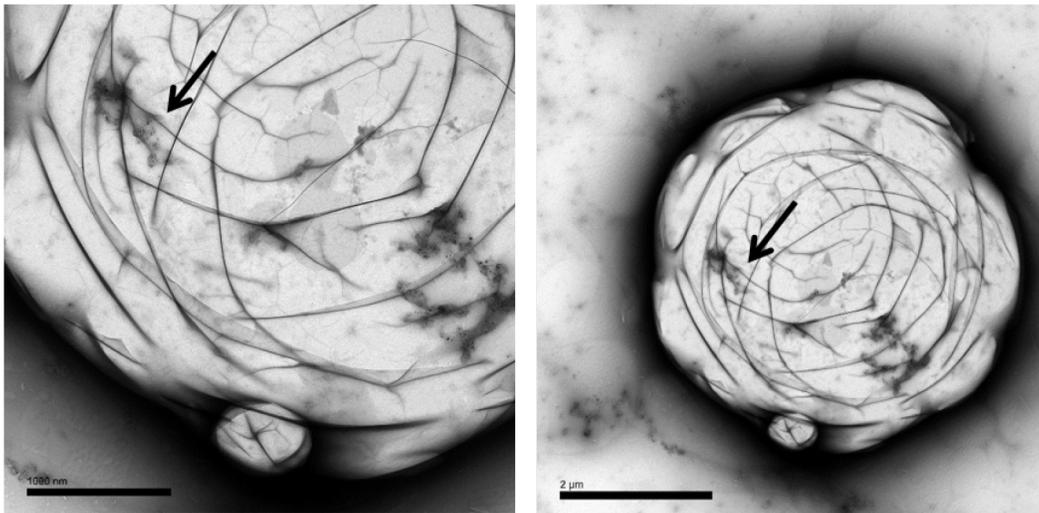


Figure 2. Transmission electron microscopy images of phospholipid microbubbles incorporating L-αPC IONP (arrow) on the microbubble shell. Stain use: 2% uranyl acetate following the method presented by [8].

## References

1. Y. Sheng et al., "Magnetically responsive microbubbles as delivery vehicles for targeted sonodynamic and antimetabolite therapy of pancreatic cancer," *J. Control. Release*, vol. 262, no. June, pp. 192–200, 2017.
2. M. de Saint Victor, D. Carugo, L. C. Barnsley, J. Owen, C.-C. Coussios, and E. Stride, "Magnetic targeting to enhance microbubble delivery in an occluded microarterial bifurcation," *Phys. Med. Biol.*, 2017.
3. E. Stride, C. Porter, A. G. Prieto, and Q. Pankhurst, "Enhancement of Microbubble Mediated Gene Delivery by Simultaneous Exposure to Ultrasonic and Magnetic Fields," *Ultrasound Med. Biol.*, vol. 35, no. 5, pp. 861–868, 2009.

4. J. Y. Lee et al., "Nanoparticle-Loaded Protein-Polymer Nanodroplets for Improved Stability and Conversion Efficiency in Ultrasound Imaging and Drug Delivery," *Adv. Mater.*, vol. 27, no. 37, pp. 5484–5492, 2015.
5. J. Owen et al., "A versatile method for the preparation of particle-loaded microbubbles for multimodality imaging and targeted drug delivery," *Drug Deliv. Transl. Res.*, 2017.
6. C. H. Fan et al., "SPIO-conjugated, doxorubicin-loaded microbubbles for concurrent MRI and focused-ultrasound enhanced brain-tumor drug delivery," *Biomaterials*, vol. 34, no. 14, pp. 3706–3715, 2013.
7. H. Mannell et al., "Targeted endothelial gene delivery by ultrasonic destruction of magnetic microbubbles carrying lentiviral vectors," *Pharm. Res.*, vol. 29, no. 5, pp. 1282–1294, 2012.
8. J. Owen and E. Stride, "Technique for the Characterization of Phospholipid Microbubbles Coatings by Transmission Electron Microscopy," *Ultrasound Med. Biol.*, vol. 41, no. 12, pp. 3253–3258, 2015.

# NSSA-Based Classification of Tissue and Adherent Microbubble Signals in a Mouse Tumor Model

*Elizabeth B. Herbst<sup>1</sup>, Shiyang Wang<sup>1</sup>, Alexander L. Klibanov<sup>1,2</sup>, F. William Mauldin Jr.<sup>1</sup>, John A. Hossack<sup>1</sup>*

<sup>1</sup>*Department of Biomedical Engineering, University of Virginia, Charlottesville, Virginia, USA;*

<sup>2</sup>*Division of Cardiovascular Medicine, University of Virginia, Charlottesville, Virginia, USA*

## Objective

Ultrasound contrast agents known as microbubbles can be targeted to disease markers on the vascular endothelium. In preclinical studies, they have shown significant potential for sensitive detection of cancer and cardiovascular disease<sup>1</sup>. Current state-of-the-art microbubble imaging techniques such as pulse inversion (PI)<sup>2</sup> or contrast pulse sequences (CPS)<sup>3</sup> rely upon the nonlinear reflections from MBs to isolate them from surrounding tissue signals. However, these methods are hampered by the presence of highly echogenic objects in tissue which produce strong reflections in both linear and nonlinear frequencies. In this study, we showed that normalized singular spectrum area (NSSA) can be used to differentiate between static tissue signal, adherent microbubble signal, and non-adherent microbubble signal in the small-vessel environment of a mouse hindlimb tumor.

## Methods

5 mice were implanted with subcutaneous adenocarcinoma tumors (MC38 cells) and administered retro-orbital bolus injections of  $2 \times 10^7$  microbubbles targeted MBs. The mouse tumors were imaged at a frame rate of 20 Hz using a programmable ultrasound system and L12-5 linear array transducer, at time points 20 s and 6 min after injection. The microbubble signals recorded 20 s post-injection were assumed to derive exclusively from non-adherent (i.e., freely circulating) microbubbles, and microbubble signals at 6 min post-injection were assumed to derive from adherent (i.e., bound) microbubbles.

After image acquisition, regions of interest (ROI) were selected in the intratumor space and in regions of bright static tissue signal (Fig. 1A). For each ROI, NSSA analysis was performed on sets of 25 sequential frames with 5x5 pixel blocks of complex data. Histograms of the NSSA from each type of signal (static tissue, adherent microbubbles, and non-adherent microbubbles) were calculated. The specificity of NSSA-based signal separation was measured using receiver operating characteristic (ROC) analysis.

## Results

NSSA-based filtering provided robust separation of tissue, adherent microbubble, and non-adherent microbubble signals (Fig. 1). ROC analysis showed that NSSA-based filtering methods differentiated adherent and non-adherent microbubble signals with an area under the curve (AUC) of 0.895. For separation of adherent MBs and tissue, the calculated AUC was 0.999. These results

are believed to be an improvement over existing methods which are reliant on “slow-time” low-pass filtering, which achieves suppression of free microbubble signal by approximately 10 dB<sup>4,5</sup>.

## Conclusions

Results from this study showed that NSSA-based filtering can provide highly specific differentiation of ultrasound signals deriving from static tissue, molecularly bound microbubbles, and circulating microbubbles. The ability to differentiate between these signals with high accuracy can allow for easier interpretation of molecular images, thus improving the reliability of disease diagnosis and monitoring. These improvements in diagnostic capability can help to encourage more rapid uptake of molecular imaging techniques in a clinical setting.

## References

1. Bachawal, et al, *Cancer Res.* **73**, 6 (2013).
2. Shen, et al, *J Med Ultrasound.* **13**, 1 (2005).
3. Phillips, *IEEE Int Ultrason Symp.* (2001).
4. Hu, et al, *IEEE UFFC.* (2010).
5. Zhao, et al, *Phys Med Biol.* **52**, 8 (2007).

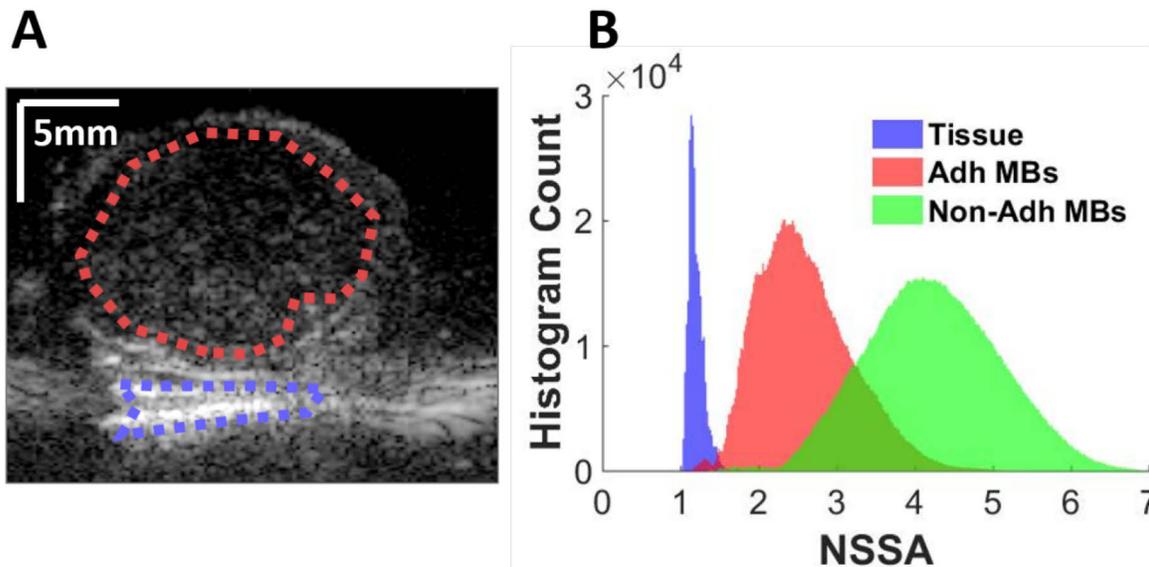


**Figure 1. NSSA-based differentiation between tissue, adherent microbubble, and free-flowing microbubble signal. (A)** Representative image of a mouse hindlimb tumor. The blue dashed line delineates a region of bright static tissue, while the red dashed line delineates a section of intratumoral space where microbubbles are present. **(B)** Histogram of NSSA signals derived from each region of interest. The blue peak shows the NSSA values derived from tissue signal (blue dashed line in (A)). The green and red peaks are the NSSA signals of intratumoral space (red dashed line in (A)) taken at 20s and 6 min after microbubble injection, respectively. Notice that the blue tissue signals and red adherent microbubble signals are clearly distinguishable using a NSSA cutoff of approximately 1.6.

# Prostate cancer localization through convective-dispersion estimation in three-dimensional contrast ultrasound

*R. R. Wildeboer<sup>1</sup>, R. J. G. van Sloun<sup>1</sup>, S. G. Schalk<sup>1,2</sup>, C. K. Mannaerts<sup>2</sup>,  
J. C. van der Linden<sup>3</sup>, P. Huang<sup>4</sup>, H. Wijkstra<sup>1,2</sup>, M. Misch<sup>1</sup>*

<sup>1</sup> *Department of Electrical Engineering, Eindhoven University of Technology, The Netherlands*

<sup>2</sup> *Department of Urology, Academic Medical Centre, University of Amsterdam, The Netherlands*

<sup>3</sup> *Department of Pathology / DNA laboratories, Jeroen Bosch Hospital, 's-Hertogenbosch, The Netherlands*

<sup>4</sup> *Second Affiliated Hospital of Zhejiang University, Hangzhou, China*

## Introduction

Detection and localization of prostate cancer (PCa) is still a challenge in today's clinical practice. Despite being the most occurring type of malignancy aside skin cancers in western men, PCa diagnosis still relies on systematic biopsy [1]. A shift towards imaging-guided targeted biopsy would reduce the risk of underdiagnosis and overtreatment, whilst alleviating the burden on patients with no or insignificant PCa [2]. However, sufficiently reliable imaging is not only of paramount importance for reducing the risks associated with the systematic biopsy procedure, it is also essential for follow-up in active surveillance protocols [3] and for selection and monitoring of focal treatment [4].

Dynamic contrast-enhanced ultrasound (DCE-US) is a promising tool in PCa diagnosis that enables investigation of the vascularity. As significant PCa exceeding a size of 1 mm<sup>3</sup> requires neovascularization and angiogenesis [5], several DCE-US analysis methods have been developed to capture the differences between benign and malignant (micro)vascular architectures. These methods were initially implemented in two dimensions (2D), quantifying dispersive effects in the contrast concentration kinetics at each pixel of the DCE-US image by e.g. model-based fitting [6] or similarity analysis [7]. As three-dimensional (3D) imaging became available, these techniques were expanded to three dimensions [8].

A 3D approach does not only prevent us from missing tumours outside the 2D imaging plane while reducing the number of bolus injections required, it also relaxes some major constraints of 2D modelling. Whereas direct 2D estimation of dispersion and velocity through system identification required strong assumptions on out-of-plane directionality [9], 3D data can be completely modelled by the convective-dispersion equation. In this work, we aim at estimating convective dispersion and velocity in a 3D DCE-US video by solving the least-squares formulation of the convection-dispersion equation.

## Materials & Methods

In this analysis, we take a macroscopic view of the concentration kinetics of contrast agents spreading through the prostate. To this end, we consider the concentration  $C$  in  $x$ ,  $y$ ,  $z$ , and  $t$  to be governed by the convective-dispersion equation [10],

$$\partial_t C = \begin{bmatrix} \partial_x \\ \partial_y \\ \partial_z \end{bmatrix} \cdot \begin{bmatrix} D_{xx} & D_{xy} & D_{xz} \\ D_{xy} & D_{yy} & D_{yz} \\ D_{xz} & D_{yz} & D_{zz} \end{bmatrix} \begin{bmatrix} \partial_x C \\ \partial_y C \\ \partial_z C \end{bmatrix} - \begin{bmatrix} v_x \\ v_y \\ v_z \end{bmatrix} \cdot \begin{bmatrix} \partial_x C \\ \partial_y C \\ \partial_z C \end{bmatrix}, \quad (1)$$

where the D- and v-elements are coefficients of dispersion and velocity, respectively.

To avoid high-frequency noise amplification during the computation of derivatives, we adopt an approach in which the concentration gradients are computed through convolution with four-dimensional Gaussian derivatives with a standard deviation  $\sigma$  and  $\sigma_t$  in space and time, respectively [11].

Assuming the D-coefficients in the dispersion tensor and the v-coefficients in the velocity vector to be locally constant, Equation (1) can be formulated as a linear least-squares problem. To avoid issues with ill-conditioning, we add an  $l_2$ -norm regularization term to the problem with a regularization parameter  $n\lambda$ , with  $n$  the number of voxels in the analysis.

We successively perform the regularized minimization in a moving spherical kernel with a diameter of 7 voxels,  $\sigma = 1.5$  mm (isotropic) and  $\sigma_t = \Delta t$ . The approach was implemented in an elastic-net fashion using the QR factorization procedure in Matlab™ (Mathworks, Natick, MA, USA) with a regularization parameter,  $\lambda$ , of 0.05. Convolutions were efficiently computed in the frequency domain using the fast Fourier transform. At each voxel, we finally quantify the convective dispersion ( $D_{ADC}$ ) as the magnitude of trace of the dispersion tensor, similar to the apparent diffusion coefficient in diffusion-weighted MRI [12]. As a measure for the velocity, we take the magnitude of the estimated velocity vector. Hence, we define:

$$D_{ADC} = \left| \frac{1}{3}(D_{xx} + D_{yy} + D_{zz}) \right| \quad \text{and} \quad v = \sqrt{v_x^2 + v_y^2 + v_z^2}. \quad (2)$$

The diagnostic performance of  $D_{ADC}$  and  $v$  for the localization of PCa is assessed in six patients that underwent a two-minute 3D DCE-US recording prior to radical prostatectomy at the Second Affiliated Hospital of Zhejiang University (Hangzhou, China). The scanning procedure comprised a 2.4 mL SonoVue® (Bracco, Milan, Italy) bolus injection and a DCE-US acquisition with a RIC9-5 probe on a LOGIQ E9 scanner (GE HealthCare, Wauwasota, WI, USA). Subsequently, the data was spatially downsampled and linearized to a volumetric video with cubic 0.75-mm sized voxels and a frame rate of ~0.25 Hz. As a reference standard, the radical prostatectomy specimens were histopathologically examined, 3D reconstructed [13], and registered to the prostate [14]. Voxels from benign and malignant tissue, excluding those in a 3.6-mm error margin from the region boundaries, were included in a Receiver Operating Characteristic (ROC) curve analysis.

## Results

Figure 1 depicts the result of the convective-dispersion analysis, showing an example case of the parametric maps of  $D_{ADC}$  and  $v$ , along with the corresponding histopathologic ground truth. The ROC curve analysis yielded areas under the curve of 0.71 and 0.79 for  $D_{ADC}$  and  $v$ , respectively, over the entire set of patients.

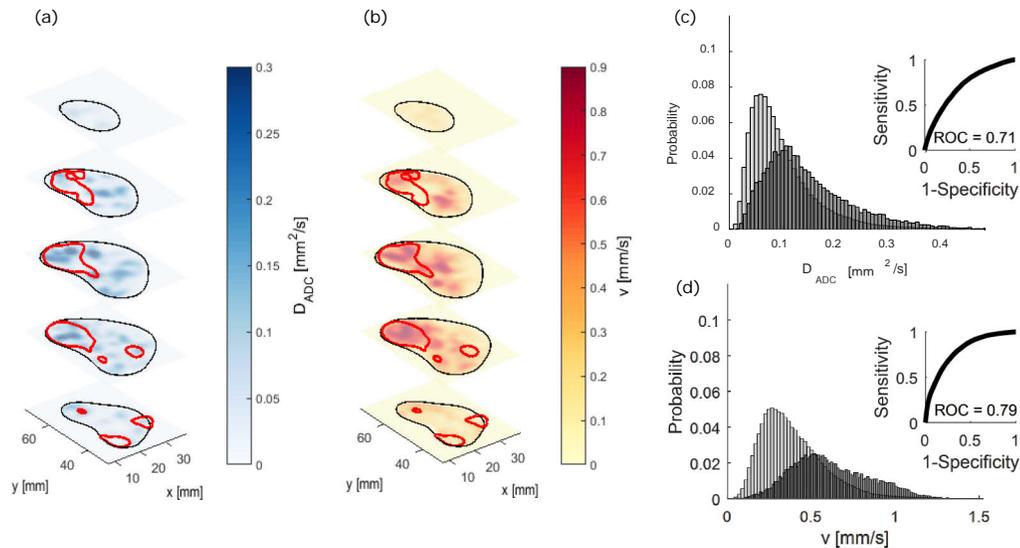


FIG 1. Example of the parametric maps of (a)  $D_{ADC}$  and (b)  $v$ , with histopathologically-confirmed malignancy delineated in red, and the histograms of (c)  $D_{ADC}$  and (d)  $v$  visualizing the PCa classification performance.

## Discussion and Conclusion

In this work, we estimated the  $D_{ADC}$  and  $v$  by solving the regularized least-squares problem of the convective dispersion equation. Despite the limited number of patients included, ROC curve analysis reveals the potential of these parameters as markers for the localization of PCa. In contrast to the previous parameters related to dispersion [6, 7, 15],  $D_{ADC}$  seems to increase in malignant tissue. An explanation for this might be that  $D_{ADC}$  includes directional effects rather than the point-to-point dispersion of quantified in previous work. This effect, as well as the feasibility of multiscale analysis, effective combination of parameters, and index-tumour detection, remains to be tested in future work.

## Acknowledgements

This work was performed in the framework of the IMPULS2-program within the Eindhoven University of Technology in collaboration with Philips. It was also supported by an unrestricted grant from the Dutch Cancer Society (#UVA2013-5941) and the European Research Council Starting Grant (#280209).

## References

1. Mottet N, Bellmunt J, Bolla M, et al. (2017) EAU-ESTRO-SIOG Guidelines on Prostate Cancer. Part 1: Screening, Diagnosis, and Local Treatment with Curative Intent. *Eur Urol* 71:618–629. doi: 10.1016/j.eururo.2016.08.003
2. van Hove A, Savoie P-H, Maurin C, et al. (2014) Comparison of image-guided targeted biopsies versus systematic randomized biopsies in the detection of prostate cancer: a systematic literature review of well-designed studies. *World J Urol* 32:847–858.
3. Dall’Era MA, Albertsen PC, Bangma C, et al. (2012) Active Surveillance for Prostate Cancer: A Systematic Review of the Literature. *Eur Urol* 62:976–983. doi: <https://doi.org/10.1016/j.eururo.2012.05.072>
4. Barret E, Durand M (2015) Technical Aspects of Focal Therapy in Localized Prostate Cancer. *Tech Asp Focal Ther Localized Prostate Cancer*. doi: 10.1007/978-2-8178-0484-2

5. Brawer MK (1996) Quantitative microvessel density: a staging and prognostic marker for human prostatic carcinoma. *Cancer* 78:345–349.
6. Kuenen MPJ, Mischi M, Wijkstra H (2011) Contrast-ultrasound diffusion imaging for localization of prostate cancer. *IEEE Trans Med Imaging* 30:1493–1502. doi: 10.1109/TMI.2011.2125981
7. Mischi M, Kuenen MPJ, Wijkstra H (2012) Angiogenesis imaging by spatiotemporal analysis of ultrasound contrast agent dispersion kinetics. *IEEE Trans Ultrason Ferroelectr Freq Control* 59:621–629. doi: 10.1109/TUFFC.2012.2241
8. Schalk SG, Demi L, Smeenge M, et al. (2015) 4-D Spatiotemporal Analysis of Ultrasound Contrast Agent Dispersion for Prostate Cancer Localization: A Feasibility Study. *IEEE Trans Ultrason Ferroelectr Freq Control* 62:839–851.
9. van Sloun RJG, Demi L, Postema AW, et al. (2017) Ultrasound-contrast-agent dispersion and velocity imaging for prostate cancer localization. *Med Image Anal* 35:610–619. doi: <http://dx.doi.org/10.1016/j.media.2016.09.010>
10. Ewing RE, Wang H (2001) A summary of numerical methods for time-dependent advection-dominated partial differential equations. *J Comput Appl Math* 128:423–445.
11. Blom J, Romeny BM te. H, Bel A, Koenderink JJ (1993) Spatial Derivatives and the Propagation of Noise in Gaussian Scale Space. *J Vis Commun Image Represent* 4:1–13. doi: <http://dx.doi.org/10.1006/jvci.1993.1001>
12. Basser PJ, Mattiello J, LeBihan D (1994) MR diffusion tensor spectroscopy and imaging. *Biophys J* 66:259–267.
13. Wildeboer RR, Schalk SG, Demi L, et al. (2017) Three-dimensional histopathological reconstruction as a reliable ground truth for prostate cancer studies. *Biomed Phys Eng Express* 3:35014. doi: 10.1088/2057-1976/aa7073
14. Schalk SG, Postema A, Saidov TA, et al. (2016) 3D surface-based registration of ultrasound and histology in prostate cancer imaging. *Comput Med Imaging Graph* 47:29–39. doi: <http://dx.doi.org/10.1016/j.compmedimag.2015.11.001>
15. van Sloun RJG, Demi L, Postema AW, et al. (2017) Entropy of ultrasound-contrast-agent velocity fields for angiogenesis imaging in prostate cancer. *IEEE Trans Med Imaging* 36:826–837.

# Dynamics and vaporization threshold of bubble/droplet system within a nonlinear elastic shell during ADV: a model

***Thomas Lacour<sup>a)</sup>, Tony Valier-Brasier and François Coulouvrat***

*Sorbonne Universités, UPMC Université Paris 06, CNRS UMR 7190, Institut Jean Le Rond  
d'Alembert, F-75005 Paris, France*

*<sup>a)</sup> thomas.lacour@upmc.fr*

Nanodroplets have great, promising medical applications such as contrast imaging, embolotherapy or targeted drug delivery. Their functions can be mechanically activated by means of focused ultrasound inducing a phase change of the inner liquid known as acoustic droplet vaporization (ADV) process. In this context, a four-phases (vapor+liquid+shell+surrounding environment) model of ADV is proposed. Attention is especially devoted to the mechanical properties of the encapsulating shell, incorporating the well-known strain-softening behavior of Mooney-Rivlin material adapted to very large deformations of soft, nearly incompressible materials.

Various responses to ultrasound excitation are illustrated, depending on linear and nonlinear mechanical shell properties and acoustical excitation parameters. Different classes of ADV outcomes are exhibited, and a relevant threshold ensuring complete vaporization is defined. The dependence of this threshold with acoustical, geometrical and mechanical parameters is also provided.

# Quantitative Contrast-Enhanced Ultrasound Imaging using a fluid dynamic model

*Baudouin Denis de Senneville<sup>1</sup>, Anthony Novell<sup>2</sup>, Chloé Arthuis<sup>2,3</sup>, Vanda Mendes<sup>2,3</sup>, Paul-Armand Dujardin<sup>2,4</sup>, Frédéric Pataf<sup>2,4</sup>, Ayache Bouakaz<sup>2</sup>, Jean-Michel Escoffre<sup>2</sup>, Franck Perrotin<sup>2,3</sup>*

<sup>1</sup>*Institut de Mathématiques de Bordeaux, UMR 5251 CNRS/University of Bordeaux/INRIA, Talence, France*

<sup>2</sup>*Inserm UMR 930, Université François-Rabelais de Tours, Tours, France*

<sup>3</sup>*Department of Obstetrics, Gynecology and Fetal Medicine, University Hospital of Tours, Tours, France*

<sup>4</sup>*Inserm CIC 1415, CHRU de Tours, Tours, France*

## Rationale and aim

Contrast-enhanced ultrasound (CEUS) is a non-invasive imaging technique extensively used for blood perfusion imaging of various organs [1]. This modality is based on the acoustic detection of gas-filled microbubble contrast agents used as intravascular flow tracers. Recent efforts aim at quantifying parameters related to the enhancement in the vascular compartment using time-intensity curve (TIC), and at using these latter as indicators for several pathological conditions [2]. However, this quantification is mainly hampered by two reasons: first, the quantification intrinsically solely relies on temporal intensity variation, the explicit spatial transport of the contrast agent being left out. Second, the exact relationship between the acquired US-signal and the local microbubble concentration is hardly accessible. In this study, we introduce the use of a fluid dynamic model for the analysis of dynamic CEUS (DCEUS) [3], in order to circumvent the two above-mentioned limitations. A new kinetic analysis is proposed in order to quantify the velocity amplitude of the bolus arrival. The efficiency of proposed methodology is evaluated in-vivo, for the classification of placental insufficiency (control versus ligation) of pregnant rats from DCEUS.

## Material & Methods

Implemented fluid dynamic model – Physiological activity and motion of the ultrasound probe were first compensated on the DCEUS images, since the latter may hamper the estimation of the apparent microbubble transport. Subsequently, the microbubble transport (noted  $\vec{V}$ ) was estimated using the following transport equation:  $I_t + \vec{V} \cdot \vec{\nabla} I = 0$  ( $I$  denotes the grey level intensity on DCEUS images and  $I_t$  the partial temporal derivative of  $I$ ). The left part of this equation is composed by a transient term ( $I_t$ ) and a transport term ( $\vec{V} \cdot \vec{\nabla} I$ ), which stand for any temporal and spatial grey intensity variations, respectively. The estimated transport field  $\vec{V}$  thus accounts simultaneously for spatio-temporal grey level intensity variations occurred during the dynamic imaging sequence. Spatio-temporal microbubble transport values were then averaged to simplify all the pixel-wise transport data down to a single averaged value (noted  $\gamma$ ).

CEUS examination – 20 pregnant rats (11 rats with a ligation of the uterine horn pedicle, 9 control rats) were individually placed under gaseous anesthesia (Aerrane<sup>®</sup>) on a thermostatically

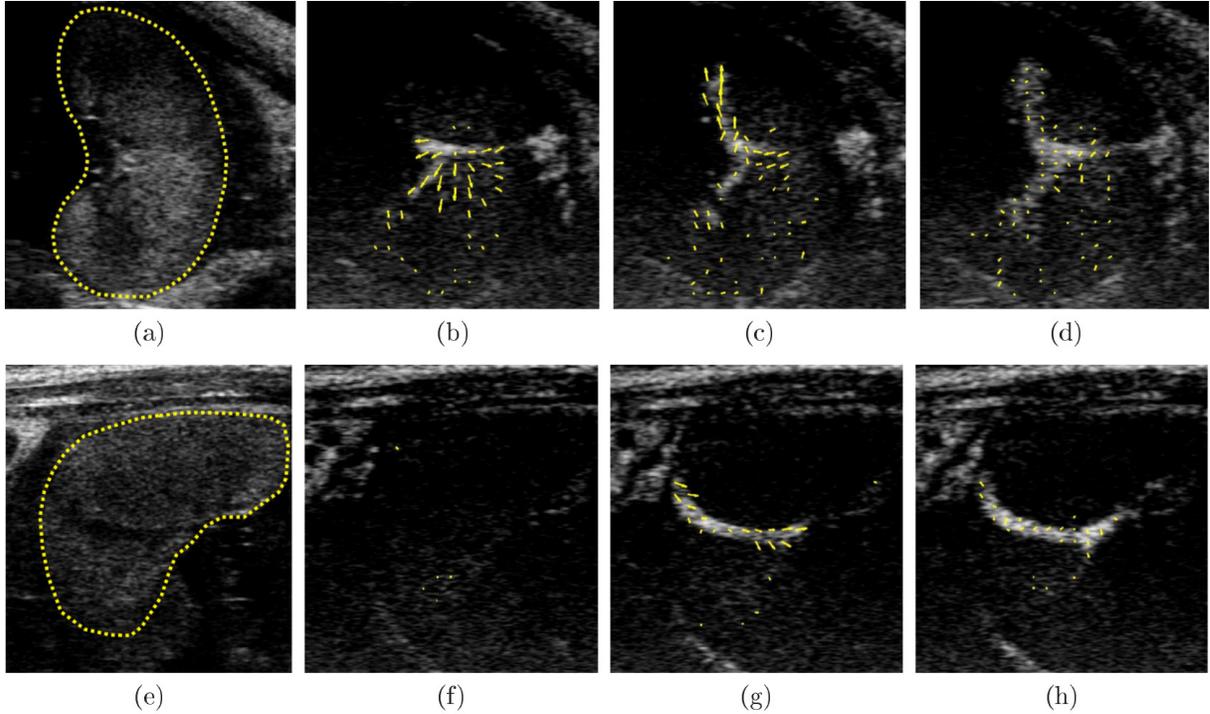
controlled pad and their abdomens were shaved before CEUS examination on the nineteenth day of gestation. A 24-gauge catheter was placed in a tail vein to inject Definity<sup>®</sup> contrast microbubbles. Ultrasound B-scans were used to image fetal-placental unit in cross-section. A bolus of 200  $\mu$ L of contrast agent (0.5 mL/kg) was intravenously injected. Subsequently, a video clip of 150 s was recorded at 10 frames per second (pixel size = 0.035 $\times$ 0.035 mm<sup>2</sup>) to investigate the utero-placental perfusion.

CEUS analysis – After image acquisition, utero-placental perfusion was quantitatively analyzed both using our methodology and using the existing TIC-based approach. The four following parameters were extracted from the TIC: peak enhancement (PE), wash-in rate (WiR), time to peak (TTP), area under the curve during wash-in (WiAUC), using the CEUS analysis software Vevo-CQ<sup>™</sup>. Considering each indicator as a classification criterion, the performance of a binary classifier system was assessed using a “receiver operating characteristic” (ROC) curve. The area under the ROC curve (AUROC) was subsequently computed: while a binary classifier acts like a completely random guess for AUROC = 0.5, the best possible prediction method would yield to a value of 1.

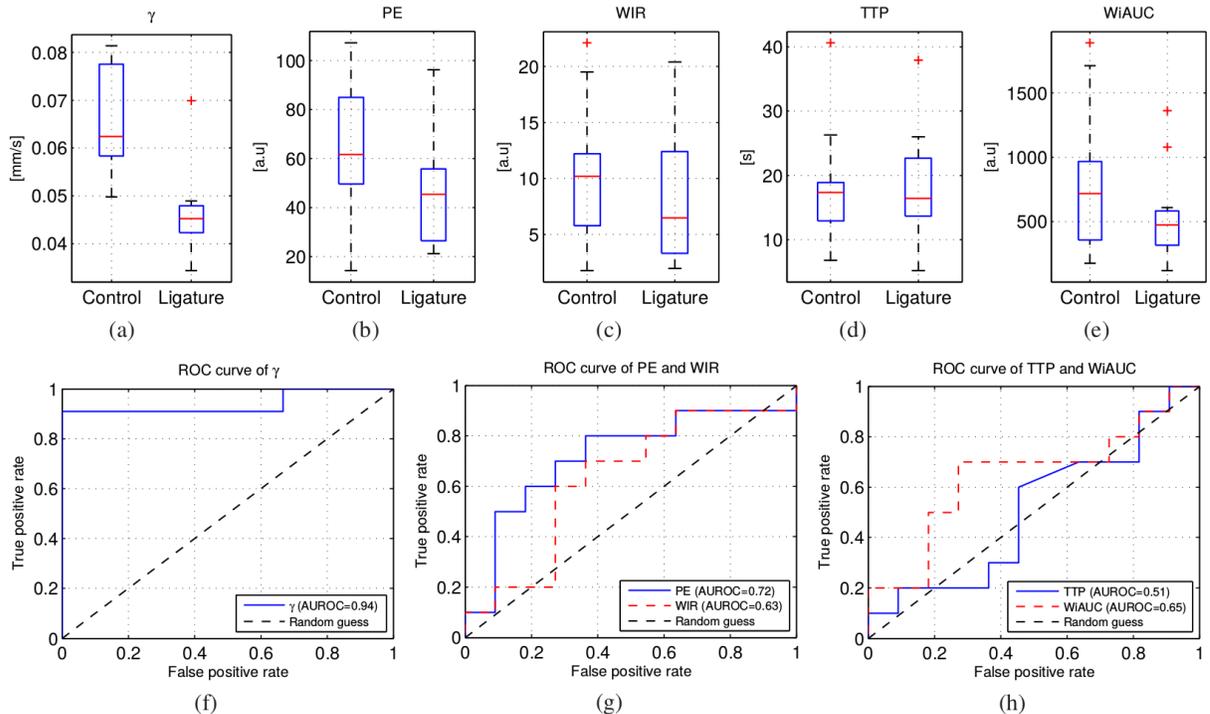
## Results

Figure 1 reports typical microbubble transport fields obtained from two dynamic contrast-enhanced experiments (one clip was selected in the control and one in the ligature population, respectively). The estimated microbubble transports are visually larger for the control population (Figs. 1b-d) as compared to the ligature population (Figs. 1f-h).

The spatio-temporally averaged microbubble transport amplitude (i.e., coefficient  $\gamma$ ) was significantly higher (p-value =  $1.1 \times 10^{-3}$ ) in the control group than in the ligature group (Fig. 2a). The associated AUROC, displayed in Fig. 2f, was equal to 0.94. On the other hand, none of tested TIC-based parameters led to a significant difference between control and ligature populations (p-values obtained using PE, WiR, TTP and WiAUC were equal to 0.098, 0.348, 0.972 and 0.285, respectively), as shown in Figures 2b-e. The best achievable AUROC was obtained using PE (AUROC=0.72), as shown in Figures 2g and 2h.



**Figure 1: Example of microbubble transport estimates from the DCEUS of two rats using the proposed fluid dynamic approach.** The first and the second rows display results associated to a control and a ligature rats, respectively. The first column displays a B-mode image with a manually drawn mask superimposed (yellow dashed line) underlying the placenta. The 2<sup>nd</sup>, 3<sup>rd</sup> and 4<sup>th</sup> columns display DCEUS images acquired 10 s, 15 s and 20 s after the determined microbubble arrival in the placenta, respectively. The corresponding transport field estimates are superimposed using yellow arrows.



**Figure 2: Assessment of proposed and TIC-based approaches for the classification of the two rat populations (i.e control and ligature).** (a): boxplots of overall microbubbles velocities ( $\gamma$ ) estimated over each rat populations using the fluid dynamic approach, (b-e): distributions of PE, WiR, TTP and WiAUC estimated over the placenta for the two rat populations using the existing TIC-based approach. (f): ROC curve obtained using  $\gamma$ , (g): ROC curves obtained using PE and WiR, (h): ROC curves obtained using TTP and WiAUC.

## Conclusions

This study introduces the use of a fluid dynamic model for the analysis of DCEUS. A complete kinetic analysis was proposed in order to quantify the velocity amplitude of the bolus arrival. The proposed classification criterion  $\gamma$ , estimated from DCEUS echography, was demonstrated to be a good binary classification criterion for ligature/non-ligature rat placentas. In particular, it outperformed TIC-based methods, which provided best results using the parameter PE (AUROC=0.72, as shown in Fig. 2g and 2h), but remained however well below our fluid dynamic approach (Fig. 2f). Our methodology opens great perspectives for the evaluation of the proposed technique for the clinical diagnostic of obstetrical disorders.

**Acknowledgement** – This work was supported by grants from Inserm (FP, AB), the University F. Rabelais of Tours (FP, AB), the AERO PERINAT Association (FP), the French Society of Perinatal Medicine (FP, CA) and the Laboratory of Excellence TRAIL ANR-10-LABX-57 (BDDS). This study has also been carried out with the financial support of the French National Research Agency (ANR) in the frame of the “Investments for the future” Programme IdEx Bordeaux-CPU (ANR-10-IDEX-03-02) (BDDS).

## References

1. Jakobsen JA (2001) “Ultrasound contrast agents: Clinical applications,” *Eur. Radiol.*, 11(8):1329-1337.
2. Tranquart F, Mercier L, Frinking P, Gaud E, Arditi M (2012) *Perfusion quantification in contrast-enhanced ultrasound (CEUS)–ready for research projects and routine clinical use*, *Ultraschall Med.-Eur. J. Ultrasound*, 33:31-38.
3. Denis de Senneville B, Novell A, Arthuis C, Mendes V, Dujardin PA, Patat F, Bouakaz A, Escoffre JM, Perrotin F (2017) *Development of a fluid dynamic model for quantitative contrast-enhanced ultrasound imaging*, *IEEE Transactions on Medical Imaging*, In press.

# Evaluation of Accuracy of Passive Acoustic Mapping for Cavitation Monitoring in Therapeutic Ultrasound

*Pilsu Kim<sup>1</sup>, Sua Bae<sup>1</sup>, Kangsik Kim<sup>2</sup>, and Tai-kyong Song<sup>1</sup>*

<sup>1</sup>*Department of Electronic Engineering, Sogang University, Seoul, Republic of Korea*

<sup>2</sup>*Samsung Medison Co., Ltd, Seoul, Republic of Korea*

## **Introduction**

Recently, the importance of cavitation monitoring has been increased in therapeutic ultrasound applications. In high intensity focused ultrasound (HIFU), acoustic cavitation should be monitored and controlled to prevent significant thermal and mechanical damage on surrounding normal tissue for safety of treatment [1]. In addition, cavitation mapping is required to confirm the location of microbubbles and to control the exposure of focused ultrasound in blood-brain barrier opening application [2-3]. Passive acoustic mapping (PAM) technique has been widely utilized in order to map the location of cavitation. Several researches have demonstrated the feasibility and clinical acceptance of PAM technique by comparing between the estimated location by PAM and the location of thermal lesion generated by HIFU [1, 4]. However, these studies indirectly confirmed the accuracy of the PAM (i.e., not the location of cavitation bubble but the location of thermal lesion was used as a reference). In this study, we verify that PAM technique can temporally and spatially monitor cavitation bubbles by comparing the results of PAM and high-speed shadowgraphic imaging (HSSI).

## **Methods**

To evaluate the accuracy of PAM technique, we simultaneously conduct HSSI and PAM. In addition, single-element passive cavitation detector was used to classify the cavitation occurrence. All systems were synchronized by the same trigger signal which generated by the digital pulse generator for spatial and temporal analysis of cavitation monitoring results. Polyacrylamide phantom was insonated by a 1.1-MHz ultrasound transducer (H-101, Sonic concept, USA) to generate cavitation bubbles. HSSI was recorded by high-speed camera (Phantom V2511, Vision Research, USA) at 50,000 frames per second with synchronous 100-ns laser pulses which provide illumination and determine the effective temporal resolution of HSSI. At the same time, ultrasound data was acquired for 100 ms by an ultrasound research system (E-cube 12R, Alpinion Medical System, Republic of Korea) with a 7.5-MHz linear array. PAM results were reconstructed by off-line processing with general-purpose graphics processing units (GeForce GTX 1060, NVIDIA) and MATLAB (R2017a, MathWorks, USA). We applied the coherence factor algorithm to PAM reconstruction to eliminate background noise and to enhance axial resolution.

## Results/Discussion

Figure 1 shows the captured images by HSSI and the reconstructed maps by PAM when (a) before and (b) after occurrence of cavitation. Coherence-factor-based PAM method can effectively suppress the background noise and enhance the contrast and spatial resolution. PAM results well agreed with HSSI; the spatial and temporal discrepancy were 0.4 mm and  $50\mu\text{s}$ , respectively. We demonstrated that PAM technique can provide enough spatial and temporal accuracy for cavitation occurrence to be used for therapeutic ultrasound monitoring.

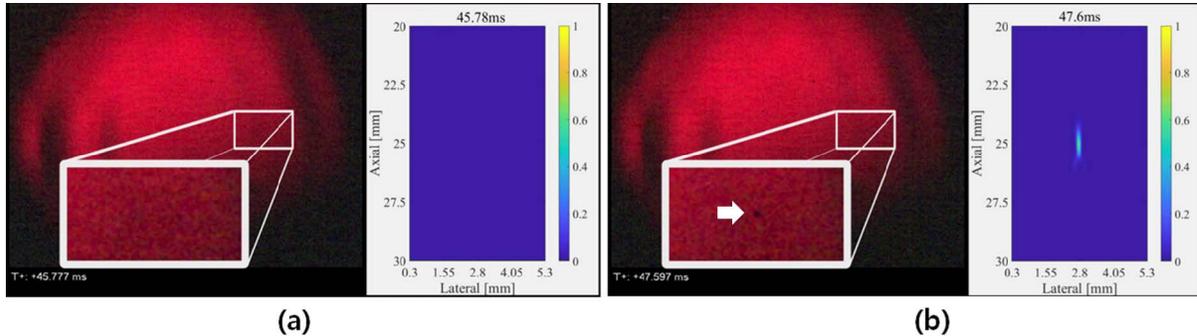


Figure 1. Cavitation images detected by HSSI and PAM (a) before occurrence of cavitation (b) after occurrence of cavitation.

## References

1. Jensen, Carl R., et al. "Spatiotemporal monitoring of high-intensity focused ultrasound therapy with passive acoustic mapping." *Radiology* 262.1 (2012): 252-261.
2. Arvanitis, Costas D., et al. "Passive Acoustic Mapping with the Angular Spectrum Method." *IEEE transactions on medical imaging* 36.4 (2017): 983-993.
3. Jones, Ryan M., Meaghan A. O'Reilly, and Kullervo Hynynen. "Transcranial passive acoustic mapping with hemispherical sparse arrays using CT-based skull-specific aberration corrections: a simulation study." *Physics in medicine and biology* 58.14 (2013): 4981.
4. Gyöngy, Miklós, and Constantin-C. Coussios. "Passive cavitation mapping for localization and tracking of bubble dynamics." *The Journal of the Acoustical Society of America* 128.4 (2010): EL175-EL180.

# Characterizing Microbubble Count and Size Distribution Using the Innovative Technique of MEMS Resonant Mass Measurement

*Rachel Bott, Judy Hadley, Bob Coyne*

Size control and count are two key characterisation factors for microbubbles used as contrast agents for ultrasound imaging and targeted drug delivery. Here we present a novel method for the characterisation of bubbles which provides buoyant mass, size and count information. Additionally, the method enables differentiation of particles of different densities such as lipid droplets and perfluorocarbon encapsulated gas bubbles using the innovative technique of resonant mass measurement (RMM). This technology utilises a suspended MEMS microchannel resonator (cantilever) which allows single particles to transit across the resonator and be individually characterised. Particles passing through the resonator alter the resonant frequency by an amount proportional to the buoyant mass of the particle, which can then be translated into mass, size or surface area. The change in resonant frequency of the cantilever is monitored via an optical based method. RMM therefore enables particle size to be determined as well as particle count in a single measurement.

When evaluating bubble particle size distribution, it is difficult to determine the identity of the particles; whether the particles are bubbles, lipid droplets or solid particle contaminants. In this work we utilize resonant mass measurement to enable this differentiation. With this technique it is also possible to evaluate the efficiency of encapsulated bubble production. Utilizing optimized instrument pressure conditions, we present data showing the impact of microbubble preparation variables via the mechanical agitation method upon the microbubble size and count.

Using RMM for microbubble characterisation enables quantitative assessment of bubble size distribution and count, but critically, also provides differentiation by buoyant mass to discriminate other particles in the sample.

# The Analysis of Sonoporation Metrics

*M. Maciulevičius, M. Tamošiūnas, M. S. Venšlauskas, S. Šatkauskas*

*Biophysical research group, Vytautas Magnus University, Kaunas, Lithuania*

## Introduction

Sonoporation (SP) is a physical modality, designed to achieve spatio-temporally controlled therapeutic agent delivery to cells and tissues. Although SP is considered to be safe, over-threshold cavitation activities can directly/ indirectly lead to cell death making SP dosimetry to be of primary importance. In the current study, we have simultaneously performed quantitative evaluation of four main SP elements: 1) MB concentration, 2) US scattering, 3) US attenuation and 4) bleomycin (BLM) sonotransfer into Chinese hamster ovary cells. This comprehensive research has led not only to preexisting metrics, inertial cavitation dose (ICD) [1] and MB sonodestruction rate [2], relation explanation, but also to the development of a new SP metric, attenuation rate. All the metrics were successfully used for BLM sonotransfer efficiency and cell viability prognostication. In addition to this, the signal-monitoring based method to determine optimal exposure duration to obtain maximal SP efficiency has been proposed.

## Materials and methods

SonoVue® MB concentration was evaluated using absorption spectroscopy. MB concentration decay curves were approximated using exponential function to obtain metric, MB sonodestruction rate.

MB scattered and attenuated US signals were recorded using passive cavitation detection system. US excitation waveform was 1 MHz central frequency, 1 kHz pulse repetition frequency, 10 % duty cycle (100  $\mu$ s on, 900  $\mu$ s off), 0 - 500 kPa peak negative acoustic pressure (PNP) and 0 - 10 s US exposure duration. Root mean square (RMS) was calculated in 1.5–1.75 and 0.9–1.1 MHz frequency ranges and used for subsequent differential RMS and attenuation quantification. Differential RMS was integrated in exposure duration scale to quantify metric, ICD. Attenuation curves were approximated using sigmoidal function to obtain estimate, attenuation rate.

SP experiments were performed separately for (MB + US) and (BLM + MB + US) groups using Chinese hamster ovary cells. Cell viability was evaluated using cell clonogenic assay. SP efficiency was calculated: (MB + BLM + US) – (MB + US) – (MB + BLM) as described by Tamosiunas et al. [2].

## Results and discussion

MB concentration decay occurs simultaneously with attenuation and cell viability decrease as well as SP efficiency increase (Fig. 1).

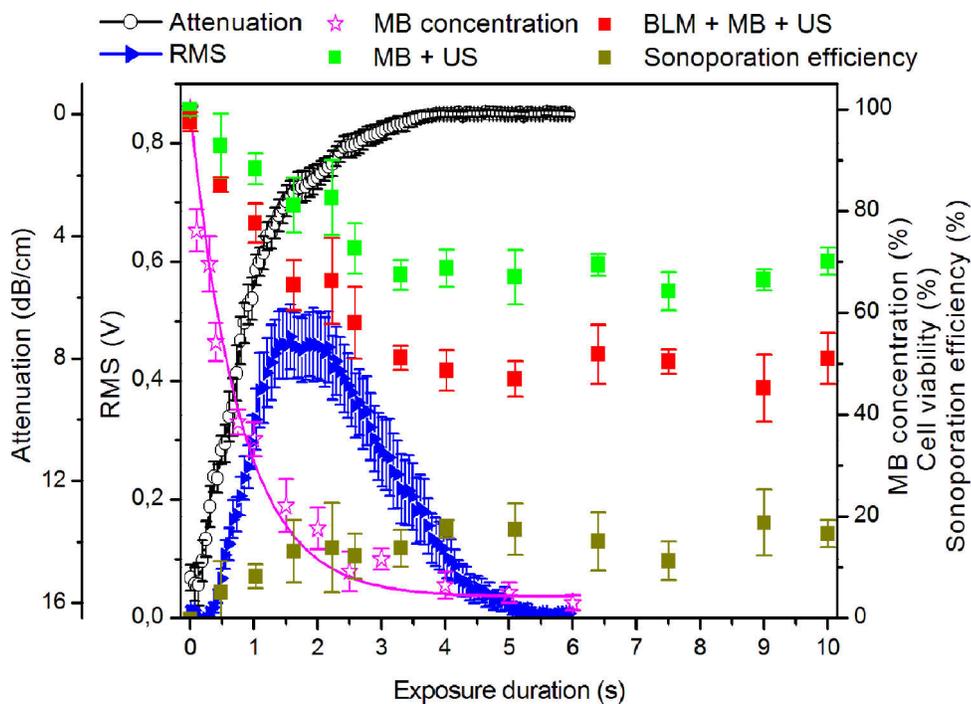


*Fig. 1. The impact of 200 kPa PNP US on MB sonodestruction, RMS, attenuation and SP efficiency in dependence of US exposure duration.*

All these processes occur within RMS peak and reach their corresponding plateau levels about the time RMS peak decreases to the background level. The saturation margin of all three sonoporation groups approximately coincides with the margin of complete MB sonodestruction as well as attenuation and RMS decrease to background levels.

We choose the criteria of RMS decrease to background level as an indicator for maximal sonotransfer efficiency while sustaining high cell viability. For this reason we have determined the approximate exposure duration when RMS decreases to background margin ( $\sim 0$  V) at different PNPs (up to 500 kPa) and used it for sonoporation. The cell viability and SP efficiency in PNP scale after optimization is given in Fig. 2a. BLM delivery increase occurs up to  $\sim 350$  kPa with achieved sonotransfer efficiency of  $\sim 31$  % and  $\sim 57$  % cell viability.

The quantified metrics, MB sonodestruction rate, ICD and attenuation rate had strong overall intercorrelation ( $R^2 > 0.85$ ) implying all physical processes to be strongly interconnected.

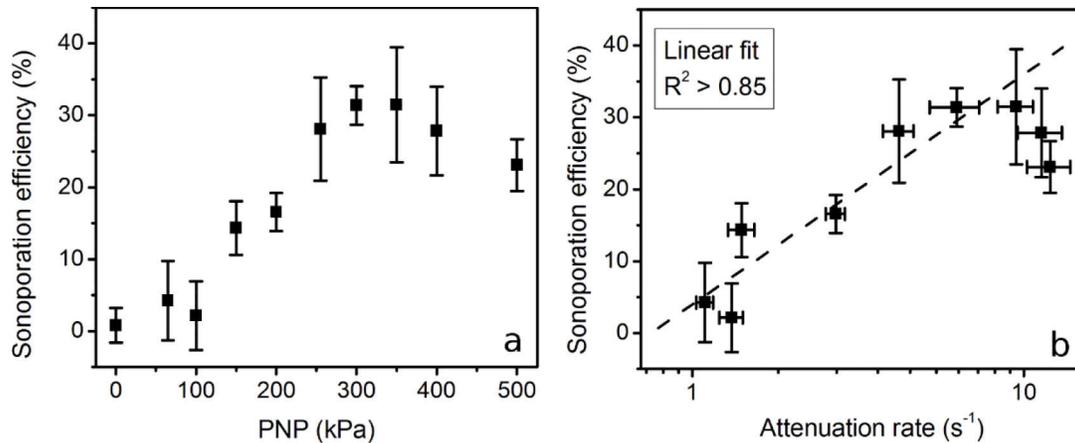


**Fig. 2.** The results of SP efficiency for different groups in dependence on US acoustic pressure (a). Correlation between attenuation rate and sonoporation efficiency (b).

In addition to this all metrics were successfully used for BLM sonotransfer efficiency ( $R^2 > 0.85$ ) and cell viability ( $R^2 > 0.9$ ) prognostication (the results for SP efficiency for new metric, attenuation rate, are shown in Fig. 2b). This indicates that all the different metrics can be interchangeably used to predict sonoporation outcome and hold promising prospects for the eventual development of universal SP dosimetry system.

Neither additional BLM sonotransfer nor cell viability decrease was observed after MB complete sonodestruction, RMS and attenuation decrease to background levels. Thus, a pattern to optimize SP efficiency in exposure duration scale by monitoring either output parameter: US attenuation, US scattering or MB concentration decrease to signal background levels was established.

ICD correlation with MB sonodestruction rate and attenuation rate imply inertial cavitation (MB concentration decrease) to be the key mechanism in all SP studies, where either ICD or attenuation estimate had been related to any cavitation induced bioeffect.

## Acknowledgements

This work was funded by Research Council of Lithuania project 3.3-LMT-K-712-01-0188.

## References

1. Chen WS, Brayman AA, Matula TJ, Crum LA. Inertial cavitation dose and hemolysis produced in vitro with or without Optison. *Ultrasound Med Biol.* 2003 May; 29(5):725-37.
2. Tamosiunas M, Jurkonis R, Mir LM, Lukosevicius A, Venslauskas MS, Satkauskas S. Microbubble sonodestruction rate as a metric to evaluate sonoporation efficiency. *J Ultrasound Med.* 2012 Dec; 31(12):1993-2000.

# Contrast enhanced ultrasound imaging: effect of flow on contrast measurements using plane wave versus focused transmissions

*Elahe Moghimirad, Jeffrey Bamber and Emma Harris*

*Joint Department of Physics and CRUK Cancer Imaging Centre, The Institute of Cancer Research and Royal Marsden NHS Foundation Trust, Sutton, London, United Kingdom*

## Background

We propose to develop a 3D dynamic contrast enhanced ultrasound (DCE-US) imaging system and use characteristics of the corresponding time-intensity curves (TIC) to monitor the response of tumors to radiotherapy. The use of 3D imaging is expected to increase reproducibility of the measured TIC characteristics between imaging sessions, thereby improving sensitivity to therapy-induced changes in the vasculature (<sup>1,2</sup>). There are, however, many choices to be made in system design, such as between imaging modes that may influence volume contrast image acquisition time and volume repetition rate. Plane wave (PW) imaging has the advantage of rapid image acquisition compared to conventional focused imaging (FI), potentially making it the most suitable for 3D data acquisition where data are acquired using a mechanically swept 1D array transducer. Although FI and PW are established techniques, their benefits and drawbacks are not well understood for CEUS applications and for 3D DCE-US in particular. CEUS image contrast is dependent on (a) imaging system parameters such as transmit frequency, F-number, mechanical index (MI) and number of coherent compounding angles (for PW), and (b) subject characteristics such as flow speed (<sup>3,4</sup>) and vessel orientation. Selection of imaging parameters and techniques for maximum image contrast is the subject of a companion paper. The aim of this work was to evaluate the effect of flow speed and vessel direction on vessel contrast for FI and PW in vitro.

## Materials and Methods

Using a flow phantom with 4 mm vessel diameter, CEUS images were obtained using the Vantage™ system (Verasonics Inc.) coupled with an ATL L7-4 transducer and reconstructed using a pulse inversion algorithm with 0.2 ms pulse intervals. 128 focused beam lines were transmitted for line-by-line imaging. Fresh diluted contrast agent (Sonozoid™) with concentration 0.4 ml/L was pumped into the flow phantom for each experiment and constant agent concentration was maintained. The transducer was initially oriented parallel to the vessel. With no flow, the F-number, MI, transmit frequency and number of PW angles were adjusted to achieve the same contrast (C) and contrast reduction (CR) for both techniques, where C was the initial ratio of signal in vessel to signal in background and CR was its reduction measured after 200 imaging frames had been acquired (a measure of bubble disruption). Figure 1(a) shows the transducer orientation, vessel and background region of interest (ROI). Flow speed was varied from 0 to 500 mm/sec (corresponding to the range of flow speeds in the body) and C was evaluated for FI and PW with 3, 7, 11 and 23 angles. All other parameters were kept constant. These measurements were repeated with the transducer perpendicular to the direction of flow (Figure 1(b)). Measurements were repeated a minimum of 3 times.

## Results

Using 4 MHz frequency, F-number = 4, MI = 0.15 and 7 angles, similar C ( $\cong$  21 dB) and CR ( $\cong$  68%) were achieved for both techniques. FI contrast increased and PW contrast decreased with increasing flow speed (see figure 2(a)). For PW imaging, the decrease in contrast with flow speed was greater with increasing number of angles. When the transducer was orientated perpendicular to the flow direction, the change in contrast was less for both techniques, compared to when the transducer was parallel to the flow direction (see figure 2(b)). The axial image profile through the vessel in the parallel orientation is illustrated in figure 3 which shows higher background levels in the PW image close to the vessel. The background level immediately posterior to the vessel increases with flow speed. The signal is also seen to rise inside the vessel for focused imaging.

## Discussion and conclusion

The change in apparent contrast with flow rate is believed to be due to two phenomena. First, a motion artefact (often called the flash artefact in clinical imaging), where displacement of microbubbles between the positive and negative pulse inversion transmissions, results in false contrast signal. This happens for both focused and PW imaging. Second, for PW only, motion occurring between plane wave transmissions at various angles will result in lack of signal coherency during coherent summation and thus loss of focusing gain, an effect which increases with the number of angles. The rise in the flash artefact for focused imaging is observed within the vessel as flow speed increases (figure 3). However, the signal stays almost constant for PW as it is affected by the combination of the two effects.

The effect of signal cancellation during summation of PW transmissions is more pronounced for greater numbers of angles and caused a greater contrast reduction (figure 2(a)). A similar finding was reported in (<sup>4</sup>), which studied the effect in the perpendicular orientation, however, they reported a greater reduction for PW imaging compared to that observed in this study probably due to using contrast pulse sequences (CPS).

High background levels close to the vessel were also observed to be another source of error for PW. These artefacts, which grow in size with flow rate posterior to the vessel (figure 3) may be due to the nonlinear content of ultrasound scattered by the bubbles and then rescattered by the background (<sup>5</sup>). When the bubbles move faster, this artefact is emphasized by combination with the phase shift motion artefact. This effect will reduce the vessel-background contrast and reduce the visibility of small vessels situated below larger vessels, possibly making them undetectable.

Overall, the effects of the pulse-inversion flash artefact and PW incoherency may be negligible for peripheral vessels where the flow is very slow (up to 1mm/sec). For veins or arteries, however, which are present in and around most tumors, and the effect needs to be compensated, or the results should be interpreted differently.

This study also shows how careful one should be in choosing the number of angles for PW imaging based on the organ of interest and its average flow rate. A greater number of angles may be used when flow rates are slow, to improve the contrast, whereas a smaller number of angles is suggested when flow rates are higher, to reduce the incoherency effect.

With the transducer orientated perpendicular to the flow direction, contrast agents take time to exit the beam and so appear at the same position for a number of pulses, reducing the flow effects

for both techniques as shown in figure 2(b). For tortuous tumour vasculature blood may flow in all directions and the effect of transducer orientation, although present locally, will average out across the imaged field. However, if there is a dominant flow direction, transducer orientation should be maintained across sequential imaging sessions. Also, maintaining the same ROI and imaging plane may be crucial in this case.

3D imaging rectifies some of these spatial considerations (such as imaging plane), although reduction and rise in contrast for PW and FI, respectively, remains an issue. Although both of the latter effects are undesirable, it may be more straightforward to account for artefacts in FI as it only suffers from the flash effect which can be compensated using flow speed. Flow correction, using multiple ways to measure flow, is the subject of future work.

**Acknowledgments:** This work is supported by Cancer Research UK Program C20892/A23557.



Figure 1. Schematics of the two transducer positions (a) parallel (longitudinal), and (b) perpendicular (cross-sectional). Vessel and background regions are highlighted in green and blue, correspondingly. The width or the diameter of all the ROIs is approximately 3.4 mm.

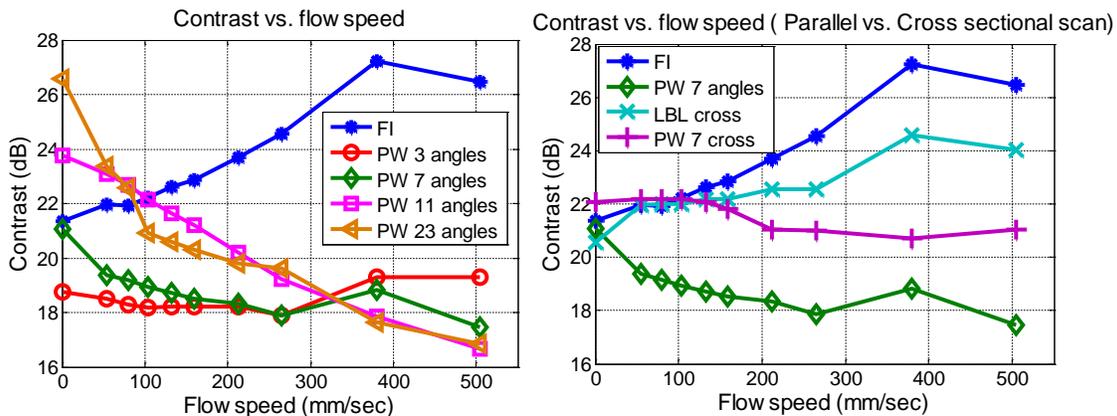


Figure 2 Contrast vs. flow speed for (a) focused imaging and plane wave imaging with varying number of angles (parallel orientation), and (b) parallel vs. cross sectional orientation (the contrast with no flow is slightly different, due to having different ROIs for different orientations).

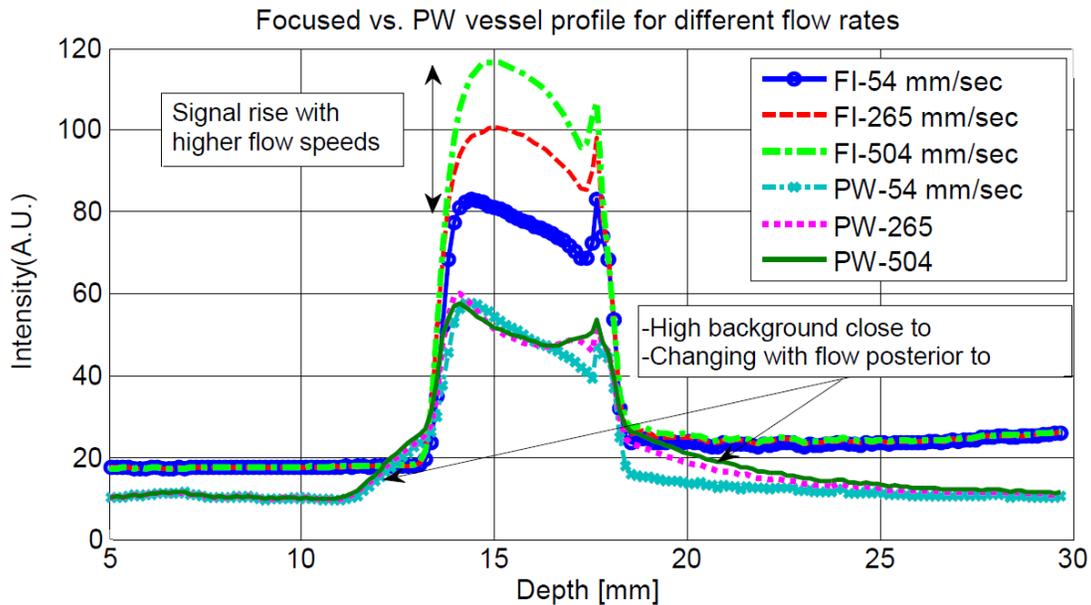


Figure 3 Axial amplitude profile across the diameter of the vessel for focused and PW imaging (7 angles, parallel direction). High background levels close to and posterior to the vessel are seen to increase with flow speed.

## References

1. H. Wang, et al. "Three-dimensional ultrasound molecular imaging of angiogenesis in colon cancer using a clinical matrix array ultrasound transducer." *Investigative radiology* 50.5 (2015): pp. 322-329.
2. J.-B. Liu, G. Wansaicheong, D. A. Merton, F. Forsberg, B. B. Goldberg, "Contrast-enhanced Ultrasound Imaging: State of the Art", *J Med Ultrasound*, vol.13 no.3, pp.109-126, 2005.
3. Y. E. Chung, K. W. Kim, "Contrast-enhanced ultrasonography: advance and current status in abdominal imaging", *Ultrasonography*, vol. 34, no. 1, pp. 3-18, 2015.
4. J. Viti, H. J. Vos, N. de Jong, F. Guidi, and P. Tortoli, "Detection of Contrast Agents: Plane Wave Versus Focused Transmission", *Trans. Ultrason., Ferroelec., Freq. Contr.*, vol. 63, no. 2, pp. 2676-2683, 2016.
5. Y. O. Yildiz, R. J. Eckersley, R. Senior, A. K. P. Lim, D. Cosgrove, and M.-X. Tang, "Correction of nonlinear propagation artifact in contrast-enhanced ultrasound imaging of carotid arteries: methods and in-vitro evaluation", *Ultrasound in Med. & Biol.*, Vol. 41, No. 7, pp. 1938-1947, 2015.

# Modeling the acoustic field produced by diagnostic ultrasound arrays in plane wave mode

*Ting-Yu Lai<sup>1</sup>, Matthew Bruce, Michalakis Averkiou*

*Department of Bioengineering, University of Washington, Seattle, USA*

## Introduction

Contrast-enhanced ultrasound (CEUS) is a real-time imaging technique that is capable of visualizing the vasculature and perfusion of organs and tumors. Recent advances in ultrafast contrast imaging that combine plane wave imaging (PWI) and contrast imaging have facilitated innovations such as super-resolution contrast-enhanced imaging and ultrafast contrast-enhanced Doppler imaging. Tissue harmonic imaging (THI) improves images and reduces clutter and reverberations in diagnostic ultrasound. As ultrasound waves propagate in tissue, harmonic components are generated with distance due to nonlinear propagation. THI utilizes the 2<sup>nd</sup> harmonic to form images that offer advantages over conventional fundamental imaging. Combining PWI and THI may offer similar improvements in applications that use PWI such as 3D THI and harmonic color flow.

No studies have yet investigated the acoustic field produced by diagnostic arrays in plane wave mode for these clinical applications. The characteristics of the beam produced by diagnostic arrays such the uniformity of the field, the spatial extend of the mechanical index (MI) of the pulse, and the magnitude of the harmonic components of the pulse are crucial for optimizing image quality for both ultrafast contrast imaging and ultrafast THI. The Khokhlov-Zabolotskaya-Kuznetsov (KZK) nonlinear parabolic wave equation is a good model to study the propagation of pulsed finite amplitude sound beams in fluids and tissues.

The aim of the present study is to model 3 diagnostic arrays, the Verasonics L11-4v linear array and C5-2v convex array, and the Philips P4-2 phased array. All 3 arrays produce plane or diverging sound fields not investigated in the past. We have 2 specific objectives: first, to investigate the variation of MI in low MI applications in order to evaluate increased nearfield bubble destruction due to the nature of the diverging fields; and second, to investigate the feasibility of combining PWI and THI by quantifying the 2<sup>nd</sup> harmonic component generated by these fields.

## Method

A numerical model that numerically solves the KZK equation in time domain and is capable of modeling the field of plane wave and diverging beams was developed. The specifications of 3 diagnostic imaging arrays (L11-4v, C5-2v, and P4-2) used in the present work are shown in Table 1. For modeling the L11-4v array, the depth was set to 4 cm, consistent with the typical field of view in carotid imaging. For the C5-2v and the P4-2 arrays, the depth was set to 15 cm, which is the typical depth in abdominal and cardiac imaging. The specifications of the 3 arrays in conventional focused mode are shown in Table 2.

<i>Transducer</i>	<i>Number of elements</i>	<i>Pitch (mm)</i>	<i>Array Width (mm)</i>	<i>Array Height (mm)</i>	<i>Elevation Elevation Focus (mm)</i>	<i>Frequency (MHz)</i>
<i>L11-4v</i>	<i>128</i>	<i>0.3</i>	<i>38.4</i>	<i>5</i>	<i>20</i>	<i>4</i>
<i>C5-2v</i>	<i>128</i>	<i>0.5</i>	<i>49.6</i>	<i>14</i>	<i>60</i>	<i>2</i>
<i>P4-2</i>	<i>96</i>	<i>0.3</i>	<i>28.8</i>	<i>16</i>	<i>80</i>	<i>2</i>

*Table 1: Specifications of L11-4v, C5-2v, and P4-2 diagnostic arrays.*

<i>Transducer</i>	<i>Number of elements used for azimuthal focusing</i>	<i>Azimuthal Focus (mm)</i>
<i>L11-4v</i>	<i>30</i>	<i>30</i>
<i>C5-2v</i>	<i>36</i>	<i>77</i>
<i>P4-2</i>	<i>96</i>	<i>77</i>

*Table 2: Specification of the L11-4v, C5-2v, and P4-2 in conventional focused mode.*

We have run our simulation for 2 cases, one linear (to investigate bubble destruction at low MI) and one nonlinear (to investigate THI). The attenuation used in the simulations was 0.3dB/cm-MHz (typically used in diagnostic ultrasound). We assume a pulse with roughly 3.5 cycles.

## **Result and Discussion**

### **Linear simulations-Ultrafast Contrast Imaging**

The linear (low MI) simulation results for L11-4 array in PWI are shown in Fig. 1a. The contours in the figure are in 6 dB increments after normalization with respect to the maximum value. For conventional focused ultrasound (1b), where a small number of elements is used in each firing, the acoustic field produced is more uniform along the axis due to beamforming. We see that in PWI (1a) there will be more bubble destruction in the nearfield due to the increased acoustic pressure.

The simulation results for P4-2 array are shown in Fig. 1c. The diverging nature of the field when all elements of this probe are used to cover a sector is appreciated. This is implemented by using a focus behind the source (not in the tissue). Increased bubble destruction is predicted here also compared to the focused beam (2d).

The simulation results for the C5-2v array are shown in Fig. 1e. Here also, the diverging nature of the field when all elements are used is expected to result in more nearfield bubble destruction. For all 3 cases, it is noted that the elevation focus continues to have a strong effect and focuses the energy to that depth.

### **Nonlinear simulations-Ultrafast Tissue Harmonic Imaging**

The simulation results for nonlinear propagation of ultrasound generated by the L11-4v array in tissue are shown in fig. 2. The fundamental component of the acoustic field produced by PWI and conventional focused ultrasound are shown in Fig. 2a and the 2<sup>nd</sup> harmonic component in 2b. The axial field at the center of the array is shown in Fig. 3. The fundamental of the focused beam (solid blue line) is 4 dB greater than that of the PWI mode (blue crosses). The 2<sup>nd</sup> harmonic of the focused beam (solid red line) is 7 dB greater than that of the PWI mode (red crosses).

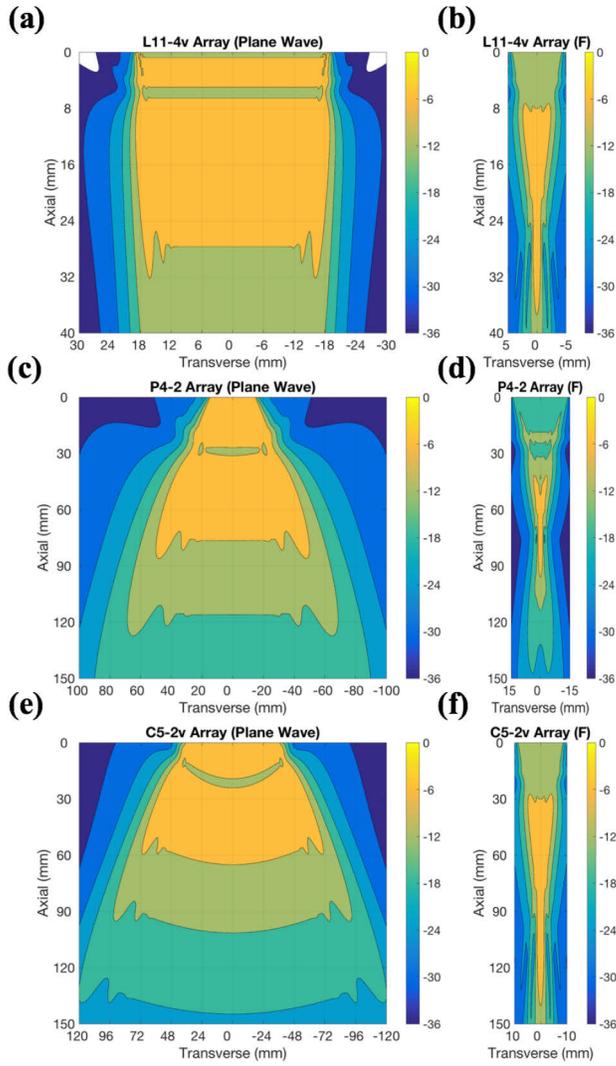


Figure 1: Simulations of the linear (low MI) acoustic field produced by L11-4v array (a-b), P4-2 array (c-d) and C5-2v (e-f) in tissue. The contours are all in 6 dB increments with 0 dB being the maximum.

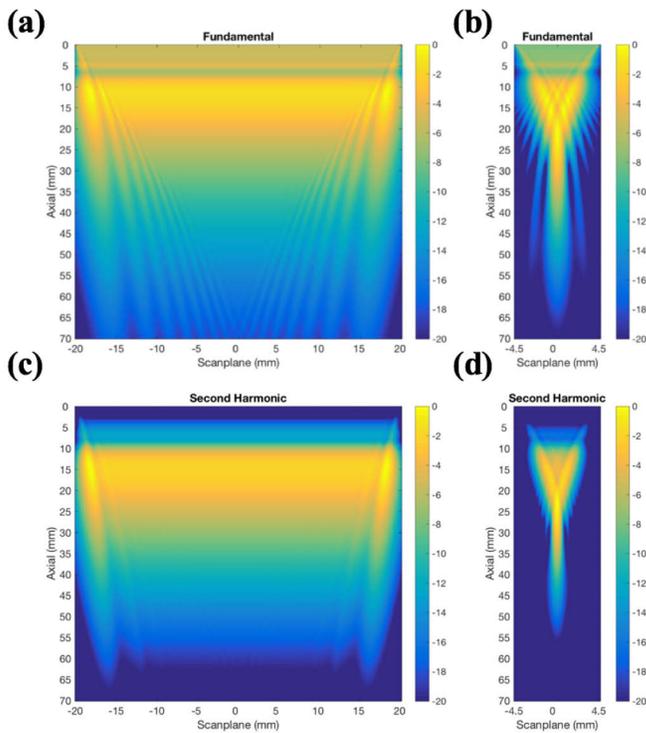


Figure 2: Simulations of the nonlinear field produced by the L11-4v array in tissue. (a-b) fundamental component and (c-d) second harmonic components produced by plane wave mode (a-c) and focused mode (b-d).

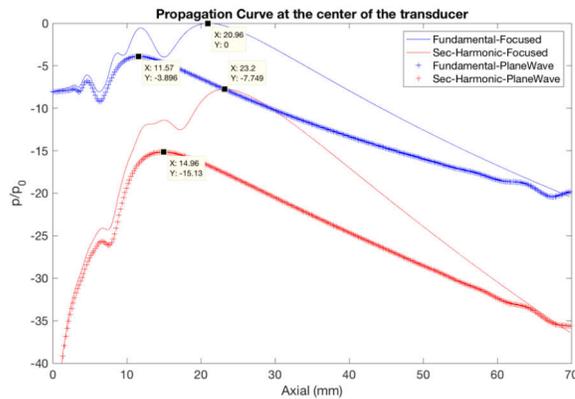


Figure 3: The axial field of the fundamental component (blue) and second harmonic component (red) produced by plane wave mode (+) and focused mode (solid line) at the center of the array.

## Conclusion

The linear and nonlinear field of 3 diagnostic ultrasound arrays operating in plane wave/diverging mode was investigated. Use of such arrays in low MI contrast imaging will produce slightly greater bubble destruction than conventional partial aperture focused beams. The -6 dB from maximum range of cardiac and abdominal arrays (C5-2v and P4-2) is up to about 6 cm from the probe and is reduced to -18 dB at 15 cm. Reducing the sector width (degree of divergence) will limit this problem at the expense of a narrower field of view. The 2<sup>nd</sup> harmonic of PWI beams was found to be lower than that of focused beams by 6-10 dB but this suggests that THI would still be possible despite the signal loss.

# Evolution of a Polymer-shelled Ultrasound Contrast Agent

*Margaret A. Wheatley<sup>1</sup>, Lauren J. Jablonowski<sup>1,2</sup>, John R. Eisenbrey<sup>1,2</sup>,  
Michael C. Cochran<sup>1,3</sup>, Nutte T. Teraphongphom<sup>1,4</sup>*

*<sup>1</sup>School of Biomedical Engineering, Science, and Health Systems, Drexel University, Philadelphia, PA 19104, USA, <sup>2</sup>Department of Radiology, Thomas Jefferson University, Philadelphia, PA 19107, USA, <sup>3</sup>Avidity Biosciences, La Jolla, CA 92037, USA <sup>4</sup>Department of Otolaryngology, Stanford University, Stanford, CA 94305, USA*

## Introduction

Shell properties of ultrasound contrast microbubbles (MB) play a pivotal role, not only in determining acoustic properties, but also determining in vivo behavior. There are complex interactions among the ultrasound, the encapsulated gas, blood components, vasculature and normal and malignant tissue. The predominant shell components used in ultrasound contrast agents are comprised of either phospholipids/surfactants or polymers. Both forms possess a shell that can house and protect a drug or multimodal species such as iron oxide, and both can be modified with a targeting ligand specific for a given cell surface receptor. However, any changes to the shell will impact the acoustic properties, and a balance must be achieved between acoustic and clinical requirements.<sup>1,2</sup> Polymer based agents differ from phospholipid agents both in the capacity of the shell to house foreign species, and their acoustic behavior, reflecting different shell elasticities.

Our group has developed polymeric MB based on polylactic acid (PLA) shells, and modified the designs to address different needs.<sup>3-6</sup> We have found that the acoustic properties are extremely sensitive to any adaptations to the shell, but the basic structure offers many opportunities in imaging and theranostics. We have also found that insonation at frequencies within the medical imaging range produces a significant size reduction, resulting in production of drug-loaded fragments which we term nano shards.<sup>7</sup>

## Methods

We produce hollow PLA MB through a water-in-oil-in-water emulsion technique (w/o/w), with encapsulation of volatile core materials (camphor and ammonium carbonate), that are later removed by sublimation. The w/o/w emulsion is ideal for encapsulating both hydrophilic and hydrophobic species. Capsules are characterized with a dynamic light scattering particle size analyzer for mean diameter, size distribution (poly dispersity index (PDI)), and zeta potential ( $\zeta$ ). Surface morphology is checked by scanning electron microscope (SEM), and in vitro acoustic properties (echogenicity and stability in the ultrasound (US) beam) using a custom-made acoustic setup. Other gases can be introduced after the lyophilizing stage. Utilizing a lyophilizer shelf attachment fitted with a piston that can be lowered onto vials into which agent has been charged and which are fitted loosely with a septum. The resulting samples, under vacuum, can then be re-inflated with the gas of choice through the resealing septum.

## Results and Discussion

### The parent microbubbles

Uniform, spherical capsules are produced into which a drug<sup>3,4</sup>, imaging agent<sup>6</sup> or targeting ligand<sup>5</sup> can be incorporated (Fig. 1). Typical SEM data for 100% PLA polymer (molecular weight of 83 kDa) are shown in Fig. 1A and B. The agents are air-filled, with average diameter of  $1.7 \pm 0.8 \mu\text{m}$ ,

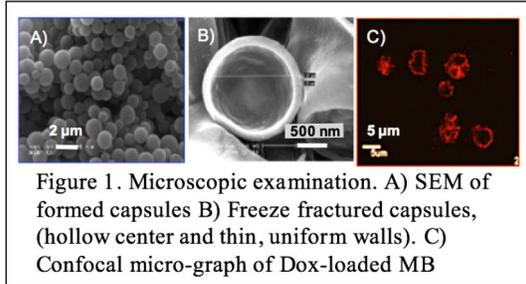


Figure 1. Microscopic examination. A) SEM of formed capsules B) Freeze fractured capsules, (hollow center and thin, uniform walls). C) Confocal micro-graph of Dox-loaded MB

exhibited a  $\zeta$  of  $-23.75 \pm 5.69$  mV. Shell thickness of 140 nm was measured on a freeze fractured sample (Fig. 1B). Shell volume is roughly  $3.5 \mu\text{m}^3$ . Confocal fluorescence microscopy detected doxorubicin (Dox) (3 wt% loading) in the shell, confirming both incorporation, and the hollow nature of the platform (Fig 1C).

### In situ nano shard production

Production of nanoshards was measured in vitro by analyzing fragment particle size upon 20 minutes of insonation (5 MHz, 0.0 -1.65 MPa, PRF=100 Hz). Suspensions showed an average size of less than 350 nm after 15 minutes (Fig. 2).<sup>7</sup>

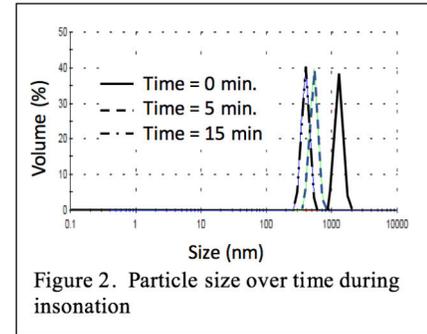


Figure 2. Particle size over time during insonation

### Extravasation to the tumor and protection of the heart

Morris hematoma 3924a tumors were established in the left lateral lobe of the liver in ACI rats.<sup>8</sup>

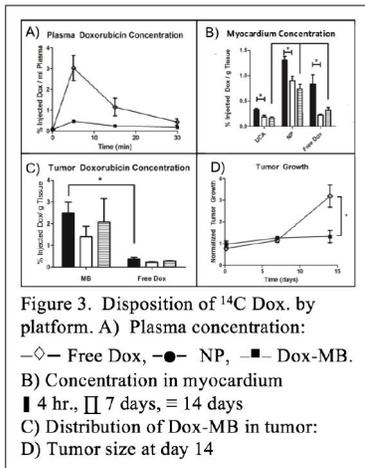
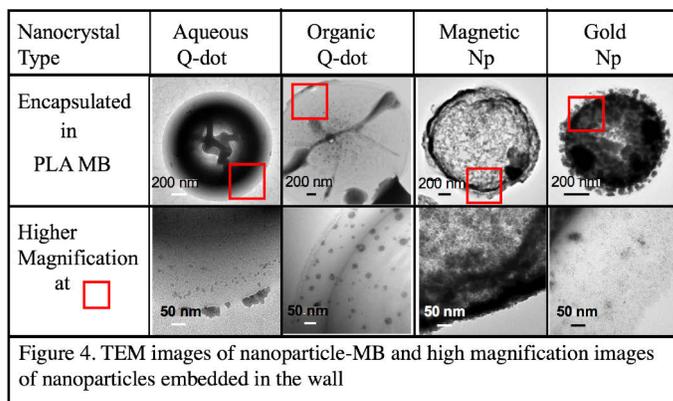


Figure 3. Disposition of <sup>14</sup>C Dox. by platform. A) Plasma concentration:  $\diamond$  Free Dox,  $\bullet$  NP,  $\blacksquare$  Dox-MB. B) Concentration in myocardium  $\blacksquare$  4 hr.,  $\square$  7 days,  $\equiv$  14 days C) Distribution of Dox-MB in tumor: D) Tumor size at day 14

After tail-vein injection of Dox-loaded MB, the tumors were insonated for 20 minutes with Doppler ultrasound at a mechanical index of 0.40–0.45 and a pulse repetition frequency of 1000 Hz, with an ATL/Philips HDI-5000 scanner (Bothel, WA) using a linear 12-5 MHz transducer. Biodistribution studies were conducted to compare the behavior of both free Dox and Dox-loaded solid nanoparticles to these Dox-MB. In all measured endpoints, the Dox-MB outperformed the free Dox and nanoparticles. (Fig.3). The plasma concentration peaked at the 5-minute reading. Free Dox was roughly 1.2 times as high as the nanoparticles and 10 times as high as Dox-MB. In the heart (Fig 3B), an organ which is susceptible to Dox cardiotoxicity, the nanoparticles fared the worst, lasting at a high level over the 14 days of the experiment and initially reaching a concentration at 4 hours of roughly 4.3 times that of MB. In the tumor, the

reaching a concentration at 4 hours of roughly 4.3 times that of MB. In the tumor, the

microbubbles achieved the highest and most sustained levels, and at the termination at 14 days, only the MB treated animals did not show tumor growth.



### Multimodal Imaging Modes

To test the effect of incorporation of semiconductor crystals and metallic nanoparticles into the PLA MB, we investigated quantum dots (QD), iron oxide magnetic nanoparticles (MNP), and gold nanoparticles (AuNP). All were accommodated in the shell of the MB (Fig. 4), each incorporated in unique ways as can be seen from the morphology under

TEM, and all retained both acoustic and nanoparticle-specific imaging properties to varying degrees.<sup>6</sup>

### Conclusions

Polymeric microbubbles have proved to be adaptable to a number of different imaging and theranostic modalities. These will be discussed in further detail at the symposium.

### References

1. Jablonowski, L.J., D. Alfego, J.I. Andorko, J.R. Eisenbrey, N. Teraphongphom, and M.A. Wheatley, *Balancing stealth and echogenic properties in an ultrasound contrast agent with drug delivery potential. Biomaterials*, 2016. **103**: 197-206.
2. Jablonowski, L.J., M.C. Cochran, J.R. Eisenbrey, N.T. Teraphongphom, and M.A. Wheatley, *Shell Effects on Acoustic Performance of a Drug-delivery System Activated by Ultrasound. J. Biomed. Mat.Res. Part A*, 2017.
3. Cochran, M.C., J. Eisenbrey, R.O. Ouma, M. Soulen, and M.A. Wheatley, *Doxorubicin and paclitaxel loaded microbubbles for ultrasound triggered drug delivery. Int. J. Pharm.*, 2011. **414**(1): 161-170.
4. Eisenbrey, J., O.M. Burstein, R. Kambhampati, F. Forsberg, J.-B. Liu, and M. Wheatley, *Development and optimization of a doxorubicin loaded poly (lactic acid) contrast agent for ultrasound directed drug delivery. J. Cont. Rel.*, 2010. **143**(1): 38-44.
5. Jablonowski, L.J., N.T. Teraphongphom, and M.A. Wheatley, *Drug delivery from a multi-faceted ultrasound contrast agent: Influence of shell composition. Mol. Pharm.*, 2017. **14**(10): 3448-3456.
6. Teraphongphom, N., P. Chhour, J.R. Eisenbrey, P.C. Naha, W.R. Witschey, B. Opananont, L. Jablonowski, D.P. Cormode, and M.A. Wheatley, *Nanoparticle loaded polymeric microbubbles as contrast agents for multimodal imaging. Langmuir*, 2015. **31**(43): 11858-11867.
7. Eisenbrey, J.R., M.C. Soulen, and M.A. Wheatley, *Delivery of encapsulated doxorubicin by ultrasound-mediated size reduction of drug-loaded polymer contrast agents. IEEE Trans. Biomed. Eng.*, 2010. **57**(1): 24-28.
8. Cochran, M.C., J.R. Eisenbrey, M.C. Soulen, S.M. Schultz, R.O. Ouma, S.B. White, E.E. Furth, and M.A. Wheatley, *Disposition of ultrasound sensitive polymeric drug carrier in a rat hepatocellular carcinoma model. Acad. Radiol.*, 2011. **18**(11): 1341-1348.

# Single-Element Transducer for Simultaneous Ultrasound Therapy and Monitoring of Microbubble-Seeded Acoustic Cavitation

*Sophie V. Heymans, Christine F. Martindale, Andrej Suler, Antonios N. Pouliopoulos, Robert J. Dickinson, and James J. Choi*

*Noninvasive Surgery and Biopsy laboratory, Department of Bioengineering, Imperial College London, SW7 2AZ, United Kingdom*

## Introduction

Microbubble-seeded acoustic cavitation is used in several therapeutic applications, such as targeted drug release, blood-brain barrier opening, sonoporation, and sonothrombolysis. One of the common challenges that these cavitation-based therapies share is that the safety and efficacy are determined by the type and magnitude of cavitation produced within the ultrasound beam. Real-time monitoring of cavitation by capturing and analysing unique acoustic emissions generated by oscillating microbubbles has thus become a common technique used during ultrasound treatments [1]. The typical configuration includes a separate transducer for monitoring microbubble acoustic emissions which is co-aligned with the therapeutic transducer [2], [3]. This arrangement was originally conceived to account for therapeutic pulses which were several milliseconds long (more than 10 000 cycles) [4] and produced high peak-rarefactional pressures (higher than 2 MPa) [5], [6]. Due to their low amplitude compared to the therapeutic signal, microbubble acoustic emissions could not be detected in real-time with the therapeutic transducer. However, recent work in therapeutic ultrasound has revealed that therapy can be achieved at lower acoustic pressures [2], which provides an opportunity for designing alternative cavitation monitoring approaches. Here, we present a compact system with a single-element transducer that can perform ultrasound therapy with long pulses while simultaneously monitoring microbubble-seeded acoustic cavitation.

## Methods

We employed a narrowband single-element therapeutic transducer, with a center frequency of 0.5 MHz and a high sensitivity to odd harmonics (Fig. 1). Microbubbles were made to flow through a vessel-mimicking tube (0.8 mm diameter), placed within the transducer's focus in a water tank, and were sonicated with therapeutic pulses (peak rarefactional pressure: 75-827 kPa, pulse lengths: 200  $\mu$ s and 20 ms). Microbubble acoustic emissions were captured using the same transducer. The received signals were separated from the therapeutic signal with a hybrid coupler [7] and a high-pass filter. In order to validate the results obtained in simultaneous transmission and reception, an inserted and co-aligned 7.5 MHz broadband transducer was employed to monitor microbubble activity in the focus, as a passive cavitation detector (PCD). Control experiments consisted in sonications in the absence of a tube and sonications of a tube filled with water. Pairwise comparisons between harmonic levels of each experimental condition were carried out with a Wilcoxon Rank Sum Test for each pressure (n=10).

## Results

We demonstrated the feasibility of monitoring microbubble-seeded acoustic cavitation using a single-element transducer in simultaneous transmission and reception mode. A significant increase of the third harmonic during sonication of microbubbles (in comparison with controls) was detected for all pressure levels that were tested ( $p < 0.001$ ). At high pressures ( $> 500$  kPa), an increase of both the fifth and seventh harmonics for the microbubble experiments was detectable and statistically significant. These higher order harmonics were not identified at low pressures because their amplitudes were below the noise level.

The capability of the system to detect changes in cavitation activity in real-time was evaluated by sonicating with long pulses of 10 000 cycles (Fig. 2). The water control signals (Fig. 2(a), (d), and (g)) showed that there was some leakage of harmonics at the beginning and end of the driving signal, coupled with a small parasitic third harmonic from the power amplifier at high pressures. At low acoustic pressures, only the microbubble's third harmonic was detected by the therapeutic transducer (Fig. 2(b)). As the pressure increased, higher order odd harmonics (fifth, seventh and ninth) were identified (Fig. 2(e) and (h)). More importantly, the detection of broadband acoustic emissions was achieved at frequencies slightly above odd harmonic values. As shown in Fig. 1, the single-element transducer was sensitive to these frequency ranges and could detect broadband signal associated with inertial cavitation. Both the PCD and the therapeutic transducer detected a decrease of the microbubble signal with time at the highest pressure (Fig. 2(h) and (i)), which may be an indicator of microbubble destruction.

## Conclusion

To our knowledge, this study is the first demonstration of simultaneous ultrasound therapy and microbubble monitoring with a single-element transducer. By combining a hybrid coupler and a high-pass filter, microbubble acoustic emissions were isolated from the therapeutic signal. With an in vitro setup, we showed that the harmonic content of the signals from microbubble-seeded cavitation activity was significantly higher than controls. More importantly, we could identify the microbubble cavitation mode and detect microbubble destruction in real-time. Future steps will aim at improving the sensitivity of the system as well as its ability to detect clinical microbubble concentrations, by upgrading the performances of the hybrid coupler and appropriately choosing an efficient and broadband transducer. Such a low-cost and simple technology has the potential to convert many existing therapeutic transducers into dual-feature systems capable of real-time cavitation monitoring; negates the need for the confocal alignment of two transducers; and improves therapeutic beam quality by not having to allocate different surface areas of a transducer to either a therapeutic or imaging purpose.

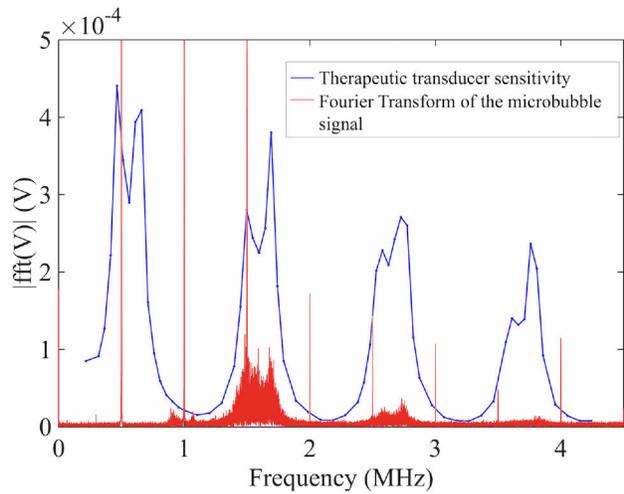


Fig. 1. Discrete Fourier Transform of the microbubble signal collected by the therapeutic transducer for a peak rarefactional pressure of 1061 kPa, with the sensitivity of the transducer superimposed.  
© [2017] IEEE. Reprinted, with permission from [8].

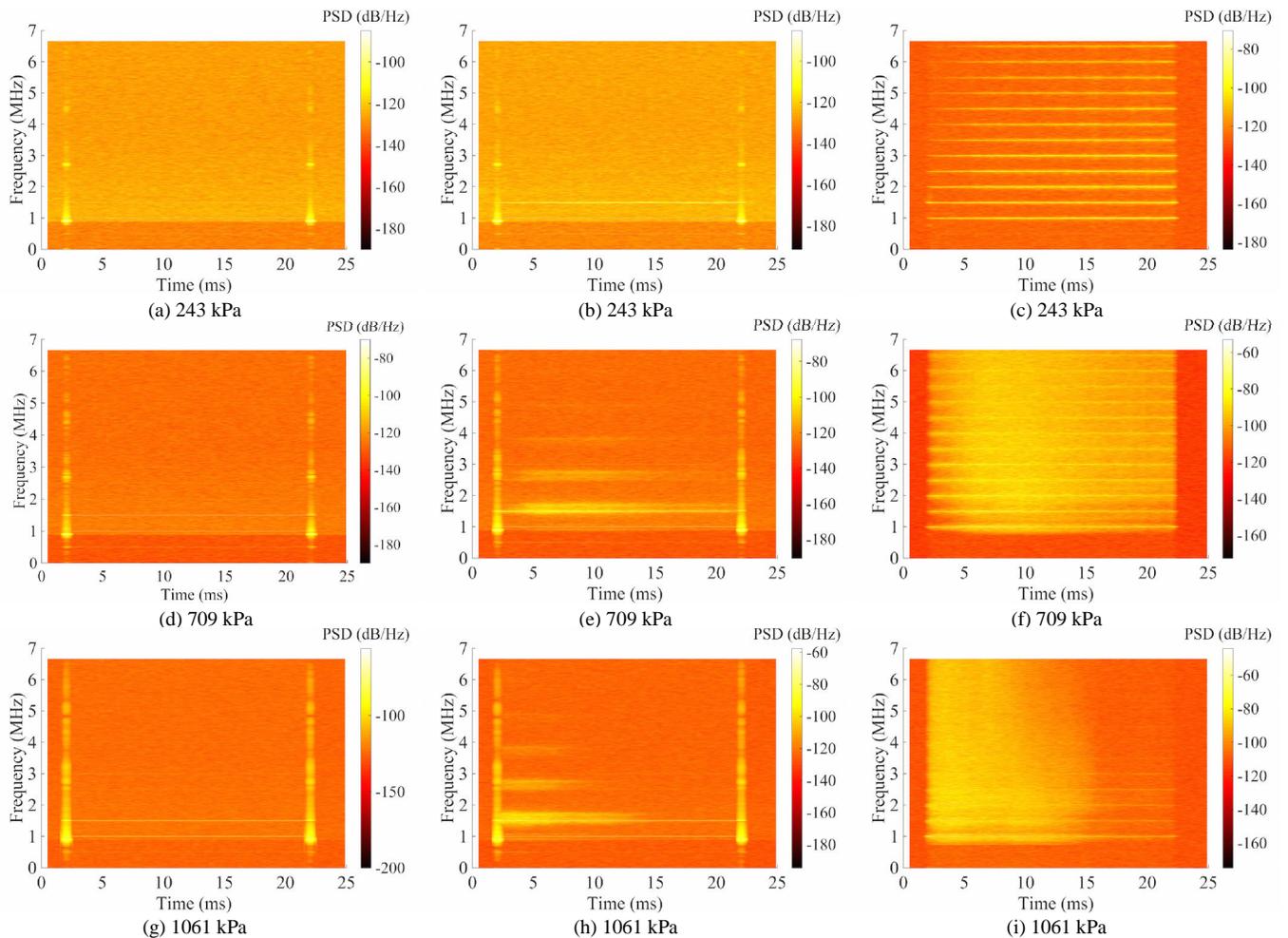


Fig 2. Spectrograms obtained when sonicating with 20-ms-long pulses. Using a single therapeutic transducer, a tube filled with (a), (d), (g) water only, or (b), (e), (h) microbubbles was exposed to a 20-ms-long ultrasound pulse. The same therapeutic transducer was used to simultaneously capture the acoustic emissions while the tube was being exposed to ultrasound. (c), (f), (i) Additionally, the microbubble activity was captured with a PCD. The PCD measurements were made to confirm that the signals obtained using the single-element transducer arrangement were microbubble-seeded acoustic emissions. PSD stands for Power Spectral Density.

© [2017] IEEE. Reprinted, with permission from [8].

## References

1. J. J. Choi, R. C. Carlisle, C. Coviello, L. Seymour, and C.-C. Coussios, "Non-invasive and real-time passive acoustic mapping of ultrasound-mediated drug delivery," *Phys. Med. Biol.*, vol. 59, no. 17, pp. 4861–4877, Aug. 2014.
2. F. E. Shamout, A. N. Pouliopoulos, P. Lee, S. Bonaccorsi, L. Towhidi, R. Krams, and J. J. Choi, "Enhancement of non-invasive trans-membrane drug delivery using ultrasound and microbubbles during physiologically relevant flow," *Ultrasound Med. Biol.*, vol. 41, no. 9, pp. 2435–2448, May 2015.
3. J. J. Pacella, J. Brands, F. G. Schnatz, J. J. Black, X. Chen, and F. S. Villanueva, "Treatment of microvascular micro-embolization using microbubbles and long-tone-burst ultrasound: An in vivo study," *Ultrasound Med. Biol.*, vol. 41, no. 2, pp. 456–464, Sep. 2015.
4. A. N. Pouliopoulos, S. Bonaccorsi, and J. J. Choi, "Exploiting flow to control the in vitro spatiotemporal distribution of microbubble-seeded acoustic cavitation activity in ultrasound therapy," *Phys. Med. Biol.*, vol. 59, no. 22, pp. 6941–57, Oct. 2014.
5. K. Hynynen, N. McDannold, N. Vykhodtseva, and F. A. Jolesz, "Noninvasive MR imaging-guided focal opening of the blood-brain barrier in rabbits," *Radiology*, vol. 220, no. 3, pp. 640–646, Aug. 2001.
6. C. C. Coussios, C. H. Farny, G. Ter Haar, and R. A. Roy, "Role of acoustic cavitation in the delivery and monitoring of cancer treatment by high-intensity focused ultrasound ( HIFU )," *Int. J. Hyperth.*, vol. 23, no. 2, pp. 105–120, Mar. 2007.
7. T. Vössing, J. Rautenberg, and B. Henning, "Simultaneous transmitting and receiving with ultrasonic sensors," in *13th International Conference Sensor+ Test, Proceedings Volume II A8.1*, 2007, pp. 69–74.
8. S. V Heymans, C. F. Martindale, A. Suler, A. N. Pouliopoulos, R. J. Dickinson, and J. J. Choi, "Simultaneous Ultrasound Therapy and Monitoring of Microbubble-Seeded Acoustic Cavitation Using a Single-Element Transducer," *IEEE Trans. Ultrason. Ferroelectr. Freq. Control*, vol. 8, no. 64, 2017.

# Explaining The Differences in Vaporization Threshold of Low Boiling-Point Phase Change Contrast Agents Between in Vivo and In Vitro Activation

*Juan D Rojas<sup>1</sup>, Mark A. Borden<sup>2</sup>, Paul A Dayton<sup>1</sup>*

*Joint Department of Biomedical Engineering, The University of North Carolina and North Carolina State University, Chapel Hill, North Carolina<sup>1</sup>  
Department of Mechanical Engineering, University of Colorado, Boulder, Colorado<sup>2</sup>*

## **Introduction**

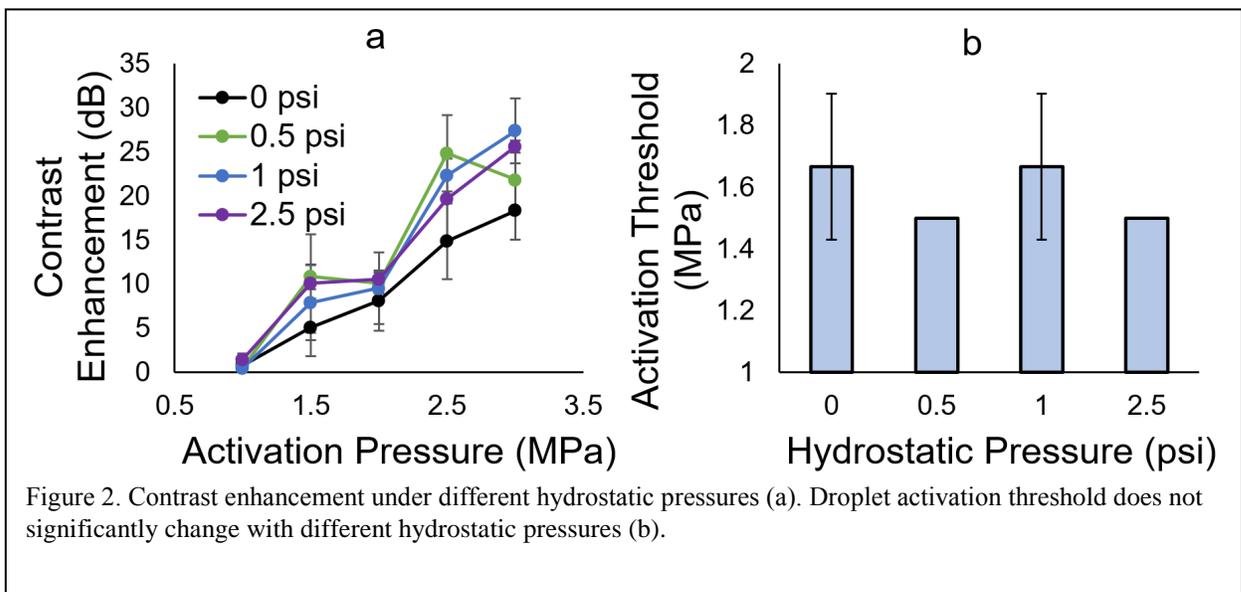
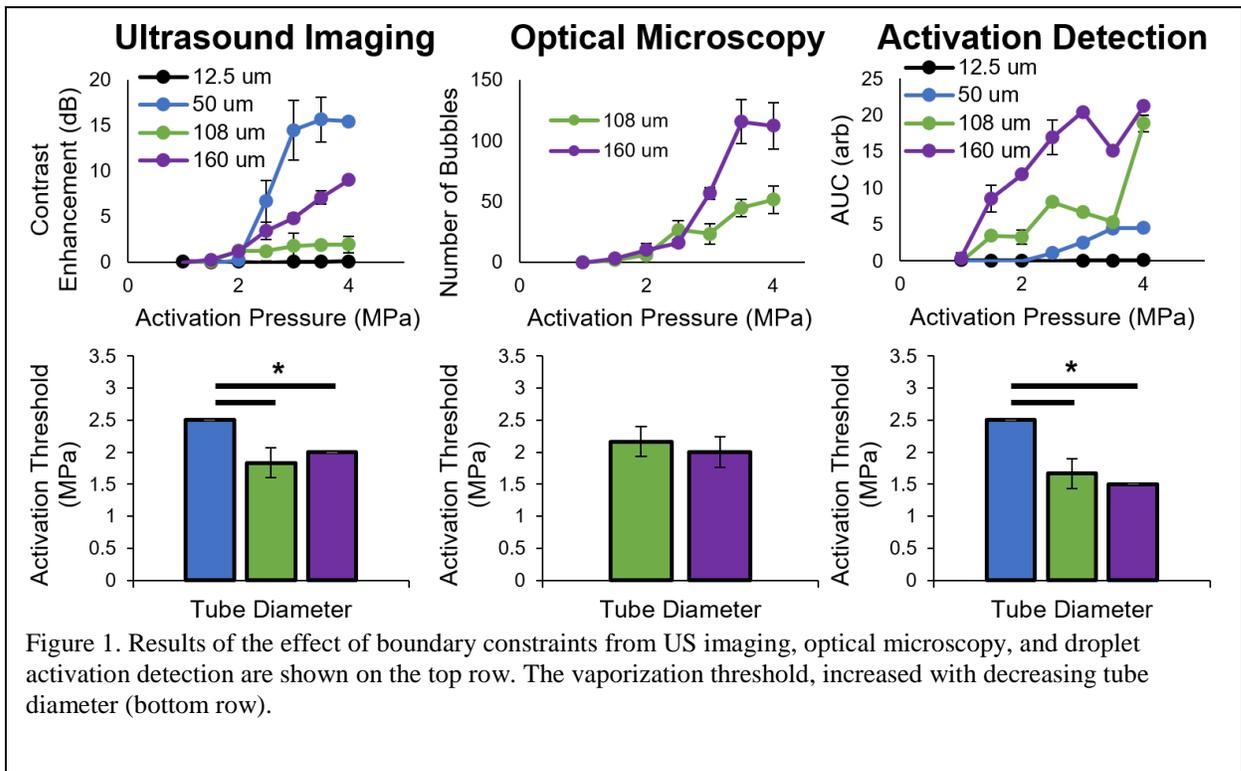
The vaporization of low boiling-point phase change contrast agents (PCCAs) using ultrasound has been explored in vitro and in vivo. However, it has been reported that the pressure required for vaporization (activation) is higher in vivo, even after attenuation is accounted for. In this study, the effect of boundary constraints and added ambient pressure on PCCA vaporization pressure threshold is explored.

## **Methods**

PCCAs with liquid decafluorobutane (DFB) cores were vaporized using an L11-5 linear array driven by a Verasonics ultrasound system, using 5-cycle pulses at 5 MHz with a range of peak-negative pressures between 1 and 4 MPa. The vaporization threshold was selected as the first pressure to produce at least 10 % of the maximum activation. The amount of activation was measured using contrast ultrasound, optical microscopy, and by capturing the vaporization signals produced when PCCAs are activated. The effect of boundary constraints was explored by activating PCCAs in microtubes with diameters of 12.5, 50, 108, and 160  $\mu\text{m}$ . A chamber was pressurized with hydrostatic pressures up to 2.5 psi to investigate the effect of ambient pressure on the activation threshold, using ultrasound imaging. Furthermore, the vaporization threshold was found In Vivo in the kidneys of rats using ultrasound imaging.

## **Results and Discussion**

The results indicate that the activation threshold of DFB droplets is higher for smaller tubes (Fig. 1). Activation was not detected in the 12.5  $\mu\text{m}$  tube with any of the measurement techniques, and was not observed in the 50  $\mu\text{m}$  tube using optical microscopy. Surprisingly, increased hydrostatic pressures did not affect the vaporization threshold (Fig. 2). The In Vivo results confirm that the vaporization threshold is higher in vivo. Some of the discrepancy may be attributed to the boundary constraints imposed on PCCAs by blood vessels, since the data presented here indicates that the threshold increases with decreasing tube size, but more work is required to discover all the factors that affect the vaporization threshold In Vivo.



# Monodisperse ultrasound contrast agents: Synthesis, stability, efficiency, and dilatational elasticity

*Tim Segers<sup>a,c,\*</sup>, Leonie de Rond<sup>a</sup>, Pieter Kruizinga<sup>b</sup>, Maarten P. Kok<sup>a</sup>, Guillaume Lajoinie<sup>a</sup>, Emmanuel Gaud<sup>a</sup>,  
Nico de Jong<sup>b</sup>, Detlef Lohse<sup>a</sup>, Peter Frinking<sup>c</sup>, and Michel Versluis<sup>a</sup>*

<sup>a</sup> *Physics of Fluids Group, University of Twente, Enschede, The Netherlands*

<sup>b</sup> *Erasmus MC, Biomedical Engineering, Erasmus MC, Rotterdam, The Netherlands*

<sup>c</sup> *Bracco Suisse SA, Geneva, Switzerland*

\* *t.j.segers@utwente.nl*

Monodisperse microbubble ultrasound contrast agents are often proposed to boost the sensitivity of contrast-enhanced ultrasound imaging. Moreover, they may improve the efficiency of therapeutic applications with microbubbles and ultrasound, such as drug or gene delivery, sonoporation and local opening of the blood-brain barrier. Here, we present an overview of our recent work on 3 different microfluidic methods to synthesize monodisperse microbubble populations, through acoustic bubble sorting<sup>4</sup> (Fig. 1A), microfluidic size sorting<sup>5</sup> (Fig. 1B), and flow-focusing<sup>2,3</sup> (Fig. 1C). In addition, we compare, for the first time, the acoustic sensitivity of monodisperse microbubble populations to that of a preclinical polydisperse agent.<sup>1</sup> The efficiency gain of the monodisperse populations as compared to that of the native agent, is approximately two orders of magnitude, see Fig. 1F. Furthermore, we show that the highly nonlinear response of monodisperse microbubbles can be exploited to confine scattering and attenuation to the focal region of clinically relevant ultrasound fields transmitted by a linear array transducer, see Figs. 1D and 1E. These nonlinear features of contrast agent behavior can be employed in monodisperse bubble suspensions to minimize shadowing effects in deep tissue imaging. Moreover, this effect will potentially allow for localized therapy with microbubbles and ultrasound through the spatial control of resonant microbubble oscillations. Finally, we present, high-precision acoustic measurements of the nonlinear shell elasticity of contrast microbubbles as a function of the surface area. These highly accurate measurements are now accessible for the first time through the use of well-controlled monodisperse bubble suspensions by tuning the surface dilatation through the ambient pressure. The shell elasticity was found to be highly dependent on the surface dilatation, see Fig. 1G. During bubble compression, the elasticity increases up to an elasticity of 0.6 N/m where the monolayer collapses upon further compression and the elasticity vanishes. During bubble expansion, the elasticity first drops monotonically to an elasticity of 0.35 N/m, after which it also collapses and drops to zero. Thus, we show by direct experimental evidence that indeed a phospholipid-coated microbubble is in a surface tensionless state when it is compressed, and that it has the interfacial tension of the surrounding medium upon expansion, see Fig. 1H. These findings not only validate the applicability of the shell buckling model that was introduced by Philippe Marmottant<sup>6</sup> in this conference in 2005, but also reveal the detailed features of the nonlinear interfacial shell behavior.

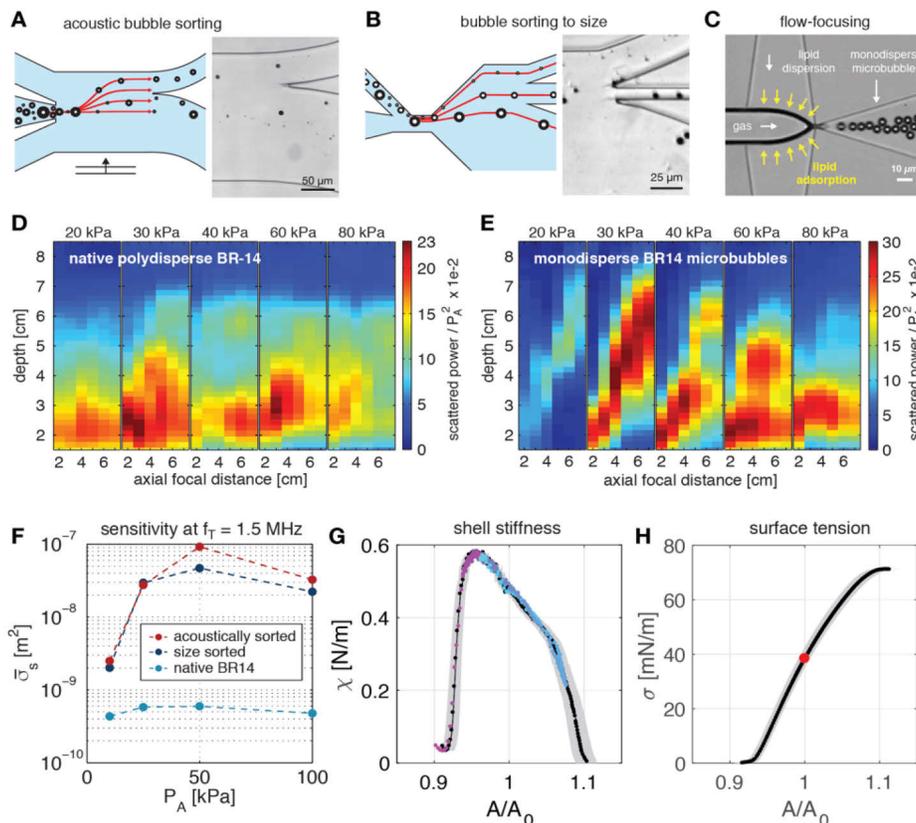


Figure 1 (A) Acoustic bubble sorting chip. (B) Bubble sorting to size. (C) Bubble formation by flow-focusing. Echo response of a polydisperse agent (D) and of a monodisperse agent (E) as a function of imaging depth and focal distance for different acoustic focal pressure amplitudes. (F) The sensitivity of a monodisperse agents compared to that of a native agent. (G) Surface dilatational shell elasticity. (H) Dilatational surface tension of phospholipid coated microbubbles.

## References

1. Segers T, Kruizinga P, Kok MP, Lajoinie GPR, de Jong N, Versluis M. "Monodisperse versus polydisperse ultrasound contrast agents: nonlinear response, efficiency, and imaging potential", to be submitted.
2. Segers T, Lohse D, Versluis M, Frinking P. Universal equations for the coalescence probability and long-term size stability of phospholipid-coated monodisperse microbubbles formed by flow-focusing. *Langmuir*, 2017;33:10329–10339.
3. T. Segers, L. de Rond, N. de Jong, M. Borden, and M. Versluis, "Stability of monodisperse phospholipid-coated microbubbles formed by flow-focusing at high production rates," *Langmuir* 32(16), 3937–3944 (2016).
4. Segers T, Versluis M. Acoustic bubble sorting for ultrasound contrast agent enrichment. *Lab. Chip*, 2014;14:1705–1714.
5. Kok MP, Segers T, Versluis M. Bubble sorting in pinched microchannels for ultrasound contrast agent enrichment. *Lab. Chip*, 2015;15.
6. P. Marmottant, S. Van Der Meer, M. Emmer, M. Versluis, N. De Jong, S. Hilgenfeldt and D. Lohse, *J. Acoust. Soc. Am.*, 2005, **118**, 3499 – 3505.

# Investigating the accumulation of submicron phase-shift droplets in tumours

*Brandon Helfield<sup>1,2</sup>, Kimoon Yoo<sup>1</sup>, Ross Williams<sup>1</sup>, Paul Sheeran<sup>1,2</sup>, David E. Goertz<sup>1,2</sup>, and Peter N. Burns<sup>1,2</sup>*

<sup>1</sup>*Physical Sciences Platform, Sunnybrook Research Institute, Toronto, Ontario, Canada*

<sup>2</sup>*Department of Medical Biophysics, University of Toronto, Ontario, Canada*

## Introduction

Submicron phase-shift droplets are an emerging class of ultrasound contrast agent. Unlike microbubble contrast agents, their relatively small size and long circulation times offer the potential to promote passive accumulation in the interstitium of solid tumours (the EPR effect). Upon acoustical conversion into detectable microbubbles, these agents could provide contrast outside of the vascular compartment as a means to detect early stage tumours, as well as a possible approach to increase the efficacy of extravascular drug delivery. Key to this work is the synthesis of droplets that are of sufficiently small size and stability to enable passive accumulation by EPR. In addition, the droplets should be capable of being vaporized by ultrasound within the diagnostic power and frequency range. Finally, the resulting interstitial bubbles should be stable enough to be detected by ultrasound, preferably using pulse sequences that rely on nonlinear resonant oscillation of the bubble. Such coupling of the bubble oscillation to incident ultrasound is also likely to be necessary to enable therapeutic effects, such as degradation of the extracellular matrix.

## Methods

Submicron droplets comprising phospholipid encapsulated liquid perfluorbutane were synthesized by a microbubble condensation method, resulting in a polydisperse distribution with a peak size of 150 nm. Droplets were administered to the tail vein (100  $\mu$ L followed by 100  $\mu$ L saline flush) of both healthy and tumour-bearing C3H mice (KHT hindlimb xenograft). Combined droplet vaporization and contrast-specific imaging was implemented on a Verasonics system with a Philips ATL L7-4 probe. First, low MI contrast images were acquired with a 4 MHz AMPI sequence for 20 frames. The system then immediately switched to a high MI droplet vaporization pulse, consisting of a series of 3-cycle, 5.2 MHz focused pulses steered over 10 mm, before collecting another 20 contrast frames. These datasets were exported and analyzed offline in MATLAB by manually drawing regions-of-interest over the contrast images prior to and post vaporization and evaluating the difference in median linearized pixel values. The in-vivo half-life of the agent was assessed in the kidney from measurements at 20 minute intervals for at least 3 hours. In a separate set of experiments, droplet extravasation was assessed by two successive activation sequences in the same imaging plane separated by 30 seconds to allow for the replenishment of intravascular agent, allowing its differentiation from stationary agent. This sequence was performed in both the kidney and hindlimb tumour of the same animal, and extravasation then estimated as a percent difference in contrast signal between the first (extravasated + intravascular agent) and second (intravascular agent only) vaporization sequences.

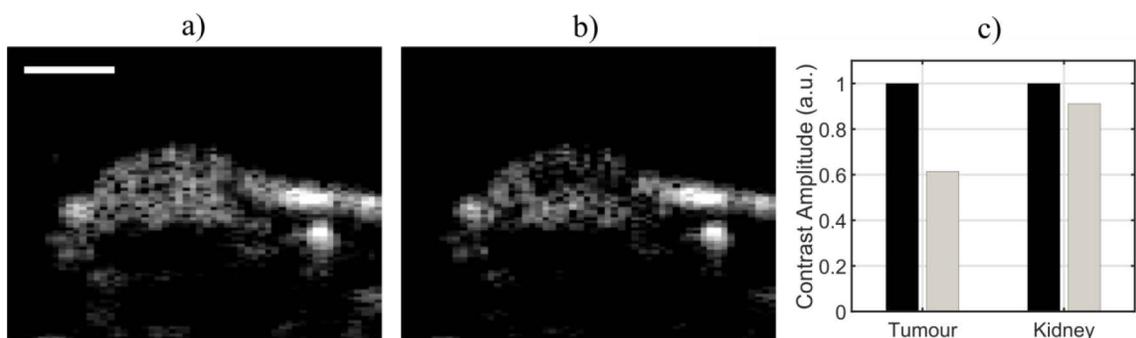


Figure 1: Contrast image (AMPI sequence at 4 MHz) of a mouse tumor xenograft immediately after (a) the first and (b) second droplet vaporization (taken 1 minute apart) at approximately 20 minutes post droplet injection. Scale bar is 5 mm. These images are log compressed with a dynamic range of 35 dB. (c) Contrast signal after successive droplet vaporization sequences in the tumour and the kidney for the mouse depicted in panels a and b, highlighting a decrease of 40% and 8.5% in the tumour and kidney, respectively.

## Results and Conclusions

The in-vivo circulating half-life of the droplet formulation was determined to be  $45 \pm 7$  minutes ( $n=5$ , reported as mean  $\pm$  standard deviation). The percent difference in contrast signal generated from the two successive vaporization sequences post-injection was significantly larger in the tumour ( $p<0.01$ ), ranging between 24% to 48%, while spanning 0.5% to 23% in the kidney ( $n=4$ ; Fig. 1). These data suggest that the droplet formulation can be vaporized in-vivo at clinical frequencies, and the subsequent microbubbles can be imaged using the same probe with an integrated pulse sequence operating within normal diagnostic limits. Further, the work suggests that this submicron phase-shift droplet formulation exhibits a sufficient circulation time to preferentially accumulate within tumour tissue, with a measurable effect within 20 minutes post-injection.

# On contrast agents for elasticity imaging

*Niloufar Saharkhiz<sup>1</sup>, Hasan Koruk<sup>1,2</sup>, James Choi<sup>1</sup>*

<sup>1</sup>*Department of Bioengineering, Imperial College London, London, UK*

<sup>2</sup>*Mechanical Engineering Department, MEF University, Istanbul, Turkey*

## Introduction

Ultrasound contrast agents in the form of microbubbles are used to enhance tissue echogenicity and aid in the diagnosis of diseases. Since its introduction 30 years ago, these microbubbles have been primarily used for its ability to improve image contrast by scattering imaging pulses. This is the basis for nearly all clinically approved ultrasound imaging methods that use contrast agents and most contrast-based imaging technologies being developed.

Here, we explore the possibility of using microbubbles as contrast agents for imaging elasticity. Rather than using scattering to improve contrast, we propose the use of the primary Bjerknes force, which pushes microbubbles in the direction of wave propagation. This technology has the potential to break fundamental limits of conventional ultrasound elasticity imaging methods that do not use contrast agents, such as contrast, depth, and spatial resolution.

## Methods

In conventional ultrasound elasticity imaging, (1) an ultrasound beam pushes tissue using an acoustic radiation force, (2) the tissue deformation is tracked using ultrasound imaging, and (3) a model is used to measure the tissue elasticity. Here, we evaluated whether a microbubble exposed to an ultrasound beam could generate enough force to displace a material of similar stiffness to human tissue. Lipid-shelled microbubbles (mean diameter:  $2.1 \pm 1.3 \mu\text{m}$ ) were administered into a wall-less 0.8-mm-in-diameter tunnel of a tissue-mimicking material (5%, 7.5%, and 10% gelatin). Ultrasound pulses ( $f_c$ : 1, 3.5, 5 MHz) were applied onto the microbubbles, which forced the microbubbles against the tissue wall to cause a transient deformation. Both the tissue deformation and microbubble movement were observed with a high-speed optical camera. Different acoustic pressures were evaluated for different microbubble concentrations (concentration: 1X to 20X the clinical dose) while a high-speed optical camera recorded the dynamics of microbubble movement and wall deformation.

## Results

We discovered that microbubbles exposed to ultrasound can generate deformations ( $>1 \mu\text{m}$ ) that are enough for measuring elasticity with ultrasound imaging. Sufficient deformations were generated using low pressures, low microbubble concentrations, and for a range of centre frequencies, providing flexibility in the range of exposure conditions that can be used. Microbubbles (5X the clinical dose) deformed 5% gelatin phantoms (Young's modulus: 1.5 kPa, similar to liver) by  $\sim 10 \mu\text{m}$  using a 1, 3.5, or 5 MHz centre frequency pulse and a peak-rarefactional pressure of 470, 785, and 1210 kPa, respectively. At high pressures, high displacements occurred rapidly ( $>20 \mu\text{m}$  within microseconds) but decreased to a lower, stable displacement over time. At low pressures, the deformation rise was slower, but remained stable throughout the ultrasound exposure.

## **Conclusions**

Our results show that microbubbles can be used to deform tissue using a diverse array of microbubble concentrations, acoustic pressures, and excitation frequencies. We are continuing to understand and control the microbubble and deformation dynamics with the hope of creating the first contrast-enhanced elasticity imaging technology.

# In vivo evaluation of monosize microbubbles: acoustic efficiency and safety

Victor Jeannot<sup>1</sup>, Alexandre Helbert<sup>1</sup>; Anne Lassus<sup>1</sup>; Emmanuel Gaud<sup>1</sup>; Tim Segers<sup>2</sup>; Catherine Botteron<sup>1</sup>; Peter Frinking<sup>1</sup>.

<sup>1</sup> Bracco Suisse SA, Geneva, Switzerland – <sup>2</sup> University of Twente, The Netherlands

## Background information

The use of ultrasound (US) and microbubbles to enhance drug or gene delivery to organs, or directly to tumors, is currently a hot topic. Monosize microbubbles (MSB) are a new generation of microbubbles having a narrow calibrated and controlled size distribution that could represent a breakthrough, not only for US imaging, but more particularly for therapeutic procedures using US. It is expected that MSB have a uniform acoustic response, contrary to the commercially available polydisperse contrast-agent microbubbles. This uniform response can potentially help improving the understanding of the different mechanisms responsible for drug and gene delivery by excluding bubble size-related effects. Moreover, by accurately controlling microbubble size, cavitation conditions could be optimized resulting in a higher efficiency and improved safety profile. However, to date, few data are available on the in vivo acoustic efficiency and safety of MSB. In this context, we present here the results of a comparison study between MSB with different sizes and BR38, a polydisperse contrast agent.

## Material and Method

Three formulations of MSB with different mean diameters (viz. 3.0, 3.9 and 5.4  $\mu\text{m}$ ) were prepared using microfluidic flow-focusing technology. These sizes were selected based on in vitro acoustic characterization of MSB with sizes ranging from 3 to 7  $\mu\text{m}$  in diameter. The 2.5-MHz resonance frequency of the 3.9- $\mu\text{m}$  MSB formulation coincided with the transmit center frequency of a curved-linear transducer (C5-1) connected to a Philips EPIQ 7 ultrasound system, which was used in this study. For the 3.0 and 5.4  $\mu\text{m}$  MSB formulations, the resonance frequencies were 3.5 and 1.9 MHz, respectively; thus these MSB formulations were excited below and above resonance, respectively.

First, multiple doses of MSB (3.9  $\mu\text{m}$ ), ranging from 0.1 to 2  $\mu\text{L}$  gas/kg, were injected into rats ( $n=3$ ), and the optimal experimental dose was determined by visual assessment of contrast enhancement in the kidneys and by quantification using VueBox® software (Bracco Suisse SA). Next, the acoustic efficiency of each MSB formulation was measured in three rats; the acoustic efficiency was determined by calculating the ratio of the mean echo power (measured using VueBox®) normalized by the microbubble number concentration. All animals received random injections of BR38 (0.16  $\mu\text{L}$  gas/kg) and the 3 different MSB formulations (0.06  $\mu\text{L}$  gas/kg). Safety of MSB was assessed by monitoring physiological parameters (viz., heart rate, breath rate, SpO<sub>2</sub>) and by evaluating potential pathological changes after injecting extremely high doses (8 to 40  $\mu\text{L}$  gas/kg).

## Results

The acoustic efficiency of all MSB formulations was at least 20 times higher than that of BR38. For the resonant MSB formulation (3.9  $\mu\text{m}$  diameter) the sensitivity gain was another factor 2 as compared to the other MSB formulations driven off-resonance (i.e. with diameters of 3.0 and 5.4  $\mu\text{m}$ ). Concerning safety, extremely high doses of MSB (viz. more than 100-600 times the efficiency dose of 0.06  $\mu\text{l}$  gas/kg) did not provoke changes in physiological parameters. In addition, safety assessment performed 24 h post injection did not reveal pathological changes in brain tissues.

## Conclusion

We demonstrated that, for the conditions used in this work, the acoustic efficiency of MSB is at least 20 times higher compared to BR38. No safety concerns were highlighted. These results demonstrate the high potential of MSB and warrant further evaluation for therapeutic US applications.

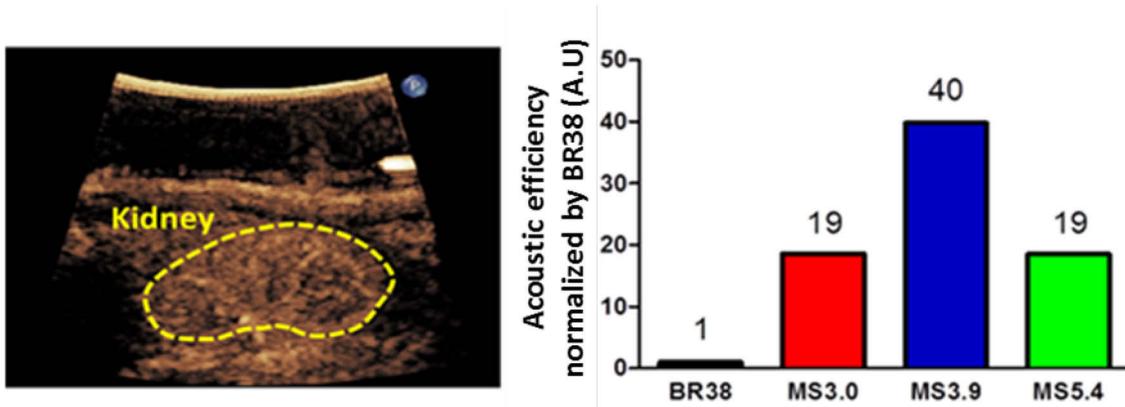


Figure 1: Monosize microbubbles in a rat kidney during peak enhancement (left). Acoustic efficiency for BR38 and MSB with different diameters (right). The increase in sensitivity was 40 times higher for the resonant MSB formulation with a mean diameter of 3.9  $\mu\text{m}$  with respect to BR38.

# Safety and feasibility of contrast echocardiography for the evaluation of patients with HeartMate 3 left ventricular assist devices

Schinkel AFL<sup>1</sup>, Akin S<sup>1,2</sup>, Strachinaru M<sup>1</sup>, Muslem R<sup>1</sup>, Soliman Oll<sup>1,3</sup>, Brughts JJ<sup>1</sup>, Constantinescu AA<sup>1</sup>, Manintveld OC<sup>1</sup>, Caliskan K<sup>1</sup>

<sup>1</sup>Department of Cardiology, Thoraxcenter Room Ba304, Erasmus MC, 's-Gravendijkwal 230, 3015 CE Rotterdam, The Netherlands.

<sup>2</sup>Department of Intensive Care, Erasmus MC, 's-Gravendijkwal 230, 3015 CE Rotterdam, The Netherlands.

<sup>3</sup>Cardialysis Clinical Trials Management and Core Laboratories, PO Box 2125, 3000 CC Rotterdam, The Netherlands

## Aims

Patients with a left ventricular assist device (LVAD) are challenging to evaluate using conventional imaging techniques, such as standard echocardiography (SE). The aim of this pilot study was to evaluate the potential of contrast echocardiography (CE) for the evaluation of the left ventricle (LV).

## Methods and results

This prospective study included 14 ambulatory patients (mean age  $58 \pm 9$  years, 79% male) with a LVAD (all HeartMate 3, Abbott Laboratories, Chicago, IL, USA). Nine (64%) patients had an ischaemic cardiomyopathy, and 5 (36%) had a non-ischaemic cardiomyopathy. All patients underwent SE and CE using intravenous administration of Sonovue contrast agent (Bracco, Milan, Italy). The echocardiograms were assessed by three observers, using a standard 17-segment model of the LV. Left ventricular end-diastolic volume (LVEDV) was assessed using the biplane Simpson method. The contrast agent was well tolerated by all patients, without any side effects. Overall, SE allowed visualization of 57% of LV segments (135/238) and CE allowed visualization of 79% of LV segments (187/238),  $P < 0.001$ . Per patient, SE resulted in visualization of  $9.6 \pm 5.2$  segments and CE was able to visualize  $13.4 \pm 5.8$  segments ( $P < 0.001$ ). Administration of contrast agent significantly improved the assessment of LVEDV (feasibility SE: 36% vs. CE: 79%,  $P < 0.05$ ).

## Conclusion

Routine use of a contrast agent appears safe when used in patients having a new third generation LVAD and may enhance the diagnostic accuracy of transthoracic echocardiography in these patients. LV size determination can be obtained more often due to improved LV visualization using contrast agent.

**Keywords:** HeartMate 3; cardiomyopathy; contrast-enhanced echocardiography; left ventricular assist device

## Reference

*Eur Heart J Cardiovasc Imaging.* 2017 Jul 26. doi: 10.1093/ehjci/jex177. [Epub ahead of print]

# Nonlinear microbubble ultrasound imaging for improved decompression stress quantification in humans

*James S. E. Hensel<sup>1</sup>, David Q. Le<sup>1</sup>, Costantino Balestra<sup>2,3</sup>, Meng-Xing Tang<sup>4</sup>, Paul A. Dayton<sup>1,5</sup>, Virginie Papadopoulou<sup>1</sup>*

<sup>1</sup> *Joint Department of Biomedical Engineering, The University of North Carolina and North Carolina State University, Chapel Hill, NC, USA;*

<sup>2</sup> *Environmental & Occupational Physiology Laboratory, Haute Ecole Paul Henri Spaak, Brussels, Belgium;*

<sup>3</sup> *Divers Alert Network (DAN) Europe Research Division;*

<sup>4</sup> *Department of Bioengineering, Imperial College London, London, UK;*

<sup>5</sup> *Eshelman School of Pharmacy, UNC Chapel Hill, Chapel Hill, NC, USA*

*\*corresponding author: papadopoulou@unc.edu*

## Background

Circulating gas bubbles can be detected with ultrasound imaging after scuba diving and are a marker of ‘decompression stress’. Higher bubble loads post-dive are associated with a higher decompression sickness risk, but bubbles are observed even after shallow, conservative and uneventful dives (completely asymptomatic). These are assessed using either subclavian Doppler or B-mode echocardiography, where they normally appear in the venous but not arterial circulation as they are filtered by the lungs [1]. DCS risk, but also the amount of venous gas emboli (VGE) observed post dive has been shown to exhibit a significant amount of yet unexplained inter- and intra- subject variability, even for a same controlled diving exposure [2].

## Aim

We hypothesize that the ability to better estimate the quantity and size of decompression bubbles, in both the venous and arterial circulation, could yield new information on degassing dynamics post dive. We investigate whether multi-pulse linear signal cancellation techniques used in contrast imaging could be adapted in post-dive echocardiography to cancel out large microbubble signal (away from resonance) so as to detect preferentially small microbubbles (<10  $\mu\text{m}$ ) that are not resolvable on standard B-mode echocardiography (estimated detectable VGE size >35  $\mu\text{m}$ ) [3].

## Methods

In **vitro**: Contrast microbubbles (<10  $\mu\text{m}$ ) at different concentrations are flown in a 200  $\mu\text{m}$  tube surrounded by free flowing gas emboli of different sizes (>50  $\mu\text{m}$ ) in a water beaker or tissue-mimicking phantom encasing filled with water. Image sequences are acquired in dual B-mode and contrast CPS mode (Siemens Sequoia with 15L8S transducer, 7 MHz transmit frequency, MI < 0.2, 11 fps), and/or dual B-mode and contrast PI (Verasonics Vantage with L12-5 transducer, 4 MHz transmit frequency, MI < 0.2, plane wave imaging with 6 angles compounding over 30°

angle range, 1000 fps), with both transducers orthogonal to each other for simultaneous acquisitions on the phantom encasing. In vivo: Image processing techniques were used to extract the venous and arterial heart chambers for previously acquired echocardiography recordings using a portable ultrasound machine (Mindray, M9), comparing bubble counts and overall intensity in various regions of interest for each subject. Data consisted of B-mode and contrast mode echocardiography recordings for 7 subjects before (baseline) and at 21, 56, 91 and 126 min post dive, after a same standardized pool scuba dive (400 kPa for 20 minutes) for 7 subjects, with all imaging settings constant between acquisitions [4].

## Results and Discussion

In vitro, large microbubbles are effectively cancelled out in contrast mode imaging (Fig. 1), although higher frame rate imaging is needed to effectively negate motion artefacts. In vivo, the intensity in the heart chambers increases post dive before decreasing again even when no emboli were observed on B-mode echocardiography for these subjects (indicating that no large bubbles were present), in both the arterial and venous sides (Fig. 2). It therefore appears that smaller microbubbles ( $<10\ \mu\text{m}$  so they can bypass the pulmonary filter in the absence of arterio-venous shunting) are present, and that these follow a different time-course post-dive than larger VGE.

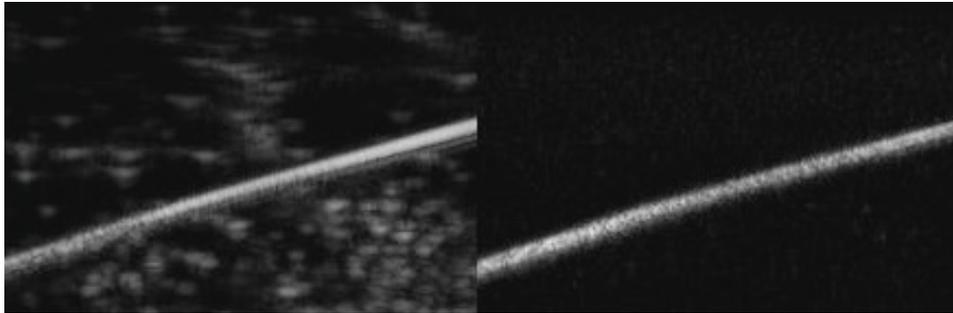


*Fig.1: Example of dual B-mode (left) and contrast CPS mode (right) (Siemens Sequoia) of large gas bubbles free flowing in a water beaker around a  $200\ \mu\text{m}$  tube filled with decafluorobutane contrast microbubbles ( $<10\ \mu\text{m}$ ). The multi-pulse linear signal cancellation used in contrast mode is seen to effectively suppress most of the large bubble signal (away from resonance) as long as they are moving slowly enough for this frame rate acquisition (here 11 Hz).*

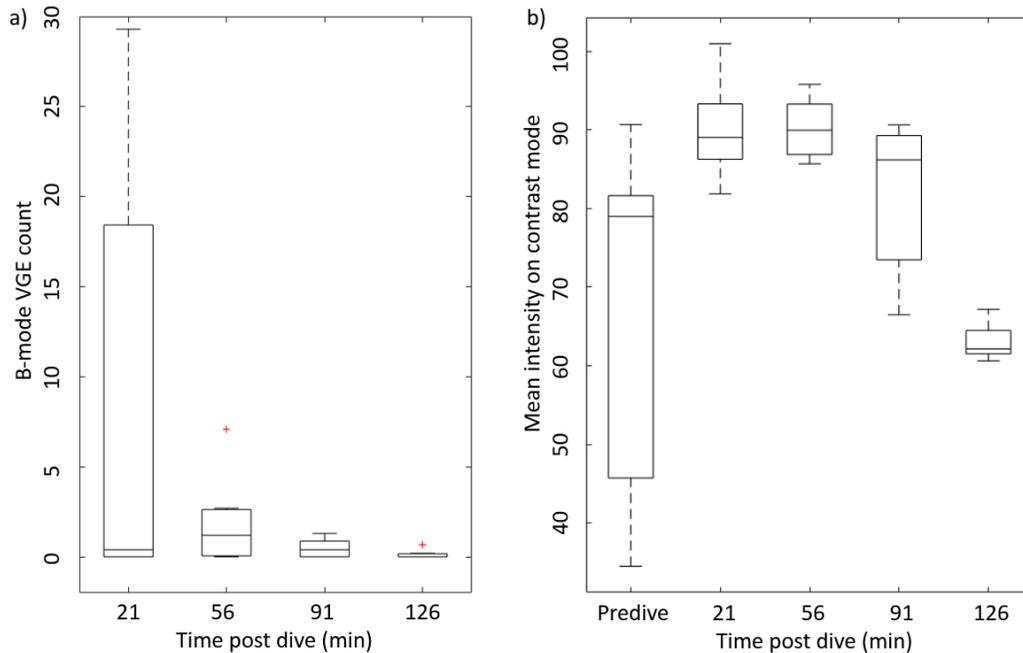


Fig.2: a) Box-plots of VGE counts in the venous heart chambers at 21, 56, 91 and 126 min post dive (no VGE pre-dive), showing large variability between subjects despite exact same dive profile and conditions. b) Box-plots of the mean intensity of the arterial/venous (similar values) heart chambers pre-dive and at 21, 56, 91 and 126 min post-dive, for all seven divers. The mean intensity of contrast mode echocardiography images increased post dive, in both the venous and arterial chambers for all seven subjects, irrespective of whether large circulating emboli were present in the venous chambers post dive. Individual peak times of large VGE or signal increase in contrast mode were not matched, indicating a different time-course of these bubble populations post-dive.

**Acknowledgements:** this study is funded by the Divers Alert Network/R.W. (Bill) Hamilton Memorial Dive Medicine Research Grant administered by the Women Divers Hall of Fame. We are grateful to all volunteer divers, the NEMO pool in Brussels for hosting experiments and Mindray for technical support, as well as Sigrid Theunissen, Peter Germonpré, George Obeid, Antoine Boutros, Robert J. Eckersley and David Cosgrove for their help with the human data acquisition.

## References

1. Papadopoulou V, Eckersley RJ, Balestra C, Karapantsios TD, Tang M-X. A critical review of physiological bubble formation in hyperbaric decompression. *Advances in colloid and interface science*. 2013;191-192(0):22-30.
2. Papadopoulou V, Germonpré P, Cosgrove D, Eckersley RJ, Obeid G, Boutros A, Tang MX, Theunissen S, Balestra C. Echocardiography bubble counting after a NEMO33 dive: The need for continuous assessment. *The 2016 European Underwater and Baromedical Society (EUBS) conference, Geneva, Switzerland, 13-16 Sept 2016*.
3. Papadopoulou V, Tang M-X, Balestra C, Eckersley RJ, Karapantsios TD. Circulatory bubble dynamics: from physical to biological aspects. *Advances in Colloid and Interface Science*. 2014 Apr;206C:239-249.
4. Papadopoulou V, Balestra C, Theunissen S, Germonpré P, Obeid G, Boutros A, Eckersley RJ, Dayton PA, Cosgrove D, Tang M-X. Can current contrast mode echocardiography help estimate bubble population dynamics post-dive? *The 2017 European Underwater and Baromedical Society (EUBS) conference, Ravenna, Italy, 13-16 Sept 2017*.

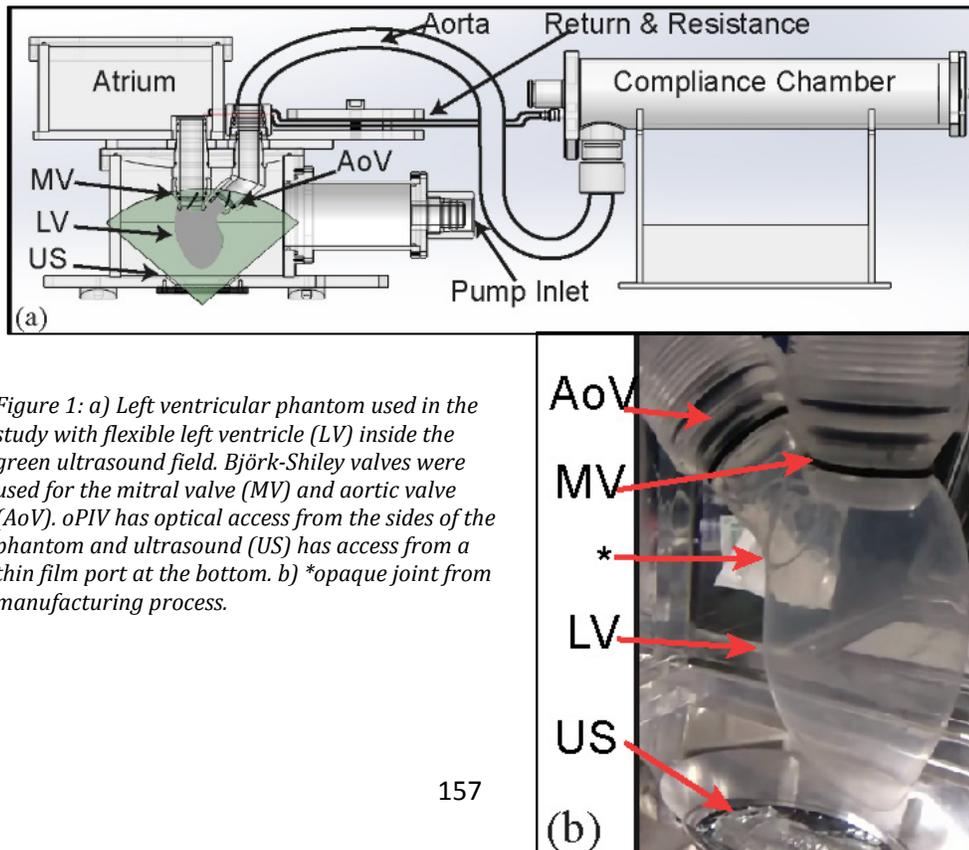
# High Frame Rate Echo-Particle Image Velocimetry for Estimating Flow Patterns in a Left Ventricular Phantom

Jason Voorneveld<sup>1</sup>, Aswin Muralidharan<sup>2</sup>, Timothy Hope<sup>1</sup>, Hendrik J. Vos<sup>1</sup>, Pieter Kruizinga<sup>1</sup>, Antonius F. W. van der Steen<sup>1</sup>, Frank J. H. Gijsen<sup>1</sup>, Sasa Kenjeres<sup>2</sup>, Nico de Jong<sup>1</sup>, and Johan G. Bosch<sup>1</sup>

<sup>1</sup> Department of Biomedical Engineering, Thoraxcenter, Erasmus MC, Rotterdam, The Netherlands

<sup>2</sup> Transport Phenomena Section, Department of Chemical Engineering, Faculty of Applied Sciences, Delft University of Technology, Delft, The Netherlands

Echocardiographic determination of multi-component blood flow dynamics in the left ventricle remains a challenge. In this study we compare contrast enhanced, high frame rate (1000 fps) echo particle image velocimetry (ePIV) against optical particle image velocimetry (oPIV, gold standard), in a realistic left ventricular phantom. We find that ePIV compares well to oPIV, even for the high velocity inflow jet (normalized RMSE =  $9\pm 1\%$ ). We show that ePIV and oPIV resolve similar flow structures. The coarser resolution of ePIV does result in increased variance and blurring of smaller flow structures when compared to oPIV. However, both modalities are in good agreement with each other for the high energy flow structures. We conclude that high frame rate ePIV can accurately estimate the high velocity diastolic inflow jet and the high energy flow structures in a left ventricular setting.



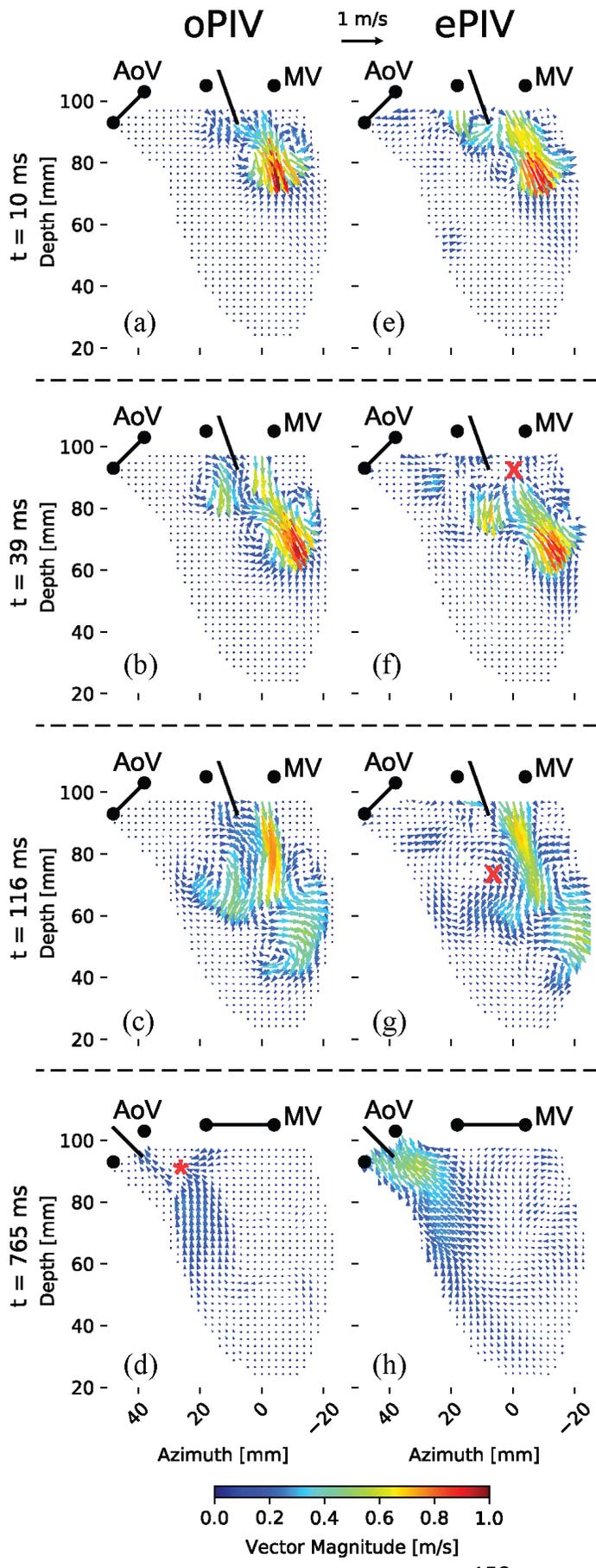


Figure 2: Side-by-side comparison of simultaneous ePIV (e-h) and oPIV (a-d) recordings. First three columns (a-c & e-g) show diastolic inflow jet. Very good agreement is observed during this high velocity filling phase, except for a few disparities (X) caused by clutter artifacts in the ePIV recordings. During systole, comparison was complicated by an opaque joint in the LV phantom (see Figure 1.b: \*) which deteriorated oPIV analysis.

# Gas Vesicles: Acoustic Biomolecules for Ultrasound Imaging

*Mikhail G. Shapiro, PhD*

*Assistant Professor of Chemical Engineering  
California Institute of Technology*

Expanding the capabilities of ultrasound for biological and diagnostic imaging requires the development of contrast agents linked to cellular and molecular processes *in vivo*. In optical imaging this is commonly accomplished using fluorescent biomolecules such as the green fluorescent protein. Analogously, we recently introduced gas vesicles (GVs) as the first acoustic biomolecules for ultrasound<sup>1</sup>. GVVs are physically stable gas-filled protein nanostructures (~250 nm) naturally expressed in aquatic photosynthetic microbes as a means to regulate buoyancy. Purified GVVs produce robust ultrasound contrast across a range of frequencies at picomolar concentrations, exhibit nonlinear scattering to enable enhanced detection versus background *in vivo*, and have sequence-determined thresholds for pressure-induced collapse to enable multiplexed imaging. Here, I will present our recent progress in understanding the biophysical and acoustic properties of these biomolecular contrast agents<sup>2</sup>, engineering their mechanics and targeting at the genetic level<sup>3,4</sup>, developing ultrasound pulse sequences to enhance their detection *in vivo*<sup>5</sup> and expressing them heterologously as acoustic reporter genes<sup>6</sup>.

## References

1. Shapiro, M.G. *et al.* *Nature Nanotechnology* 9, 311-316 (2014)
2. Cherin, M. *et al.* *Ultrasound in Medicine and Biology* 43, 1016-1030 (2017)
3. Lakshmanan, A. *et al.* *ACS Nano* 10, 7314-7322 (2016)
4. Lakshmanan, A. *et al.* *Nature Protocols* 12, 2050-2080 (2017)
5. Maresca, D. *et al.* *Applied Physics Letters* 110, 073704 (2017)
6. Bourdeau, R.W. *et al.* *In press.*

*More information at <http://shapirolab.caltech.edu>.*

# A Versatile Chromo-responsive Photopolymerized Phase-Change Droplets as Contrast Agent for Ultrasound Imaging

*Yosra Toumia, Barbara Cerroni, Livia Bianchi, Letizia Oddo, Fabio Domenici and Gaio Paradossi*

*Università degli Studi di Roma Tor Vergata, Dipartimento di Scienze e Tecnologie Chimiche, Via della Ricerca Scientifica, 00144, Rome, Italy*

Ultrasound imaging (US) is one of the most used diagnostic tools in medicine. Many studies focused on improving the US contrast by the means of echogenic microbubbles (MBs) made of a polymeric or lipid shell encapsulating a gaseous core (air, SF<sub>6</sub>, etc). Recently, phase-change contrast agents have particularly attracted interest as next generation US contrast agents in order to approach diagnostic and therapeutic modalities that are beyond the functionality of the simple MBs such as extravasation in tumour tissues and drug loading and delivery capacity. Phase-change contrast agents consist of perfluorocarbons (PFC) droplets stabilized with lipid or polymer shells. The hydrophobic core provides an extended life time and its liquid-gas transition can be triggered by US to produce MBs with echogenic properties in a process called acoustic droplet vaporization (ADV).<sup>1</sup> Effort is dedicated to improve the colloidal stability of the droplets and therefore their shelf-life by hindering the coalescence process typical of physical self-assembly. In this context, lipids with photopolymerizable diacetylene moieties were suggested as possible systems combining the good echogenicity of MBs with lipid shells and the high stability of those with polymeric shells.<sup>2</sup> Herein, we present novel submicron PFC droplets, with an average diameter of 500 nm, stabilized with a monolayer of an amphiphilic fatty acid, i.e. 10,12-Pentacosadiynoic acid (PCDA), crosslinkable upon UV irradiation. The PCDA molecule is oriented with its lipophilic tail towards PFC, whereas its hydrophilic carboxylic head points towards the aqueous phase. This arrangement gives the system a chemical versatility for a facile functionalization. The photocrosslinking is evidenced by an intense blue color appearance due to a ene-yne conjugation sequence conjugation. Moreover, the poly-PCDA droplets can undergo an irreversible chromatic transition from a non-fluorescent blue color to a red fluorescent color when exposed to external stimuli (pH, temperature, amine binding).<sup>3</sup> Polymerized PCDA-PFC droplets were characterized by dynamic light scattering (DLS), bright field and confocal microscopy and their cytotoxicity was evaluated on NIH 3T3 fibroblast cells. ADV efficiency and acoustic attenuation measurements of both the red and the blue form have been tested using a sonoprotator at 1 MHz. Poly-PCDA-PFC droplets show good stability and an average diameter of  $5 \pm 2 \mu\text{m}$  after ADV which makes them a potential new ultrasound contrast agent.

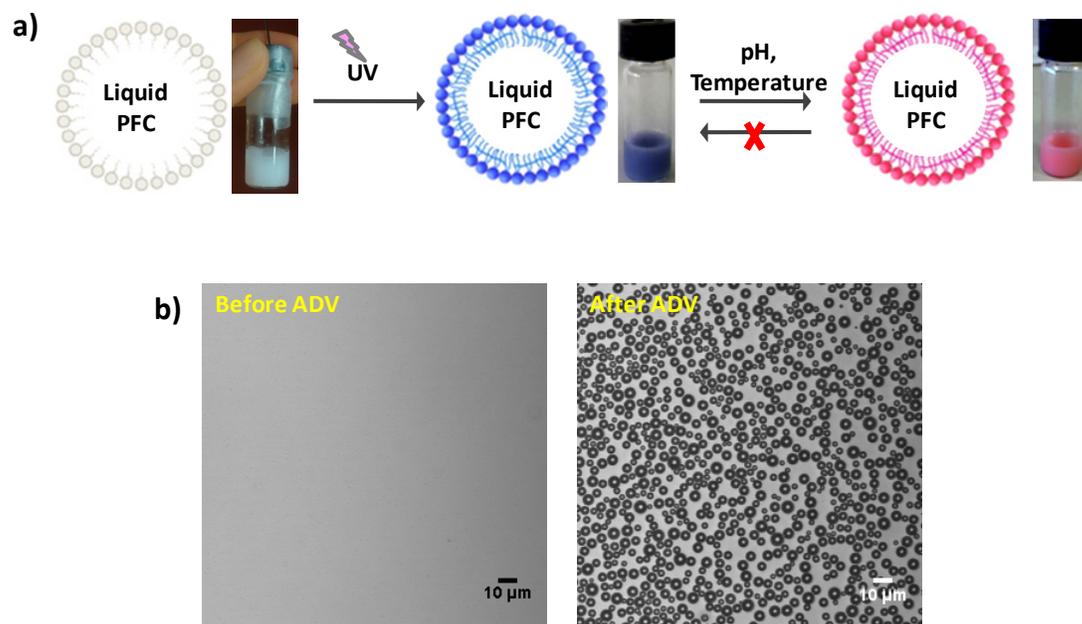


**Figure 1.** a) Schematic representation of crosslinked poly-PCDA-PFC droplets and their chromatic transition under external stimuli, b) Bright field microscopy of poly-PCDA-PFP droplets before and after phase transition in human serum upon 30s ultrasound exposure.

## References

1. Sheeran, P. S.; Dayton, P. A. Phase Change Contrast Agents for Imaging and Therapy. *Curr. Pharm. Des.* 2012, 18, 2152-2165.
2. Park, Y.; Luce, A. C.; Whitaker, R. D.; Amin, B.; Cabodi, M.; Nap, R. J.; Szeleifer, I.; Cleveland, R. O.; Nagy, J. N.; Wong, Y. J. Tunable Diacetylene Polymerized Shell Microbubbles as Ultrasound Contrast Agents. *Langmuir* 2012, 28, 3766-3772.
3. de Oliveira, C. P.; de Fátima Ferreira Soares, N.; Fontes, E. A. F.; de Oliveira, T. V.; Filho, A. M. M. Behaviour of polydiacetylene vesicles under different conditions of temperature, pH and chemical components of milk. *Food Chem.* 2012, 135, 1052–1056.

# Magnetically and biochemically targeted ultrasound-responsive nanodroplets for therapy of brain metastases

*Oliver Vince<sup>a</sup>, Luca Bau<sup>a</sup>, Alex Richards<sup>a</sup>, Sarah Peeters<sup>b</sup>, Nicola Sibson<sup>b</sup> and Eleanor Stride<sup>a</sup>*

*<sup>a</sup>Institute of Biomedical Engineering, Department of Engineering Science, University of Oxford, OX3 7DQ*

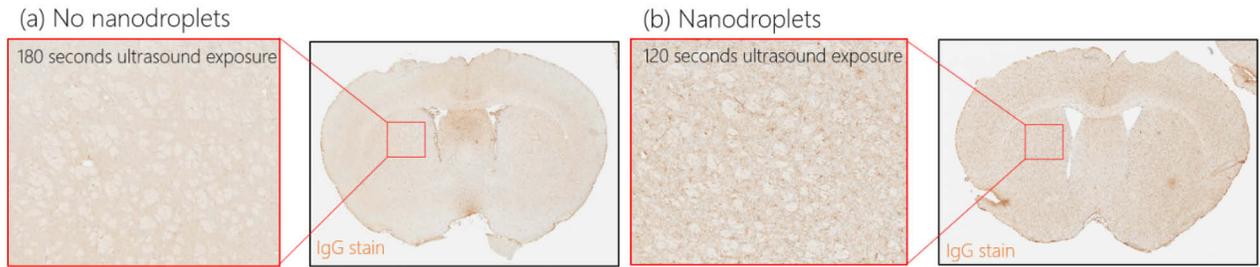
*<sup>b</sup>Oxford Institute for Radiation Oncology, Department of Oncology, University of Oxford, OX3 7DQ*

Metastatic tumors in the brain represent one of the leading causes of death from cancer, becoming increasingly prevalent as systemic therapies for primary tumors continue to improve[1]. They often cause severe disability before they are large enough to detect with conventional imaging and current treatments are largely ineffective and/or associated with significant side effects due to their lack of targeting[2].

As metastatic tumors form in existing blood vessels in the brain, they cause the endothelial cells adjacent to them to increase the expression of vascular cell adhesion molecule-1 (VCAM1). Conjugating MRI contrast agents with a monoclonal antibody for VCAM1 (anti-VCAM1) has previously allowed detection of brain tumor volumes two to three orders of magnitude smaller ( $0.3\text{--}3 \times 10^5$  cells) than those volumes currently detectable clinically ( $10^7\text{--}10^8$  cells)[3].

In this study, a novel magnetic nanodroplet formulation has been developed and successfully conjugated with anti-VCAM-1. Preliminary in vivo tests have shown that these anti-VCAM-1 nanodroplets can be successfully targeted to both inflamed areas of the brain and brain metastases (Figure 1c) in a murine model. When subjected to sufficient peak-negative pressures or temperature increases, these perfluorocarbon-based nanodroplets undergo a phase transition from liquid to gas and a volumetric expansion occurs in a process referred to as Acoustic Droplet Vaporisation (ADV). ADV of the anti-VCAM1 droplets, confirmed by passive cavitation detection, was also shown to cause blood brain barrier permeabilisation in vivo (Figures 1a and 1b).

## Blood brain barrier breakdown



## Tumour targeting

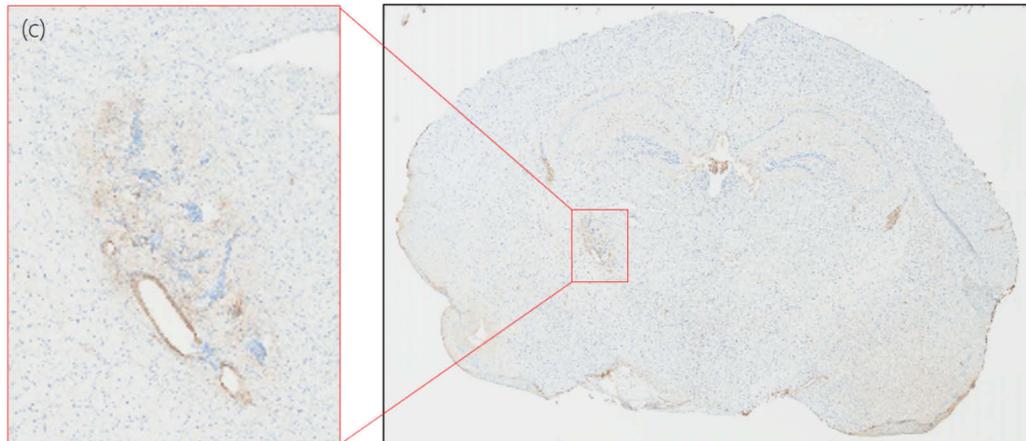


Figure 1: (a) and (b) IgG staining used to assess the integrity of the blood brain barrier with and without nanodroplets delivered intravenously, (c) Prussian blue staining (for the iron oxide in the nanodroplets) coaligned with immunohistochemical VCAM-1 staining (brown) around tumour cells

Quantifying the targeting efficiency of the droplets is extremely important for the eventual clinical utility. To this end, a total internal reflection fluorescence (TIRF) set-up was used to quantify binding of single droplets to immobilised VCAM1 under flow conditions, and the benefit of temporary magnetic accumulation on longer-term binding was also analysed. The in vitro dependence of the magnetic accumulation of these droplets on vessel diameter and flow rate was found to agree well with mathematical modelling.

The dependence of the in vitro threshold pressure required for ADV on the droplet concentration and magnetic accumulation was also investigated by monitoring acoustic emissions and B-mode imaging. This has been compared to passive cavitation detector (PCD) data from the in vivo experiments. The implications of these findings and the plans for future investigations into the therapeutic potential of these highly selective, ultrasound responsive agents will be discussed.

## References

1. A. F. Eichler, E. Chung, D. P. Kodack, J. S. Loeffler, D. Fukumura, and R. K. Jain, "The biology of brain metastases—translation to new therapies," *Nat. Rev. Clin. Oncol.*, vol. 8, no. 6, pp. 344–56, Apr. 2011.
2. P. Y. Wen and J. S. Loeffler, "Management of brain metastases.," *Oncology (Williston Park)*, vol. 13, no. 7, pp. 941–54, 957–61–2, 9, Jul. 1999.
3. S. Serres et al., "Molecular MRI enables early and sensitive detection of brain metastases.," *Proc. Natl. Acad. Sci. U. S. A.*, vol. 109, no. 17, pp. 6674–9, Apr. 2012.

# Tunable Oxygen Scavenging Using Acoustic Droplet Vaporization

*Haili Su<sup>1</sup>, Karla P. Mercado-Shekhar<sup>1</sup>, Rohan Srivastava<sup>3</sup>, P. Arunkumar<sup>1</sup>, Bin Zhang<sup>4</sup>, Christy Holland<sup>1,2</sup>, Kevin Haworth<sup>1,2</sup>*

<sup>1</sup> *Department of Internal Medicine, University of Cincinnati, Cincinnati, OH, USA*

<sup>2</sup> *Department of Biomedical Engineering, University of Cincinnati, Cincinnati, OH, USA*

<sup>3</sup> *Medical Science Program, University of Cincinnati, Cincinnati, OH, USA*

<sup>4</sup> *Division of Biostatistics and Epidemiology, Cincinnati Children's Hospital Medical Center, Cincinnati OH, USA*

## Background and Objective

Acoustic droplet vaporization (ADV) is the ultrasound-mediated phase transition of liquid perfluorocarbon droplets into gas microbubbles (Kripfgans et al. 2000). The partial pressure of non-perfluorocarbon gases in the newly formed microbubbles is significantly lower than the surrounding fluid. This difference in partial pressures creates a concentration gradient that drives nitrogen and oxygen into the microbubbles (Kripfgans et al. 2000; Radhakrishnan et al. 2016; Reznik et al. 2012; Sheeran et al. 2011), effectively providing a means of scavenging these gases from the surrounding fluid. Gas scavenging may have both beneficial and deleterious bioeffects. The magnitude of gas scavenging depends on the volume of perfluorocarbon phase-transitioned (Radhakrishnan et al. 2016), which in turn depends on the droplet population and ultrasound insonation parameters (Fabiilli et al. 2010; Kawabata et al. 2005; Martz et al. 2011). The objectives of this study were to 1) manufacture perfluorocarbon droplets of different sizes, 2) determine whether the surrounding fluid affects the amount of oxygen scavenged, and 3) demonstrate the ability to vary the amount of gas scavenged.

## Methods

Perfluorocarbon droplets were manufactured using either high-speed shaking (Kripfgans et al. 2000; Radhakrishnan et al. 2016) or a high-throughput microfluidic manufacturing technique (Haworth et al. 2017; Moncion et al. 2017). Droplets manufactured with high-speed shaking were made by mixing either 0.75 mL of 4 mg/mL bovine serum albumin (BSA) in phosphate-buffered saline (PBS) with 0.25 mL of perfluoropentane (PFP) or 1.5 mL of 500 mg/mL Pluronic F68 in deionized water with 0.212 mL of PFP. The surfactant, saline, and PFP were shaken at 4800 rpm for 30 s at 4°C. Differential centrifugation was used to isolate the droplet populations by size (Mercado et al. 2016). High-throughput microfluidic manufacturing was performed by extruding a 62.5 mg/mL solution of Pluronic F68 in PBS at 5.5  $\mu\text{L}/\text{min}$  and PFP at 1.0  $\mu\text{L}/\text{min}$  through a flow focusing device with 14  $\mu\text{m}$   $\times$  17  $\mu\text{m}$  channels (Haworth et al. 2017).

Droplets were diluted in PBS, a PBS and polyvinylpyrrolidone (PVP) mixture, a PBS and BSA mixture, or in porcine plasma, and pumped through a flow phantom in a 37 °C water bath at 10 mL/min, mimicking branching arteries. The properties of each of these fluids are shown in Table 1. The PVP solutions mimicked the viscosity of porcine plasma and whole blood (Walker et al. 1976) without modifying the protein content. The droplets were exposed to pulsed

ultrasound (5 MHz center frequency, 10 cycles, 2 ms pulse repetition period) at 0 MPa or 4.25 MPa peak negative pressure. A dissolved oxygen sensor was placed 10 s downstream of the ultrasound insonation location. The effluent of the system was collected. The concentration and size distribution of the droplets in the effluent were measured with a Multisizer 4. Statistical differences in oxygen scavenging were assessed by ANOVA.

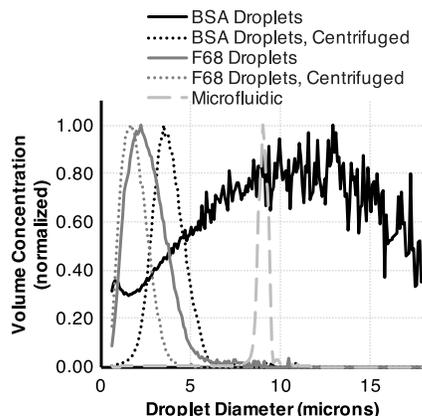
To assess whether the amount of oxygen scavenged could be tuned, droplet volume concentrations between  $8 \times 10^{-5}$  and  $4 \times 10^{-3}$  mL of PFP per mL of diluent fluid were pumped at 40 mL/min through the flow phantom and exposed to ultrasound (5 MHz, 5 cycles, 1 ms pulse repetition period) at 0 MPa or 4.05 MPa peak negative pressure. The total volume percent of PFP in the effluent fluid was measured and used with an empirical model to predict the extent of oxygen scavenging (Radhakrishnan et al. 2016). The model was modified to include the effect of surface tension (Evans et al. 2006). The measured and predicted dissolved oxygen values were compared using intra-class correlation.

**Table 1:** Fluid properties of diluent fluids. Values are the mean and standard deviation of three measurements.

Fluid Type	Dynamic Viscosity (cP)	Protein Concentration (mg/mL)	Dynamic Surface Tension (mN/m)
0.01 M PBS	0.74±0.01	0.0±0.0	68.1±0.5
3 mg/mL PVP	1.18±0.02	0.0±0.0	64.7±0.2
15 mP/mL PVP	4.04±0.05	0.0±0.0	65.1±0.1
68.4 mg/mL BSA	0.98±0.03	68.4±0.0	64.0±0.5
Porcine Plasma	1.20±0.01	68.7±0.0	62.2±1.1

## Results

Figure 1 is a plot of the size distribution of each droplet formulation. Table 2 lists the mean volume-weighted droplet diameter, polydispersity index, and volume-weighted concentration in the manufactured stock solutions. The approximate production rates to obtain approximately 1 mL of stock solution using 1) high-speed shaking with BSA, 2) high-speed shaking with BSA and centrifugation for size-isolation, 3) high-speed shaking with Pluronic F68, 4) high-speed shaking with Pluronic F68 and centrifugation for size-isolation, and 5) F68 microfluidic manufacturing were  $3.41 \times 10^{10} \mu\text{m}^3/\text{min}$ ,  $0.02 \times 10^{10} \mu\text{m}^3/\text{min}$ ,  $0.14 \times 10^{10} \mu\text{m}^3/\text{min}$ ,  $0.04 \times 10^{10} \mu\text{m}^3/\text{min}$ , and  $0.07 \times 10^{10} \mu\text{m}^3/\text{min}$ , respectively. High-speed shaking using a BSA solution produced the largest volume of droplets both per unit time and per unit volume. However, the size distribution had the highest polydispersity index. Centrifugation decreased the polydispersity, but also decreased the production rate and volume concentration. Microfluidic manufacturing produced the least polydisperse droplets, though at a relatively large mean diameter.



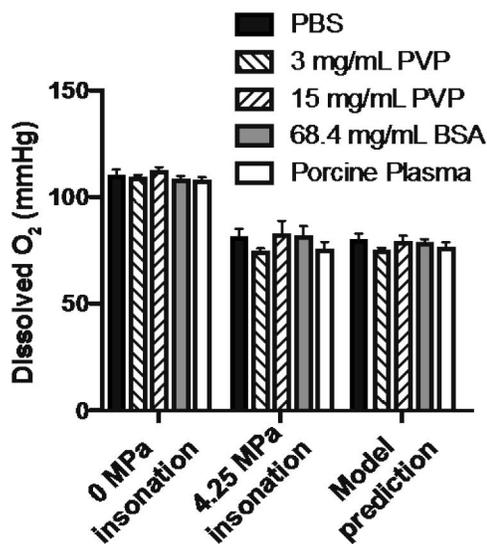
**Figure 1:** Normalized volume-weighted size-distribution of perfluoropentane droplets.

Figure 2 is a plot of the partial pressure of oxygen in each fluid after no ultrasound exposure (0 MPa) or ultrasound exposure (4.25 MPa). The predicted partial pressure of oxygen, based on the numerical model using the volume concentration of PFP is also shown. There is no statistically significant difference in the partial pressure of oxygen between the fluid types within the no ultrasound group, ultrasound group, or model group ( $p > 0.05$ ). Additionally, there is no statistically significant difference between the measured and predicted partial pressure of oxygen ( $p > 0.05$ ). These results indicate that for the range of fluid properties studied, there was no measurable effect on the magnitude of oxygen scavenging.

**Table 2:** Droplet volume-weighted mean diameter, polydispersity index, and volume concentration for each formulation.

Droplet Formulation Method	Mean Diameter $r$ ( $\mu\text{m}$ )	Poly-dispersity Index	Volume Concentration ( $\mu\text{m}^3/\text{mL}$ , $\times 10^{11}$ )
High-speed shaking with BSA	10.0	7.8	1.71
High-speed shaking with BSA and centrifugation	3.8	1.3	0.02
High-speed shaking with F68	2.7	1.9	0.17
High-speed shaking with F68 and centrifugation	1.9	1.6	0.04
Microfluidic formation	9.0	1.2	0.56

Figure 3 is a plot of the measured and predicted partial pressures of oxygen in the diluent fluid after ADV. The initial centrifuged BSA droplet concentration was varied. The top graph plots the partial pressure of oxygen as a function of the volume of PFP phase-transitioned. The predicted and observed partial pressures were in agreement (intraclass correlation coefficient of 0.94 and  $p$ -value  $< 0.0001$ ; Pearson correlation coefficient of 0.97 and  $p$ -value  $< 0.0001$ ). The average volume of PFP phase-transitioned across all experiments was  $27\% \pm 7\%$ . The bottom graph plots the data as a function of the initial volume of PFP in the diluent fluid. The model prediction assumed a transition efficiency of 27%.



**Figure 2:** The dissolved oxygen partial pressure without ultrasound (0 MPa), with ultrasound (4.25 MPa), or the predicted values. No significant difference between the measured and predicted values for the different fluid types.

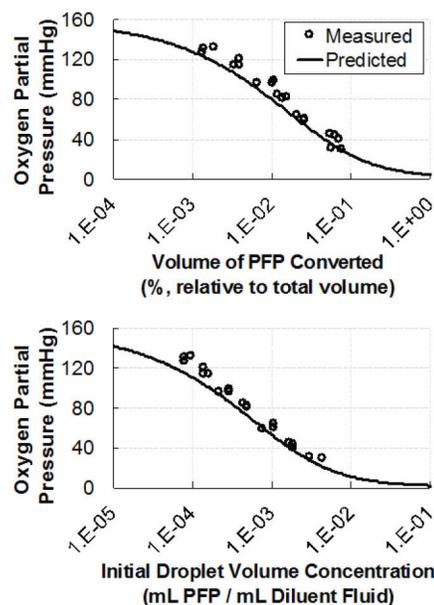


**Figure 3:** Measured and predicted partial pressure of oxygen in the diluent fluid after ADV. (Top) Predicted value computed from the measured volume of PFP converted. (Bottom) Predicted value computed from the initial droplet concentration assuming 27% droplet transition efficiency.

## Discussion and Conclusions

The concentration, production rate, and size distribution of droplets can be modified through changes in both the formulation and manufacturing technique. High concentrations and production rates are needed to achieve the nominal droplet concentrations in the diluent fluid, approximately  $10^5$  droplets/mL to  $10^8$  droplets/mL, necessary to enhance scavenging of dissolved oxygen. The fraction of droplets that phase-transition has been shown to increase with increasing droplet diameter (Fabiilli et al. 2010; Mercado et al. 2016). However, large droplets may occlude vessels (Kripfgans et al. 2005; Radhakrishnan et al. 2016; de Jong et al. 1993). Thus, it is necessary to control the droplet size distribution. Using centrifugation for size-isolation of the droplets resulted in low concentrations, due in part to a significant loss in the number of droplets, thus wasting much of the constituent materials. For the diluent fluid properties examined, surface tension, viscosity, and protein content did not affect the magnitude of dissolved gas scavenging, thus enabling future in vitro experiments to be performed in simple buffers. The partial pressure of oxygen could be reduced between 20% and 80% by varying the initial droplet concentration. The in situ Mechanical Index of the insonation was 1.8. A high correlation was found between the final partial pressure of oxygen and the initial droplet concentration, potentially allowing the reduction in partial pressure to be tuned without the need for in situ measurements. These results help set the stage for investigating the beneficial and negative bioeffects of gas scavenging caused by ADV in vivo.

## Acknowledgements

This work was supported by the United States National Institutes of Health through grant K25HL133452 and the American Heart Association through grant 16SDG27250231.

## References

1. de Jong N, ten Cate FJ, Vletter WB, Roelandt JRTC. Quantification of Transpulmonary Echocontrast Effects. *Ultrasound Med Biol* 1993;19:279–288.
2. Evans DR, Parsons DF, Craig VSJ. Physical properties of phase-change emulsions. *Langmuir* 2006;22:9538–9545.
3. Fabiilli ML, Haworth KJ, Sebastian IE, Kripfgans OD, Carson PL, Fowlkes JB. Delivery of Chlorambucil Using an Acoustically-Triggered Perfluoropentane Emulsion. *Ultrasound Med Biol* 2010;36:1364–1375.
4. Haworth KJ, Goldstein BH, Mercado-Shekar KP, Srivastava R, Arunkumar P, Su H, Privitera EM, Holland CK, Redington AN. Dissolved Oxygen Scavenging by Acoustic Droplet Vaporization using Intravascular Ultrasound. *IEEE Int Ultrason Symp Washington DC, 2017*. pp. 1–4.
5. Kawabata K-I, Sugita N, Yoshikawa H, Azuma T, Umemura S-I. Nanoparticles with Multiple Perfluorocarbons for Controllable Ultrasonically Induced Phase Shifting. *Jpn J Appl Phys* 2005;44:4548–4552.
6. Kripfgans OD, Fowlkes JB, Miller DL, Eldevik OP, Carson PL. Acoustic droplet vaporization for therapeutic and diagnostic applications. *Ultrasound Med Biol* 2000;26:1177–1189.
7. Kripfgans OD, Orifici CM, Carson PL, Ives KA, Eldvik OP, Fowlkes JB. Acoustic Droplet Vaporization for Temporal and Spatial Control of Tissue Occlusion: A Kidney Study. *IEEE Trans Ultrason Ferroelectr Freq Control* 2005;52:1101–1110.
8. Martz TD, Sheeran PS, Bardin D, Lee AP, Dayton PA. Precision Manufacture of Phase-Change Perfluorocarbon Droplets Using Microfluidics. *Ultrasound Med Biol* 2011;37:1952–1957.
9. Mercado KP, Radhakrishnan K, Stewart K, Snider L, Ryan D, Haworth KJ. Size-isolation of ultrasound-mediated phase change perfluorocarbon droplets using differential centrifugation. *J Acoust Soc Am* 2016;139:EL142–EL148.
10. Moncion A, Lin M, O'Neill EG, Franceschi RT, Kripfgans OD, Putnam AJ, Fabiilli ML. Controlled release of basic fibroblast growth factor for angiogenesis using acoustically-responsive scaffolds. *Biomaterials* 2017;140:26–36.
11. Radhakrishnan K, Holland CK, Haworth KJ. Scavenging dissolved oxygen via acoustic droplet vaporization. *Ultrason Sonochem* 2016;31:394–403.
12. Reznik N, Seo M, Williams R, Bolewska-Pedyczak E, Lee M, Matsuura N, Garipey J, Foster FS, Burns PN. Optical studies of vaporization and stability of fluorescently labelled perfluorocarbon droplets. *Phys Med Biol* 2012;57:7205.
13. Sheeran PS, Wong VP, Luois S, McFarland RJ, Ross WD, Feingold S, Matsunaga TO, Dayton PA. Decafluorobutane as a Phase-Change Contrast Agent for Low-Energy Extravascular Ultrasonic Imaging. *Ultrasound Med Biol* 2011;37:1518–1530.
14. Walker A, Naylor GP, Humphries WV. Measurement of blood viscosity using a conicylindrical viscometer. *Med Biol Eng* 1976;14:551–557.

# Acoustic Cluster Therapy

## Microdroplets boost microbubbles enhanced drug delivery

A. van Wamel<sup>1</sup>, A.K.O. Åslund<sup>1</sup>, P. Sontum<sup>2</sup>, Paul Prentice<sup>3</sup>, A. Healey<sup>2</sup>, S. Snipstad<sup>1</sup>, Melina Mühlenpfordt<sup>1</sup>, S. Kvåle<sup>2</sup>, N. Bush<sup>4</sup>, J. Bamber<sup>4</sup>, and C. de Lange Davies<sup>1</sup>.

<sup>1</sup>Dept. of Physics, NTNU, Trondheim, Norway, <sup>2</sup>Phoenix Solutions AS, Oslo, Norway., <sup>3</sup>Cavitation Research Laboratory, Medical and Industrial Ultrasonics, University of Glasgow, Scotland, <sup>4</sup>Joint Dept. of Physics, ICR, London, UK.

Acoustic Cluster Therapy is a novel microtechnology delivery platform based on clusters of microbubbles and microdroplets. The ACT formulation is formed by reconstitution of commercially available, negatively charged microbubbles (Sonazoid™, GE Healthcare) with an emulsion of positively charged microdroplets of inert, perfluorated oil. The microbubbles/microdroplet clusters formed from electrostatic attraction are engineered to phase shift (vaporize) in-vivo in a controlled manner. After i.v. injection of the clusters together with a drug, when exposed to regular diagnostic ultrasound at the targeted pathology, the microbubbles transfer acoustic energy to the attached droplets, which undergo a liquid-to-gas phase shift (the “Activation” Step). The resulting vapor bubbles undergo a rapid expansion to approximately 25 μm and are temporarily deposited in a small fraction of the capillaries, transiently stopping blood flow for up to 10 min. Further application of ultrasound (the “Enhancement” step) oscillates the bubbles and induces non-thermal mechanisms such as cavitation and shear forces that increase the local permeability of the vasculature, and increase transport of the co-administered drug across the capillary wall and through the extracellular matrix. The concept is described in (1,2) and the Figure below.

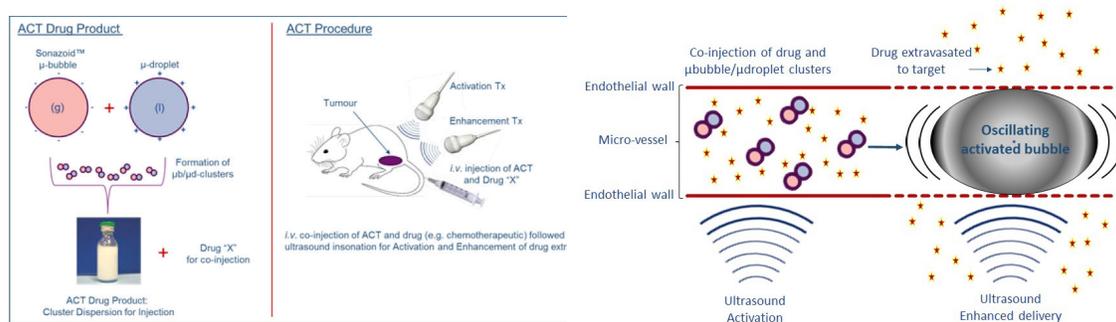


Figure: Microdroplet-microbubble clusters are injected into mice. Diagnostic ultrasound is applied for activation of the bubbles and enhance delivery of injected drugs. During activation, the microdroplet undergo a phase shift and form a large microbubble which blocks the capillary.

The ACT concept is shown to very efficiently deliver co-injected macromolecules (3) and drugs (4). Injecting the drugs paclitaxel and Abraxane® into mice with subcutaneously growing prostate tumors and applying the ACT, induced a very strong increase in the therapeutic efficacy compared to the drugs alone. All of the treated mice were alive 120 days after study start and

67% were in stable, complete remission (4). Furthermore, we have shown that ACT can open the blood-brain barrier safely, allowing macromolecules to enter into the brain tissue (5).

Ultrafast optical imaging (frame rate 10MHz) of the “activation” and “enhancement” steps of ACT in a small capillary revealed the behavior of ACT-bubbles under exposure to a focused ultrasound field. This will help to understand the mechanism behind the microdroplet-microbubble interactions and their interactions with the vessel wall.

## References

1. P. Sontum, S. Kvåle, A. Healey, R. Skurtveit, R. Watanabe, M. Matsumura, J. Ostensen. *Acoustic Cluster Therapy (ACT) - A novel concept for ultrasound mediated, targeted drug delivery*, *Int J Pharm*, 495 (2015) 1019-1027.
2. A. Healey, P. Sontum, S. Kvåle, M. Eriksen, R. Bendiksen, A. Tornes, J. Ostensen. *Acoustic Cluster Therapy: In Vitro and Ex Vivo Measurement of Activated Bubble Size Distribution and Temporal Dynamics*, *Ultrasound Med Biol*, 42 (2016) 1145–1166.
3. A. van Wamel, A. Healey, P. Sontum, S. Kvåle, N. Bush, J. Bamber, C. de Lange Davies. *Acoustic Cluster Therapy (ACT) - pre-clinical proof of principle for local drug delivery and enhanced uptake*, *J Control Release*, 224 (2016) 158-164.
4. A. van Wamel, P. Sontum, A. Healey, S. Kvåle, N. Bush, J. Bamber, C. de Lange Davies. *Acoustic Cluster Therapy (ACT) enhances the therapeutic efficacy of paclitaxel and Abraxane® for treatment of human prostate adenocarcinoma in mice*, *J Control Release*, 236 (2016) 15-21.
5. A.K.O. Åslund, S. Snipstad, A. Healey, S. Kvåle, S.H. Torp, P.C. Sontum, C. de Lange Davies, A. van Wamel. *Efficient Enhancement of Blood–Brain Barrier Permeability Using Acoustic Cluster Therapy (ACT)*, *Theranostics*, 7(1) (2017) 23-30.

# Super-Localisation Ultrasound Imaging using Sparse Activation of Low-Boiling-Point Nanodroplets

*Ge Zhang<sup>1</sup>, Sevan Harput<sup>1</sup>, Shengtao Lin<sup>1</sup>, Chee Hau Leow<sup>1</sup>, Kirsten Christensen-Jeffries<sup>2</sup>, Jemma Brown<sup>2</sup>, Christopher Dunsby<sup>3</sup>, Robert J. Eckersley<sup>2</sup>, Meng-Xing Tang<sup>1\*</sup>*

<sup>1</sup>*Department of Bioengineering, Imperial College London, London, UK, SW7 2AZ, United Kingdom*

<sup>2</sup>*Biomedical Engineering Department, Division of Imaging Sciences, Kings College London, London, SE1 7EH, UK*

<sup>3</sup>*Department of Physics and Centre for Pathology, Imperial College London, London, SW7 2AZ, UK*

*\*E-mail: (Ge.Zhang15@imperial.ac.uk & MengXing.Tang@imperial.ac.uk)*

## Background & Objective

Microbubble contrast agents have been widely investigated in super-resolution ultrasound imaging in-vitro [1], in-vivo [2, 3] and 3D [4-6]. Nanodroplets (also called phase-change contrast agents) are an alternative to microbubble contrast agents. They are physically smaller and have longer lifetime in-vivo [7]. Moreover, nanodroplets can be spatially and temporally selected to be converted into microbubbles via acoustic pressure dependent activation [8]. The feasibilities of performing super-resolution imaging [9] and sub-wavelength drug-delivery [10] have been respectively demonstrated using high-boiling-point nanodroplets. However, the clinical translation of this technique may be limited by the high energy/pressure required, particularly for deep tissue imaging.

In this study, we used low-boiling-point decafluorobutane (boiling point = -2 °C) nanodroplets to perform super-localisation imaging at a clinical imaging frequency. Instead of injecting a low concentration of microbubbles, the proposed method can selectively activate a subset of a high concentration of nanodroplets into microbubbles after injection by tuning the acoustic pressure and activation beam profile, potentially creating spatially isolated microbubbles which can be used to achieve ultrasound super-resolution imaging at clinically relevant frequencies. To the best of our knowledge, this is the first study using low-boiling-point nanodroplets to perform super-localisation ultrasound imaging.

## Methodology & Experimental Setup

The nanodroplet solution was prepared and characterised as described in previous literature [11]. The experiment was set up as illustrated in Figure 1. A 200 µm cellulose tube was fixed and clamped in a water tank surrounded by acoustic absorbers. The nanodroplet solution was infused to the syringe equipped with a syringe pump. Experiments were performed using deionised and degassed water at 37 °C. A Verasonics L11-4v linear array transducer was clamped and held 16mm above the tube. A customised activation and imaging pulse sequence [12] using Verasonics platform was used to activate the nanodroplets into microbubbles and obtain images before and after the activation. Super-localisation of spatially isolated vaporised nanodroplets signals was performed as explained in [2, 13]. The ‘centroiding method’ was used to determine

the signal locations [2]. The full-width-half-maximum of the microbubble localisation distribution was used to estimate the diameter of the 200  $\mu\text{m}$  cellulose tube.

## Results & Discussion

As can be seen from Figure 2, different spatial distributions of spatially isolated vaporised nanodroplets are seen in 3 different frames. The centroid of each vaporised nanodroplet was counted as a single localisation event. Figure 3 shows the original B-mode and super-localisation images of the 200  $\mu\text{m}$  cellulose tube. The resulting localisation map was created from all the localisations detected over all the imaging frames. As shown in Figure 4, a histogram plot shows the detection of individual vaporised nanodroplet events in the axial direction across the region of interest at the central 5 mm of tube along the lateral direction for both B-mode and super-localisation images. The B-mode image shows a full-width-half-maximum estimation of 560  $\mu\text{m}$  while the super-localisation technique gives an estimation of 202  $\mu\text{m}$ .

## Conclusion

In this study, we report the use of low-boiling-point nanodroplets to perform acoustic super-localisation imaging in a 200  $\mu\text{m}$  cellulose tube, taking advantages of sparse activation of PCCAs at a clinically safe acoustic pressure level.

**Acknowledgement:** special thanks to all the members in the Ultrasound Laboratory for Imaging and Sensing (ULIS) Group, Imperial College London.

## Reference

1. Viessmann, O.M., et al., *Acoustic super-resolution with ultrasound and microbubbles*. *Phys Med Biol*, 2013. 58(18): p. 6447-58.
2. Christensen-Jeffries, K., et al., *In Vivo Acoustic Super-Resolution and Super-Resolved Velocity Mapping Using Microbubbles*. *Ieee Transactions on Medical Imaging*, 2015. 34(2): p. 433-440.
3. Errico, C., et al., *Ultrafast ultrasound localization microscopy for deep super-resolution vascular imaging*. *Nature*, 2015. 527(7579): p. 499-502.
4. O'Reilly, M.A. and K. Hynynen, *A super-resolution ultrasound method for brain vascular mapping*. *Med Phys*, 2013. 40(11): p. 110701.
5. Desailly, Y., et al., *Sono-activated ultrasound localization microscopy*. *Applied Physics Letters*, 2013. 103(17): p. 174107.
6. Christensen-Jeffries, K., et al., *3-D In Vitro Acoustic Super-Resolution and Super-Resolved Velocity Mapping Using Microbubbles*. *IEEE TRANSACTIONS ON ULTRASONICS, FERROELECTRICS, AND FREQUENCY CONTROL*, 2017. 64.
7. Sheeran, P.S. and P.A. Dayton, *Improving the performance of phase-change perfluorocarbon droplets for medical ultrasonography: current progress, challenges, and prospects*. *Scientifica (Cairo)*, 2014. 2014: p. 579684.
8. Lin, S., et al., *Effects of microchannel confinement on acoustic vaporisation of ultrasound phase change contrast agents*. *Physics in Medicine & Biology*, 2017. 62(17): p. 6884.
9. Luke, G.P., A.S. Hannah, and S.Y. Emelianov, *Super-Resolution Ultrasound Imaging in Vivo with Transient Laser-Activated Nanodroplets*. *Nano Lett*, 2016. 16(4): p. 2556-9.
10. Hingot, V., et al., *Subwavelength far-field ultrasound drug-delivery*. *Applied Physics Letters*, 2016. 109(19): p. 194102.
11. Lin, S., et al. *Vaporising phase change ultrasound contrast agent in microvascular confinement*. in *2016 IEEE International Ultrasonics Symposium (IUS)*. 2016.
12. Zhang, G., et al. *Acoustic response of targeted nanodroplets post-activation using high frame rate imaging*. in *2017 IEEE International Ultrasonics Symposium (IUS)*. 2017.
13. Harput, S., et al. *Two stage sub-wavelength motion correction in human microvasculature for CEUS imaging*. in *2017 IEEE International Ultrasonics Symposium (IUS)*. 2017.

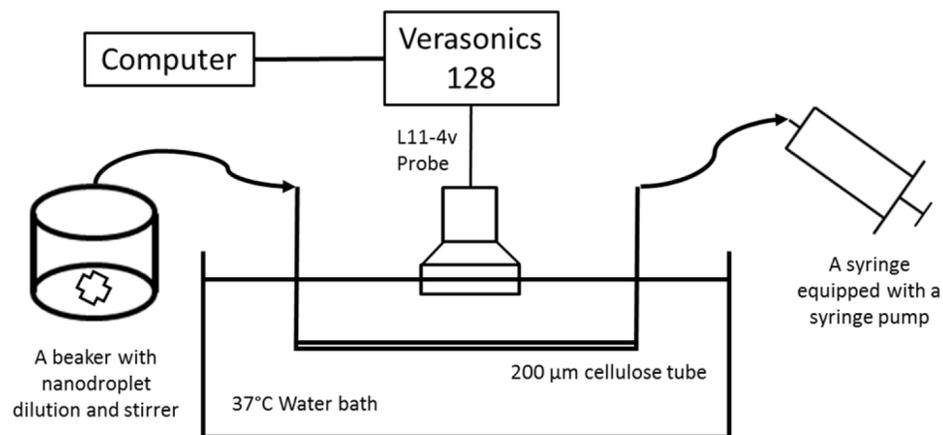


Figure 1. Experimental Setup (Not to scale).

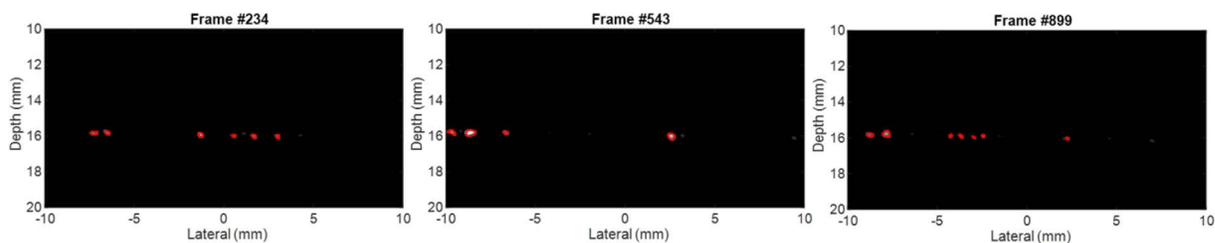


Figure 2. The localisation events of individual vaporised nanodroplets at frame 234, 543 and 899 respectively. The flow rate is 10 mL/hr from the left to right.

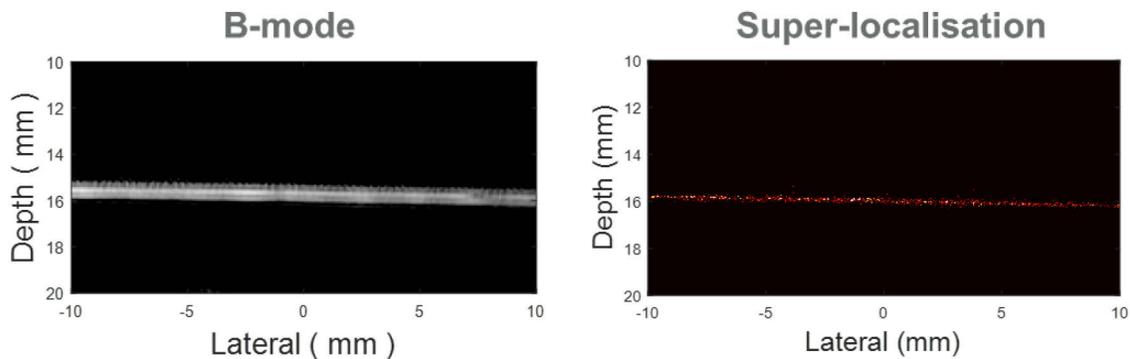


Figure 3. The B-mode (Left) and super localisation (Right) images of a 200 µm cellulose tube.

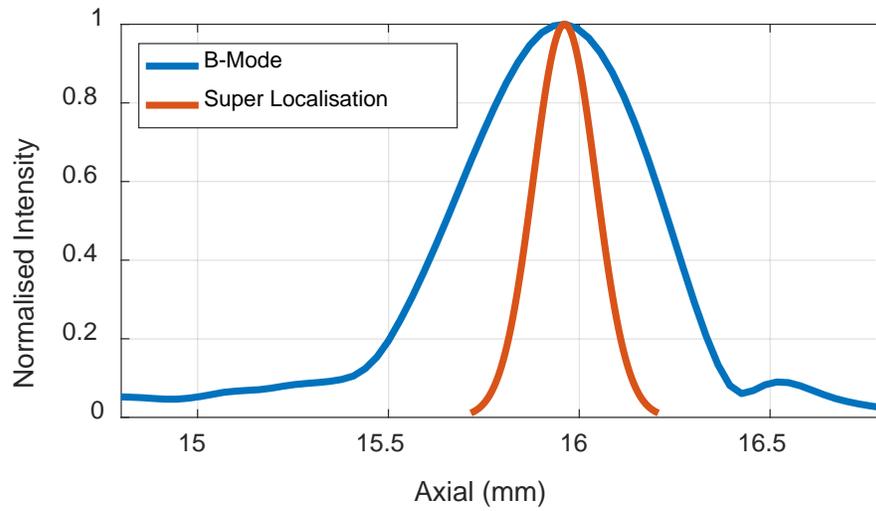


Figure 4. Normalised axial intensity plot at the central 5mm of tube (in lateral direction) was selected to compare the B-mode and super-localisation image.

# Perfluorocarbon nanodroplets in liposomes: preparation and triggered contents release by ultrasound

*Alexander L Klibanov<sup>1</sup>, Nikita Meka<sup>1</sup>, Galina B Diakova<sup>1</sup>, Kazuo Maruyama<sup>2</sup>, Ryo Suzuki<sup>1,2</sup>.*

*<sup>1</sup> Cardiovascular Division, Robert M Berne Cardiovascular Research Center, University of Virginia School of Medicine, Charlottesville, VA 22908-1394 USA; <sup>2</sup> School of Pharmacy, Teikyo University, Tokyo, Japan.*

Stimuli-responsive drug release from pharmaceutical carriers is widely investigated as a next-generation targeted delivery approach. Ultrasound - as a trigger for drug release from the carrier micro- or nanoparticles - offers numerous advantages: medical ultrasound equipment is portable and inexpensive; ultrasound can be tightly focused; therapeutic ultrasound is used in image-guided therapy. However, microbubbles only circulate for several minutes, and longer circulation time is necessary for repeated recirculation through the target area, to improve drug delivery efficacy and therapeutic index. Perfluorocarbon nanodroplets can carry only limited amounts of hydrophobic drugs in the shell. Here we report simplified methods for the preparation of a “concentric” liposome-nanodroplet complex: liposomes can entrap water-soluble drugs along with the liquid perfluorocarbon nanoparticles (e.g., decafluorobutane or perfluoropentane) in superheated state: perfluorocarbon liquid nanoparticles are stable even at 37°C yet achieve shift to gas phase, i.e., convert to gas bubbles in response to ultrasound. Volume is increased over 100x, and the membrane of carrier liposome should rupture, releasing the drug. These liposomes loaded with liquid perfluorocarbon nanodroplets and co-entrap calcein dye demonstrate efficient ultrasound-triggered contents release.

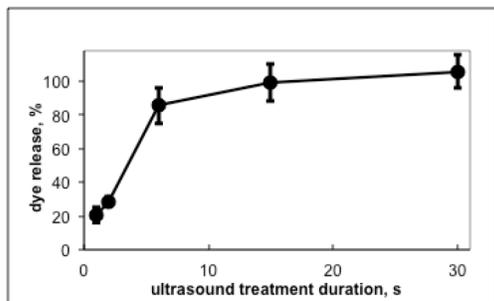
Liposomes were prepared by a proliposome method. Briefly, DOPC/ethanol/aqueous calcein (1:1:1 mass ratio) solution was prepared; to 0.15 ml of this mixture 10 ml of decafluorobutane gas was added, pressurized to achieve gas conversion to liquid, and mixture emulsified by a repeated passage through 0.4  $\mu\text{m}$  Nuclepore membrane. Alternatively, perfluoropentane or perfluorobutane-perfluoropentane mixture was used. Fluorocarbon-ethanol-water emulsion was rapidly diluted with 20x excess of normal saline, resulting in liposome formation. Free calcein dye was removed by repeated centrifugation (sedimentation) in normal saline; liposomes co-entrapping perfluorocarbon nanoparticles were then diluted with normal saline and stored on ice. If necessary, free liposomes were separated from the liposome-nanodroplet complexes as well as from free perfluorocarbon nanodroplets by gradient centrifugation in high-density media (sucrose, Omnipaque). A physical therapy ultrasound apparatus (Birtcher Megason, generating continuous 1 MHz ultrasound) was used for insonation. Liposome samples in thin-walled PCR tubes were embedded in the ultrasound gel stack connected to the transducer. Rapid conversion of liquid perfluorocarbon to gas during insonation was clearly observed as turbidity increase. Calcein release from liposomes upon insonation was assessed by fluorescence dequenching using a Spectramax XS fluorometer; addition of Triton X-100 was used to achieve complete dye release (100% control).

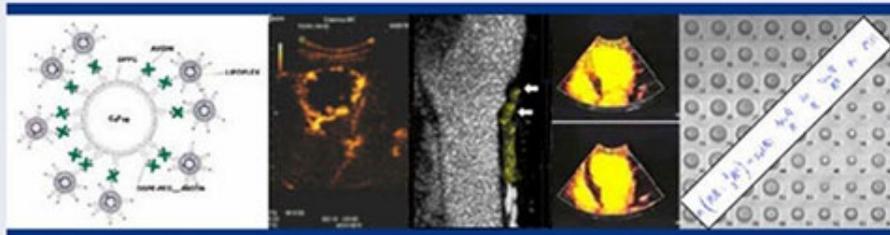
At maximum ultrasound power ( $\sim 3\text{W}/\text{cm}^2$ ), over 80% dye release was achieved within 6 s of insonation from perfluorobutane-based particles; they provided much better release efficacy than

perfluoropentane. Control liposomes lacking perfluorocarbon nanodroplets demonstrated very slow dye leakage, even in response to ultrasound treatment.

Overall, “concentric” perfluorocarbon liquid nanoparticle liposome complexes may provide ultrasound-triggered liposome drug delivery platform with a wide variety of applications.

This study was supported in part via NIH R21 EB016752 and R01 EB023055.



**Congresses | The 23rd European symposium on Ultrasound Contrast Imaging****18-19 January 2018 - Hilton Hotel  
Rotterdam, The Netherlands****The 23rd European symposium on  
Ultrasound Contrast Imaging****An ICUS Conference**

Organised by Nico de Jong, Folkert ten Cate, Rik Vos, Klazina Kooiman, and Arend Schinkel  
Scientific board: Mike Averkiou, Paolo Colonna, David Cosgrove, Edward Leen, and Eleanor Stride

**WEBCASTING**

Introducing exciting news for our friends who are not able to join the 23rd European symposium on Ultrasound Contrast Imaging in Rotterdam! To learn from the best in the world even if travel is not an option, you can join the Symposium through worldwide live streaming by the WEB CONFERENCE CHANNEL, through Livemedia [www.livemedia.com/23symposium](http://www.livemedia.com/23symposium). For info of the the previous symposium check [www.livemedia.com/22symposium](http://www.livemedia.com/22symposium).

Videos will remain hosted on Livemedia indefinitely and available for on demand viewing. Once registered, remote participants will receive log in credentials that will allow them access and will monitor the viewing time. GAIN ONLINE ACCESS to the well known 23rd European symposium on Ultrasound Contrast Imaging.

Please register here: [www.livemedia.com/23symposium](http://www.livemedia.com/23symposium). For any inquiries please contact Irene Syraki [irene@livemedia.gr](mailto:irene@livemedia.gr) or the symposium secretariat.





**The 23<sup>rd</sup> European Symposium on Ultrasound Contrast Imaging Rotterdam is sponsored by:**

***Bracco Suisse SA***

Marco Graf, Senior  
Communication Events Manager  
Centro Galleria 2  
Via Cantonale  
CH-6928 Manno - Switzerland

***GE Healthcare***

Marta Gonzalez de Suso  
Global Product Manager  
Ultrasound Contrast Media  
Life Sciences-Core Imaging  
The Grove Centre, White Lion  
Road, Amersham, HP7 9LL UK

***Philips Healthcare***

John MacQuarrie  
Senior Product Manager -  
Ultrasound  
Philips Healthcare  
22100 Bothell Everett  
Highway  
Bothell, WA 98021 U.S.A.

***Siemens Healthcare***

Richard Medley, Product Manager  
Ultrasound-EMEA  
Sir William Siemens Square  
Newton House, Frimley,  
Camberley, SY GU16 8QD – UK

***Samsung Electronics***

***Benelux***

Luc van Dalen, Business  
Development Manager  
Health Medical Equipment  
Evert van de Beekstraat 310  
1118 CX Schiphol – Neth.

***Toshiba Medical***

***Systems Europe BV***

Christoph Simm, MD, PhD  
Business Unit Manager  
Ultrasound  
Zilverstraat 1  
2718 RP Zoetermeer  
The Netherlands

***Hitachi Medical Systems***

Romea Wallnoefer  
Marketing Communications  
Manager  
Europe Holding AG  
Sumpfstrasse 13  
CH-6300 Zug - Switzerland

***Visualsonics***

Adrie Gubbels  
Joop Geesinkweg 140  
1114 AB Amsterdam  
The Netherlands

***Oldelft Ultrasound***

Stefan Roggeveen  
Commercial Manager  
Elektronicaweg 10  
2628 XG Delft  
The Netherlands

***Verasonics, Inc.***

Mike Vega  
Vice President of Business  
Development & Sales  
11335 NE 122 Way, Suite 100  
Kirkland, WA 98034  
USA

***Coeur***

Eric Boersma  
Erasmus MC - Thoraxcenter  
Dr. Molewaterplein 50  
3015 GE Rotterdam  
The Netherlands

***Nederlandse***

***Hartstichting***

Mrs. E. Buitenhuis  
Manager Research Dept.  
P.O. Box 300  
2501 CH Den Haag  
The Netherlands

***Mindray Medical***

***Germany GmbH***

Hongbo Zhu  
Marketing Ultrasound Europe  
Goebelstrasse 21  
64293 Darmstadt  
Germany

***Advanced Microbubbles***

***Laboratories LLC***

Jameel Feshitan PhD,  
Chief Executive Officer  
1880 S. Flatiron Ct Unit H-2,  
Boulder CO, USA 80301  
USA

FIRST ANNOUNCEMENT 2019

**24<sup>th</sup> EUROPEAN SYMPOSIUM ON  
ULTRASOUND CONTRAST IMAGING**

**17-18 JANUARY 2019**

**ROTTERDAM, THE NETHERLANDS**

Information on the 24<sup>th</sup> EUROPEAN SYMPOSIUM ON ULTRASOUND CONTRAST  
IMAGING: Mieke Pruijsten, [m.pruijsten@erasmusmc.nl](mailto:m.pruijsten@erasmusmc.nl)

# sponsors:

## Golden sponsor



GE Healthcare



PHILIPS

SIEMENS  
Healthineers

## Silver sponsor

TOSHIBA  
MEDICAL



Oldelft  
Ultrasound

mindray  
healthcare within reach

SAMSUNG

HITACHI  
Inspire the Next

VISUALSONICS  
FUJIFILM

# The 23<sup>rd</sup> European Symposium of Ultrasound Contrast Imaging, Rotterdam is sponsored by:



GE Healthcare



**SIEMENS**  
**Healthineers**

**PHILIPS**

 **Verasonics**  
The leader in Research Ultrasound™

 **Oldelft**  
**Ultrasound**

**SAMSUNG**

**mindray**  
healthcare within reach



  
**VISUALSONICS**  
**FUJIFILM**

**TOSHIBA**  
**MEDICAL**



  
**AMB**  
*Labs*

**HITACHI**  
Inspire the Next